Forschungszentrum Karlsruhe
Technik und Umwelt

Wissenschaftliche Berichte
FZKA 6295

Experimental and Calculational Results of the Experiments QUENCH-02 and QUENCH-03

P. Hofmann, C. Homann, W. Leiling,
A. Miassoedov, D. Piel, G. Schanz,
L. Schmidt, L. Sepold, M. Steinbrück

Institut für Materialforschung
Institut für Reaktorsicherheit
Projekt Nukleare Sicherheitsforschung

Juli 2000

Forschungszentrum Karlsruhe

Technik und Umwelt

Wissenschaftliche Berichte

FZKA 6295

Experimental and Calculational Results of the Experiments QUENCH-02 and QUENCH-03

P. Hofmann, C. Homann, W. Leiling, A. Miassoedov,
D. Piel, G. Schanz, L. Schmidt, L. Sepold, M. Steinbrück

Institut für Materialforschung
Institut für Reaktorsicherheit
Projekt Nukleare Sicherheitsforschung

Forschungszentrum Karlsruhe GmbH, Karlsruhe
2000

Forschungszentrum Karlsruhe GmbH
Postfach 3640, 76021 Karlsruhe

Mitglied der Hermann von Helmholtz-Gemeinschaft
Deutscher Forschungszentren (HGF)

ISSN 0947-8620

Abstract

The QUENCH experiments are to investigate the hydrogen source term that results from the water injection into an uncovered core of a Light Water Reactor (LWR).

The test bundle is made up of 21 fuel rod simulators with a length of approximately 2.5 m. 20 fuel rod simulators are heated over a length of 1024 mm, the one unheated fuel rod simulator is located in the center of the test bundle. Heating is carried out electrically using 6-mm-diameter tungsten heating elements installed in the center of the rods and surrounded by annular ZrO_2 pellets. The rod cladding is identical to that used in LWRs: Zircaloy-4, 10.75 mm outside diameter, 0.725 mm wall thickness. The test bundle is instrumented with thermocouples attached to the cladding and the shroud at 17 different elevations with an axial distance between the thermocouples of 100 mm.

During the heatup or transient phase superheated steam together with the argon as carrier gas enters the test bundle at the bottom end and leaves the test section at the top together with the hydrogen that is produced in the zirconium-steam reaction. The hydrogen is analyzed by two different instruments: a mass spectrometer and a ”Caldos 7 G” hydrogen measuring device (a heat conductivity measurement system).

This report presents the results of Tests QUENCH-02 and QUENCH-03 performed in the QUENCH test facility at the Forschungszentrum Karlsruhe on July 7, 1998 and January 20, 1999, respectively. The objective of Experiments QUENCH-02 and QUENCH-03 was the investigation of the behavior on reflood of PWR fuel rods with little oxidation, i.e. on test rods without a pre-oxidation phase (reference tests to those with a pre-oxidation phase).

Both experiments consisted of a heatup phase to temperature plateau of around 900 K, a transient phase, and a quenching phase. All phases except the quenching phase were conducted in an argon/steam atmosphere. At the beginning of the transient phase both test bundles were ramped at around 0.4 K/s in the temperature range 900 – 1400 K and 1.6 K/s (QUENCH-02) and 1.0 K/s (QUENCH-03) from 1400 K to the temperature excursion which led to a maximum rod cladding temperature of 2500 K.

The quench phase was initiated by turning off the argon and steam flow, filling the lower plenum with quench water at a high rate (90 g/s), and injecting argon at the bundle head. About 25 s later the test section was reflooded from the bottom at 40 - 50 g/s H_2O

achieving an injection velocity of 1.6 cm/s (QUENCH-02) and 1.3 cm/s (QUENCH-03). During the flooding phase the electrical power was reduced to 4 kW to simulate the decay heat level.

The onset of cooling of the rod claddings occurred within one second for all axial positions. The quench temperatures that were determined on the basis of the cladding temperatures of Test QUENCH-03 were between 677 K at the -250 mm and 846 K at the 650 mm elevation. (Due to a failure in the data acquisition during the QUENCH-02 experiment only a limited number of data were obtained in this test). An evaluation of the quench rates in Test QUENCH-03 resulted in 0.2 - 2.5 cm/s for the cladding, 0.2 – 2.0 cm/s for the shroud, and 1.4 cm/s based on the thermocouple signals installed inside the corner rods.

The total amount of hydrogen released during the QUENCH-02 and QUENCH-03 experiments was 190 g and 123 g, respectively.

The posttest appearance of both test bundles reveals melt formation and relocation as well as severe oxidation and embrittlement (fragmentation) of the rod claddings and shroud in the upper part. Above the axial midplane the shroud formed a kind of bubble where a blockage zone with solidified melt had formed and where debris had accumulated.

For both tests pretest calculations were performed with the SCDAP/RELAP5 computer code to determine important parameters which must be known to run the test properly. Posttest calculations were performed with the correct initial and boundary conditions. Temperature histories and hydrogen production are in good agreement with experimental data up to the beginning of the temperature excursion. The temperature excursion is calculated to occur somewhat later than in the experiment and to begin at the upper end of the heated zone.

Experimentelle und analytische Ergebnisse der Versuche QUENCH-02 und QUENCH-03

Zusammenfassung

In den QUENCH-Versuchen soll der Wasserstoffquellterm, der sich bei einer Einspeisung von Notkühlwasser in einen trockenen, überhitzten Reaktorkern eines Leichtwasserreaktors (LWR) ergibt, ermittelt werden.

Das QUENCH-Testbündel ist mit 21 Brennstabsimulatoren bestückt und hat eine Gesamtlänge von ca. 2,50 m. 20 Brennstabsimulatoren sind auf einer Länge von 1024 mm beheizt, der Zentralstab ist unbeheizt. Als Heizer werden Wolfram-Stäbe von 6 mm Durchmesser verwendet, die im Zentrum der Brennstabsimulatoren angeordnet und von ZrO_2-Ringtabletten umgeben sind. Die Stabhüllen sind identisch mit LWR-Hüllrohren: Zircaloy-4, 10,75 mm Außendurchmesser und 0,725 mm Wanddicke. Testbündel und Shroud sind mit Thermoelementen instrumentiert. Sie sind auf 17 Messebenen im Abstand von 100 mm angeordnet.

Während der Aufheizphase oder Transiente wird überhitzter Dampf zusammen mit Argon als Trägergas am unteren Ende in die Teststrecke eingespeist und verläßt diese zusammen mit dem Wasserstoff, der sich durch die Zirkonium-Dampf-Reaktion gebildet hat, am oberen Ende. Der Wasserstoff wird mit Hilfe von zwei Messgeräten analysiert: einem Massenspektrometer und einem Caldos-7G-Analysegerät (Wärmeleitfähigkeits-Meßsystem).

In diesem Bericht sind die Ergebnisse der Experimente QUENCH-02 und QUENCH-03, die am 7. Juli 1998 und am 20. Januar 1999 in der QUENCH-Versuchsanlage des Forschungszentrums Karlsruhe durchgeführt wurden, beschrieben. Ziel der Versuche QUENCH-02 und QUENCH-03 war die Untersuchung des Verhaltens von nicht oder leicht voroxidierten LWR-Brennstäben während der Flutung eines Brennstabbündels mit Notkühlwasser. Diese Experimente dienen als Referenzversuche für die Tests mit voroxidierten Stäben.

Beide Experimente liefen mit folgenden Versuchsphasen ab: einer Anfahr- oder Aufheizphase, um das Gesamtsystem bei ca. 900 K Bündeltemperatur ins thermische Gleichgewicht zu bringen, einer transienten (Aufheiz)-Phase und einer Abschreck- bzw. Quench-Phase. In der transienten Phase wurden die Bündel mit einer Aufheizrate von

ca. 0.4 K/s im Temperaturbereich von 900 bis 1400 K hochgeheizt. Ab 1400 K bis zum Beginn der Temperatureskalationen betrug die Aufheizrate 1,6 K/s (QUENCH-02) bzw. 1 K/s (QUENCH-03). Während der Temperatureskalationen wurden maximale Bündeltemperaturen von 2500 K gemessen.

Die Quench-Phase wurde mit dem Abschalten der Argon/Dampf-Zufuhr, dem Auffüllen des unteren Bündel-Plenums mit einem erhöhten Quench-Wasserstrom (90 g/s) und der gleichzeitigen Argon-Einspeisung in den Bündelkopf vorbereitet. 30 Sekunden nach dieser Aktion begann das Fluten der Teststrecke von unten mit einer Wassereinspeiserate von 47 g/s (QUENCH-02) bzw. 40 g/s (QUENCH-03), entsprechend einer Einspeiserate von 1,6 bzw. 1,3 cm/s. Als die Abschreckfront die Bündelmitte erreicht hatte wurde die Büdelleistung innerhalb von 15 s vom hohen Niveau auf Nachwärmeniveau von 4 kW reduziert.

Die Quench-Temperaturen, die für Hüllrohre des Versuchs QUENCH-03 ermittelt wurden, lagen zwischen 680 K am unteren Bündelende und 850 K etwas oberhalb Bündelmitte. (Wegen fehlerhafter Datenaufzeichnung während des Experiments QUENCH-02 steht für die Auswertung dieses Versuchs nur eine beschränkte Datenmenge zur Verfügung). Die Auswertung der sog. Quenchraten, bzw. Abschreckgeschwindigkeiten, für den Versuch QUENCH-03 ergab folgende Werte: 0,2-2,5 cm/s für die Hüllrohren, 0,2-2,5 cm/s für das Shroud. Die Quenchrate, die auf der Grundlage der in den Eckstäben installierten Thermoelemente ermittelt wurde, liegt bei ca. 1,4 cm/s.

Die Gesamtmenge an Wasserstoff, die während der Versuche QUENCH-02 und QUENCH-03 freigesetzt wurde, wurde zu 190 bzw. 123 g ermittelt.

Das Versuchsbündel zeigt nach dem Experiment Schmelzebildung und –verlagerung sowie eine starke Oxidation und Versprödung (Fragmentierung) von Shroud und Stabhüllen im oberen Bündelbereich. Oberhalb der axialen Mitte wurde der Shroud zu einer Art Blase geformt, in dessen Bereich sich eine Blockadezone aus erstarrter Schmelze mit einer Anhäufung von Bruchstücken gebildet hat.

Für beide Experimente wurden Vorausrechnungen mit dem SCDAP/RELAP5-Rechenprogramm durchgeführt, um diejenigen Parameter zu bestimmen, die für die Testdurchführung von Bedeutung sind. Für die Nachrechnungen wurden die

gemessenen Anfangs- und Randbedingungen verwendet. Die Temperatur-Zeit-Verläufe und die analytischen Ergebnisse hinsichtlich der Wasserstofferzeugung sind bis zum Beginn der Temperatureskalation in guter Übereinstimmung mit den experimentellen Daten. In den Rechnungen eskaliert die Temperatur etwas später als im Experiment und beginnt am oberen Ende der Heizzone.

Contents

List of Tables

List of Figures

Figures to Experiment QUENCH-02

Figures to Experiment QUENCH-03

Figures to Calculational Results of QUENCH-02 and QUENCH-03

Introduction

The most important accident management measure to terminate a severe accident transient in a Light-Water Reactor (LWR) is the injection of water to cool the uncovered degraded core. Analysis of the TMI-2 [1] accident and the results of integral out-of-pile (CORA [2]) and in-pile experiments (LOFT [3], PHEBUS, PBF) have shown that before the water succeeds in cooling the fuel pins there will be an enhanced oxidation of the Zircaloy cladding that in turn causes a sharp increase in temperature, hydrogen production and fission product release.

Besides, quenching is considered a worst-case accident scenario regarding hydrogen release to the containment. For in- and ex-vessel safety analyses one has to prove that the hydrogen release rates and total amounts do not exceed limits for the considered power plant. The hydrogen generation rate must be known to design appropriately accident mitigation measures for the following reasons.

- Passive autocatalytic recombiners require a minimum hydrogen concentration to start. Moreover, they work slowly, and their surface area and their position in the containment have to be quantified carefully.
- The air-steam-hydrogen mix in the containment may be combustible for only a short time before detonation limits are reached. This limits the time period during which ignitors can be used.

The physical and chemical phenomena of the hydrogen release are, however, not sufficiently well understood. Presently it is assumed that new metallic surfaces are formed by cracking and fragmentation of the oxygen-embrittled cladding tubes as a result of the thermal shock during flooding leading to enhanced oxidation and hydrogen generation. Consequently, in most of the code systems describing severe fuel damage, the quench phenomena are either not considered or only modeled in a simplified empirical manner.

No models are yet available to predict correctly the thermal-hydraulic or the clad behavior of the quenching processes in the CORA and LOFT LP-FP-2 tests. No experiments have been conducted that are suitable for calibrating the existing models. Since the increased hydrogen production during quenching cannot be determined on the basis of the available Zircaloy/steam oxidation correlations, new experiments are

therefore necessary. An extensive experimental database is needed as a basis for model development and code improvement.

The Forschungszentrum Karlsruhe has therefore started the QUENCH program on the determination of the hydrogen source term. The main objectives of this program are:

- The provision of an extensive experimental database for the development of detailed mechanistic fragmentation models,
- The examination of the physico-chemical behavior of overheated fuel elements under different flooding conditions,
- The provision of an improved understanding of the effects of water injection at different stages of a degraded core,
- The determination of cladding failure criteria, cracking of oxide layers, exposure of new metallic surfaces to steam which are currently supposed to result in renewed temperature escalation and hydrogen production, and
- The determination of the hydrogen source term.

The experimental part of QUENCH program began with small-scale experiments with short Zircaloy fuel rod segments [5]. On the basis of these results well-instrumented large-scale bundle experiments with fuel rod simulators under nearly adiabatic conditions are performed in the QUENCH facility at the Forschungszentrum Karlsruhe. For a number of reasons the large-scale bundle experiments are more representative of prototypic reactor accident conditions than are the single-rod experiments. Important parameters of the bundle test program are (see Table 1): quench medium, i.e. water or steam, fluid injection rate, cladding oxide layer thickness, and the temperature at onset of quenching.

After the commissioning tests [6] and the QUENCH-01 experiment with pre-oxidized cladding [7] tests QUENCH-02 and QUENCH-03 were performed to investigate the behavior on reflood of LWR fuel rods with little oxidation, i.e. on test rods without a pre-oxidation phase (reference tests to those with a pre-oxidation phase). The power transients in both tests, however, were different. It was planned to initiate flooding in both experiments at the earliest time at which a clear temperature excursion could be observed.

This report describes the test facility and the test bundle, and the main results of the QUENCH-02 and QUENCH-03 experiments. In addition, one section is dedicated to the calculational support performed with the SCDAP/RELAP5 computer code.

1 Description of the Test Facility

The QUENCH test facility consists of the following groups:

- the test section with 21 fuel rod simulators
- the electric power supply for the test bundle heating
- the water and steam supply system
- the argon gas supply system
- the hydrogen measurement devices
- the process control system
- the data acquisition system.

A simplified flow diagram of the QUENCH test facility is given in Fig. 1, a three-dimensional schematic of the components in Fig. 2. The main component of the facility is the test section with the test bundle (Fig. 3). The superheated steam from the steam generator and superheater together with argon as the carrier gas for the hydrogen detection systems enter the test bundle at the bottom end. The steam that is not consumed, the argon, and the hydrogen produced in the zirconium-steam reaction flow from the bundle outlet through a water-cooled off-gas pipe to the condenser (Figs. 1 through 3). Here the steam is separated from the non-condensable gases argon and hydrogen. During the quench phase the quench water enters the test bundle at the bottom through a separate line and argon is injected at the upper end of the test bundle.

The design characteristics of the test bundle are given in Table 2. The test bundle is made up of 21 fuel rod simulators, each with a length of approximately 2.5 m, and of four corner rods (see cross section in Figs. 4 and 5). The fuel rod simulators are held in their positions by five grid spacers, four of Zircaloy, and one of Inconel in the lower bundle zone (Fig. 6). The cladding of the fuel rod simulators is identical to that used in PWRs with respect to material and dimensions, i.e. Zircaloy-4, 10.75 mm outside diameter, 0.725 mm wall thickness. The rods are filled with a mixture of 95 % argon and 5 % krypton to approx. 0.22 MPa, i.e. a pressure slightly above the system pressure. The gas

filling of all rods is realized by a channel-like connection system inside the lower sealing plate. The krypton additive allows to detect fuel rod failure during the experiment with help of the mass spectrometer.

Twenty fuel rod simulators are heated electrically over a length of 1024 mm, the one unheated fuel rod simulator is located in the center of the test bundle. The unheated fuel rod simulator (Fig. 7) is filled with ZrO_2 pellets (bore size 2.5 mm ID). For the heated rods (Fig. 6) 6 mm diameter tungsten heating elements are installed in the center of the rods and are surrounded by annular ZrO_2 pellets. The tungsten heaters are connected to electrodes made of molybdenum and copper at each end of the heater. The molybdenum and copper electrodes are joined by high-frequency/high-temperature brazing performed under vacuum. For electrical insulation the surfaces of both types of electrodes are plasma-coated with 0.2 mm ZrO_2. To protect the copper electrodes and the O-ring-sealed wall penetrations against excessive heat they are water-cooled (lower and upper cooling chamber). The copper electrodes are connected to the DC electric power supply by means of special sliding contacts at the top and bottom. The total heating power available is 70 kW, distributed among the two groups of heated rods with 35 kW each. The first group consists of the inner eight rods (rod numbers 2 – 9), the second group consists of the outer twelve rods (rod numbers 10 – 21). The rod designation can be taken from Figs. 8 and 9.

The four corner positions of the bundle are occupied in QUENCH-02 by solid zircaloy rods with a diameter of 6 mm and in QUENCH-03 by solid rods (upper part)/Zry tubes (lower part) of 6 ∅ x 0.5 mm for thermocouple instrumentation at the inside (Figs. 8 and 9). The positioning of the four corner rods avoids an atypically large flow cross section at the outer positions and hence helps to obtain a rather uniform radial temperature profile. One of the solid Zry rods can be pulled out during the test to determine the axial oxide layer thickness profile at that time.

The lower boundary for the lower cooling chamber is a sealing plate made of stainless steel with plastic inlays for electrical insulation, sealed to the system by O-shaped rings. The upper boundary of the lower cooling chamber is a sealing plate of stainless steel. An insulation plate made of plastic (PEEK) forms the top of the upper cooling chamber, and a sealing plate of Al_2O_3, functioning as a heat-protection shield, is the lower boundary of the upper cooling chamber (see Fig. 6).

In the region below the upper Al_2O_3 plate the copper electrode is connected firmly to the cladding. This is done by hammering the cladding onto the electrode with a sleeve of boron nitride put between electrode and cladding for electrical insulation. The axial position of the fuel rod simulator in the test bundle is fixed by a groove and a locking ring in the top Cu electrodes. Referred to the test bundle the fixing of the fuel rod simulators is located directly above the upper edge of the upper insulation plate. So, during operation the fuel rod simulators are allowed to expand downwards. Clearance for expansion of the test rods is provided in the region of the lower sealing plate. Also in this region relative movement between cladding and internal heater/electrode can take place.

The test bundle is surrounded by a 2.38 mm thick shroud (80 mm ID) made of Zircaloy with a 35 mm thick ZrO_2 fiber insulation and an annular cooling jacket made of stainless steel (Figs. 4 and 5). The 6.7 mm annulus of the cooling jacket is cooled by an argon flow. Above the heated zone, i.e. above the 1024 mm elevation, there is no ZrO_2 fiber insulation to allow for higher radial heat losses. This region of the cooling jacket is cooled by a water flow (Fig. 3). Both the lack of ZrO_2 insulation above the heated region and the water cooling force the axial temperature maximum downward.

2 Test Bundle Assembly

The test section consists of three subassemblies pre-assembled separately. One subassembly comprises the cooling jacket with the bundle head casing; the second subassembly includes the instrumented shroud with the bundle foot; and the third subassembly is composed of the instrumented test bundle with the bundle head. The test bundle and the shroud, including the respective thermocouples, must be replaced for each experiment. The instrumentation of the bundle head and the foot as well as the cooling jacket, however, remains unchanged.

3 Test Bundle Instrumentation

The test bundle was instrumented with sheathed thermocouples attached to the rod claddings at 17 different elevations between -250 mm and 1350 mm and at different orientations (Figs. 10 through 14). In addition, two thermocouples were inserted in the center of the unheated fuel rod simulator, one thermocouple from the bottom and one from the top. The elevations of the surface-mounted shroud thermocouples are from -250 mm to 1250 mm.

In the lower bundle region, i.e. up to the 350 mm elevation (QUENCH-02) or 550 mm elevation (QUENCH-03) NiCr/Ni thermocouples (1 mm diameter) are used for temperature measurement of rod cladding and shroud. The thermocouples of the hot zone are high-temperature thermocouples with W-5Re/W-26Re wires, HfO_2 insulation, and a duplex sheath of tantalum (internal)/Zircaloy with an outside diameter of 2.1 mm (Fig. 11). The leads of the thermocouples from -250 mm to 650 mm leave the test section at the bottom whereas the TCs above 650 mm penetrate the test section at the top.

The wall of the inner tube of the cooling jacket is instrumented between -250 mm and 1150 mm with 22 NiCr/Ni thermocouples (designation “TCI”). Five NiCr/Ni thermocouples are fixed at the outer surface of the outer tube of the cooling jacket (“TCO”). The designations of the surface-mounted cladding thermocouples are “TFS” and “TCR” (for the central rod). “TCRC” is the designation for the thermocouples at the center of the central rod installed at two levels, i.e. at 550 and 950 mm (QUENCH-02) and at 850 and 950 mm (QUENCH-03). The designation of the shroud thermocouples is “TSH”, that of the thermocouples inside the Zircaloy instrumentation rods is “TIT” (QUENCH-03, Fig. 14). The four rods of the QUENCH-03 test bundle were instrumented as follows:

- Rod A: W/Re, duplex sheath, 950mm elevation
- Rod B: NiCr/Ni, stainless steel sheath, 350mm elevation
- Rod C: NiCr/Ni, stainless steel sheath, 550mm elevation
- Rod D: W/Re, duplex sheath, 850mm.

The corner rods of the QUENCH-02 test bundle were not instrumented.

The lists of all instruments for experiments QUENCH-02 and QUENCH-03 installed in the test section and at the test loop are given in Tables 3 and 4, respectively.

The thermocouple attachment technique for the surface-mounted high-temperature TCs is illustrated in Figs. 12 and 13. The TC tip is held in place by two clamps of Zr.

4 Hydrogen Measurement Devices

The hydrogen is analyzed by two different measurement systems: (1) a mass spectrometer (Fig. 15) located at the off-gas pipe between the test section and the condenser, (2) a hydrogen detection system ”Caldos 7 G” (Figs. 16 and 17) located in a

bypass to the off-gas line behind the condenser. So, the argon and hydrogen pass the Caldos analyzer before they exit to the outside (Figs. 1 and 2). Due to the different locations the response time of the mass spectrometer to changes in the gas composition within the test bundle is very short (less than 5 s) whereas there is a delay time of the Caldos system of approx. 100 s.

The mass spectrometer (MS) “BALZERS GAM 300“ used is a completely computer-controlled quadrupole MS with an 8 mm rod system which allows quantitative measurement of gas concentrations down to about 10 ppm. For the MS measurement a sampling tube is inserted in the off-gas pipe. It has several holes at different elevations to guarantee a representative gas composition. To avoid steam condensation in the gas pipes between the sampling position and the MS the temperature of the gas at the MS inlet is controlled by a heat exchanger to be between 110 °C and 150 °C (the upper operating temperature of the MS inlet valves). This allows the MS to analyze the steam production rate. As the fuel rod simulators are filled with krypton as a tracer gas in addition to the argon (argon 5%krypton mix) the measurement of krypton can be used as an indicator for the first cladding failure. Besides, the concentrations of the following species were continuously measured by the mass spectrometer during all test phases: argon, hydrogen, steam, nitrogen, oxygen, and krypton. Additionally, the MS is used to control the atmosphere in the facility, e.g., to monitor the gas composition at the beginning of the test.

The temperature and pressure of the analyzed gas are measured near the inlet valve of the MS. The MS is calibrated for hydrogen with well-defined argon/hydrogen mixtures and for steam with mixtures of argon and steam supplied by the steam generator of the QUENCH facility. The MS off-gas is released into the atmosphere because the amount of hydrogen taken out of the system is negligible.

The principle of measurement of the Caldos system is based on the different heat conductivities of different gases. The Caldos device used is calibrated for the hydrogen-argon gas mixture. To avoid any moisture in the analyzed gas a gas cooler, which is controlled at 296 K, and a drier (molecular sieve, zeolite) are connected in series before the gas analyzer (Fig. 17). The response of the gas analyzer is documented to be 2 s, i.e. in this time 90 % of the final value is reached. In contrast to the mass spectrometer the Caldos device only measures the hydrogen content. Gases other than H_2 cannot be analyzed by this system.

For the Caldos device as well as for the MS the hydrogen mass flow rate is calculated by referring the measured H_2 concentration to the known argon mass flow rate according to equation (1):

$$\dot{m}_{H_2} = \frac{M_{H_2}}{M_{Ar}} \cdot \frac{C_{H_2}}{C_{Ar}} \cdot \dot{m}_{Ar} \tag{1}$$

with M representing the molecular masses, C the concentrations and $\dot{m}$ the mass flow rates of the corresponding gases.

With an argon-hydrogen (two-component) mixture that in fact exists at the location of the Caldos analyzer equation (1) can be written as follows

$$\dot{m}_{H_2} = \frac{M_{H_2}}{M_{Ar}} \cdot \frac{C_{H_2}}{1 - C_{H_2}} \cdot \dot{m}_{Ar} \tag{2}$$

5 Data Acquisition and Process Control

A computer-based control and data acquisition system is used in the QUENCH facility. Data acquisition, data storage, online visualization as well as process control, control engineering and system protection are accomplished by three computer systems that are linked in a network.

The data acquisition system allows recording of about 200 measurement channels at a maximum frequency of 25 Hz per channel. The experimental data and the date and time of the data acquisition are stored as raw data in binary format. After the experiment the raw data are converted into SI units and stored as ASCII data.

For process control, a system flow chart with the most important actual measurement values is displayed on the computer screen. Furthermore, the operating mode of the active components (pumps, steam generator, superheater, DC power system, valves) is indicated. Blocking systems and limit switches ensure safe plant operation. Pre-defined operating test phases, e.g. heatup or quenching phases, are pre-programmed and can be started on demand during the experiment. The parameter settings of the control circuits and devices can be modified online.

Online visualization allows to observe and to document the current values of selected measurement positions in the form of tables or plots. Eight diagrams with six curves each can be displayed as graphs. This means that altogether 48 measurement channels can be selected and displayed online during the course of the experiment.

The data of the test facility and of the mass spectrometer (MS) are stored on different computers. Both computers are synchronized by radio-controlled clocks. The data files have different structures: the MS data are stored in one file starting with time zero, whereas the acquisition of the data of the facility restarts at every new test phase.

Data Acquisition QUENCH-02

As the storage of the test data with the main data acquisition system did not function properly during Test QUENCH-02 only the temperature data which were saved from the online visualization system as graphs are available. They were digitized after the test. The data of the mass spectrometer which are recorded on a separate acquisition system are the only ones which were directly available.

The failure times and temperatures of the thermocouples of the QUENCH-02 test bundle are listed in Table 6 b.

Data Acquisition QUENCH-03

The data of the main acquisition system were stored at frequencies of 0.125 Hz (heatup), 1 Hz (transient, < 1273 K), and 5 Hz (> 1273 K), respectively. The mass spectrometer data were recorded at a frequency of around 1 Hz during the entire test. The experimental data and the date and time of the data acquisition are stored as raw data in binary format.

The thermocouples that failed during the QUENCH-03 experiment are listed in Table 11.

6 General Test Performance

The QUENCH experiments consist of several test phases, i.e., a first heatup phase, a thermal equilibrium phase, a second heatup phase, a pre-oxidation phase (optional), a transient phase, and a quenching phase. Heatup during the transient phase is accomplished by raising the electrical bundle power. All phases, except for the quenching phase, proceed in an argon/steam atmosphere (3 g/s each). Quenching the test bundle from the bottom with water at approx. 395 K (saturation temperature at

0.2 MPa) is initiated by turning off the steam flow through the test section, switching the argon inlet from the bundle foot to the bundle head, and injecting water at the high rate of 80 - 90 g/s to fill the lower plenum, i.e. the void volume up to the -250 mm level of the test section. After approx. 30 s, the lower plenum has filled, and the water injection is reduced to some 40 - 50 g/s. At this flow rate the test bundle is cooled under two-phase flow conditions. When the water level is at -250 mm or at a later point in time, e.g. when the water level has risen to 500 mm, which is the axial midplane of the heated zone, the electrical bundle power is reduced to 4 kW to simulate the decay heat level of the fission products.

6.1 Test Conduct and Results of Test QUENCH-02

The conduct of test QUENCH-02 is illustrated in Fig. 18 and the sequence of events is summarized in Table 5.

The bundle was heated by a series of stepwise increases of electrical power from room temperature to ~ 900 K in an atmosphere of flowing argon and steam. The bundle was stabilized at this temperature in a mixture of 3 g/s argon and 3 g/s steam for 4800 s, with the bundle electrical power being 3.75 kW.

At the end of the thermal stabilization period the bundle was ramped from 3.75 kW to 16.35 kW with an average heatup rate of 0.37 K/s (900 – 1400 K) and later of 1 K/s (1400 – 1870 K; for heatup rates see Fig. 19) until an uncontrolled temperature excursion due to the exothermal zirconium-steam reaction was detected at the 950 mm level, which had then reached ~1820 K. From this level the excursion spread downwards to 750 mm and upwards to 1150 mm (150 mm above the heated zone). With respect to the axial level the excursions started at different temperatures, e.g. 1820 K at 950 mm (TFS2/13), 1700 K at 850 mm (TFS3/12), and 1490 K at 1150 mm elevation (TFS2/15). The temperature excursion of the shroud at the 950 mm level occurred almost simultaneously with that of the rods at the 850 mm elevation. The temperature excursion of the shroud at the 850 mm level followed about 25 s later with the maximum heatup rate of approx. 48 K/s (TSH12/0). For comparison, the maximum escalation rate of the rods amounted to approx. 23 K/s (TFS5/12). At the end of the transient phase the electrical power input was 16.35 kW.

At a maximum temperature of about 2270 K the pre-planned reflood sequence was initiated, with water being injected firstly at the high rate of 89 g/s to fill the lower plenum.

The steam (3 g/s) through the test section was turned off, the argon flow of 3 g/s was injected at the bundle head to continue the provision of a carrier gas for the hydrogen. The water injection was reduced to 47 g/s after 30 s. At this time, i.e. at 2211 s, it was estimated that the lower plenum had been filled, up to the level of -250 mm. The water mass flow was reduced to 47 g/s resulting in a local flooding rate (at the bottom) of 1.6 cm/s. The electrical power was stabilized at 19 kW and held at this level for 77 s (based on pretest calculations, see section 11.2.1) the bundle had become half full (temperature drop at 550 mm elevation, thermocouple TFS 5/9). At that time the bundle electrical power was reduced to 4 kW within 15 s. Reflood of the main test section to 1300 mm (above the heated zone) was completed in 263 s, after which the experiment was terminated by shutting off the electrical power. The amount of water injected at a rate of 89 g/s and 47 g/s was 2.7 l and 11 l, respectively, so that the total amount of water injected was 13.7 l. (For comparison: The void volume of the test section between water inlet and outlet amounts to approx. 5 l).

During the reflood phase strong secondary temperature excursions were observed starting from 1770 – 2270 K (see also Table 5). The maximum rod cladding temperature recorded was TFS5/15: ~2460 K (see also Tables 6 a and 6 b). The shroud reached the following maximum temperatures TSH12/0: ~2290 K, TSH13/90: ~2250 K, and the gas temperature at the outlet of the test section increased to T512: ~1700 K (see Fig. 20).

6.2 Test Conduct and Results of Test QUENCH-03

The conduct of test QUENCH-03 is illustrated in Fig. 58, and the sequence of events is summarized in Table 10.

The bundle was heated by a series of stepwise increases of electrical power from room temperature to ~900 K in an atmosphere of flowing argon (3 g/s) and steam (3 g/s). The bundle was stabilized at this temperature for about 8000 s, the electrical power being 3.75 kW.

At the end of the stabilization period the bundle was ramped from 3.75 kW at 0.42 W/s per rod to 18.4 kW giving an average temperature increase of ~0.4 K/s between 900 K and 1400 K and ~1.6 K/s between 1400 K and 2070 K (for heatup rates see Fig. 59). The coolant temperatures at the bottom of the bundle (TFS2/1, -250 mm), at the bundle inlet (T511), and at the bundle outlet (T512) can be taken from Fig. 60.

It was planned to initiate flooding of the test bundle at the time when a temperature escalation was recognizable. Contrary to expectation and to the pretest calculations, a temperature excursion of the fuel rod simulator cladding did not start at the 950 mm level which usually is the axial hot spot but at elevation 750 mm at around 1400 K. As operators were concentrated on the 950 mm level the pre-planned reflood sequence was initiated when the peak rod temperatures had already reached ~2400 K, i.e. when the bundle temperature was almost at its maximum. The reflood water was injected firstly at the high rate of 90 g/s for 25 s to fill the lower plenum with the total electrical power being increased from 18.4 kW to 44 kW to compensate for increased convective heat losses due to the boiling of the quenching water at the hot structure material (based on pretest calculations). The water injection rate then was reduced to 40 g/s. The water mass flow of 40 g/s resulted in a local flooding rate at the bottom of 1.3 cm/s. Two and a half minutes after flooding had been initiated, when the bundle had become half full (temperature at 550 mm, thermocouple TFS 5/9), the bundle electrical power was reduced to 4 kW within 15 s.

Reflood of the main test section to 1300 mm was completed in 904 s, after which the experiment was terminated by shutting off the electrical power. During the reflood phase argon was injected into the upper plenum at 3 g/s to continue to provide carrier gas for the mass spectrometer and Caldos device.

The total electric energy that was put into the bundle during test QUENCH-03 amounts to 30.3 MJ. The amount of water injected at a rate of 90 g/s for 25 s and 40 g/s for 879 s was 2.3 l and 35.7 l, respectively, so that the total amount of water injected was 38 l.

Figs. 61 and 62 show the entire test rod temperature history (TFS) of the elevations from -250 mm to 1350 mm and Figs. 63 and 64 the shroud temperatures (TSH) from -250 mm to 1250 mm. Smooth, regular cooling by the two-phase mix led to quenching of the rods below 650 mm without any excursion. Strong temperature excursions were observed during the reflood phase from 750 mm upwards (see Table 12). In Fig. 65 the temperature of escalation is plotted versus time showing accumulations of data depending on the locations of the thermocouples, e.g. shroud (TSH), upper bundle elevations (TFS x/11 – TFS x/14) and upmost bundle elevations (TFS x/15 – TFS x/17). The maximum measured temperatures of each elevation (TFS temperatures) are listed in Table 13 and plotted in Fig. 66, the maximum measured shroud temperatures (TSH) are provided in Table 14.

For the axial temperature plots the following time steps were selected: 2250 s, 2550 s, 2570 s (for the transient), 2619 s (beginning of quenching), and 2625 s (representing the quenching phase). The data plots of Figs. 67 – 70 show the axial temperature distribution of each thermocouple type, i.e. TFS 2 (inner coolant channel), TFS 5 (outer coolant channel), TSH (shroud), and TIT (corner rods), for the time steps indicated above. In Figs. 71 – 75 the data of TFS 2, TFS 5, TSH, and TIT are presented together in one diagram for one specific time. In the lower axial region, i.e. up to around 550 mm the temperatures of the different TC types lie withinin a narrow band (Figs. 67 – 70). Above this region great temperature differences are to be found. During the transient the axial temperature maximum of TFS 2 is shifted from 850 mm to 750 mm elevation (Fig. 67). Also for TFS 5 the axial temperature maximum is shifted with time from 950 mm to various other levels. Above the heated zone the shroud temperature is larger than the rod temperatures for the time steps of 2550 s and 2570 s (Figs. 72 and 73).

There were unexpected features concerning the thermal behavior of the shroud. Prior to flooding, excursions were observed in the shroud at 1050 mm starting at ~1160 K and at 1250 mm starting at ~1100 K, even though no escalation was observed in the fuel rod simulators at those elevations before quenching took place (Table 10). Based on the temperature data of the inner cooling jacket (designation TCI) shroud failure occurred at 2627 s. The shroud failure is clearly indicated by a sudden increase in the temperature of the inner cooling jacket as is presented in Figs. 76 and 77. The largest temperature rise of the cooling jacket temperature at this time was recorded between the 750 mm and the 950 mm level so that it can be assumed that the failure of the shroud started in this region.

7 Reflooding Behavior

7.1 General Behavior

The flooding of the hot test bundle is initiated by turning off the steam flow. As a consequence of the shutoff of the steam flowing through the test bundle the test rod temperatures increase slightly at lower levels up to the middle of the heated zone, but drop at the higher levels.

The first cooling of the bundle is indicated by thermocouples below the heated zone, e.g. TFS2/1 at the -250 mm level. In the heated region, cooling of the test bundle generally

occurs in two stages, first a cooling period (period before the water level is at a given axial location) with a moderate cooling rate, then very pronounced cooling (Fig. 21). In the first period, the cladding temperatures start dropping when cooling exceeds the heat generated and stored in the rods. The steam generated provides an immediate cooling effect by convective heat transfer from the wall surfaces to the coolant. The evaporation of the quenching water occurs swiftly at the bottom of the test bundle because the test rods are heated, the surrounding shroud wall is hot, and the fluid is at saturation temperature. The velocity of the generated steam allows the first cooling to occur simultaneously, i.e. within 1 s, for all axial positions. This ”onset of cooling” occurred in both experiments exactly at the time when the thermocouple at the -250 mm level showed a quenching effect, i.e. a sharp temperature drop. Besides the efficient heat transfer by steam on one hand the simultaneous cooling for all levels is on the other hand made possible by a thermal decoupling of the rod cladding from the heat source (tungsten heater and rod pellets) [8]. The maximum cooldown rate, which follows the so-called ”quench temperature” or ”onset of quenching”, is caused by a drastic improvement in heat transfer during transition boiling. Eventually, when the rod cladding is completely wetted, the rods reach the saturation temperature. At the upper rod elevations, however, before saturation temperature is reached the rod temperatures there fluctuate due to changes in local dryout and wetting [10]. These fluctuations indicate that the upper end of the test bundle is not completely wetted at that time. Wetting in the hot region is impeded by supplying more heat by the ongoing zirconium oxidation of the test rods and the thick-walled shroud.

7.2 Quenching of Test Bundle QUENCH-02

In the heated zone, i.e. from the 150 mm to the 1150 mm elevation, the cooling of the test bundle began between 1000 K and 2200 K (Figs. 22 and 23). The quench temperatures of the test rod thermocouples in this region were between 950 K (150 mm) and 1470 K at the 1150 mm elevation (see also Table 7). Table 8 provides the quench temperatures of the shroud thermocouples.

The evaluation of the quenching temperature with respect to the problem of the location of the thermocouples will be discussed in the next section (Quenching of Test Bundle QUENCH-03).

To obtain information on the fractions of water and steam in the test section as a function of time in experiment QUENCH-02 the following balance for the quenching phase is considered (see mass flow rates in Fig. 24):

$$m_{H2O,inj} - m_{st,MS} - m_{st,cons} = m_{rest} \quad (3)$$

where

$m_{H2O,inj}$	mass of water injected
$m_{st,MS}$	mass of steam measured by the mass spectrometer (MS)
$m_{st,cons}$	mass of steam consumed by zirconium oxidation (re-calculated on the basis of the total hydrogen generation and the ratio of the molecular weights)
m_{rest}	mass of remaining water.

The integral values evaluated are

- Mass of water injected: 13.7 kg
- Mass of steam measured by the MS: 6.5 kg
- Mass of steam consumed: 1.7 kg
- Mass of remaining water: 5.5 kg.

The integral steam mass fraction thus amounts to

$$m_{steam}/m_{total} = m_{steam}/m_{H2O,inj} = 8.2/13.7 = 0.60.$$

The axial temperature distributions for the times 2250 s (onset of cooling) and 2275 s (during the flooding phase) are presented in Figs. 25 and 26. At 2250 s all temperature data, i.e. TFS 2, TFS 3, and TFS 5, lie within a relatively narrow band with the maximum between 850 and 1050 mm (Fig. 25). At this time the maximum temperatures are 2200 – 2300 K. At 2275 s the test bundle is quenched up to the elevation 350 mm whereas between 850 and 1250 mm still temperatures of up to 2400 K prevail (Fig. 26).

7.3 Quenching of Test Bundle QUENCH-03

Figs. 78 and 79 show the quenching phase of the fuel rod simulator temperatures (TFS) of the elevations from -250 mm to 1350 mm and Figs. 80 and 81 the same phase for the

shroud temperatures (TSH) from -250 mm to 1250 mm, all diagrams starting at around 2300 s. In the plots of the lower elevations (Figs. 78 and 80) the initiation of flooding and the onset of cooling can easily be recognized.

For test bundle QUENCH-03 the integral values of water and steam are as follows:

- Mass of water injected, from the -250 mm level upwards: ~35.7 kg
- Mass of steam measured by the mass spectrometer: ~13.0 kg
- Mass of steam consumed (based on 123 g total H_2): ~1.1 kg
- Mass of remaining water, calculated from the difference: ~21.6 kg.

The remaining mass of water (21.6 kg) has filled the void volumes of the test section, i.e. ~4.7 l between -250 and 1300 mm, and in addition the annulus between the shroud and the inner cooling jacket, i.e. ~16.9 l, due to shroud failure described above.

The quench temperatures of the test rods in the heated zone (designation TFS) were between 716 K (50 mm) and 866 K at the 150 mm elevation (Table 15).

With respect to the evaluation of the so-called quench temperature it should generally be noted that the cladding thermocouples experience quenching, i.e. a sharp temperature drop, before there is any wetting of the test rods. This behavior of rods with external cladding surface thermocouples, namely being quenched earlier than bare rods, is due to the fin effect, i.e. the exposure of external cladding surface thermocouples to the coolant channel. It was demonstrated in various flooding experiments, e.g. in the PBF Thermocouple Effects Tests at INEL (Idaho National Engineering Laboratory, USA) [9]. The quenching temperature indicates a first local wetting of the rods by water droplets at the locations of cladding thermocouples. An earlier detection of the quenching means higher quenching temperatures.

Comparing the signals of the external cladding TCs (designation TFS) with those of the internal TCs one can look at the responses of the shroud thermocouples (designation TSH) and in addition to those of the thermocouples installed inside the corner rods of Test Bundle QUENCH-03 (designation TIT). The shroud thermocouples are mounted outside the wall which means a slightly delayed signal on one hand but no disturbance by a coolant flow on the other hand. They measure wall temperature. Also the thermocouples that were mounted inside the tubes of the corner positions (designation “TIT”) are not disturbed by the coolant flow. (There is by the way another advantage

having internally mounted TCs: they are not exposed to the steam atmosphere and are able to survive an entire test, even with pre-oxidation.)

During heatup all three types of thermocouples lie within a narrow band. The situation is different during quenching. In general, the onset of quenching as measured by the shroud thermocouples occurs later and thus at lower temperatures. This is demonstrated for the 350 mm level in Fig. 82 and for the 550 mm level in Fig. 83. The temperature TIT B/7 in Fig. 82 demonstrates the same flooding behavior as the cladding surface thermocouples (designation TFS), and the temperature TIT C/9 in Fig. 83 shows an even earlier quenching of the corner rod C at 550 mm elevation than of the test rods No. 8 and 10. The reason for this behavior is not understood yet since the thermocouples installed inside the corner rods are not affected by the coolant flow and should therefore behave in a similar way as the shroud temperatures.

The correct time of wetting could lie between the responses of the cladding and the shroud thermocouples. Nevertheless, even the shroud thermocouples demonstrate quenching so early that the majority of quench temperatures are well above the Leidenfrost temperature, i.e. above 600 K.

An evaluation of the quench rates on the basis of thermocouple readings of adjacent levels (see also Table 15) resulted in: 0.2 - 2.5 cm/s for the cladding thermocouples (designation TFS), 0.2 – 2.0 cm/s for the shroud thermocouples (designation TSH), and 1.4 cm/s for the thermocouples installed inside the corner rods (designation TIT), respectively.

8 Hydrogen Measurements

8.1 Results of Hydrogen Measurements of Test QUENCH-02

In test QUENCH-02 the hydrogen data were available from the mass spectrometer but not from the Caldos device because of the failure of the main data acquisition system. A notable hydrogen production started when the escalation period (level 950 mm) began reaching a maximum H_2 concentration of 42% in the offgas. This value corresponds to a maximum hydrogen production rate of 2.5 g/s at 2260 s (Fig. 27). The total hydrogen release measured by the mass spectrometer is 190 g with most of it, i.e. 170 g, associated with the reflood phase. This amount of hydrogen is comparable to that observed in previous tests under similar conditions, e.g. CORA experiments. The

maximum hydrogen production rate, however, is about twice the highest value in the CORA experiments (CORA-17: 1.3 g/s, total H_2 = 150 g) [4].

Assuming that the oxidation

$$Zr + 2\,H_2O\,(steam) = ZrO_2 + 2\,H_2 + 6400\ J/g\ Zr \qquad (4)$$

is complete by neglecting the formation of the α-Zr(O) phase, 190 g of H_2 correspond to the formation of 5.8 kg of ZrO_2.

The influence of electric power input, rod temperature, and quench water injection on the hydrogen generation is given in Fig. 28.

8.2 Results of Hydrogen Measurements of Test QUENCH-03

The onset of cooling (at 2619 s) was accompanied by the onset of hydrogen production as can be taken from Fig. 84 presenting the influence of electric power input, rod temperature, and quench water injection on the hydrogen generation measured by the mass spectrometer. The hydrogen mass fraction in the offgas (maximum gas temperature at bundle outlet 1700 K) reached 53 vol % at the mass spectrometer (H_2/argon/steam mixture) and a H_2 concentration at the Caldos analyzer of 65 vol % (H_2/argon mixture). Converting these values into H_2 production rates the results obtained by mass spectrometer and Caldos differ significantly (Fig. 85). The mass spectrometer gives a maximum production rate of 3.6 g/s and a total hydrogen production of 288 g whereas the respective Caldos data are 0.28 g/s and 47 g. Problems with the mass spectrometer were noticed after the experiment: the flow of the analyzing gas from the off-gas pipe to the mass spectrometer was temporarily blocked so that the gas was stagnant in the analyzer for a certain time. This caused an over-estimation of the total amount of H_2. For the Caldos system the problem was that the gas sampling, which is performed with help of a pump, was too slow to detect the analyzing gas correctly. An additional pump that was added to the existing one after test QUENCH-03 improved the sampling process significantly. (This measure together with a reduction in the void volume of the inlet line of the Caldos system decreased the delay time from approx. 100 s to around 20 s.)

An estimate of the total hydrogen production on the basis of the F 901 flow meter (upstream of Caldos) is 123 g (Fig. 86), a value that seems more reasonable and lies

between mass spectrometer and Caldos data. The major portion of this amount of H_2, i.e. 109 g, was produced during the flooding phase, i.e. from 2619 s on.

9 Posttest Examination of the Bundle QUENCH-02

9.1 Posttest Appearance of the Bundle QUENCH-02

The disassembly of the fuel element simulator led to a break-off of the upper third of the shroud and some parts of the cladding tubes due to severe embrittlement by oxidation and by localized melt formation and relocation, i.e. from the 870 mm elevation upward there are only shroud fragments left (see Figs. 29, 30, and 31). The post-test status of the test bundle reveals significant oxidation and fragmentation of the rod claddings, at least from the 870 mm level upwards. Below and above this elevation parts of the bundle were molten and had formed a blockage zone upon solidification. The shroud appears to have formed a kind of bubble, i.e. an accumulation of molten material. The remnants of the upper part of the shroud indicate a deformation caused by melting. The strong reaction between shroud and steam in the hot region (e.g. high escalation rate of element TSH12/0) cannot be completely explained at the moment. The severe embrittlement of the shroud and rod claddings caused the posttest state to change by any contact with the test bundle complicating the encapsulation procedure with epoxy resin.

9.2 Sectioning of the Test Bundle

Due to the severe destruction of both test bundles the mould for filling the bundle with epoxy resin had to be set up vertically. For the encapsulation of the bundle the epoxy system Rütapox 0273 with the hardener designated LC (Epoxy resin and hardener manufactured by Bakelite GmbH, Iserlohn) was chosen based on the experience with the CORA test bundles. The epoxy generally shows some heating during the curing stage but the shrinkage effect is negligible. After epoxying the bundle the resin is allowed to harden for one week. To obtain the cross sections a saw with a 2.0 mm-thick diamond blade (mean diamond size 138 µm) of 350 mm OD is used to cut the slabs at 1300 rpm. As an overview the sectioning map is given for test bundle QUENCH-02 in Fig. 32. The exact elevations are listed in Table 9. One cross-section is taken as reference, i.e. from a lower region (as-received condition).

The cross sections that were selected for metallographic examination (see also Table 9) were polished. For this purpose, the samples were infiltrated by "Araldit" resin to close up residual voids, then ground and polished. The work is performed using a semi-automatic machine with a closed water circuit for grinding and an automatic lubricant feeder for the polishing steps.

The cross sections (unpolished condition) are shown as bottom and top of the various bundle discs in Figs. 33 through 37 for QUENCH-02.

9.3 Metallographic Examination of the Bundle QUENCH-02

The physico-chemical state of the Zircaloy cladding material was investigated and evaluated by light microscope and by scanning electron microscope examinations. Of special interest was the determination of the oxide layer thickness on the Zircaloy cladding tubes and the shroud, the formation of through-wall cracks in the cladding tubes and the oxidation of the crack surfaces. Oxidation of the metallic part of the crack surfaces and the steam exposed area of the inner cladding surface could result in an additional generation of hydrogen during flooding.

As can be seen even from the unpolished cross sections of the QUENCH-02 bundle (Figs. 33 - 37) significant amounts of melt have been formed and relocated during the test. Therefore, a further point of interest was the behavior of this melt, especially its interaction with the Zircaloy cladding material and its oxidation by steam.

The original state of the bundle could be recognized at the lowest examined cross-section elevation of 550 mm, where one Zircaloy grid spacer was located. Figure 38 shows details of the grid spacer and the Inconel springs which keep the fuel rods in place. One of the fuel rods (#17) was taken out for chemical examinations (oxide layer thickness and absorbed hydrogen in the cladding tube as function of the bundle elevation). The oxidation of the Zircaloy components at the 550 mm bundle elevation is very small as a result of the low bundle temperatures. The Inconel spring shows no evidence of any oxidation.

Due to the severe damage of the bundle and the complete oxidation of the Zry cladding material over a wide axial range (~ 900 - 1250 mm), quench effects as they were observed in test QUENCH-01 could be seen only to a minor extent. So, only at one elevation (1350 mm) oxidized through-wall cracks have been detected (Fig. 39). This is

also in accordance with the single rod quench tests where the formation of through wall cracks and the oxidation of the newly formed metallic crack surfaces during quenching only occurred at oxide layers thicker than 200 µm and temperatures at onset of quenching ≤ 1400 °C. Obviously, these conditions were not met in most parts of the QUENCH-02 test bundle. On the one hand, the quench temperatures were higher than 1600 °C at elevations with thick oxide layers and on the other hand, the oxide layer thickness was ≤ 200 µm at elevations with lower quench temperatures.

Another indication (from the metallographical point of view) for high temperatures in the bundle before quenching is the appearance of metallic α-Zr(O) precipitates in the oxide scale at elevations 850 mm – 1350 mm due to the phase transition from the more substoichiometric cubic to the tetragonal oxide phase at temperatures above 1500 °C (Fig. 40).

Due to the very high temperatures at the end of the transient phase and during the quench phase large amounts of melt have been formed and relocated from the higher to the lower elevations of the bundle. Most of the relocated melt was found at elevation 850 - 1150 mm (Figs. 33 - 37, Fig. 41). The solidified melt is mainly metallic with oxidized surfaces in the lower, heated part of the bundle, the melt at higher elevations >950 mm is almost completely oxidized even in large volumes. The oxidation kinetics in this bundle region had to be very fast and cannot be explained only by simple parabolic behavior, since the temperature excursion in the upper unheated zone started only after the beginning of the quench phase. Figure 41 (left photo) also shows a considerable interaction of the melt with the molybdenum electrodes at high bundle elevations. Large amounts of mainly metallic melt solidified outside the shroud, likely coming from molten shroud material at higher elevations (Fig. 41, right photo).

The relocated metallic melt dissolved parts of the oxide scales as can be seen in Fig. 42. The position of the former oxide layer is sometimes still visible. Obviously the surrounding melt has been already saturated with respect to oxygen content.

The ten cross-section elevations of 73, 550, 750, 850, 868, 883, 950, 1050, 1150, and 1350 mm were examined concerning the oxide layer thickness of all cladding tubes except that of fuel rod simulator #17 which was taken out for detailed chemical examinations (hydrogen uptake). The results are given in Figures 43 through 52 together with those of the four Zircaloy corner rods and the shroud.

The evaluation of the oxide layer thickness versus axial bundle elevation was done for the central rod cladding tube, for the remaining 19 cladding tubes of the fuel element simulator, the four Zircaloy corner rods of 6 mm diameter, and the shroud (Figure 53). The cladding of the central rod is more oxidized than the others (compared with the mean value). The range of the oxide layer thickness at the examined cross-section elevations for the 19 fuel rods is given in Figure 54. The oxidation of the bundle occurred very homogeneously up to the 750 mm bundle elevation. At higher elevations there is a strong scattering of oxide scale thickness.

The remarkable radial gradient in the oxide layer thickness at elevation 1350 mm from almost complete oxidation of central cladding tube to only about 30 µm at the outer parts of the outer cladding tubes indicates a strong temperature gradient in the upper, unheated part of the bundle. Figure 55 also shows that even at one single tube this gradient is very pronounced. It can also be recognized that Zircaloy material from this high bundle elevation relocated to lower ones.

The cladding tube of rod #17 was examined over its total length. The results are plotted in Fig. 56 as a function of the bundle elevation together with the axial profile of the maximum temperature.

In all the various plots one can recognize the strongest oxidation of the bundle components in the very upper part of the heated zone and the upper, unheated part of the bundle (900-1250 mm). This observation is in agreement with the temperature measurements which are also shown in Figure 56.

9.4 Hydrogen Absorption by Zircaloy in the Bundle QUENCH-02

The axial distribution of hydrogen absorption in the Zry-4 was analyzed in the cladding of rod # 17 which was removed from the test bundle before it was epoxied. Additionally, some specimens of the shroud and a corner rod from the hot region were examined. Hydrogen was absorbed in a wide range of the bundle, with a peak between the 800 mm and the 1300 mm elevation (Fig. 57). This range includes the region where most of the H_2 was produced, but is extended to higher levels. It seems that some hydrogen was absorbed downstream the region of maximum production. Between 1000 mm and 1200 mm, no data were obtained as the rod cladding had been oxidized completely in this zone. Extrapolation of the data obtained from one cladding tube and from the shroud specimens gives approx. 5 g of hydrogen absorbed by the whole bundle. The part of the

hydrogen that was absorbed by the Zircaloy but released at high temperatures cannot be evaluated after the experiment.

Due to the severe damage of the QUENCH-03 bundle no cladding tube could be removed from the bundle for this kind of analysis.

9.5 Metallographic Examination of the Bundle QUENCH-03

As an overview the sectioning map is given for test bundle QUENCH-03 in Fig. 94. The exact elevations are listed in Table 16.

The cross sections are shown as bottom and top view of the various bundle discs in Figs. 95 through 98 for QUENCH-03.

In the following the observations of the metallographic investigation of the bundle are described in detail and in the sequence from the lower to the higher elevations.

At the reference elevation 73 mm (section QUE-03-1, top) the polished cross section of the bundle (Fig. 99) does not show any sign of deterioration of the rod arrangement and the spacer within the still circular shroud. (One heater stub got lost during handling.) Since the oxide scales on the cladding and both sides of the shroud were measured to be only 1-2 µm and 0-1 µm, respectively (Fig. 127), no micrographs of the structures are presented for this elevation.

At the bundle elevation 550 mm (section QUE-03-3, top) the polished macrograph shows the still intact fuel rod simulators surrounded by the considerably bent spacer grid and shroud (Fig. 100). (One heater plus pellet slab got lost during handling.) By closer view (right side) spacer grid bulging and buckling can be interpreted as result of the impact of bending rods. In higher magnification (Fig. 101) some spacer grid cross positions show the spot welds from grid assembling and the isolated cut through an Inconel spring. The micrographs are documenting the dense, adherent and regular scale grown on spacer and rod cladding external surface, whereas no visible pellet/cladding interaction occurred. The scale thickness variation observed is summarised in Fig. 128 and will be described later.

At the bundle elevation 650 mm (section QUE-03-4, top) the simulator rods are still almost intact and in regular arrangement (Fig. 102). In contrast, the shroud is heavily deformed and the two tubular corner rods are collapsed. The deformation mode of the

latter can be interpreted to be due to external overpressure at least for some time window during the transient. A further important feature is the massive melt accumulation outside the shroud (Fig. 102, below).

The morphology of the externally relocated melt is rather non-uniform (Fig. 103). At a part of the contact zone, the position where candling had taken place, massive thinning of the shroud by dissolution is observed. Partial detachment from the shroud and formation of a system of coarse cracks have occurred during cooling. Variations in melt composition as indicated by variable tint of the macrographs are documented in high magnification (Fig. 103, lower image) for the example of a zone of dense melt in which the different oxygen contents correspond to variable volume fractions of ZrO_2 phase in the (Zr, O) matrix. This precipitation took place during cooling from originally single phase (Zr, O) melt. Other zones of the melt pool might indicate by considerable porosity the presence of additional components, whereas a separate droplet attached to the shroud is Zry melt.

Fig 104 gives a selection of micrographs showing morphology and extent of oxidation of exposed material surfaces. (For the distribution of the scale thickness see Fig. 129 and the description below.) Compared to fuel rod oxidation (upper image) the mentioned Zry melt shows a thicker but also regular scale, comparable to that of the shroud, whereas the porous melt variant shows an even thicker scale, having grown with irregular front and containing metallic inclusions. It was speculated that this melt might have formed and relocated during the strong interaction of the shroud upper flange with the stainless steel flange at 1300 mm bundle elevation, which was realised during post-test inspection. However, the analysis of this melt by SEM/EDX, performed at several positions, did not identify steel components, but only tantalum as unusual minor constituent, which indicates interaction with sheaths of thermocouples.

At 750 mm bundle elevation (QUE-03-5, top) the shroud is even more distorted than below (Fig. 105). It is no more complete after local dissolution into either external or internal melts which have partly disappeared by relocation. On the other hand segments of the shroud got thickened by accumulation of melt within the confinement of their external scale or the adjacent fibre insulation and their internal scale (see at top of overview macrograph). Morphological details are given in Fig. 106. In the central micrograph a shroud position is shown, where an originally developed internal contact to a rod is found broken, and where the shroud is externally thinned by originally metallic

and molten, finally almost ceramic material. To the right strong oxidation and liquid phase interaction is seen to have taken place so that the ZrO_2 pellet is found in intimate contact with the product melt.

In the following the rod oxidation is treated in detail to draw conclusions not only on the variations in the final status but also on the sequence of events and phenomena.

Fig. 107 documents the fact that the steam oxidation is usually regular and often restricted to the external cladding surface (upper micrograph). Bulging of the cladding away from the pellet under scale growth stress alone is not sufficient for steam access to the internal side, so that internal clad oxidation starts under limited steam supply across through-wall cracks but requires the later formed larger crack and fragmentation openings to become important. Consequently, as often noticed the extent of internal oxidation is considerably below the external. An example is shown in Fig. 107, lower micrograph, together with the late spalling of the outer sub-layer of the external scale, which is an event of minor overall importance. Fig. 108 is presented to stress the necessity of distinguishing between the bundle status at temperature, which is only indirectly accessible, and the status after quenching including the related mechanical damage. The micrograph (right side) reveals only negligible internal oxidation, whereas the overview macrograph (left) seems convincing for sufficient steam supply. Obviously, clad fragmentation must have occurred late during the quenching phase.

Internal melt relocation between cladding and pellet can displace molten cladding material in azimuthal as well as axial direction, thus filling the gap or even a bulge, together with the thinning or complete metal relocation from the source position. (There, the bare scale can quickly transform to the brittle stoichiometric form.) Fig. 109, illustrating a rod position where relocated cladding melt has maintained the pellet contact during scale bulging, documents external oxidation at temperature above 1800 K (sequence of partial layers of tetragonal and cubic oxide modification), thickened and melt-modified cladding (ZrO_2 precipitates), together with a pellet/cladding interaction zone of uniform thickness.

By distortion of the fuel rod simulator arrangement adjacent rods came in mutual contact and in touch with the shroud, as seen in Fig. 110, upper macrograph. This must have occurred rather early in the transient, since the scale, formed up to then, got dissolved again due to oxygen diffusion into the contacting metal during the limited access of further steam to the contact zone. As a consequence a kind of “necking”, i.e. formation of

a stable and axially extended contact zone of metallic character, is formed (and preserved during an eventual melting) together with the growth of a protective scale between the “neck” and the surrounding steam supplying void channel (Fig 110, lower micrograph). The net effect of external (channel side) growth and internal (neck side) dissolution of oxide is the formation of self-healing protective scale structures, by which the original rod arrangement is transformed into a massive bundle body with penetrating flow channels. It is clear that this body will be broken up by any non-uniform force field, built up during differential temperature changes and oxidation related material volume changes. This can lead to coarse cracking of scales, melt release or infiltration, which, in turn, will change the oxidation processes locally. Melt infiltration into an original flow channel can block the free passage of a steam flow and convert the conditions via steam starved oxidative towards inert or even reductive. Consequently, respective scales will stop to grow in thickness, in contact with metallic residues will be reduced under the diffusive oxygen loss, and when completely embedded by metallic melt will be dissolved even more quickly. An example for complete channel filling by metallic melt is shown in Fig. 111 as convincing support of this interpretation. (The melt-enclosed voids were obviously not connected with active flow channels, since their surface is free of scale.) The scale thickness distribution for the 750 mm elevation is given in Fig. 130.

At 800 mm bundle elevation (QUE-03-6, top), 50 mm above the elevation described before, the bundle status is qualitatively rather similar, however it corresponds to a much more advanced destruction as shown in the overview (Fig. 112). Fig. 131 summarises the systematic scale thickness measurements. The boundary conditions of the bundle are addressed with Figs. 113 and 114, showing necking between shroud and rods, melt relocation at the outer side of the shroud, internal shroud oxidation and shroud fragmentation, the latter observed on almost the whole bundle circumference. The described necking between touching rods and thus the flow channel formation is demonstrated in Fig. 115 together with an example of pellet/cladding interaction, which is described later. By the necking effect the separation into completely oxidised regions and positions with retained or accumulated metallic melt has been supported, as shown in Figs. 116 and 117: Cladding scale isolated from residual metal but in contact with steam has reached stoichiometry, whereas close to contacting metal substoichiometry is indicated by typical decomposition microstructures of the oxide (Fig. 116). In contrast, larger melt pools and metallic melt without direct steam access were able to reduce adjacent oxide, especially when this got completely embedded (Fig. 117).

For rod positions with essentially intact cladding no internal cladding oxidation by steam is observed; interaction with the fuel pellet was avoided completely (Fig. 118, left micrograph) or locally (central micrograph), or close pellet contact allowed the formation of an interaction layer of uniform thickness (Fig. 118, right; Fig 115, low, right). At positions of direct contact between metallic melt and a bare pellet the latter tends to be reduced, as indicated by the change in pellet microstructure (Fig. 119).

In Fig. 120 the final status of W/Re thermocouples is presented. Degradation of externally attached thermocouples begins by neck formation and complete oxidation of the external Zry sub-layer of the duplex sheath. In case of the depicted central thermocouple within the pellet of the centre rod Zry melt had filled the bore hole and got subsequently oxidised via the pellet, except an excentrically positioned metallic residue. This was identified by SEM/EDX analysis to contain small amounts of tantalum from thermocouple degradation, both in the residual metallic melt as well as in ceramic precipitates.

At 950 mm bundle elevation (QUE-03-7, top) the overview of the cross section (Fig. 121) shows all rods with partially exposed bare pellets and local bridges to adjacent rods, which were formed during the already described necking process and the melt accumulation. The destroyed shroud has relocated almost completely from this elevation in form of rubble fragments and melt. The remaining cladding material is essentially oxidised as shown by the macrograph on the right side of this figure. Fig. 122 is documenting residual melt of cladding type at a neck between two rods. During cooling ZrO_2 precipitation by decomposition of the originally single phase melt of homogeneous oxygen content has occurred. It is mentioned that the separation of the melt from the upper pellet, which was originally confined by the oxide shells of the rods, took place during cooling as well. Fig. 123 is an example for molten metallic cladding remaining in intimate contact with its scale and the pellet after solidification and quenching. In this case stress relief took place by crack propagation within the metallic material and into the pellet. Quenching occurred from a temperature at least above 1800 K as indicated by the decomposition microstructure (α-Zr(O) precipitation) of the originally cubic ZrO_2 modification of the internal part of the scale. At the position depicted by Fig. 124 a similar temperature history is deduced from the scale microstructure, whereas the thickness of the molten zone indicates closure of an originally present gap between cladding and pellet by melt accumulation. Finally the molten zone is found advanced towards a ceramic status after continued oxidation. The microstructure is complicated by obvious

variations in composition and porosity. Cracking has occurred along the interface of the pellet interaction layer (see overview micrograph). In Fig. 125 microstructural details of melt between pellets and of a pellet at a position near to a crack are shown. The melt has advanced in dissolving the pellet interaction zone and has precipitated ZrO_{2-x} phase above 1800 K as indicated by the fine structure of those precipitates. The reducing effect of the hot metallic melt on the pellet proceeded along the melt infiltrated crack and along the grain boundaries of the pellet.

The region of the thermocouple, which is still visible is shown in higher magnification in Fig. 126, in order to explain its status of advanced destruction: The wires of this W/Re thermocouple including the HfO_2 insulation seem to be intact, whereas the duplex sheath of Zry/Ta is completely destroyed after severe oxidation and lateral relocation, respectively. Interaction of tantalum with the originally metallic melt and the oxidation of the products are the reason of unusual microstructures of the ceramic material in the vicinity. The ceramic surrounds globular islands of metallic melt (photo in middle), analysed by SEM/EDX to consist of the relatively oxidation resistant metal tantalum and to contain zirconium together with traces of molybdenum, tin, iron and nickel. At the position of the right macrograph the main constituents of the ceramic material with eutectic microstructure are zirconium, tantalum, oxygen and traces of probably molybdenum. For the scale thickness distribution see Fig. 132.

The results of the systematic scale thickness measurements (Figs. 127 to 133) are discussed in the following. The oxide scale thickness of each rod was measured in four azimuthal directions, if possible. The lower bundle elevations show rather uniform thickness distribution across the bundle, indicating a rather flat temperature profile (Figs. 127 to 129). Only the outer rods have somewhat thinner scales at outward directions. At the 73 mm elevation the scale thickness is 2 µm or less. At 550 mm the oxidation extent is 10-20 µm scale on the rod cladding, slightly less at the bundle periphery compared to the centre. The shroud carries 5-10 µm on the inner and typically ca. 6 µm at the outer surface, at some external positions no scale can be distinguished. Across the bundle on the 650 mm elevation (Fig.129) the general extent of the rod and shroud oxidation is rather homogeneous with ca. 30-50 µm and 20-40 µm, respectively. This regular distribution is disturbed near the shroud orientation where external melt relocation and resulting accelerated heating of shroud and neighbouring rods have occurred: Close to the position of the external melt the adjacent rod is oxidised to 50 - 90 µm and the shroud up to 240 µm.

At the 750 mm elevation the scatter in scale thickness is large, indicating correspondingly strong variations in the local temperature history (Fig.130). The relatively fast oxidation of the central rod is mentioned, as observed in previous tests, explained by the lower heat capacity of this unheated rod, and in accordance with the TC measurements. At the 800 mm elevation (Fig. 131) the broad range of scale thickness reflects large temperature differences as well as cladding melt relocation or accumulation and complete oxidation. At 950 mm elevation complete oxidation and fragmentation of the scale are the general status and only a few rods remain with incomplete cladding oxidation (Fig. 132).

The results of the oxide scale thickness measurements for the individual elevations were combined to axial thickness distribution profiles in Fig. 133. In the upper graph a comparison of the bundle components is drawn, in the lower the statistical evaluation of all components together with maximum and minimum values are given. Both graphs illustrate the effect of the pronounced axial profile of time at temperature along the bundle.

Summarising statements drawn from the detailed metallographic investigation of the bundle are the following: The materials behaviour, the component interaction and the oxidation can be interpreted on the basis of a careful inspection of the final bundle status and the experience gained from separate effects investigations. The development sequence of the finally observed damage, however, cannot be always deduced, since the earlier status is often obscured by later events. In the actual context the interest is focused on bundle specific and quench related phenomena. In this respect the most important observation is the formation of a more or less rigid bundle body within the hot zone by neck formation between contacting rods and their oxidation. The flow channels formed thereby may either remain active (effective steam flow path), resistive (steam starvation tendency) or can get blocked by infiltrating melt.

Cladding melt relocation, which is known to start within the individual rods is occurring laterally and axially within the confinement of the scale by which the surface area is diminishing and the thermal contact to the pellets is improving. This contributes to the development of large temperature variations. Together with the embrittlement of bare scale (without contact to metallic cladding but in contact with steam) this can result in scale cracking and triggering of internal oxidation and outward melt penetration, which will accelerate the steam oxidation. The net effect on the total surface area of oxidising

metallic materials in temperature/time dependence is the main uncertainty in the interpretation of the measured hydrogen source term. It is clear that mechanisms as cladding through-wall cracking, crack surface oxidation, cladding shattering and scale or sub-layer spalling alone cannot explain the effects of quenching.

Concerning the oxidation of metallic melts it is not possible to apply usual kinetic correlations, since the fast diffusion and convection will maintain an almost homogeneous oxygen content in the melt. Further, the LWR Severe Accident typical (Zr, U, O) melt cannot be simulated in the QUENCH program and further efforts are required to quantify its oxidation kinetics in separate effect tests and to describe it mechanistically. Melt oxidation together with melt relocation, dispersion and fragmentation is obviously one of the most important quench phenomena which deserve careful further consideration.

10 Posttest Examination of the Bundle QUENCH-03

10.1 Posttest Appearance of the Bundle QUENCH-03

The post-test appearance (see Figs. 87 through 93) reveals significant melting, oxidation and fragmentation of the test bundle, from around 700 mm elevation upwards. The strongest bundle degradation is between the 700 and 1200 mm level. Below about 400 mm the shroud appears intact. Between the 550 and 750 mm elevation melt that relocated from upper zones is to be seen on the shroud surface. Also in this region, i.e. 600 - 780 mm, the shroud is partially collapsed suggesting a pressure difference across the shroud existed with the larger pressure between shroud and cooling jacket. Above this region, i.e. between 700 and 860 mm elevation the shroud appears to have formed a kind of bubble over half of the circumference (270° - 45°). This radial extension functioned as a debris catcher, where debris and molten material accumulated. Between ~800 and 1100 mm the shroud is completely gone and the insight into the bundle demonstrates severe melting and complete degradation. In addition, a strong reaction between shroud and fuel rod simulators as well as shroud and ZrO_2 fiber insulation took place in this region. As described in section 6.2 shroud failure was detected at 2627 s by the thermocouples of the inner cooling jacket.

At the upper edge of the flange of the shroud, i.e. at ~1300 mm, a strong reaction of molten Zircaloy and the stainless steel flange took place. This led to melt formation

complicating the disassembly of the test bundle such that the compensator of the inner cooling jacket connecting to the shroud flange had to be cut into pieces. In the upmost zone, i.e. above 1100 mm the shroud was in a molten stage, showing considerable thinning of the material (to some tenths of a millimeter) and a strong deformation. At about 1450 mm the fuel rod simulators and the upmost grid spacer of Zircaloy are destroyed. The severe embrittlement of the test bundle, caused the posttest state to change by any contact as it was the case for bundle QUENCH-02. Again, this fact complicated the encapsulation procedure which had to be realized having the bundle in vertical position.

10.2 Metallographic Examination of the Bundle QUENCH-03

As an overview the sectioning map is given for test bundle QUENCH-03 in Fig. 94. The exact elevations are listed in Table 16.

The cross sections are shown as bottom and top view of the various bundle discs in Figs. 95 through 98 for QUENCH-03.

In the following the observations of the metallographic investigation of the bundle are described in detail and in the sequence from the lower to the higher elevations.

At the reference elevation 73 mm (section QUE-03-1, top) the polished cross section of the bundle (Fig. 99) does not show any sign of deterioration of the rod arrangement and the spacer within the still circular shroud. (One heater stub was removed during handling.) Since the oxide scales on the cladding and both sides of the shroud were measured to be only 1-2 µm and 0-1 µm, respectively (Fig. 1xx), no micrographs of the structures are presented for this elevation.

At the bundle elevation 550 mm (section QUE-03-3, top) the polished macrograph shows the still intact fuel rod simulators surrounded by the considerably bent spacer grid and shroud (Fig. 100). (One heater plus pellet stack was removed during handling.) By closer view (right side) spacer grid bulging and buckling can be interpreted as a result of the impact of bending rods. At higher magnification (Fig. 101) spacer grid crosses are shown thickened due to adherence of some relocated melt together with one single relocated rubble fragment. The micrographs show the dense, adherent and regular scale grown on spacer and rod cladding and the absence of any pellet/cladding reaction. The scale thickness variation observed is summarised in Fig. 1xx and will be described later.

At the bundle elevation 650 mm (section QUE-03-4, top) the simulator rods are still almost intact and in regular arrangement (Fig. 102). In contrast, the shroud is heavily deformed and the two corner rods, hollow at this elevation, collapsed. Both deformation forms could be interpreted to be due to external overpressure on the shroud and corner rod circumference, respectively, at least for some time window during the transient. A further important feature is the massive melt accumulation outside the shroud (Fig. 102, below).

The morphology of the externally relocated melt is rather non-uniform (Fig. 103). At a part of the contact zone, the position where candling had taken place, massive thinning of the shroud by dissolution is observed. Partial detachment from the shroud and formation of a system of coarse cracks has occurred during cooling. Variations in melt composition as indicated by variable tint of the macrographs is documented in high magnification (Fig. 103, lower image) for the example of a zone of dense melt in which the different oxygen contents correspond to variable volume fractions of ZrO_2 phase in the (Zr, O) matrix. This precipitation took place during cooling from originally single phase (Zr, O) melt. Other zones of the melt pool indicate by considerable porosity the presence of additional components, whereas a separate small drop on the shroud is Zry melt.

Fig 104 gives a selection of micrographs showing morphology and extent of oxidation of exposed material surfaces. (For the distribution of the scale thickness see Fig. 1xx and the description below.) Compared to fuel rod oxidation (above image) the mentioned Zry melt shows a thicker but also regular scale, comparable to that of the shroud, whereas the porous melt variant shows an even thicker scale, having grown with an irregular front and containing metallic inclusions. It is speculated that those are probably enriched in nickel, resulting from interaction with steel structures. It is possible that this melt has formed and relocated during the strong interaction of the shroud upper flange with the stainless steel flange at 1300 mm bundle elevation, which was realised during post-test inspection.

At 750 mm bundle elevation (QUE-03-5, top) the shroud is even more distorted than below (Fig. 105). It is no more complete after local dissolution into either external or internal melts which have disappeared almost completely by relocation. On the other hand segments of the shroud were thickened by accumulation of melt within the confinement of their external and internal scale (see at the top of the overview

macrograph). Morphological details are given in Fig. 106. In the central micrograph a shroud position is shown, where an originally developed internal contact to a rod is found broken, and where the shroud is externally thinned by originally metallic and molten, finally almost ceramic material. To the right strong oxidation and liquid phase interaction is seen to have taken place so that the pellet is found in intimate contact with the product melt.

In the following the rod oxidation is treated in detail to draw conclusions not only on the variations in the final status but also on the sequence of events and phenomena.

Fig. 107 documents the fact that the steam oxidation is usually regular and often restricted to the external cladding surface (upper micrograph). Bulging of the cladding away from the pellet under scale growth stress alone is not sufficient for steam access to the internal side, so that internal clad oxidation starts under limited steam supply across through-wall cracks but requires the later formed larger crack and fragmentation openings to become important. Consequently, as often noticed the extent of internal oxidation is considerably below the external. An example is shown in Fig. 107, lower micrograph, together with the late spalling of the outer sub-layer of the external scale, which is an event of minor overall importance. Fig. 108 is presented to stress the necessity of distinguishing between the bundle status at temperature, which is only indirectly accessible, and the status after quenching including the related mechanical damage. The micrograph (right side) reveals only unimportant internal oxidation, whereas the overview macrograph (left) seems convincing for sufficient steam supply. Obviously, clad fragmentation must have occurred late during the quenching phase.

Internal melt relocation between cladding and pellet can displace molten cladding material in azimuthal as well as axial direction, thus filling the gap or even a bulge, together with the thinning or complete metal relocation from the source position. (There, the bare scale can quickly transform to the brittle stoichiometric form.) Fig. 109, illustrating a rod position where relocated cladding melt has maintained the pellet contact during scale bulging, documents external oxidation at temperature above 1800 K (sequence of tetragonal and cubic oxide modification), thickened and melt-modified cladding (ZrO_2 precipitates), together with a pellet/cladding reaction layer of uniform thickness.

By distortion of the fuel rod simulator arrangement adjacent rods came in mutual contact and in touch with the shroud, as seen in Fig. 110, upper macrograph. This must have

occurred rather early in the transient, since the scale, formed up to then, got dissolved again due to oxygen diffusion into the contacting metal during the limited access of further steam to the contact zone. As a consequence a kind of “necking”, i.e. formation of a stable and axially extended contact zone of metallic character is formed (and preserved during an eventual melting) together with the growth of a protective scale between the “neck” and the surrounding steam supplying void channel (Fig 110, lower micrograph). The net effect of external (channel side) growth and internal (neck side) dissolution of oxide is the formation of self-healing protective scale structures, by which the original rod arrangement is transformed into a massive bundle body with penetrating flow channels. It is clear that this body will be broken up by any non-uniform force field, built up during differential temperature changes and oxidation-related material volume changes. This can lead to coarse cracking of scales, melt release or infiltration, which, in turn, will change the oxidation processes locally. Melt infiltration into an original flow channel can block the free passage of a steam flow and convert the conditions via steam starved oxidizing towards inert or even reducing. Consequently, respective scales will stop growing in thickness, in contact with metallic residues will be reduced under the diffusive oxygen loss, and if completely embedded by metallic melt will be dissolved even more quickly. An example for complete channel filling by metallic melt is shown in Fig. 111 as convincing support of this interpretation. The scale thickness distribution for the 750 mm elevation is given in Fig. 1xx.

At 800 mm bundle elevation (QUE-03-6, top), 50 mm above the elevation described before, the bundle status is qualitatively rather similar, however it corresponds to a much more advanced destruction as shown in the overview (Fig. 6). The described neck and flow channel formation between touching rods is demonstrated in Fig. 6f. By this effect the separation into completely oxidised regions and positions with retained or accumulated metallic melt has been supported, as shown for examples to be described in the following figures. For rod positions with essentially intact cladding no internal cladding oxidation by steam is observed; interaction with the fuel pellet was avoided completely or locally, or close pellet contact allowed the formation of an interaction layer of uniform thickness (Fig. 6b, from left to right). Cladding scale isolated from residual metal but in contact with steam has reached stoichiometry, whereas close to contacting metal substoichiometry is indicated by typical decomposition microstructures of the oxide (Fig. 6g). In contrast, metallic melt without direct steam access was able to reduce adjacent oxide, especially if completely embedded (Fig. 6d). At positions of direct contact

between metallic melt and a bare pellet the letter tends to be reduced, as indicated by the change in pellet microstructure (Fig. 6h). Fig. 1xx summarizes the scale thickness measurements.

In Fig. 6e the final status of W/Re thermocouples is presented. Degradation of externally attached thermocouples begins by neck formation and complete oxidation of the external Zry sub-layer of the duplex sheath. In case of the centre rod pellet central thermocouple depicted Zry melt had filled the bore and was subsequently oxidized by the pellet except an excentrically positioned metallic residue. The boundary conditions of the bundle are illustrated in Figs. 6c and 6a, showing melt relocation at the outer side of the shroud, necking between shroud and rod, internal shroud oxidation and shroud fragmentation, the latter observed on almost the whole bundle circumference.

At 950 mm bundle elevation (QUE-03-7, top) the overview of the cross section (Fig. 7) shows all rods with partially exposed bare pellets and local bridges to adjacent rods, which were formed during the already described necking mechanism and the melt accumulation. The destroyed shroud has relocated almost completely from this elevation in form of rubble fragments and melt. The remaining cladding material is essentially oxidised as shown by the macrograph on the right side of this figure. The region of the thermocouple, which is still visible is shown in higher magnification in Fig. 7a, in order to explain its status of advanced destruction: the wires of this W/Re thermocouple including the HfO_2 insulation seem to be intact, whereas the duplex sheath of Zry/Ta is completely destroyed after severe oxidation and lateral relocation, respectively. Interaction of tantalum with the originally metallic melt and their oxidation have resulted in an unusual eutectic microstructure of the ceramic material in the vicinity. The ceramic surrounds globular islands of metallic melt, probably containing the relatively oxidation resistant metals tantalum and tin.

Fig. 7b shows residual melt of cladding type at a neck between two rods. During cooling ZrO_2 precipitation by decomposition of the originally single phase of homogeneous oxygen content has occurred. It is mentioned that the separation of the melt, originally confined between the pellet and the oxide shell of a rod took place during cooling as well. Fig. 7c is an example for molten metallic cladding remaining in intimate contact with its scale and the pellet after solidification and quenching. In this case stress relief took place by crack propagation within the metallic material and into the pellet. Quenching occurred from a temperature at least above 1800 K as indicated by the decomposition

microstructure (α-Zr(O) precipitation) of the originally cubic ZrO_2 modification of the internal part of the scale. At the position depicted by Fig. 7d a similar temperature history is deduced from the scale microstructure, whereas the thickness of the molten zone indicates closure of an originally present gap between cladding and pellet by melt relocation. Finally the molten zone is found advanced towards a ceramic status after continued oxidation. The microstructure is complicated by obvious variations in composition and porosity; cracking has occurred along the pellet interaction interface. In Fig. 7e microstructural details of melt between pellets and of a pellet near to a crack are shown. The melt has dissolved the pellet interaction zone and has precipitated a ZrO_{2-x} phase above 1800 K as indicated by the fine structure of those precipitates. The reducing effect of the hot metallic melt on the pellet proceeded along the melt infiltrated crack and along the grain boundaries of the pellet. For the scale thickness distribution see Fig. 1xx, the last of the series (Figs. 1xx to 1xx) to be discussed in the following:

The oxide scale thickness of each rod was measured in four azimuthal directions, if possible. The lower bundle elevations show rather uniform thickness distribution across the bundle, indicating a rather flat temperature profile (Figs. 1xx to 1xx). Only the outer rods have somewhat thinner scales at outward directions. At the 73 mm elevation the scale thickness is 2 µm or less. At 550 mm the oxidation extent is 10-20 µm scale on the rod cladding, slightly less at the bundle periphery compared to the centre. The shroud carries 5-10 µm on the inner and typically ca. 6 µm at the outer surface, at some external positions no scale can be distinguished. Across the bundle on the 650 mm elevation (Fig.1xx) the general extent of the rod and shroud oxidation is rather homogeneous with ca. 30-50 µm and 20-40 µm, respectively. This regular distribution is disturbed near the shroud orientation where external melt relocation and resulting accelerated heating of shroud and neighbouring rods have occurred: Close to the position of the external melt the adjacent rod is oxidised to 50-90 µm and the shroud up to 240 µm.

At the 750 mm elevation the scatter in scale thickness is large, indicating correspondingly strong variations in the local temperature history (Fig.1xx). The relatively fast oxidation of the central rod is mentioned, as observed in previous tests, explained by the lower heat capacity of this unheated rod. At the 800 mm elevation (Fig. 1xx) the broad range of scale thickness reflects large temperature differences as well as cladding melt relocation or accumulation and complete oxidation. At 950 mm elevation complete oxidation and fragmentation of the scale are the general status and only a few rods remain with incomplete scale oxidation (Fig. 1xx).

The following summarising statements can be drawn from the detailed metallographic investigation of the bundle: The materials behaviour, the component interaction and the oxidation can be interpreted on the basis of a careful inspection of the final bundle status and the experience gained from separate effects investigations. The development sequence of the finally observed damage, however, cannot be always deduced, since the earlier status is often obscured by later events. In the actual context the interest is focused on bundle specific and quench related phenomena. In this respect the most important observation is the formation of a more or less rigid bundle body within the hot zone by neck formation between contacting rods and their oxidation. The flow channels formed thereby may either remain active (effective steam flow path), resistive (steam starvation tendency) or can become blocked by infiltrating melt.

Cladding melt relocation, which is known to start within the individual rods is occurring laterally and axially within the confinement of the scale by which the surface area is diminishing and the thermal contact to the pellets is improving. This contributes to the development of large temperature variations. Together with the embrittlement of bare scale (without contact to metallic cladding but in contact with steam) this can result in scale cracking and triggering of internal oxidation and outward melt penetration, which will accelerate the steam oxidation. The net effect on the total surface area of oxidising metallic materials and the temperature/time dependence of their oxidation are main uncertainties in the interpretation of the measured hydrogen source term. It is clear that mechanisms as cladding through-wall cracking, crack surface oxidation, cladding shattering and scale or sub-layer spalling alone cannot explain the effects of quenching.

Concerning the oxidation of metallic melts it is not possible to apply usual kinetic correlations, since the fast diffusion and convection will maintain an almost homogeneous oxygen content in the melt. Further, the LWR Severe Accident typical (Zr, U, O) melt cannot be simulated in the QUENCH program and further efforts are required to quantify its oxidation kinetics in separate effect tests and to describe it mechanistically. Melt oxidation together with melt relocation, dispersion and fragmentation is obviously one of the most important quench phenomena which deserve careful further consideration.

11 Calculational Support

Within FZK institutional R&D activities calculations have been made to define experimental parameters of the QUENCH experiments and to interpret the experimental results after the experiment had been performed. As a code SCDAP/RELAP5 (S/R5) mod 3.1 rel. F [11], made available for the planning of the QUENCH experiments, S/R5 mod 3.2 [12], which became operable after the tests, have been used. The improved model for heat transfer in the transition boiling region [13] and an adaptation of the CORA heater rod model to the conditions of the QUENCH facility are included in the FZKA version of both programme versions. Furthermore, in S/R5 mod 3.2, we included the material property data for ZrO_2 instead of those for UO_2 to model the pellets. S/R5 mod 3.2 can also be used for the quench phase.

The various calculations also rely on the experience gained from calculations, done up to then. Especially the adjustment of the electrical resistance of the circuit outside the electrical heater rods, performed on the basis of test QUENCH-01 [7], was kept for the subsequent calculations with S/R5 mod 3.1.

11.1 Modelling of the QUENCH Facility

The modelling of the QUENCH facility is shown in Fig. 134. In the radial direction the whole facility including the containment is modelled, because the radial heat losses out of the bundle depend ultimately on the ambient room temperature. This modelling is mandatory for all work performed before experimental data are available, and it is desirable for all post-test analyses, because the calculated data are more detailed than the experimental ones.

Axially the heated part is modelled with ten 0.1 m long meshes. In the lower and upper electrode zones 0.45 and 0.6 m, respectively, of the test section are considered, each by three meshes, assuming molybdenum as electrode material. The unheated rod, the two rows of rods to be heated independently, the four Zircaloy corner rods, the inner and outer cooling jacket walls, and the containment are modelled as SCDAP components. In this way two-dimensional heat conduction within the structures and radiation between adjacent structures are taken into account. The temperature at the end of the rods is set to 300 K. The ZrO_2 fibre insulation is modelled to end at the upper end of the heated zone. With this exception all structures must be modelled to have the same length

because of limitations in the code. Therefore the upper and lower head cannot be modelled in all details.

The bundle flow and the gas atmospheres outside the outer cooling jacket, i. e. in the containment and the laboratory, are represented by a single channel each. Besides the gas atmospheres outside the outer cooling jacket are assumed to be stagnant, thus neglecting natural convection in these regions. Because of restrictions in the code, where only a limited number of materials can be specified, these atmospheres are modelled to consist of argon.

The off-gas pipe is taken into account with its whole length of 3 m, including the orifice at the position where the gas sample for the mass spectrometer is taken and the orifice at the outlet of the off-gas pipe. The mass flows in the off-gas pipe and the adjacent cooling jacket are modelled to be one-dimensional, the structures are modelled as RELAP heat structures, thus taking into account radial heat transfer within the structures.

11.2 QUENCH-02

11.2.1 Pre-Test Calculations

In contrast to experiment QUENCH-01 a power ramp was to be applied in test QUENCH-02 without any additional pre-oxidation, when the bundle has reached a stationary temperature of about 900 K at the end of the heated zone. Besides in the bundle the temperature increase with time was intended to be rather high. Therefore the execution of the experiment should be performed in much less time than QUENCH-01. So the requests to prepare the experiment were much higher and implied essentially two challenges. Firstly, when the test was performed, the quality of pre-test calculations could only be tested against experimental data at rather low temperatures, where discrepancies are less obvious. Secondly the fast temperature increase gave only a short time for all decisions which had to be taken during the test performance. Due to the temperature escalation during the transient, this constraint became even more urgent at the time of quench initiation. To meet these demands the test conduct had to be pre-defined as far as possible, and its details had to be pre-programmed on the basis of the pre-test calculations.

In detail the following scenario was assumed for the pre-test calculations. As initial conditions room temperature (300 K) was assumed for all structures. The temperatures

at both ends of the heated rods were assumed to be 300 K during the whole calculation. The reference pressure at the outlet of the off-gas pipe was 1.9 bar during the whole calculation. An argon mass flow in the bundle of 3 g/s was assumed up to quench initiation, its inlet temperature increasing from 300 K to 700 K or 800 K within 100 s. Then steam at the same inlet temperature as the argon flow was added with a mass flow rate of 4.5 g/s up to t = 1000 s and 3 g/s afterwards. The argon and the water cooling were counter-current flows with mass flow rates of 6 g/s and 100 g/s, respectively, and an inlet temperature of 300 K.

A power pulse and a plateau were assumed up to t = 3000 s to simulate the heat-up phase and the stabilisation phase (Fig. 135), where elevated temperatures in the bundles were to be reached and checks were performed to verify the correct working of the various systems. During that time the temperature had, however, to be low enough to avoid premature oxidation. Then a linear power increase was assumed to reach the desired high rod temperatures before quenching. In the pre-test calculations the slope of the power increase was varied. In some calculations electrical power was kept constant when a temperature of 1300 K or 1500 K was reached. In all cases the rod power for the inner an the outer heated rings were equal.

Fig. 135 shows representative results for these calculations. During the first 700 s temperatures are still rather low, and a small amount of steam is predicted to condense in the bundle. In the off-gas pipe condensation occurs during much longer times. For the problems to be solved by pre-test calculations steam condensation in the off-gas pipe is, however, not important, because in the experiment the stabilisation phase is much longer than assumed in the pre-test calculations. In the experiment any condensed water can evaporate during this time. During the transient the uppermost heated volume is predicted to become and then to stay the hottest part of the bundle and to be the first volume where temperature escalation begins. The temperature escalation can be seen well from the sharp temperature increase and the corresponding enhanced growth of oxide layer thickness and hydrogen production.

A summary of the pre-test calculations is given in Table 17. The time intervals to reach the various temperatures can be used to assess the time for operator intervention, and the number of nodes with temperatures above 2300 K gives an impression of the bundle destruction at the end of the transient.

The temperature and temperature increase at the end of the heated zone are given in Fig. 136 for the various cases. The temperature increase is non-linear and varies strongly with time. Therefore any value for temperature increase is meaningful only when the respective temperature level is indicated. The nearly constant temperature increase at a temperature of about 1100 K comes from a change of material properties of Zry in that region. The results show furthermore that switching from a linear power increase to a plateau does not change the results significantly. Evidently the energy stored in the rods and the amount of chemical power, released due to oxidation, are high enough to continue temperature escalation.

When the quench water reaches the hot structures near the bundle inlet part of the water evaporates and cools the bundle. To compensate this heat loss at least partly, electrical power should be increased sufficiently for a certain time at the beginning of the quench phase. However, in QUENCH-01 mass spectrometer measurement of the steam flow was not reliable and modelling of the bundle inlet region with S/R5 is not detailed enough. Therefore no estimate could be made, neither on the basis of S/R5 calculations nor on the basis of hand calculations.

Pre-test calculation q02v05 was chosen as a basis for the experiment. Instead of the power pulse at the beginning of the heat-up period, assumed for the pre-test calculations, a stepwise power increase was applied in the experiment to reduce thermal stresses in the facility, especially in the fuel rods. Since it was not clear in advance whether a test could be run in exactly the same manner as assumed in the pre-test calculations and whether the pre-test calculations were sufficiently accurate it was decided to pre-programme two power transients with different slopes, the first one being the first choice, the second one, with a steeper slope, to be used if the temperature rise in the experiment up to a temperature of about 1000 K at the end of the heated zone were not fast enough. Further choices for pre-programming were not possible, because the number of possible programmes in the process-control system was limited. As a basis to initiate quenching the bundle temperature in the hottest zone was used. In contrast to QUENCH-01 the hydrogen production was not used as a basis for decisions, because the sampling frequency, displayed on the monitor, was judged to be too low. The plateau value of 19 kW for bundle power to be applied during the first part of the quench phase was assessed from the pre-defined power transient to be a reasonable value at the time of quench initiation. It was decided to apply this power until the temperature is seen to drop sharply at the axial level 550 mm.

11.2.2 Post-Test Calculations

Post-test calculations were performed without any changes except the exact experimental values of inlet temperatures, mass flow rates, and power history. The fluid inlet temperature has been adjusted according to the reading of thermocouple TFS 2/1, bent into the flow channel to measure fluid inlet temperature. The results, given in Figs. 137 - 139 for S/R5 mod 3.2, indicate that the agreement between measured and calculated data is quite good more or less up to the beginning of temperature escalation. This is even true for hydrogen production, which is a sensible measure of the quality of the modelling. Radial differences in measured temperatures can only partly be reproduced by the calculations, because radiation heat transfer gives a certain radial temperature decrease, but the thermal-hydraulic modelling of the bundle is one-dimensional, such giving the same fluid temperature for all components in the bundle at a given axial level. When temperature escalation begins, calculated temperatures are lower than in the experiment. The temperature escalation is calculated to begin about 25 s later than observed in the experiment. A more detailed comparison for the power transient is not possible because of the lack of experimental data.

Fig. 140 demonstrates the programme capability to describe the quench phase for the various programme versions. Whereas programme version S/R5 mod 3.1 is completely inappropriate, S/R5 mod 3.2 gives better results, both for the original INEEL model and that developed at Paul Scherrer Institut (PSI) in Switzerland, where a special heat transfer correlation is used for the quench phase. It seems that the measured sharp temperature decrease to saturation temperature is not representative of the actual rod surface temperature, but that it is caused by the positioning of the thermocouples on the outside rod surface, as it is discussed in section 7.3. Therefore a more detailed comparison between calculated and measured temperatures during the quench phase is not possible. Further work suggests, however, that the calculated results are not yet satisfactory, and more modelling work has still to be done.

11.3 QUENCH-03

11.3.1 Pre-Test Calculations

In a similar manner as for test QUENCH-02 pre-test calculations have been made for test QUENCH-03. Since a steeper power transient than for the previous experiment was intended, that of run q02v03 (0.42 W/s, see Tab. tch1) was selected as a basis for the

test conduct. As the behaviour of the system during heat-up, especially with respect to condensation of steam at the cold structures is known from test QUENCH-02, the calculation starts near the end of the stabilisation period after the heat-up phase, i. e. at bundle temperatures of up to about 900 K, to allow for shorter computing times. In detail the temperatures, reached in test QUENCH-02 at t = 0 s are taken as initial conditions. Typical results are given in Fig. 141. In comparison to the test conduct for QUENCH-02 (see Fig. 135) it shows that the time to perform the transient and hence time for operator intervention to initiate quenching becomes sensibly shorter, once elevated temperatures are reached.

It was planned to increase electrical power in the beginning of the quench phase to compensate the additional heat losses due to the rather cold steam which is produced when the water comes into contact with the hot structures in the inlet pipe and the lower plenum of the test section. Since quench initiation was planned just after the beginning of the temperature escalation, it was a concern during the preparation of the test that the additional heat loss might decrease the bundle temperature too much and to an extent which is not representative of commercial reactors. When quenching begins at higher temperature, increase of electric power does not help much to counterbalance the additional heat loss. Firstly the release of chemical power due to oxidation quickly becomes higher than electrical power. Secondly rather a large portion of the electric power is released in the region of temperature escalation, because local electric power release increases with temperature and therefore cannot compensate heat loss due to steam production globally.

Because of the importance of this topic some effort has been spent to deduce a value of electrical power to be applied at quench initiation. Since it is not possible to treat water quenching adequately with S/R5 mod 3.1, the following approximate solution was tried. After switching off the argon and steam flow at the end of the transient, a pure steam flow at an inlet temperature of 400 K has been assumed for the calculations, the time dependent mass flow rate being that which has been measured with the mass spectrometer after quench initiation in test QUENCH-01. Though the first peak of steam production may be caused by system response during the sharp increase of mass flow rate and not by water evaporation in the inlet pipe, no change was made for that time period. The electric power was varied, aiming at getting constant temperature in the bundle for the whole time when in the experiment the inlet pipe and the lower plenum are filled with water.

As an example results for the beginning of the quench phase are given in Fig. 142. The minimum of hydrogen production at quench initiation stems from the prescription of mass flow rates in the bundle: for a short time the fluid in the bundle is stagnant, and no oxidation is calculated. When rather a high constant power is applied at quench initiation, it is possible to keep bundle temperatures more or less constant over several ten seconds. With increasing oxide layer thickness, heat generation due to oxidation and hence rod temperatures decrease. However, this is predicted to occur at times when the rather crude model is probably no longer adequate. In the beginning of the quench phase sensible oxidation is predicted to occur in a single node only, namely at the end of the heated zone. Shattering is not calculated, because the actual conditions are outside of the range where the shattering model is triggered.

The test conduct was defined on the basis of the pre-test calculations and the test conduct of test QUENCH-02. As for test QUENCH-02 a constant value for electrical power was applied from quench initiation to the time when temperature is seen to drop at the axial level of 550 mm. In contrast to test QUENCH-02 it was much higher, the value of 44 kW being deduced from the pre-test calculations. The calculated hydrogen production was to be used during the test as a criterion for quench initiation, but since escalation began in a zone which was used for control during the test, it proved to be difficult to interpret the data during the test.

11.3.2 Post-Test Calculations

After the experiment post-test calculations have been made similarly to test QUENCH-02. Results are given in Figs. 139 - 145. In Fig. 144 the triangles reprenting the measured temperatures in the shroud and the cooling jackets point at the azimuthal positions of the respective thermocouples. The measured and calculated temperatures agree well until the onset of temperature escalation. In contrast to the experimental findings the temperature escalation is calculated to begin at the end of the heated zone, i. e. at 950 mm instead of level 11 (750 mm), and the calculated temperature escalation at the end of the heated zone begins about 80 s later than detected at level 11. Since local input of electrical energy increases with temperature, calculated temperature profiles begin to deviate from experimental values in the whole bundle after onset of escalation. In the lower part this leads to a reduced temperature increase. A calculated temperature escalation in the shroud seems to begin about 60 s before quench initiation.

The steps in the measured hydrogen production rate come from a smoothing procedure for the experimental data.

The beginning of the temperature escalation at another level than that at the end of the heated zone and the temperature escalation in the shroud are not understood up to now, and two ideas are actually considered. The first one is that some of the hydrogen, produced during oxidation may be absorbed in the structures. This is an exothermic process, increasing temperature and oxidation rates locally. It might trigger escalation in the shroud in the upper electrode region. Another idea is that in this region - and perhaps elsewhere - some of the oxide layer might ablate (break-away oxide), such enhancing oxidation. However, these ideas still need further examination, and in the actual state of the understanding major programme development work does not seem to be promising and should be postponed.

The results for the transient show that the escalation, detected in the experiment, is not well reproduced in the calculations. For this reason and because of the shortcoming in the modelling of the reflood phase, calculations for the quench phase are not presented for QUENCH-03.

References

[1] J.M. Broughton, P. Kuan, and D.A. Petti, “A Scenario of the Three Mile Island Unit 2 Accident,” Nuclear Technology, 87, 34, 1989.

[2] P. Hofmann, S. Hagen, V. Noack, G. Schanz, L. Sepold, “Chemical-Physical Behavior of Light Water Reactor Core Components Tested under Severe Reactor Accident Conditions in the CORA Facility,” Nuclear Technology, vol. 118, 1997, p. 200.

[3] R.R. Hobbins and G.D. McPherson, “A Summary of Results from the LOFT LP-FP-2 Test and Their Relationship to Other Studies at the Power Burst Facility and of the Three Mile Island Unit 2 Accident,” OECD/LOFT Final Event, ISBN 92-64-03339-4, 1991.

[4] S. Hagen, P. Hofmann, V. Noack, L. Sepold, G. Schanz, G. Schumacher, “Comparison of the Quench Experiments CORA-12, CORA-13, CORA-17,” FZKA 5679, Forschungszentrum Karlsruhe, 1996.

[5] P. Hofmann, V. Noack, M.S. Veshchunov, A.V. Berdyshev, L.V. Matweev, A.V. Palagin, V.E. Shestak, “Physico-Chemical Behavior of Zircaloy Fuel Rod Cladding Tubes During LWR Severe Accident Reflood,” FZKA 5846, Forschungszentrum Karlsruhe, 1997.

[6] P. Hofmann, W. Hering, C. Homann, W. Leiling, A. Miassoedov, D. Piel, L. Schmidt, L. Sepold, M. Steinbrück, “Results of the Commissioning Tests,” FZKA 6099, Forschungszentrum Karlsruhe, 1998.

[7] P. Hofmann, W. Hering, C. Homann, W. Leiling, A. Miassoedov, D. Piel, L. Schmidt, L. Sepold, M. Steinbrück, “QUENCH-01, Experimental and Calculational Results,” FZKA 6100, Forschungszentrum Karlsruhe, 1998.

[8] P. Ihle and K. Rust, “PWR Reflood Experiments Using Full Length Bundles of Rods With Zircaloy Cladding and Alumina Pellets,” Nuclear Engineering and Design 99, 1987, 223-37.

[9] R.W. Garner, P.E. MacDonald, “Power Burst Facility Thermocouple Effects Test Results Report, Test Series TC-1,TC-3, and TC-4,” U.S. Nuclear Regulatory Commission, 1982.

[10] L. Sepold, P. Hofmann, W. Leiling, A. Miassoedov, D. Piel, L. Schmidt, M. Steinbrück, “Reflooding Experiments with LWR-Type Fuel Rod Simulators in the QUENCH Facility,” Proceedings of the Ninth International Topical Meeting on Nuclear Reactor Thermal Hydraulics (NURETH-9), San Francisco, Oct. 3 – 8, 1999.

[11] C. M. Allison et al., “SCDAP/RELAP5/MOD 3.1 Code Manual,” NUREG/CR-6150, EGG-2720, Idaho Falls, Idaho, USA,1993.

[12] The SCDAP/RELAP5 Development Team, “SCDAP/RELAP5/MOD 3.2 Code Manual,” NUREG/CR-6150, INEL-96/0422, Idaho Falls, Idaho, USA,1997.

[13] V. Sanchez, E. Elias, Ch. Homann, W. Hering, D. Struwe, “Development and Validation of a Transition Boiling Model for the RELAP5/MOD3 Reflood Simulation,” FZKA 5954, 1997.

Acknowledgements

Experiment QUENCH-02 was co-financed by the European Commission under the Euratom Fourth Framework Programme on Nuclear Fission Safety 1994 – 1998 (Report No. INV-COBE (98)-D010, EVR 18982 EN9, contract FI4S-CT95-0013, Investigation of Core Degradation). Both tests were also part of the cooperation with the German nuclear industry, co-financed by Siemens/KWU and the German utilities under the leadership of EnBW and RWE.

At the Karlsruhe Research Center the broad support needed for preparation, execution, and evaluation of the experiment is gratefully acknowledged. In particular, the authors would like to thank Mr. E. Mackert for the assembly of the test rods, Messrs. J. Moch and R. Vouriot for assembling and instrumenting the test bundle, and S. Horn for the preparation of the hydrogen measurement with the Caldos system and the support for the test data selection. Furthermore, the authors would like to express their gratitude to Mrs. M. Heck, Mrs. J. Laier, and Mr. T. Schreibmaier for helping in the test data processing, to Mr. L. Anselment for sectioning of the epoxied bundle and for the preparation of the metallographic samples, Mr. H. Metzger and Mrs. U. Stegmaier for the examination of the metallographic samples by optical microscope.

Special thanks are extended to Dr. T. Haste, AEA Technology, on attachment to JRC Ispra, for the review of the manuscript.

Table 1: QUENCH Test Matrix

Test	Quench medium	Flooding rate[1)]	Heat-up rate	Max. ZrO_2 layer thickness[2)]	Temp. at onset of flooding[3)]	Remarks	Date of test conduct
QUENCH-00	water	2.8 cm/s; from the bottom	1.0 K/s	≈ 500 µm	≈ 1500 °C	commissioning tests	Oct. 9 - 16, 97
QUENCH-01	water	1.6 cm/s; from the bottom	0.5 K/s	≈ 300 µm	≈ 1600 °C	partial fragmentation of pre-oxidized cladding	February 26, 98
QUENCH-02	water	1.6 cm/s; from the bottom	0.5 K/s	completely oxidized	≈ 1900 °C	no additional pre-oxidation; quenching from high temperatures	July 7, 98
QUENCH-03	water	1.4 cm/s; from the bottom	0.6 K/s	completely oxidized	≈ 2100 °C	delayed flooding; 240 s after temperature escalation has started	January 20, 99
QUENCH-04	steam	≈ 49 g/s; from the bottom	0.5 K/s	≈ 170 µm	≈ 1800 °C	cool-down (quench) behavior of cladding by injected cold steam;	June 30, 99
QUENCH-05	steam	≈ 50 g/s; from the bottom	0.5 K/s	> 200 µm	≈ 1800 °C	physico-chemical behavior of oxygen-embrittled cladding	2000
QUENCH-06	water	1.5 cm/s; from the bottom	1.0 K/s	> 200 µm	1600 – 1800 °C	OECD-ISP, prediction of H_2 source term by different code systems	2000
QUENCH-07	steam	to be determined from the bottom	to be de-termined	determined by heat-up rate	1400 – 1600 °C	impact of B_4C absorber rod failure on H_2, CO, CO_2 and CH_4 generation	2001

[1)] Flooding rate: rise of the water level at the -250 mm bundle elevation
[2)] Measured at the bundle elevation of max. temperature before flooding
[3)] Maximum measured temperature in test section

Revised: March 2000

Table 2: Design characteristics of the QUENCH test bundle

Bundle type		PWR
Bundle size		21 rods
Number of heated rods		20
Number of unheated rods		1
Pitch		14.3 mm
Rod outside diameter		10.75 mm
Cladding material		Zircaloy-4
Cladding thickness		0.725 mm
Rod length	heated rod (levels)	2480 mm (-690 mm to 1790 mm)
	unheated rod (levels)	2842 mm (-827 mm to 2015 mm, incl. extension piece)
Heater material		Tungsten (W)
Heater length		1024 mm
Heater diameter		6 mm
Annular pellet	heated rod	ZrO_2; ∅ 9.15/6.15 mm; L=11 mm
	unheated rod	ZrO_2; ∅ 9.15/2.5 mm; L=11 mm
Pellet stack	heated rod	0 mm to ~ 1020 mm
	unheated rod	0 mm to 1553 mm
Grid spacer	material	Zircaloy-4, Inconel 718
	length	Zry 42 mm, Inc 38 mm
	location of lower edge	-200 mm Inconel 50 mm Zircaloy-4 550 mm Zircaloy-4 1050 mm Zircaloy-4 1410 mm Zircaloy-4
Shroud	material	Zircaloy-4
	wall thickness	2.38 mm
	outside diameter	84.76 mm
	length (extension)	1600 mm (-300 mm to 1300 mm)
Shroud insulation	material	ZrO_2 fiber
	insulation thickness	~ 37 mm
	elevation	-300 mm to 1000 mm
Molybdenum-copper electrodes:		
length of upper electrodes		766 mm (576 Mo, 190 mm Cu)
length of lower electrodes		690 mm (300 Mo, 390 mm Cu)
diameter of electrodes:		
- prior to coating		8.6 mm
- after coating with ZrO_2		9.0 mm
Cooling jacket	material	1.4541 stainless steel
	inner tube	∅ 158.3 / 168.3 mm
	outer tube	∅ 181.7 / 193.7 mm

Table 3: List of instrumentation for the QUENCH-02 Test

Chan-nel	Designation	Instrument, location	Output in
0	TCR 13	TC (W/Re) central rod, cladding, 950 mm	°C
1	TFS 2/11	TC (W/Re) fuel rod simulator 8 (type 2), 750 mm, 135°	°C
2	TFS 2/13	TC (W/Re) fuel rod simulator 2 (type 2), 950 mm, 225°	°C
3	TFS 2/15	TC (W/Re) fuel rod simulator 4 (type 2), 1150 mm, 315°	°C
4	TFS 2/17	TC (W/Re) fuel rod simulator 6 (type 2), 1350 mm, 45°	°C
5	TFS 3/8	TC (W/Re) fuel rod simulator 5 (type 3), 450 mm, 45°	°C
6	TFS 3/10	TC (W/Re) fuel rod simulator 7 (type 3), 650 mm, 135°	°C
7	TFS 3/12	TC (W/Re) fuel rod simulator 9 (type 3), 850 mm, 225°	°C
8	TFS 3/13	TC (W/Re) fuel rod simulator 3 (type 3), 950 mm, 315°	°C
9	TFS 3/14	TC (W/Re) fuel rod simulator 5 (type 3), 1050 mm, 45°	°C
10	TFS 4/11	TC (W/Re) fuel rod simulator 14 (type 4), 750 mm, 45°	°C
11	TFS 4/13	TC (W/Re) fuel rod simulator 20 (type 4), 950 mm, 135°	°C
12	TFS 5/10	TC (W/Re) fuel rod simulator 12 (type 5), 650 mm, 225°	°C
13	TFS 5/11	TC (W/Re) fuel rod simulator 13 (type 5), 750 mm, 45°	°C
14	TFS 5/12	TC (W/Re) fuel rod simulator 15 (type 5), 850 mm, 315°	°C
15	TFS 5/13	TC (W/Re) fuel rod simulator 16 (type 5), 950 mm, 135°	°C
16	TFS 5/14	TC (W/Re) fuel rod simulator 18 (type 5), 1050 mm, 45°	°C
17	TSH 16/180	TC (W/Re) shroud outer surface, 1250 mm, 180°	°C
18	TSH 13/90	TC (W/Re) shroud outer surface, 950 mm, 90°	°C
19	TSH 14/90	TC (W/Re) shroud outer surface, 1050 mm, 90°	°C
20	TSH 11/0	TC (W/Re) shroud outer surface, 750 mm, 0°	°C
21	TSH 12/0	TC (W/Re) shroud outer surface, 850 mm, 0°	°C
22	TFS 2/5	TC (NiCr/Ni) fuel rod simulator 2 (type 2), 150 mm, 225°	°C
23	TFS 2/7	TC (NiCr/Ni) fuel rod simulator 6 (type 2), 350 mm, 45°	°C
32	TCRC 9	TC (W/Re) central rod, center, 550 mm	°C
33	TCRC13	TC (W/Re) central rod, center, 950 mm	°C
34	TCR 9	TC (W/Re) central rod, cladding, 550 mm	°C
37	TFS 3/16	TC (W/Re) fuel rod simulator 7 (type 3), 1250 mm, 135°	°C
40	TFS 5/8	TC (W/Re) fuel rod simulator 21 (type 5), 450 mm, 225°	°C
41	TFS 5/9	TC (W/Re) fuel rod simulator 10 (type 5), 550 mm, 315°	°C
47	TFS 5/15	TC (W/Re) fuel rod simulator 19 (type 5), 1150 mm, 225°	°C
48	TFS 5/16	TC (W/Re) fuel rod simulator 21 (type 5), 1250 mm, 225°	°C
49	TFS 5/17	TC (W/Re) fuel rod simulator 10 (type 5), 1350 mm, 315°	°C
50	TSH 9/270	TC (W/Re) shroud outer surface, 550 mm, 270°	°C
51	TSH 11/270	TC (W/Re) shroud outer surface, 750 mm, 270°	°C
52	TSH 13/270	TC (W/Re) shroud outer surface, 950 mm, 270°	°C
53	TSH 14/270	TC (W/Re) shroud outer surface, 1050 mm, 270°	°C
54	TSH 11/180	TC (W/Re) shroud outer surface, 750 mm, 180°	°C
55	TSH 12/180	TC (W/Re) shroud outer surface, 850 mm, 180°	°C
56	TSH 13/180	TC (W/Re) shroud outer surface, 950 mm, 180°	°C
57	TSH 15/180	TC (W/Re) shroud outer surface, 1150 mm, 180°	°C
59	TSH 9/90	TC (W/Re) shroud outer surface, 550 mm, 90°	°C

Chan-nel	Designation	Instrument, location	Output in
60	TSH 11/90	TC (W/Re) shroud outer surface, 750 mm, 90°	°C
65	TSH 13/0	TC (W/Re) shroud outer surface, 950 mm, 0°	°C
66	TSH 15/0	TC (W/Re) shroud outer surface, 1150 mm, 0°	°C
67	TSH 16/0	TC (W/Re) shroud outer surface, 1250 mm, 0°	°C
68	T 512	Gas temperature bundle outlet	°C
71	Ref. T 01	Reference temperature 1	°C
72	TFS 2/1	TC (NiCr/Ni) fuel rod simulator 4 (type 2), -250 mm, 315°	°C
73	TFS 2/2	TC (NiCr/Ni) fuel rod simulator 6 (type 2), -150 mm, 45°	°C
74	TFS 2/3	TC (NiCr/Ni) fuel rod simulator 8 (type 2), -50 mm, 135°	°C
76	TFS 2/6	TC (NiCr/Ni) fuel rod simulator 4 (type 2), 250 mm, 315°	°C
78	TFS 5/4/0	TC (NiCr/Ni) fuel rod simulator 15 (type 5), 50 mm, 315°	°C
79	TFS 5/4/180	TC (NiCr/Ni) fuel rod simulator 21 (type 5), 50 mm, 135°	°C
80	TFS 5/5	TC (NiCr/Ni) fuel rod simulator 16 (type 5), 150 mm, 225°	°C
81	TFS 5/6	TC (NiCr/Ni) fuel rod simulator 18 (type 5), 250 mm, 45°	°C
82	TFS 5/7	TC (NiCr/Ni) fuel rod simulator 19 (type 5), 350 mm, 225°	°C
83	TSH 4/270	TC (NiCr/Ni) shroud outer surface, 50 mm, 270°	°C
84	TSH 3/180	TC (NiCr/Ni) shroud outer surface, -50 mm, 180°	°C
85	TSH 4/180	TC (NiCr/Ni) shroud outer surface, 50 mm. 180°	°C
86	TSH 7/180	TC (NiCr/Ni) shroud outer surface, 350 mm, 180°	°C
87	TSH 4/90	TC (NiCr/Ni) shroud outer surface, 50 mm, 90°	°C
88	TSH 1/0	TC (NiCr/Ni) shroud outer surface, -250 mm, 0°	°C
89	TSH 4/0	TC (NiCr/Ni) shroud outer surface, 50 mm, 0°	°C
90	TSH 7/0	TC (NiCr/Ni) shroud outer surface, 350 mm, 0°	°C
91	TCI 9/270	TC (NiCr/Ni) cooling jacket inner tube wall, 550 mm, 270°	°C
92	TCI 10/270	TC (NiCr/Ni) cooling jacket inner tube wall, 650 mm, 270°	°C
93	TCI 11/270	TC (NiCr/Ni) cooling jacket inner tube wall, 750 mm, 270°	°C
94	TCI 13/270	TC (NiCr/Ni) cooling jacket inner tube wall, 350 mm, 270°	°C
95	TCO 16/180	TC (NiCr/Ni) cooling jacket outer tube surface, 1250 mm, 180°	°C
96	TCI 1/180	TC (NiCr/Ni) cooling jacket inner tube wall, -250 mm, 180°	°C
97	TCI 4/180	TC (NiCr/Ni) cooling jacket inner tube wall, 50 mm, 180°	°C
98	TCI 7/180	TC (NiCr/Ni) cooling jacket inner tube wall, 350 mm, 180°	°C
99	TCI 11/180	TC (NiCr/Ni) cooling jacket inner tube wall, 750 mm, 180°	°C
100	TCI 12/180	TC (NiCr/Ni) cooling jacket inner tube wall, 850 mm, 180°	°C
101	TCI 13/180	TC (NiCr/Ni) cooling jacket inner tube wall, 950 mm, 180°	°C
102	TCI 15/180	TC (NiCr/Ni) cooling jacket inner tube wall, 1150 mm, 180°	°C
104	TCI 9/90	TC (NiCr/Ni) cooling jacket inner tube wall, 550 mm, 90°	°C
105	TCI 10/90	TC (NiCr/Ni) cooling jacket inner tube wall, 650 mm, 90°	°C
106	TCI 11/90	TC (NiCr/Ni) cooling jacket inner tube wall, 750 mm, 90°	°C
107	TCI 13/90	TC (NiCr/Ni) cooling jacket inner tube wall, 850 mm, 90°	°C
109	TCI1/0	TC (NiCr/Ni) cooling jacket inner tube wall, -250 mm, 0°	°C
110	TCI 4/0	TC (NiCr/Ni) cooling jacket inner tube wall, 50 mm, 0°	°C
111	TCI 7/0	TC (NiCr/Ni) cooling jacket inner tube wall, 350 mm, 0°	°C
112	TCI 11/0	TC (NiCr/Ni) cooling jacket inner tube wall, 750 mm, 0°	°C
113	TCI 12/0	TC (NiCr/Ni) cooling jacket inner tube wall, 850 mm, 0°	°C

Chan-nel	Designation	Instrument, location	Output in
114	TCI 13/0	TC (NiCr/Ni) cooling jacket inner tube wall, 950 mm, 0°	°C
115	TCI 15/0	TC (NiCr/Ni) cooling jacket inner tube wall, 1150 mm, 0°	°C
117	TCO 9/270	TC (NiCr/Ni) cooling jacket outer tube surface, 550 mm, 270°	°C
118	TCO 4/180	TC (NiCr/Ni) cooling jacket outer tube surface, 50 mm, 180°	°C
120	TCO 1/0	TC (NiCr/Ni) cooling jacket outer tube surface, -250 mm, 0°	°C
121	TCO 7/0	TC (NiCr/Ni) cooling jacket outer tube surface, 350 mm, 0°	°C
122	TCO 13/0	TC (NiCr/Ni) cooling jacket outer tube surface, 950 mm, 0°	°C
123	T 601	Temperature before off-gas flow instrument F 601	°C
124	T 513	Temperature bundle head top (wall)	°C
125	T 514	Temperature bundle head, at outlet (wall)	°C
128	T 104	Temperature quench water	°C
129	T 201	Temperature steam generator heating pipe	°C
130	T 204	Temperature before steam flow instrument location 50 g/s	°C
131	T 205	Temperature before steam flow instrument location 10 g/s	°C
132	T 301A	Temperature behind superheater	°C
133	T 302	Temperature superheater heating pipe	°C
134	T 303	Temperature before total flow instrument location	°C
135	T 401	Temperature before gas flow instrument location	°C
136	T 403	Temperature at inlet cooling gas	°C
137	T 404	Temperature at outlet cooling gas	°C
138	T 501	Temperature at containment	°C
139	T 502	Temperature at containment	°C
140	T 503	Temperature at containment	°C
141	T 504	Temperature at containment	°C
142	T 505	Temperature at containment	°C
143	T 506	Temperature at containment	°C
144	T 507	Temperature at containment	°C
145	T 508	Temperature at containment	°C
146	T 509	Temperature bundle head outside (wall)	°C
147	T 510	Temperature at containment	°C
148	T 511	Gas temperature at bundle inlet	°C
149	T 901	Temperature before off-gas flow instrument F 901	°C
151	Ref. T 02	Reference temperature 2	°C
152	P 201	Pressure steam generator	bar
153	P 204	Pressure at steam flow instrument location 50 g/s	bar
154	P 205	Pressure at steam flow instrument location 10 g/s	bar
155	P 303	Pressure before total flow instrument location	bar
156	P 401	Pressure before gas flow instrument location	bar
157	P 511	Pressure at bundle inlet	bar
158	P 512	Pressure at bundle outlet	bar
159	P 601	Pressure before off-gas flow instrument F 601	bar
160	P 901	Pressure before off-gas flow instrument F 901	bar
161	L 201	Liquid level steam generator	mm
162	L 501	Liquid level quench water	bar

Chan-nel	Designation	Instrument, location	Output in
163	L 701	Liquid level main condenser	mm
164	Q 901	H_2 concentration, off-gas (Caldos)	% H_2
165	P 411	Pressure Ar-Kr supply	bar
168	F 104	Flow rate quench water	l/h
169	F 204	Flow rate steam 50 g/s	m³/h
170	F 205	Flow rate steam 10 g/s	m³/h
171	F 303	Flow rate at bundle inlet (steam + argon), orifice	mbar
172	F 401	Argon gas flow rate	Nm³/h
173	F 403	Flow rate cooling gas	Nm³/h
174	F 601	Flow rate off-gas (orifice)	mbar
175	F 901	Off-gas flow rate before Caldos (H_2)	m³/h
176	E 201	Electric current steam generator	A
177	E 301	Electric current superheater	A
178	E 501	Electric current inner ring of fuel rod simulators	A
179	E 502	Electric current outer ring of fuel rod simulators	A
180	E 503	Electric voltage inner ring of fuel rod simulators	V
181	E 504	Electric voltage outer ring of fuel rod simulators	V
183	Ref. T 03	Reference temperature 3	°C
184	Notaus	Emergency switch for test facility	-
185	Ü 24 V	Check of 24 V fuse	-
186	P 501	Containment pressure	bar
187	P 701	Condenser pressure	bar
188	F 801	Water flow, intermediate cooler	l/s
189	F 802	Water flow, intermediate cooler	l/s
190	E 101	Current feed water pump on	-
191	E 102	Current quench pump on	-
192	E 701	Current condensate pump on	-
193	GS 1 Ein	DC supply 1 on	-
194	GS 1 STÖ	DC supply 1 interruption	-
195	GS 2Ein	DC supply 2 on	-
196	GS 2 STÖ	DC supply 2 interruption	-

7/98

Note: Tip of thermocouple TFS 2/1 bent into flow channel to measure the fluid temperature

Table 4: List of instrumentation for the QUENCH-03 Test

Chan-nel	Designation	Instrument, location	Output in
0	TCR 13	TC (W/Re) central rod, cladding, 950 mm	°C
1	TFS 2/11	TC (W/Re) fuel rod simulator 8 (type 2), 750 mm, 135°	°C
2	TFS 2/13	TC (W/Re) fuel rod simulator 2 (type 2), 950 mm, 225°	°C
3	TFS 2/15	TC (W/Re) fuel rod simulator 4 (type 2), 1150 mm, 315°	°C
4	TFS 2/17	TC (W/Re) fuel rod simulator 6 (type 2), 1350 mm, 45°	°C
5	TCRC 12	TC (W/Re) central rod, center, 850 mm	°C
6	TFS 3/10	TC (W/Re) fuel rod simulator 7 (type 3), 650 mm, 135°	°C
7	TFS 3/12	TC (W/Re) fuel rod simulator 9 (type 3), 850 mm, 225°	°C
8	TFS 3/13	TC (W/Re) fuel rod simulator 3 (type 3), 950 mm, 315°	°C
9	TFS 3/14	TC (W/Re) fuel rod simulator 5 (type 3), 1050 mm, 45°	°C
10	TFS 4/11	TC (W/Re) fuel rod simulator 14 (type 4), 750 mm, 45°	°C
12	TFS 5/10	TC (W/Re) fuel rod simulator 12 (type 5), 650 mm, 225°	°C
13	TFS 5/11	TC (W/Re) fuel rod simulator 13 (type 5), 750 mm, 45°	°C
14	TFS 5/12	TC (W/Re) fuel rod simulator 15 (type 5), 850 mm, 315°	°C
15	TFS 5/13	TC (W/Re) fuel rod simulator 16 (type 5), 950 mm, 135°	°C
16	TFS 5/14	TC (W/Re) fuel rod simulator 18 (type 5), 1050 mm, 45°	°C
17	TSH 16/180	TC (W/Re) shroud outer surface, 1250 mm, 206°	°C
18	TSH 13/90	TC (W/Re) shroud outer surface, 950 mm, 116°	°C
19	TSH 14/90	TC (W/Re) shroud outer surface, 1050 mm, 116°	°C
20	TSH 11/0	TC (W/Re) shroud outer surface, 750 mm, 26°	°C
21	TSH 12/0	TC (W/Re) shroud outer surface, 850 mm, 26°	°C
22	TFS 2/5	TC (NiCr/Ni) fuel rod simulator 2 (type 2), 150 mm, 225°	°C
23	TFS 2/7	TC (NiCr/Ni) fuel rod simulator 6 (type 2), 350 mm, 45°	°C
32	TIT A/13	TC (W/Re) Corner rod A, 950 mm	°C
33	TCRC13	TC (W/Re) central rod, center, 950 mm	°C
34	TFS 2/12	TC (W/Re) fuel rod simulator 2 (type 2), 850 mm, 315°	°C
35	TSH 9/90	TC (NiCr/Ni) shroud outer surface, 550 mm, 116°	°C
36	TSH 9/270	TC (NiCr/Ni) shroud outer surface, 550 mm, 296°	°C
37	TFS 3/16	TC (W/Re) fuel rod simulator 7 (type 3), 1250 mm, 135°	°C
38	TFS 5/9	TC (NiCr/Ni) fuel rod simulator 10 (type 5), 550 mm, 315°	°C
39	TFS 2/9	TC (NiCr/Ni) fuel rod simulator 8 (type 2), 550 mm, 135°	°C
40	TIT D/12	TC (W/Re) Corner rod D, 850 mm	°C
42	TFS 5/8	TC (NiCr/Ni) fuel rod simulator 21 (type 5), 450 mm, 135°	°C
43	TFS 3/8	TC (NiCr/Ni) fuel rod simulator 5 (type 3), 450 mm, 45°	°C
44	TIT B/7	TC (NiCr/Ni) Corner rodB, 350 mm	°C
46	TIT C/9	TC (NiCr/Ni) Corner rod C, 550 mm	°C
47	TFS 5/15	TC (W/Re) fuel rod simulator 19 (type 5), 1150 mm, 225°	°C
48	TFS 4/13	TC (W/Re) fuel rod simulator 20 (type 4), 950 mm, 135°	°C
49	TFS 5/17	TC (W/Re) fuel rod simulator 10 (type 5), 1350 mm, 315°	°C
52	TSH 13/270	TC (W/Re) shroud outer surface, 950 mm, 296°	°C
53	TSH 14/270	TC (W/RE) shroud outer surface 1050 mm, 296°	°C
54	TSH 11/180	TC (W/Re) shroud outer surface, 750 mm, 206°	°C

Chan-nel	Designation	Instrument, location	Output in
55	TSH 12/180	TC (W/Re) shroud outer surface, 850 mm, 206°	°C
57	TSH 15/180	TC (W/Re) shroud outer surface, 1150 mm, 206°	°C
66	TSH 15/0	TC (W/Re) shroud outer surface, 1150 mm, 26°	°C
67	TSH 16/0	TC (W/Re) shroud outer surface, 1250 mm, 26°	°C
68	T 512	Gas temperature bundle outlet	°C
71	Ref. T 01	Reference temperature 1	°C
72	TFS 2/1	TC (NiCr/Ni) fuel rod simulator 4 (type 2), -250 mm, 315°, Note: TC tip bent into flow channel	°C
73	TFS 2/2	TC (NiCr/Ni) fuel rod simulator 6 (type 2), -150 mm, 45°	°C
74	TFS 2/3	TC (NiCr/Ni) fuel rod simulator 8 (type 2), -50 mm, 135°	°C
76	TFS 2/6	TC (NiCr/Ni) fuel rod simulator 4 (type 2), 250 mm, 315°	°C
78	TFS 5/4/0	TC (NiCr/Ni) fuel rod simulator 15 (type 5), 50 mm, 315°	°C
79	TFS 5/4/180	TC (NiCr/Ni) fuel rod simulator 21 (type 5), 50 mm, 135°	°C
80	TFS 5/5	TC (NiCr/Ni) fuel rod simulator 16 (type 5), 150 mm, 225°	°C
81	TFS 5/6	TC (NiCr/Ni) fuel rod simulator 18 (type 5), 250 mm, 45°	°C
82	TFS 5/7	TC (NiCr/Ni) fuel rod simulator 19 (type 5), 350 mm, 225°	°C
83	TSH 4/270	TC (NiCr/Ni) shroud outer surface, 50 mm, 296°	°C
84	TSH 3/180	TC (NiCr/Ni) shroud outer surface, -50 mm, 206°	°C
85	TSH 4/180	TC (NiCr/Ni) shroud outer surface, 50 mm. 206°	°C
86	TSH 7/180	TC (NiCr/Ni) shroud outer surface, 350 mm, 206°	°C
87	TSH 4/90	TC (NiCr/Ni) shroud outer surface, 50 mm, 116°	°C
88	TSH 1/0	TC (NiCr/Ni) shroud outer surface, -250 mm, 26°	°C
89	TSH 4/0	TC (NiCr/Ni) shroud outer surface, 50 mm, 26°	°C
90	TSH 7/0	TC (NiCr/Ni) shroud outer surface, 350 mm, 26°	°C
91	TCI 9/270	TC (NiCr/Ni) cooling jacket inner tube wall, 550 mm, 270°	°C
92	TCI 10/270	TC (NiCr/Ni) cooling jacket inner tube wall, 650 mm, 270°	°C
93	TCI 11/270	TC (NiCr/Ni) cooling jacket inner tube wall, 750 mm, 270°	°C
94	TCI 13/270	TC (NiCr/Ni) cooling jacket inner tube wall, 350 mm, 270°	°C
96	TCI 1/180	TC (NiCr/Ni) cooling jacket inner tube wall, -250 mm, 180°	°C
97	TCI 4/180	TC (NiCr/Ni) cooling jacket inner tube wall, 50 mm, 180°	°C
98	TCI 7/180	TC (NiCr/Ni) cooling jacket inner tube wall, 350 mm, 180°	°C
99	TCI 11/180	TC (NiCr/Ni) cooling jacket inner tube wall, 750 mm, 180°	°C
100	TCI 12/180	TC (NiCr/Ni) cooling jacket inner tube wall, 850 mm, 180°	°C
101	TCI 13/180	TC (NiCr/Ni) cooling jacket inner tube wall, 950 mm, 180°	°C
102	TCI 15/180	TC (NiCr/Ni) cooling jacket inner tube wall, 1150 mm, 180°	°C
104	TCI 9/90	TC (NiCr/Ni) cooling jacket inner tube wall, 550 mm, 90°	°C
105	TCI 10/90	TC (NiCr/Ni) cooling jacket inner tube wall, 650 mm, 90°	°C
106	TCI 11/90	TC (NiCr/Ni) cooling jacket inner tube wall, 750 mm, 90°	°C
107	TCI 13/90	TC (NiCr/Ni) cooling jacket inner tube wall, 850 mm, 90°	°C
109	TCI1/0	TC (NiCr/Ni) cooling jacket inner tube wall, -250 mm, 0°	°C
110	TCI 4/0	TC (NiCr/Ni) cooling jacket inner tube wall, 50 mm, 0°	°C
111	TCI 7/0	TC (NiCr/Ni) cooling jacket inner tube wall, 350 mm, 0°	°C
112	TCI 11/0	TC (NiCr/Ni) cooling jacket inner tube wall, 750 mm, 0°	°C
113	TCI 12/0	TC (NiCr/Ni) cooling jacket inner tube wall, 850 mm, 0°	°C

Chan-nel	Designation	Instrument, location	Output in
114	TCI 13/0	TC (NiCr/Ni) cooling jacket inner tube wall, 950 mm, 0°	°C
115	TCI 15/0	TC (NiCr/Ni) cooling jacket inner tube wall, 1150 mm, 0°	°C
117	TCO 9/270	TC (NiCr/Ni) cooling jacket outer tube surface, 550 mm, 270°	°C
118	TCO 4/180	TC (NiCr/Ni) cooling jacket outer tube surface, 50 mm, 180°	°C
120	TCO 1/0	TC (NiCr/Ni) cooling jacket outer tube surface, -250 mm, 0°	°C
121	TCO 7/0	TC (NiCr/Ni) cooling jacket outer tube surface, 350 mm, 0°	°C
122	TCO 13/0	TC (NiCr/Ni) cooling jacket outer tube surface, 950 mm, 0°	°C
123	T 601	Temperature before off-gas flow instrument F 601	°C
124	T 513	Temperature bundle head top (wall)	°C
125	T 514	Temperature bundle head, at outlet (wall)	°C
128	T 104	Temperature quench water	°C
129	T 201	Temperature steam generator heating pipe	°C
130	T 204	Temperature before steam flow instrument location 50 g/s	°C
131	T 205	Temperature before steam flow instrument location 10 g/s	°C
132	T 301A	Temperature behind superheater	°C
133	T 302	Temperature superheater heating pipe	°C
134	T 303	Temperature before total flow instrument location	°C
135	T 401	Temperature before gas flow instrument location	°C
136	T 403	Temperature at inlet cooling gas	°C
137	T 404	Temperature at outlet cooling gas	°C
138	T 501	Temperature at containment	°C
139	T 502	Temperature at containment	°C
140	T 503	Temperature at containment	°C
141	T 504	Temperature at containment	°C
142	T 505	Temperature at containment	°C
143	T 506	Temperature at containment	°C
144	T 507	Temperature at containment	°C
145	T 508	Temperature at containment	°C
146	T 509	Temperature bundle head outside (wall)	°C
147	T 510	Temperature at containment	°C
148	T 511	Gas temperature at bundle inlet	°C
149	T 901	Temperature before off-gas flow instrument F 901	°C
151	Ref. T 02	Reference temperature 2	°C
152	P 201	Pressure steam generator	bar
153	P 204	Pressure at steam flow instrument location 50 g/s	bar
154	P 205	Pressure at steam flow instrument location 10 g/s	bar
155	P 303	Pressure before total flow instrument location	bar
156	P 401	Pressure before gas flow instrument location	bar
157	P 511	Pressure at bundle inlet	bar
158	P 512	Pressure at bundle outlet	bar
159	P 601	Pressure before off-gas flow instrument F 601	bar
160	P 901	Pressure before off-gas flow instrument F 901	bar
161	L 201	Liquid level steam generator	mm
162	L 501	Liquid level quench water	bar

Chan-nel	Designation	Instrument, location	Output in
163	L 701	Liquid level main condenser	mm
164	Q 901	H_2 concentration, off-gas (Caldos)	% H_2
165	P 411	Pressure Ar-Kr supply	bar
168	F 104	Flow rate quench water	l/h
169	F 204	Flow rate steam 50 g/s	m³/h
170	F 205	Flow rate steam 10 g/s	m³/h
171	F 303	Flow rate at bundle inlet (steam + argon), orifice	mbar
172	F 401	Argon gas flow rate	Nm³/h
173	F 403	Flow rate cooling gas	Nm³/h
174	F 601	Flow rate off-gas (orifice)	mbar
175	F 901	Off-gas flow rate before Caldos (H_2)	m³/h
176	E 201	Electric current steam generator	A
177	E 301	Electric current superheater	A
178	E 501	Electric current inner ring of fuel rod simulators	A
179	E 502	Electric current outer ring of fuel rod simulators	A
180	E 503	Electric voltage inner ring of fuel rod simulators	V
181	E 504	Electric voltage outer ring of fuel rod simulators	V
183	Ref. T 03	Reference temperature 3	°C
184	Notaus	Emergency switch for test facility	-
185	Ü 24 V	Check of 24 V fuse	-
186	P 501	Containment pressure	bar
187	P 701	Condenser pressure	bar
188	F 801	Water flow, intermediate cooler	l/s
189	F 802	Water flow, intermediate cooler	l/s
190	E 101	Current feed water pump on	-
191	E 102	Current quench pump on	-
192	E 701	Current condensate pump on	-
193	GS 1 Ein	DC supply 1 on	-
194	GS 1 STÖ	DC supply 1 interruption	-
195	GS 2Ein	DC supply 2 on	-
196	GS 2 STÖ	DC supply 2 interruption	-

5.03.99

Note: Tip of thermocouple TFS 2/1 bent into flow channel to measure the fluid temperature

Table 5: QUENCH-02; Sequence of events

Time [s]	Event
90	Begin of transient
2139	Begin of temperature escalation at 950 mm: TFS2/13 = 1547 °C; TCRC13 = 1530 °C; TFS3/13 = 1492 °C; and at 14:48:17 h TFS4/13 and TFS5/13 = 1466 °C
2148	Begin of temperature escalation at 850 mm: TFS3/12 = 1426 °C; TFS5/12 = 1386 °C
2151	Begin of temperature escalation of the shroud at 950 mm: TSH13/180 = 1482 °C
2165	Begin of temperature escalation at 1050 mm: TFS3/14 = 1400 °C; TFS5/14 = 1329 °C
2175	Begin of temperature escalation of the shroud at 850 mm: TSH12/0 and TSH12/180 = 1387 °C
2186	Begin of significant H_2 production
2195	Start of quench water injection 89 g/s
2195	Begin of temperature escalation at 1150 mm: TFS2/15 = 1221 °C; TFS5/15 = 1071 °C
2211	Onset of simultaneous rod cladding cooling at various elevations
2214	Begin of escalation of the gas temperature at outlet (T512 = 616 °C)
2215	Begin of temperature escalation at 1250 mm: TFS3/16 = 1100 °C
2215	First test rod failure detected by Kr signal at mass spectrometer
2218	Quench water reduction from 89 g/s to 47 g/s
2220	Quenching at 150 mm elevation (TFS2/5)
2230	Begin of temperature escalation at 750 mm: TFS4/11= 1250 °C
2250	Quenching at 250 mm elevation (TFS2/6)
2260	Maximum H_2 production
2262	Quenching at 350 mm elevation (TFS2/7) and at 950 mm elevation (TFS5/9 and TCR9)
2285	Quenching at 450 mm elevation (TFS3/8)
2305	Quenching at 650 mm elevation (TFS5/10)
2458	Termination of quench water injection

0 s = 14:13:30 h on July 7,1998

Table 6 a: QUENCH-02; Maximum measured temperature at each elevation

Elevation [mm]	Thermocouple	Maximum temperature [K]
250	TFS 2/6	1100
350	TFS 2/7	1180
450	TFS 3/8	1275
650	TFS 5/10	1430
950	TCRC 13	2440
1150	TFS 5/15	2456
1250	TFS 3/16	2430

Table 6 b: QUENCH-02; Thermocouple maximum temperatures and failure temperatures

Thermocouple	Maximum temperature		TC failure	
	Time [s]	Temp. [K]	Time [s]	Temp. [K]
TFS 2/1	2180	687		
TFS 2/2	2199	780		
TFS 2/3	2199	865		
TFS 2/5	2199	1008		
TFS 2/6	2198	1098		
TFS 2/7	2197	1183		
TFS 3/8	2200	1276		
TCR 9	2199	1311		
TFS 3/13	2195	2205	2199	1311
TFS 5/10	2212	1432		
TFS 3/12	2202	2333	2212	2225
TFS 5/12	2201	2230	2206	2083
TSH 12/0	2216	2187		
TSH 12/180	2232	1988		
TCRC 13	2213	2402		
TFS 2/13	2275	2391	2302	2302
TFS 4/13	2234	2328	2276	2007
TFS 5/13	2204	2210	2209	2182
TSH 13/90	2219	2251		
TSH 13/180	2206	2176		
TSH 13/270	2215	2152	2292	2456
TFS 3/14	2213	2213	2348	1833
TFS 5/14	2210	2382	2213	2341
TFS 2/15	2233	2201	2294	1739
TFS 5/15	2292	2456	2292	2456
TFS 3/16	2288	2424	2288	2424

Table 7: QUENCH-02; Evaluation of quench temperatures based on cladding data

Cladding Thermo-couple	Elevation (Rod number)	Onset of cooling		Onset of quenching	
		Time (s)	Temp. (°C)	Time (s)	Temp. (°C)
TFS 2/1	- 250 mm (rod 4)	2211	432	2211	370
TFS 2/2	- 150 mm (rod 6)	2211	500	2211	500
TFS 2/3	- 50 mm (rod 8)	2211	584	2215	524
TFS 2/5	150 mm (rod 2)	2211	728	2220	675
TFS 2/6	250 mm (rod 4)	2211	819	2250	562
TFS 2/7	350 mm (rod 6)	2211	907	2262	667
TFS 3/8	450 mm (rod 5)	2211	1003	2285	610
TFS 5/9	550 mm (rod 10)	2211	1003	2262	720
TFS 5/10	650 mm (rod 12)	2211	1162	2305	581
TFS 3/14	1050 mm (rod 5)	2244	1886		
TFS 2/15	1150 mm (rod 4)	2233	1930	2305	1200
TFS 5/15	1150 mm (rod 19)	2235	1850		
TCR 9	550 mm (rod 1)	2211	1032	2262	720

0 s = 14:13:30 h on July 7,1998

Table 8: QUENCH-02; Quench temperatures based on shroud data

Shroud thermocouple	Elevation	Onset of quenching		Mean values	
	[mm]	Time [s]	Temp. [°C]	Time [s]	Temp. [°C]
TSH 12/0	850	2378	1231	2378	1139
TSH 12/180	850	2378	1047		
TSH 13/90	950	2334	1360	2355	1306
TSH 13/180	950	2357	1394		
TSH 13/270	950	2375	1163		

0 s = 14:13:30 h on July 7, 1998

Table 9: QUENCH-02; Cross sections for posttest examinations

Sample	Sample length (mm)	Axial position bottom (mm)	Axial position top (mm)	Remarks
QUE-02-a	90	-32	58	Remnant
Cut	2	58	60	
QUE-02-1	13	60	73	Reference, 73 mm polished
Cut	2	73	75	
QUE-02-b	460	75	535	
Cut	2	535	537	
QUE-02-2	13	537	550	Elevation 9, 550 mm polished
Cut	2	550	552	
QUE-02-c	183	552	735	
Cut	2	735	737	
QUE-02-3	13	737	750	Elevation 11, 750 mm polished
Cut	2	750	752	
QUE-02-d	83	752	835	
Cut	2	835	837	
QUE-02-4	13	837	850	Elevation 12, 850 mm polished
Cut	2	850	852	
QUE-02-e	16	852	868	868 mm polished
Cut	2	868	870	
QUE-02-5	13	870	883	883 mm polished
Cut	2	883	885	
QUE-02-f	50	885	935	
Cut	2	935	937	
QUE-02-6	13	937	950	Elevation 13, 950 mm polished
Cut	2	950	952	
QUE-02-g	83	952	1035	
Cut	2	1035	1037	
QUE-02-7	13	1037	1050	Elevation 14, 1050 mm polished
Cut	2	1050	1052	
QUE-02-h	83	1052	1135	
Cut	2	1135	1137	
QUE-02-8	13	1137	1150	Elevation 15, 1150 mm polished
Cut	2	1150	1152	
QUE-02-i	83	1152	1235	
Cut	2	1235	1237	
QUE-02-9	13	1237	1250	Elevation 16, 1250 mm polished
Cut	2	1250	1252	
QUE-02-j	83	1252	1335	
Cut	2	1335	1337	
QUE-02-10	13	1337	1350	Elevation 17, 1350 mm polished
Cut	2	1350	1352	
QUE-02-k	438	1352	1790	Remnant

14.09.1998

Table 10: QUENCH-03; Sequence of events

Time [s]	Event
0	Start of data recording
900	Start of electric power transient
2379	Begin of temperature escalation at the 750 mm level (TFS 4/11, ~ 1402 K)
2404	Begin of temperature escalation of the shroud at the 1050 mm level (TSH 14/270, ~1156 K)
2455	Begin of temperature escalation of the shroud at the 1250 mm level (TSH 16/0, ~987 K)
2474	Begin of temp. escalation at the 850 mm level (TFS 5/12, ~1669 K)
2590	Begin of temp. escalation at the 1150 mm level (TFS 5/15, ~1372 K)
2600	Quenching program initiated, electric power increase 18.4 kW → 44 kW, onset of quenching water injection (90 g/s)
2602	44 kW of electric bundle power reached
2606	Steam flow shut off, argon flow switched to upper bundle head
2616	Maximum quench water flow of 90 g/s
2618	Begin of temp. escalation at the 1350 mm level (TFS 2/17, ~974 K)
2619	Onset of cooling (TFS 2/1)
2619	Begin of significant H_2 production based on F 901 data
2627	Shroud failure, starting between 750 and 950 mm
2630	Quench water flow of 40 g/s reached → flooding rate of 1.4 cm/s
2734	Temperature drop at 550mm (TFS 5/9)
2747	Start of electric power reduction from 37.5 kW to 4 kW
2762	Electric power of 4 kW reached
3501	Electric power shut off
3508	Quench water flow at 0 g/s

0 s = 13:30:00 h on January 20, 1999

Table 11: QUENCH-03; Failure of thermocouples

Thermocouple	Elevation [mm]	Time at failure [s]	Failure temperature [K]
TFS 2/11	750	2628	2041
TFS 4/11	750	2567	2452
TFS 5/11	750	2560	2465
TFS 3/12	850	2591	2454
TFS 5/12	850	2588	2232
TFS 2/13	950	2596	2458
TFS 3/13	950	2609	2454
TFS 4/13	950	2625	2275
TFS 5/13	950	2567	2463
TFS 3/14	1050	2591	2132
TFS 5/14	1050	2625	2422
TFS 2/15	1150	2628	2127
TFS 5/15	1150	2645	2090
TFS 3/16	1250	2647	2405
TFS 5/16	1250	Pre-test failure	
TSH 12/0	850	2626	2239
TSH 12/180	850	2627	2380
TSH 13/90	950	2627	1957
TSH 13/270	950	2962	351
TSH 14/270	1050	2869	2328
TSH 15/0	1150	2714	1332
TSH 15/180	1150	Pre-test failure	
TSH 16/0	1250	2701	1960
TCR 13	950	2567	1948
TCRC 13	950	2635	2412
TIT D/12	850	2638	2461
TIT A 13	950	2799	2418

Table 12: QUENCH-03; Escalation temperatures

Elevation [mm]	Thermocouple	Time of escalation [s]	Escalation temperature [K]
750	TFS 2/11	2466	1587
750	TFS 4/11	2379	1402
750	TFS 5/11	2421	1490
850	TFS 3/12	2469	1700
850	TFS 5/12	2474	1669
850	TIT D/12	2610	1986
950	TFS 2/13	2576	2080
950	TFS 3/13	2583	2080
950	TIT A/13	2620	2071
1050	TFS 3/14	2539	1778
1050	TFS 5/14	2517	1600
1050	TSH 14/90	2508	1213
1050	TSH 14/270	2404	1156
1150	TFS 2/15	2591	1438
1150	TFS 5/15	2590	1372
1150	TSH 15/0	2434	1093
1250	TFS 3/16	2616	1331
1250	TSH 16/0	2455	987
1250	TSH 16/180	2502	1119
1350	TFS 2/17	2618	1060
1350	TFS 5/17	2618	1022

Table 13: **QUENCH-03; Maximum measured temperature at each elevation**

Elevation [mm]	Thermocouple	Time [s]	Maximum temperature [K]
- 250	TFS 2/1	2598	702
- 150	TFS 2/2	2616	776
- 50	TFS 2/3	2618	856
50	TFS 5/4/180	2618	909
150	TFS 2/5	2619	1054
250	TFS 2/6	2619	1166
350	TFS 2/7	2618	1226
450	TFS 3/8	2618	1299
550	TFS 2/9	2618	1427
650	TFS 5/10	2619	1608
750	TFS 5/11	2560	2465
850	TFS 3/12	2591	2454
950	TFS 3/13	2609	2454
1050	TFS 5/14	2625	2422
1150	TFS 5/15	2627	2460
1250	TSH 16/0	2629	2382
1350	TFS 2/17	2644	2332

Table 14: QUENCH-03; Maximum measured shroud temperatures

Elevation [mm]	Thermocouple	Time [s]	Maximum temperature [K]
- 250	TSH 1/0	2618	641
-50	TSH 3/180	2631	766
50	TSH 4/0	2618	825
50	TSH 4/90	2611	831
50	TSH 4/180	2618	826
50	TSH 4/270	2624	812
350	TSH 7/0	2631	1149
350	TSH 7/180	2624	1142
550	TSH 9/90	2631	1290
550	TSH 9/270	2618	1310
750	TSH 11/0	2631	2336
750	TSH 11/180	2638	2233
850	TSH 12/0	2628	2239
850	TSH 12/180	2631	2380
950	TSH 13/90	2624	1957
950	TSH 13/270	2679	2194
1050	TSH 14/90	2583	2303
1050	TSH 14/270	2664	2216
1150	TSH 15/0	2618	2143
1250	TSH 16/0	2631	2382
1250	TSH 16/180	2638	2190

Table 15: QUENCH-03; Quench temperatures and quench rates based on cladding and shroud temperature data

Cladding/shroud thermocouple	Elevation [mm]	Onset of quenching		Mean values		Quench rate [cm/s]
		Time [s]	Temp. [K]	Time [s]	Temp. [K]	
	- 250	2619	677	2619	677	
TFS 2/2	- 150	2620	776	2620	776	
TFS 2/3	- 50	2624	767	2624	767	2.5 (level 2→3)
TFS 5/4/0	50	2628	686	2628	716	2.5 (level 3→4)
TFS 5/4/180	50	2628	745			
TFS 2/5	150	2632	844	2632	866	2.5 (level 4→5)
TFS 5/5	150	2632	888			
TFS 2/6	250	2662	833	2660	829	0.4 (level 5→6)
TFS 5/6	250	2658	824			
TFS 2/7	350	2700	697	2688	761	0.4 (level 6→7)
TFS 5/7	350	2675	824			
TFS 3/8	450	2732	727	2730	678	0.2 (level 7→8)
TFS 5/8	450	2727	628			
TFS 2/9	550	2740	732	2737	789	1.4 (level 8→9)
TFS 5/9	550	2734	845			
TFS 3/10	650	2787	771	2786	809	0.2 (level 9→10)
TFS 5/10	650	2785	846			
TFS 2/12	850	*	*	-	-	
TFS 5/15	1150	*	*	-	-	
TFS 3/16	1250	*	*	-	-	
TFS 2/17	1350	*	*	-	-	
TFS 5/17	1350	*	*			
TSH 1/0	- 250	2625	587	2625	587	
TSH 3/180	- 50	2635	687	2635	687	2.0 (level 1→3)
TSH 4/0	50	2648	657	2647	658	0.8 (level 3→4)
TSH 4/90	50	2649	636			
TSH 4/180	50	2649	648			
TSH 4/270	50	2642	692			
TSH 7/0	350	2710	746	2710	746	0.5 (level 4→7)
TSH 7/180	350	2710	746			

Cladding/shroud thermocouple	Elevation [mm]	Onset of quenching		Mean values		Quench rate [cm/s]
		Time [s]	Temp. [K]	Time [s]	Temp. [K]	
TSH 9/90	550	2771	662	2772	658	0.3 (level 7→9)
TSH 9/270	550	2773	654			
TSH 11/0	750	2810	1347	2786	1365	1.4 (level 9→11)
TSH 11/180	750	2762	1383			
TSH 13/270	950	2869	1193	2869	1193	0.2 (level 11→13)
TSH 14/270	1050	2854	1770	2854	1770	-0.7 (level 13→14)
TSH 15/0	1150	*	*	-	-	
TSH 16/0	1250	*	*	-	-	
TSH 16/180	1250	*	*			
TCRC 12	850	*	*	-	-	
TIT B/7	350	2680	765	2680	765	
TIT C/9	550	2694	861	2694	861	1.4 (level 7→9)

* No clear indication

Table 16: QUENCH-03; Cross sections for posttest examinations

Sample	Sample length (mm)	Axial position bottom (mm)	Axial position top (mm)	Remarks
QUE-03-a	70	-12	58	Remnant
Cut	2	58	60	
QUE-03-1	13	60	73	Reference, 73 mm polished
Cut	2	73	75	
QUE-03-b	360	75	435	
Cut	2	435	437	
QUE-03-2	13	437	450	
Cut	2	450	452	
QUE-03-c	83	452	535	
Cut	2	535	537	
QUE-03-3	13	537	550	Elevation 9, 550 mm polished
Cut	2	550	552	
QUE-03-d	83	552	635	
Cut	2	635	637	
QUE-03-4	13	637	650	Elevation 10, 650 mm polished
Cut	2	650	652	
QUE-03-e	83	652	735	
Cut	2	735	737	
QUE-03-5	13	737	750	Elevation 11, 750 mm polished
Cut	2	750	752	
QUE-03-f	33	752	785	
Cut	2	785	787	
QUE-03-6	13	787	800	800 mm polished
Cut	2	800	802	
QUE-03-g	133	802	935	
Cut	2	935	937	
QUE-03-7	13	937	950	Elevation 13, 950 mm polished
Cut	2	950	952	
QUE-03-h	183	952	1135	
Cut	2	1135	1137	
QUE-03-8	13	1137	1150	
Cut	2	1150	1152	
QUE-03-i	83	1152	1235	

Sample	Sample length (mm)	Axial position bottom (mm)	Axial position top (mm)	Remarks
Cut	2	1235	1237	
QUE-03-9	13	1237	1250	
Cut	2	1250	1252	
QUE-03-j	41	1252	1293	
Cut	2	1293	1295	Below shroud flange
QUE-03-10	20	1295	1315	
Cut	2	1315	1317	Above shroud flange
QUE-03-k	483	1317	1800	Remnant

24.01.2000

Table 17: Parameters of pre-test calculations for QUENCH-02

	t s	prof	T_{in} K	P' W/s	T' K/s	P_{oxm} kW	W_{ox} MJ	dt_1 s	dt_2 s	n s
q02v01	1000	r	700	0.83						
q02v02	3000	r	800	0.28	0.8	41.0	23.2	249	65	9
q02v03	2000	r	800	0.42	1.1	41.2	13.6	180	49	7
q02v04	3000	rp	800	0.24	0.5	15.6	5.3	566	164	1
q02v05	3000	r	700	0.28	0.8	38.7	30.1	257	67	6
q02v06	3000	rp	700	0.28	0.8	33.7	16.7	278	76	6

t	duration of elevated power
prof	form of power transient r ramp; p plateau
T_{in}	bundle inlet temperature
T'	temperature increase
P'	power increase
P_{oxm}	max chemical power
W_{ox}	total chemical energy
dt_1	time for temperature increase from 1500 K to 1800 K
dt_2	time for temperature increase from 1800 K to 2300 K
n	number of nodes above 2300 K

Note: Run q02v01 ended before sufficiently high temperatures were reached.

QUENCH Test Facility Flow Diagram

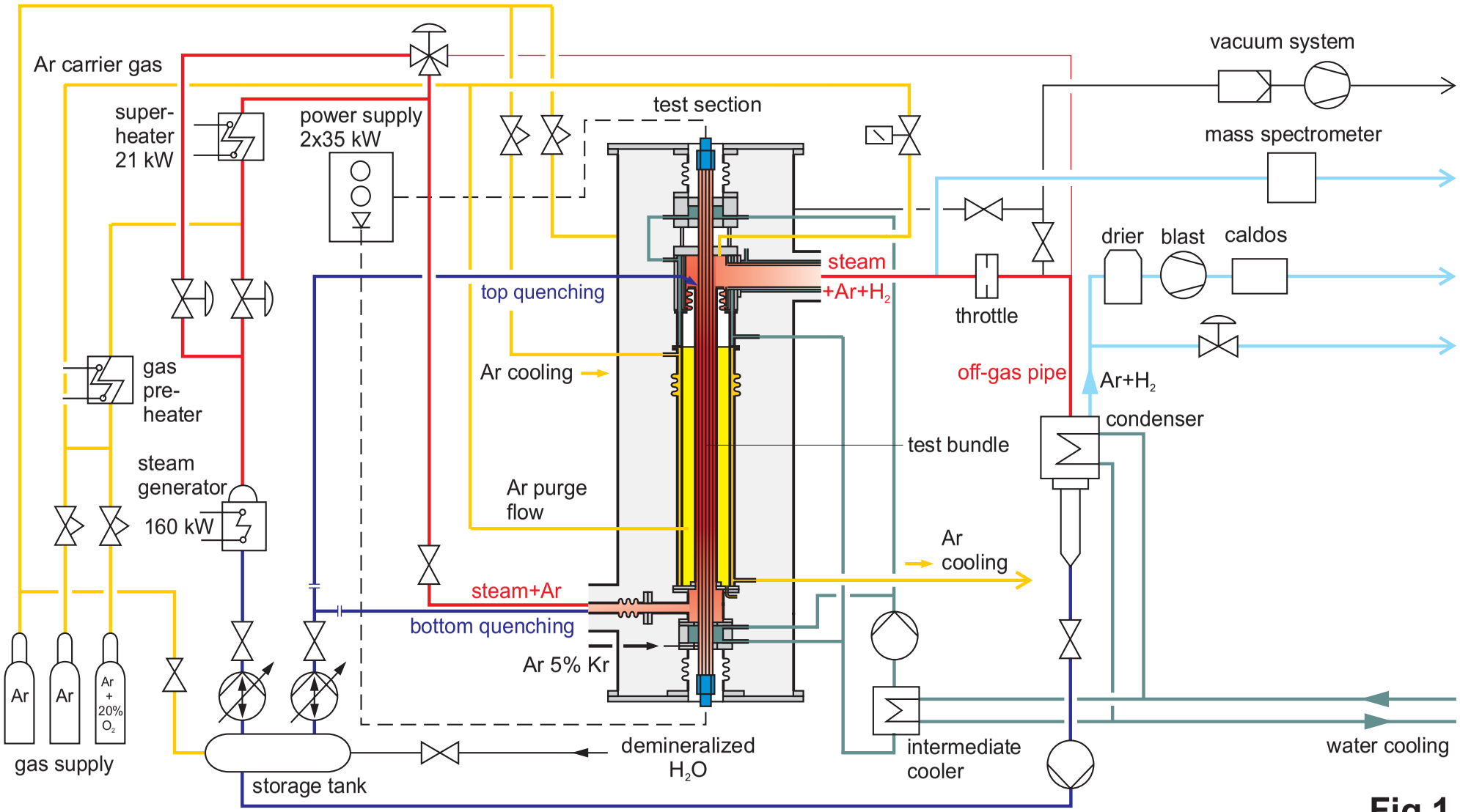

Fig 1

QUENCH Facility

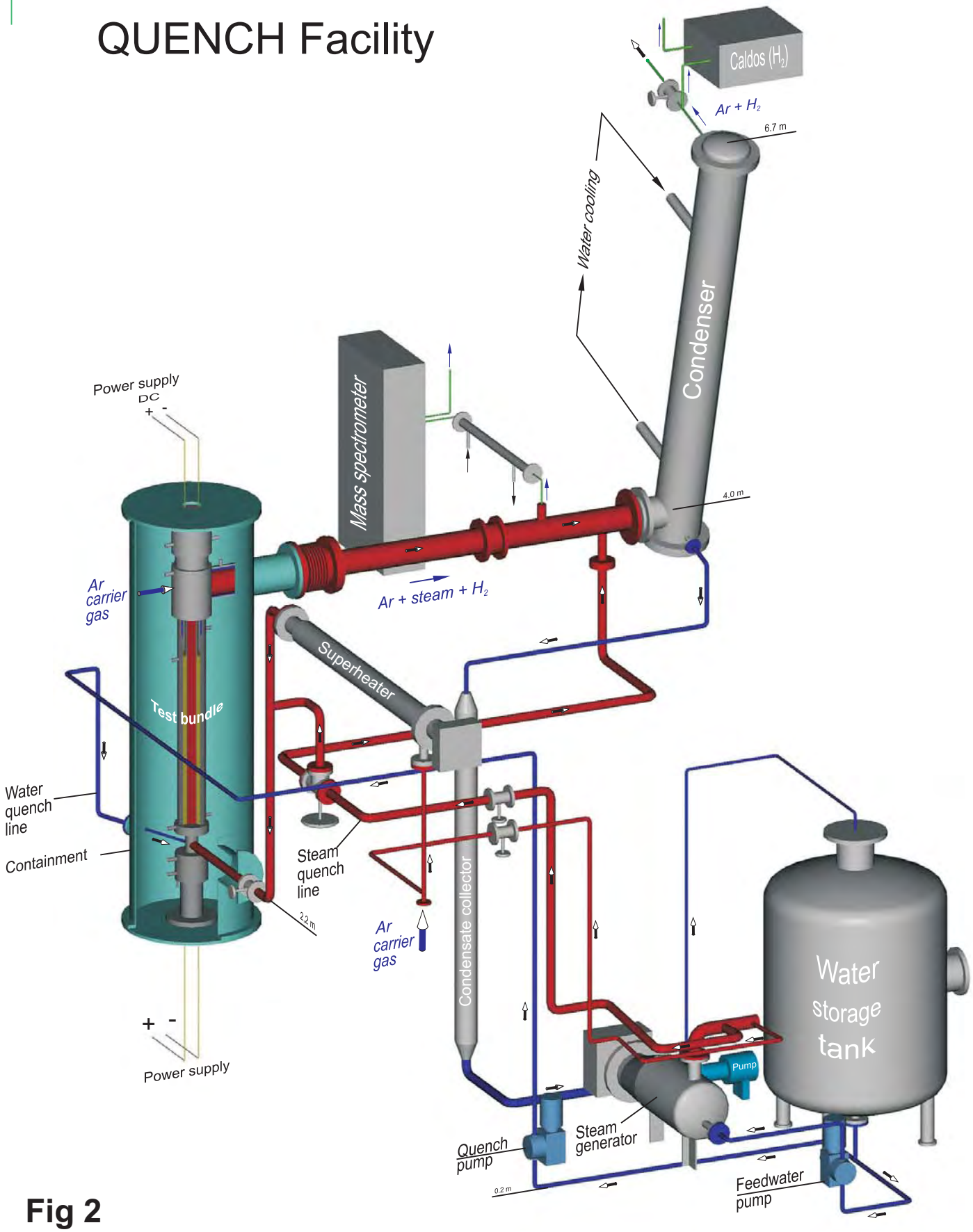

Fig 2

QUENCH Test Section - Flow lines

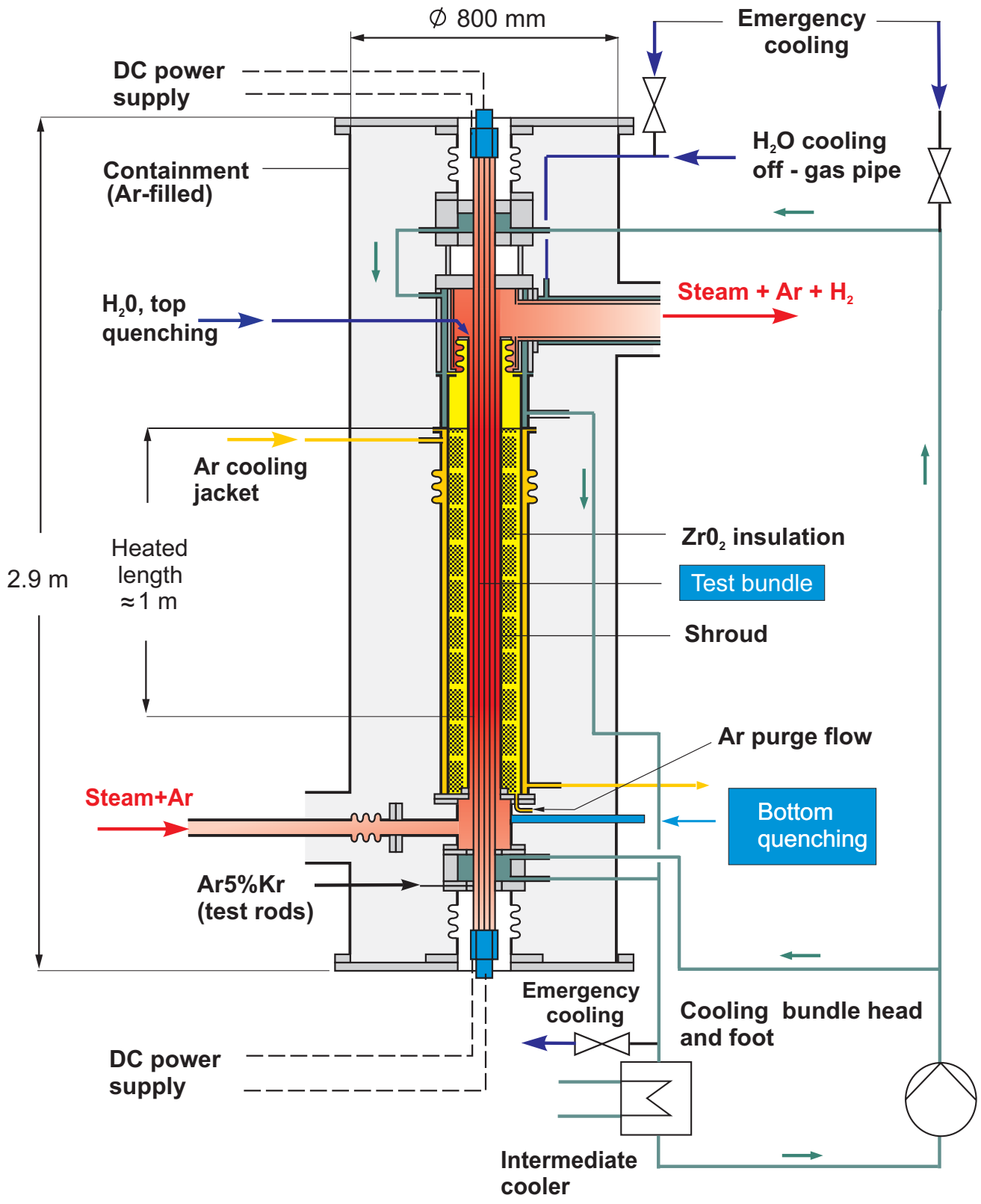

Fig 3

QUENCH-02
Fuel Rod Simulator Bundle (Top View)

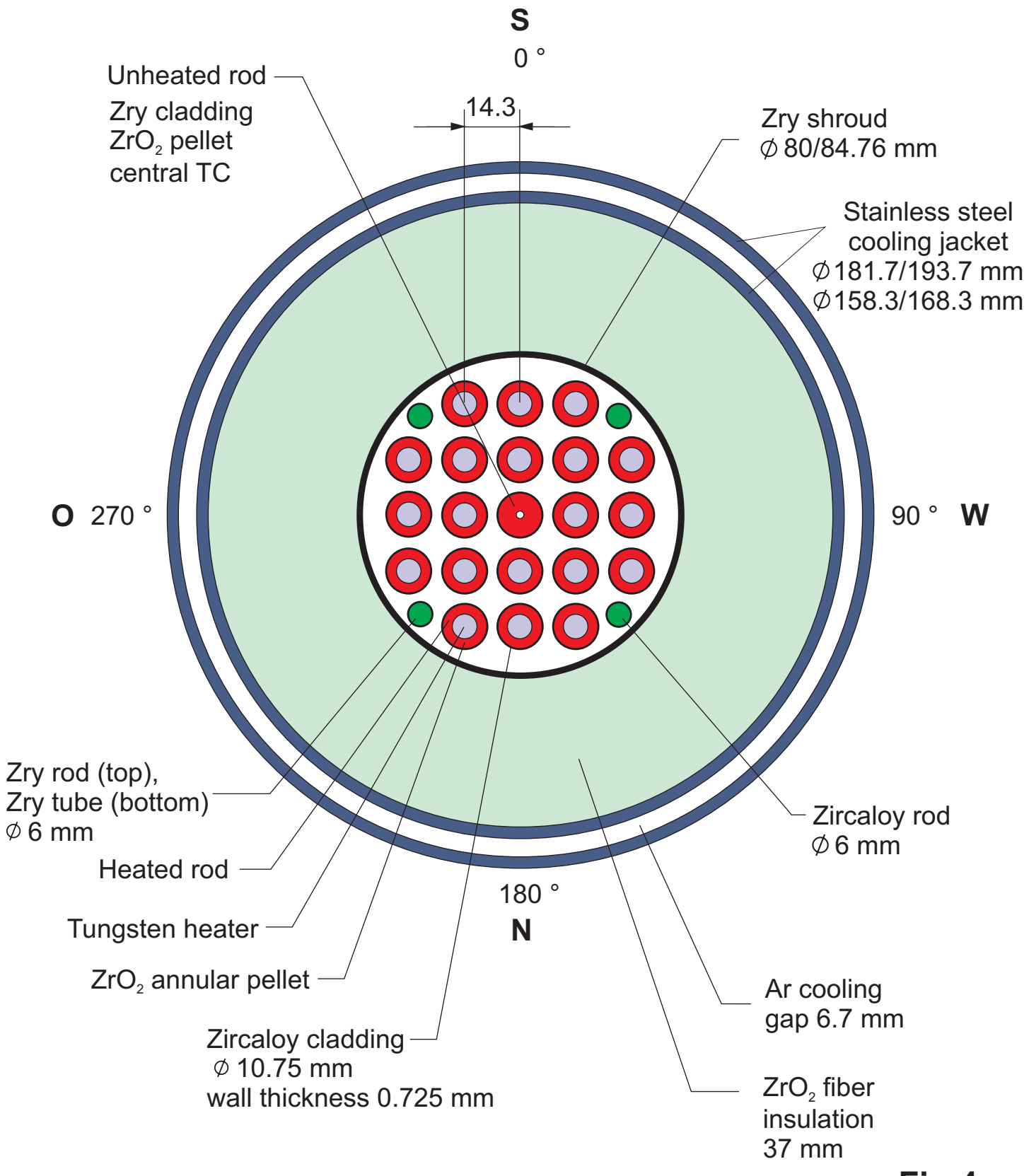

Fig 4

QUENCH-03
Fuel Rod Simulator Bundle (Top View)

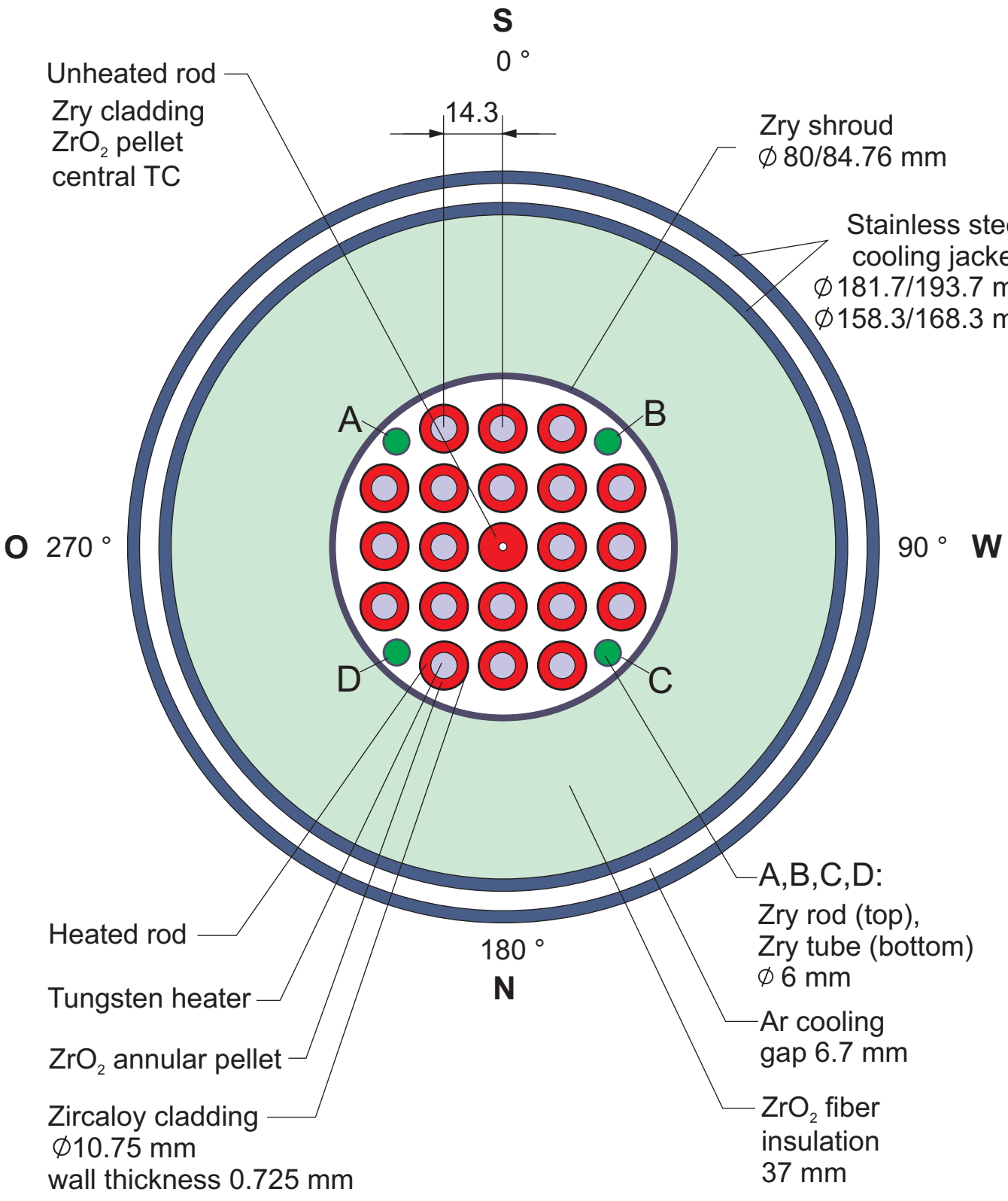

Fig 5

Heated Fuel Rod Simulator

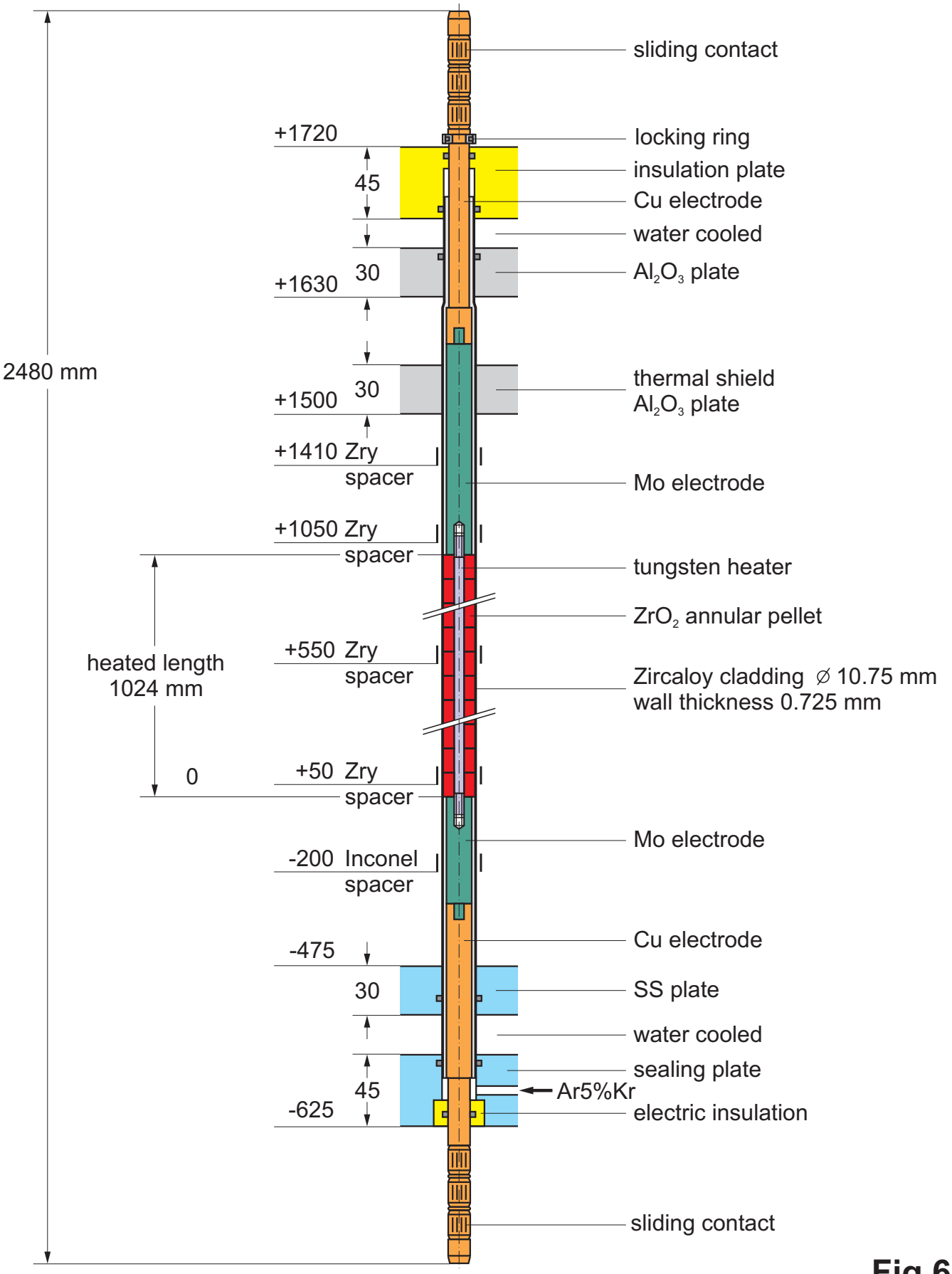

Fig 6

Unheated Fuel Rod Simulator

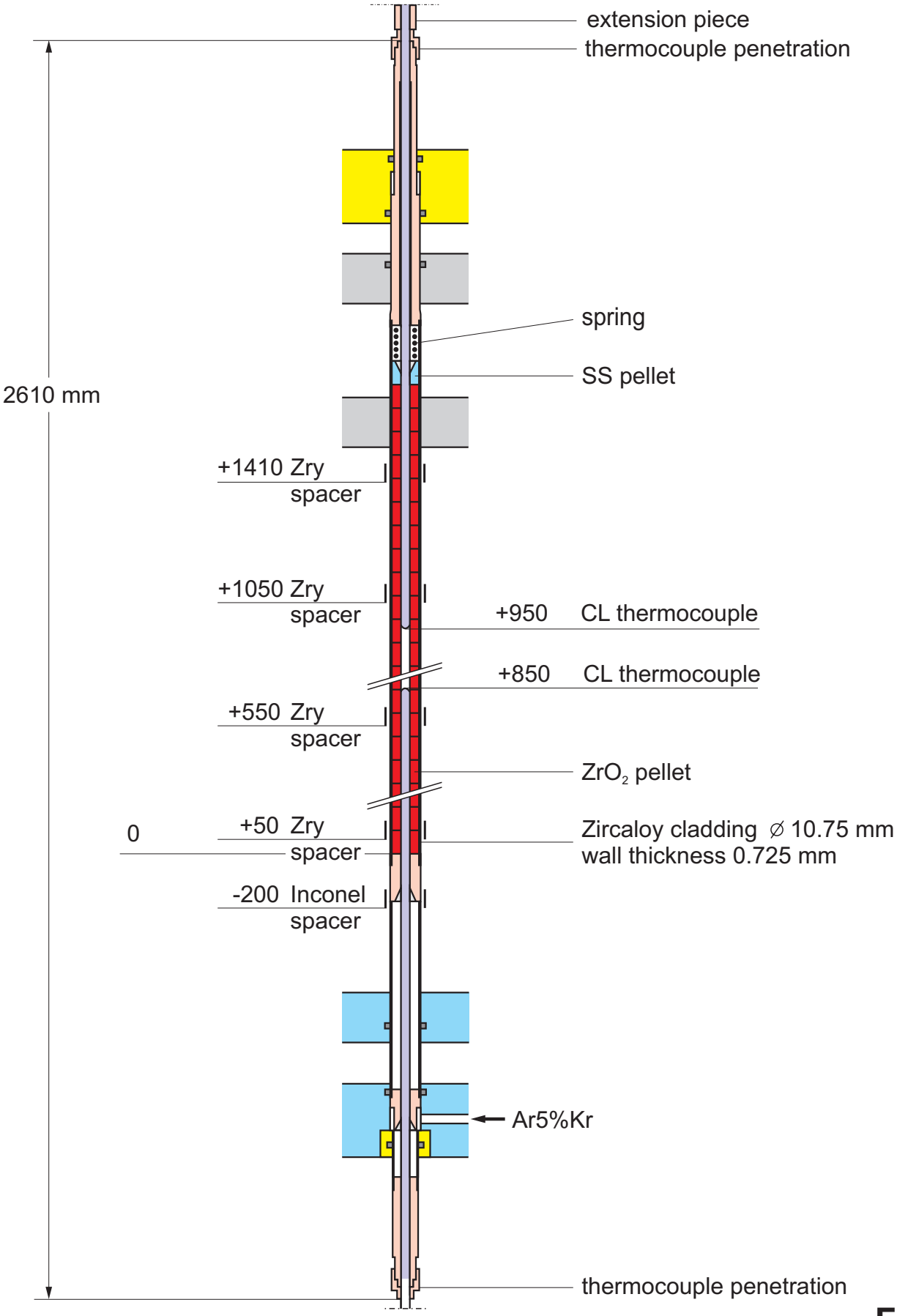

Fig 7

QUENCH-02 Test Bundle

TC Instrumentation and Rod Designation (Top View)

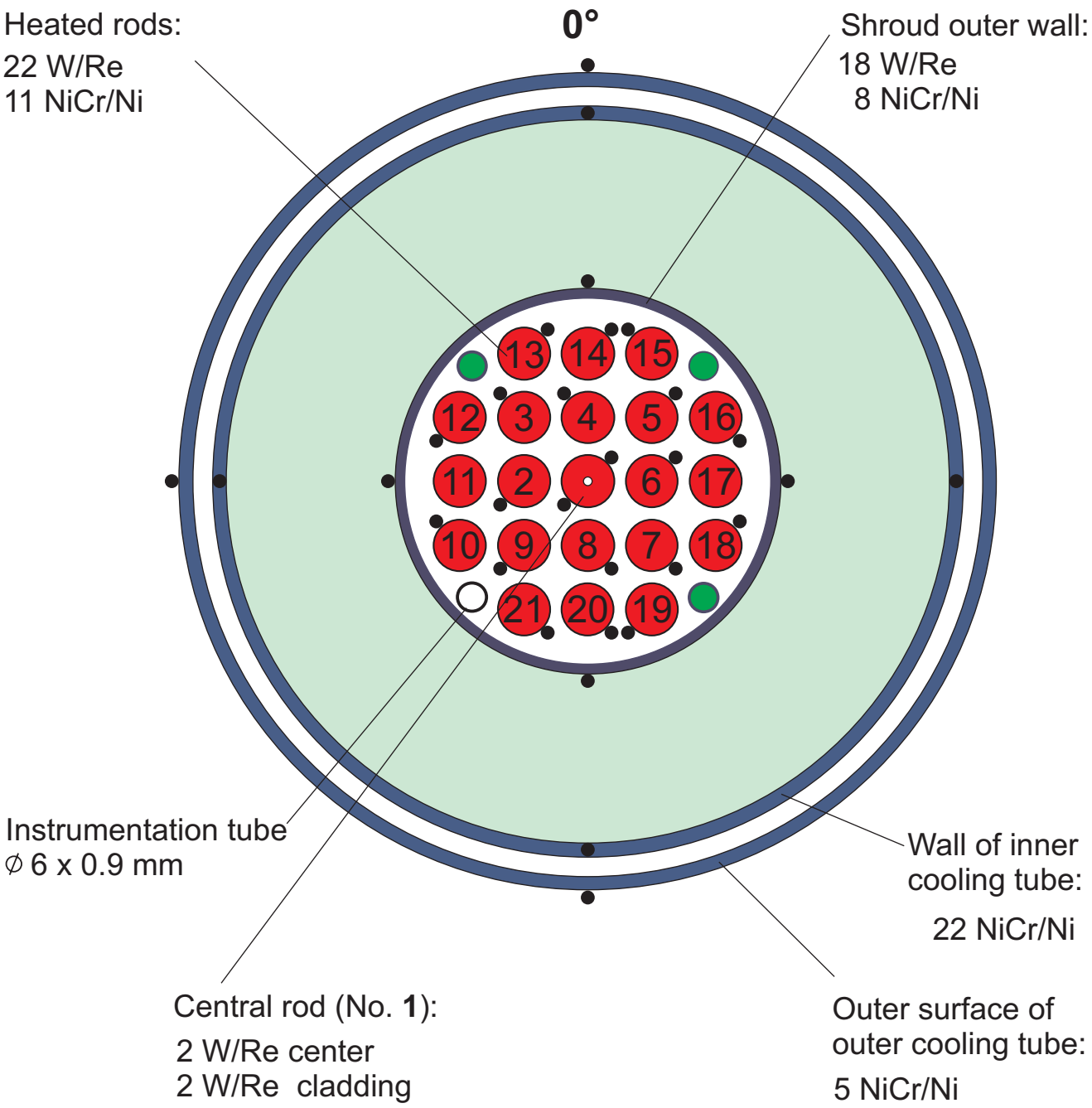

Fig 8

QUENCH-03 Test Bundle

TC Instrumentation and Rod Designation (Top View)

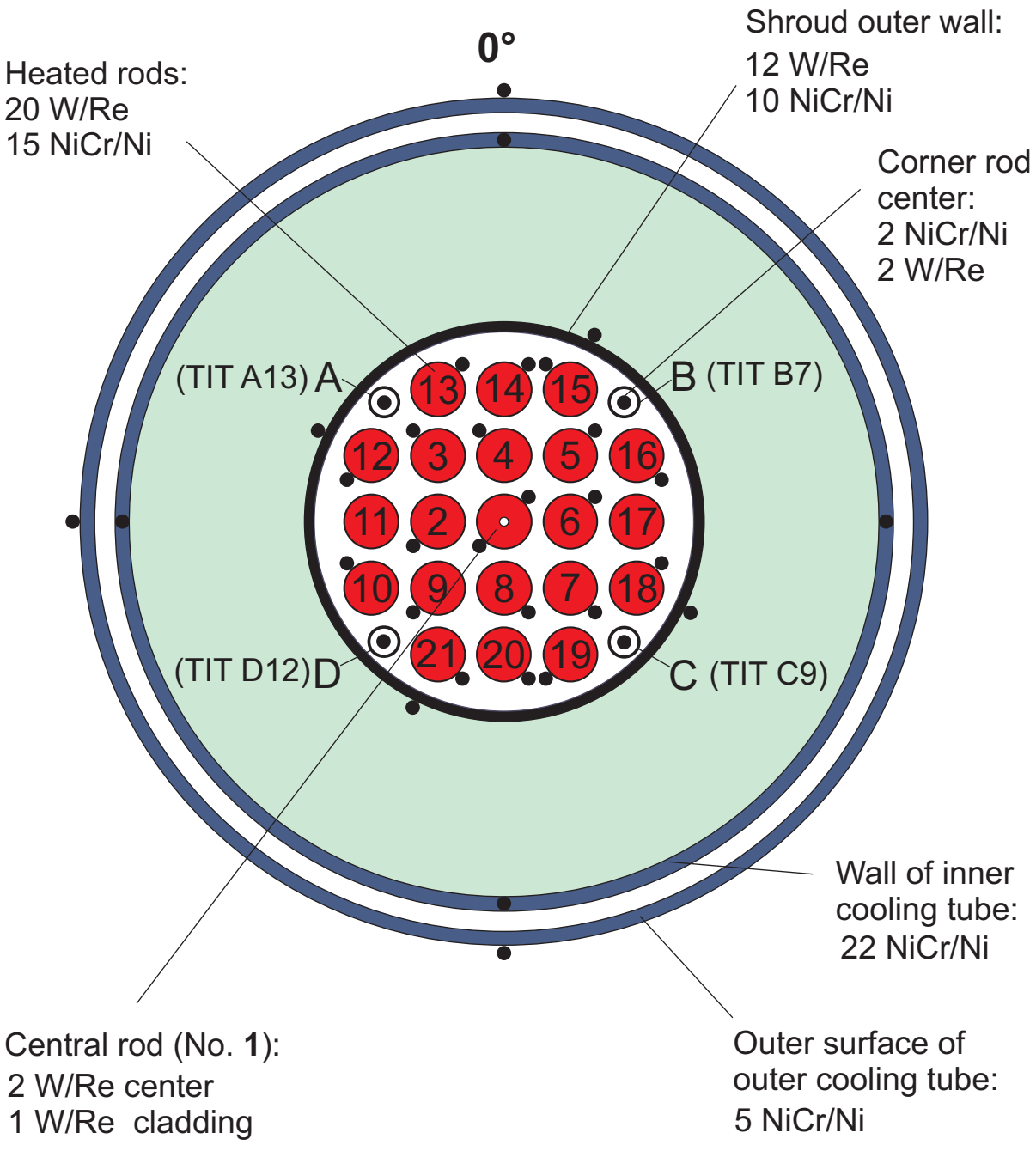

Fig 9

QUENCH Test Section Instrumentation

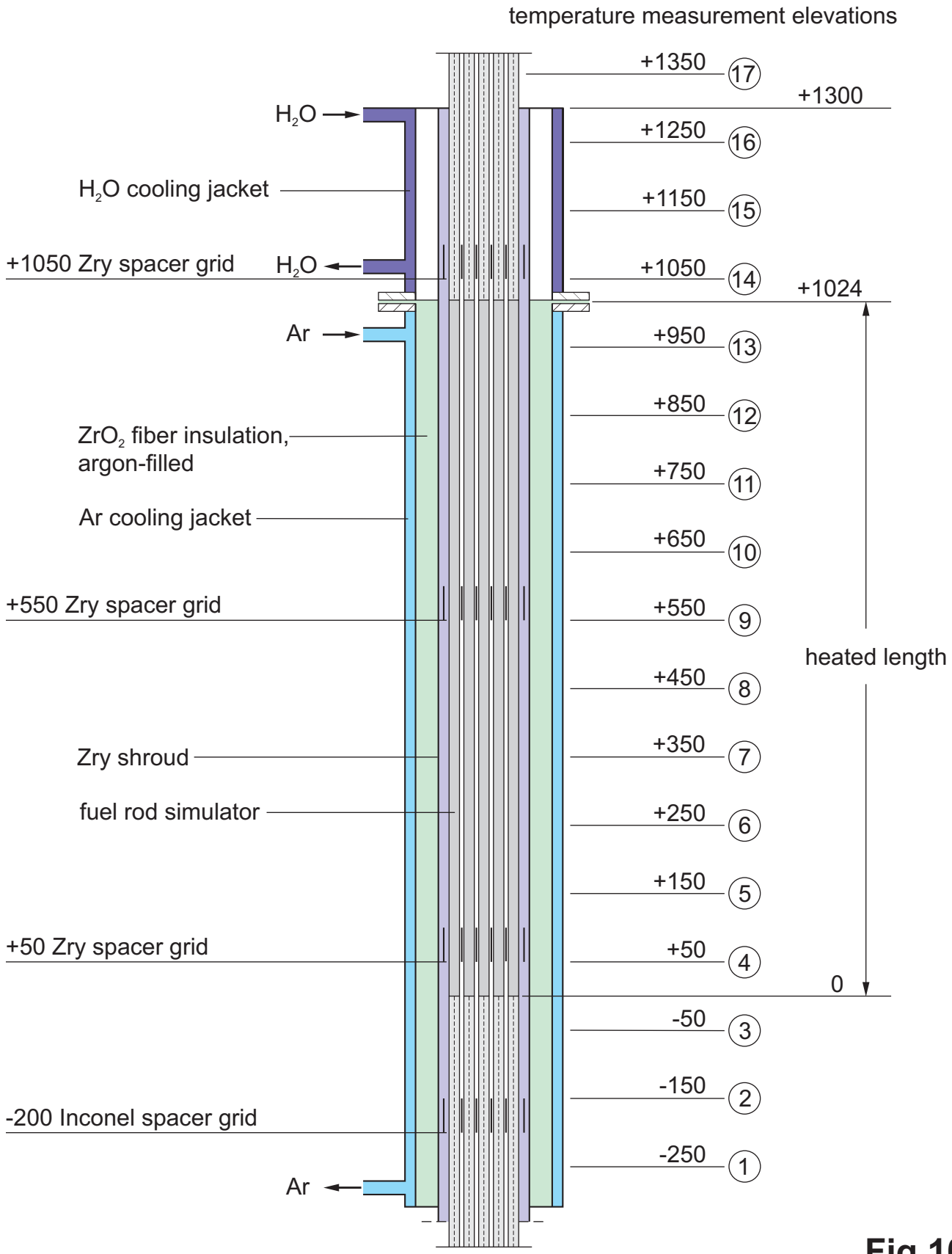

Fig 10

QUENCH High-temperature thermocouple

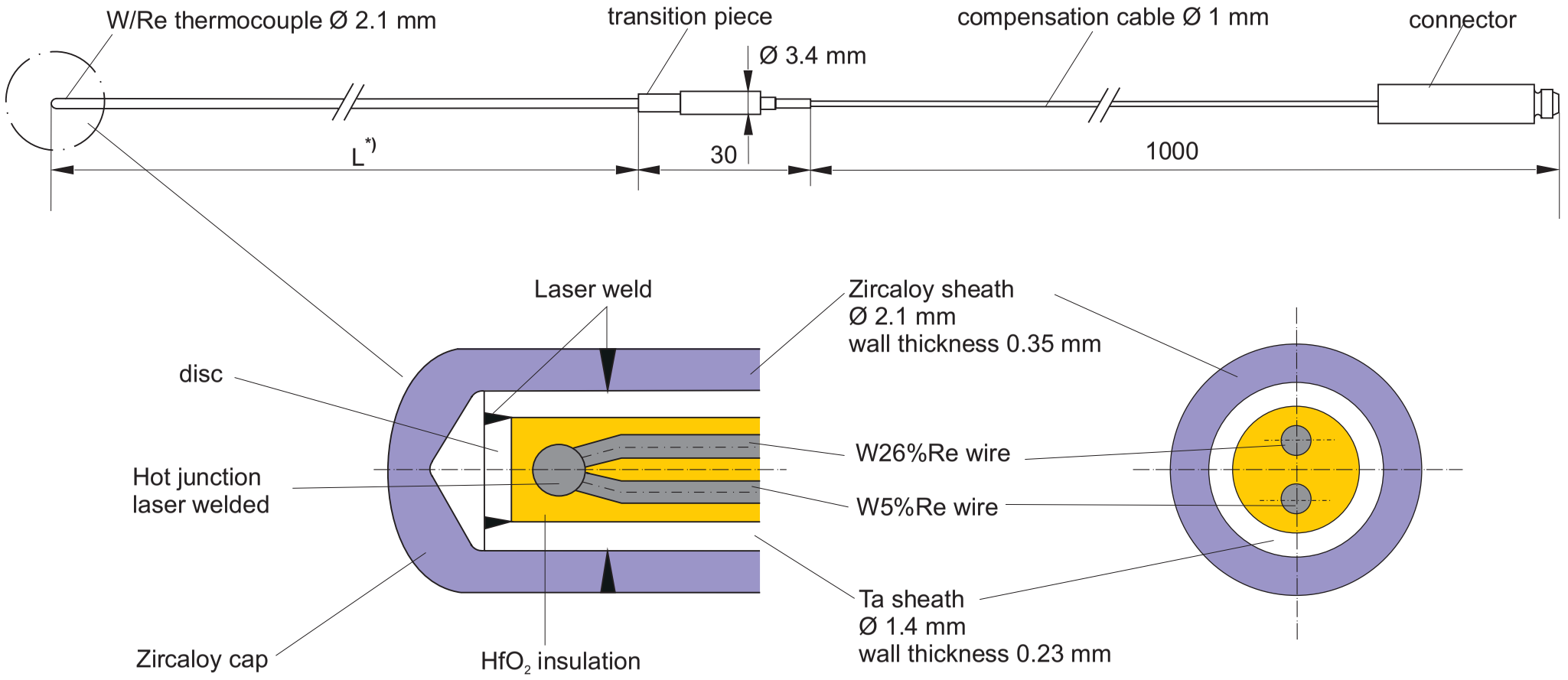

*) L: high-temperature section length dependent on the TC position in the test bundle 500 mm - 1700 mm

Fig 11

Zr Clip for Fixing the TC Tip at the Rod Cladding

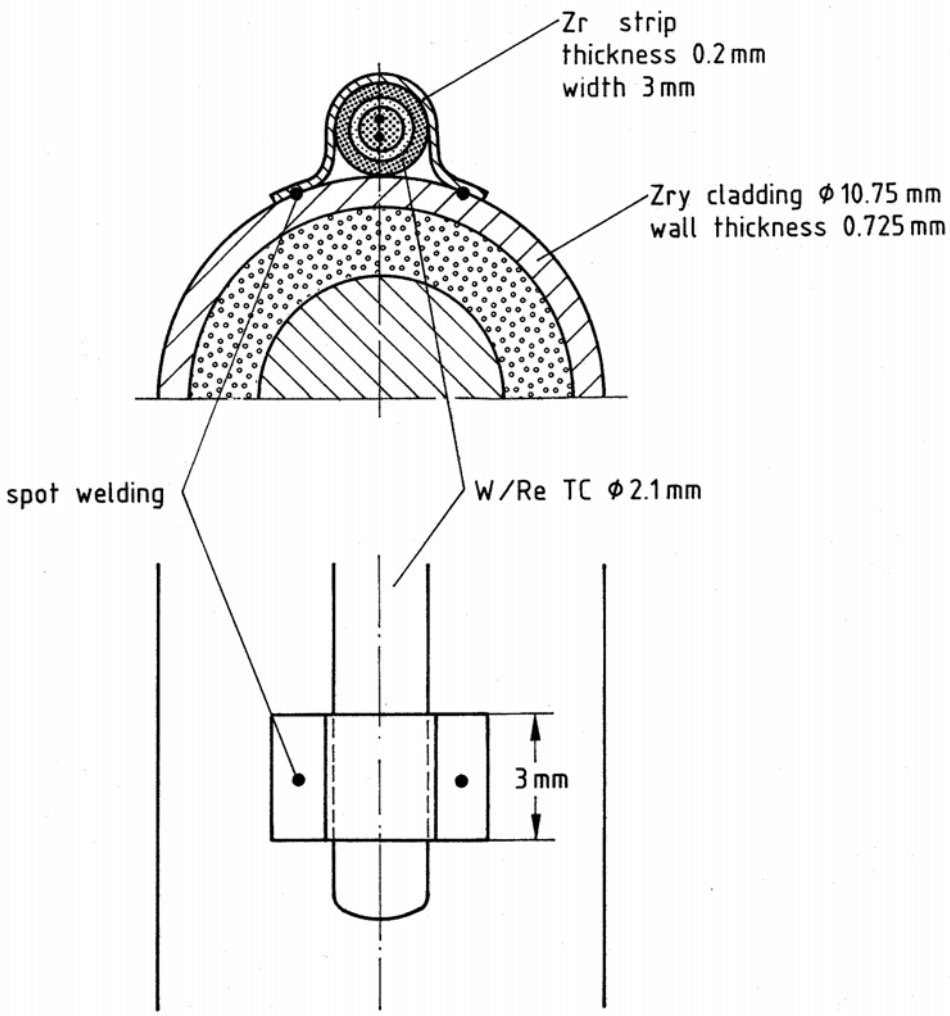

Fig 12

TC Fastening Concept for the QUENCH Test Rods

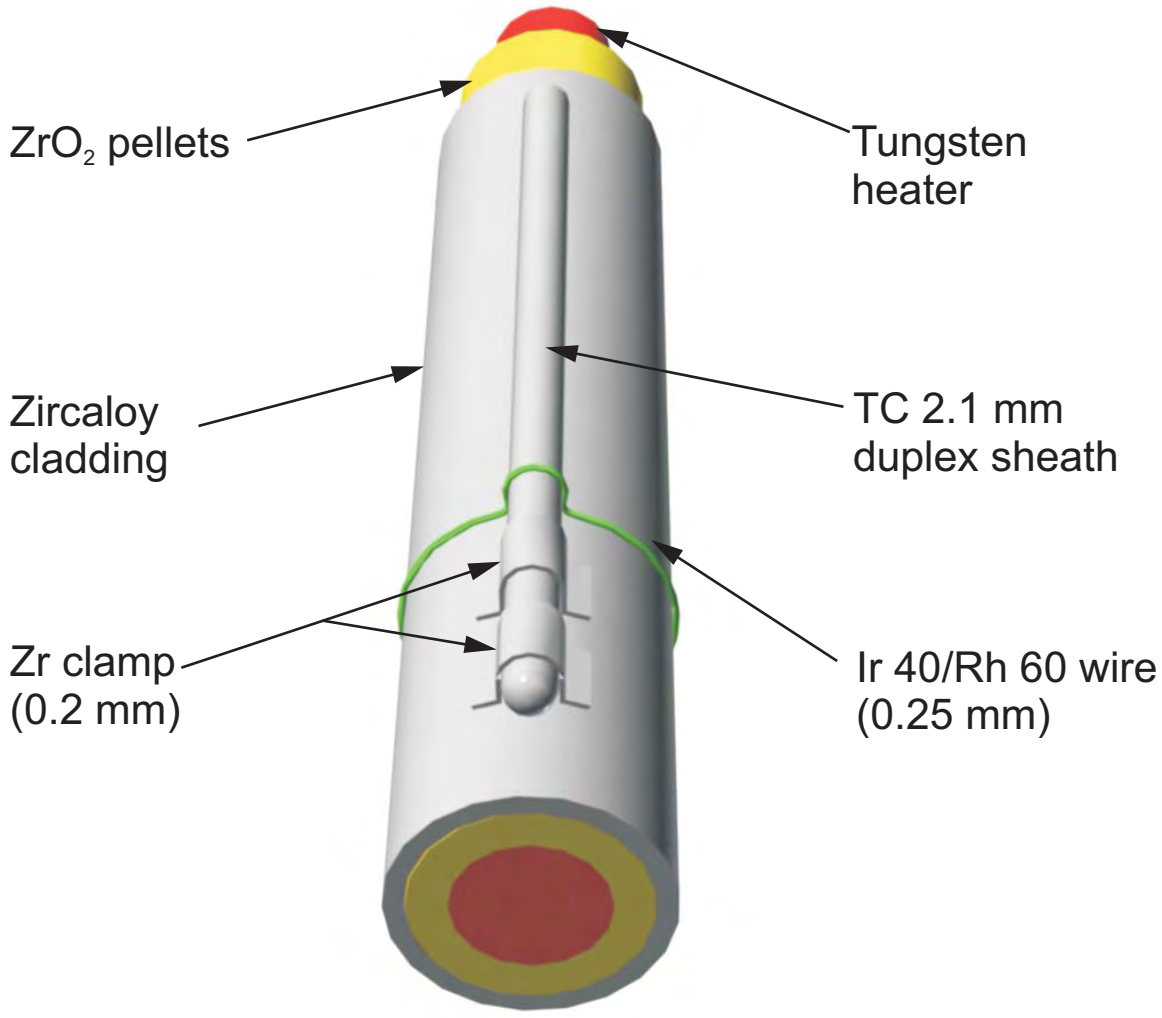

With pre-oxidation: Zr clamp + wire

Without pre-oxidation: Zr clamp

Fig 13

QUENCH-03

Schematic of the arrangement of the thermocouples inside the corner rods

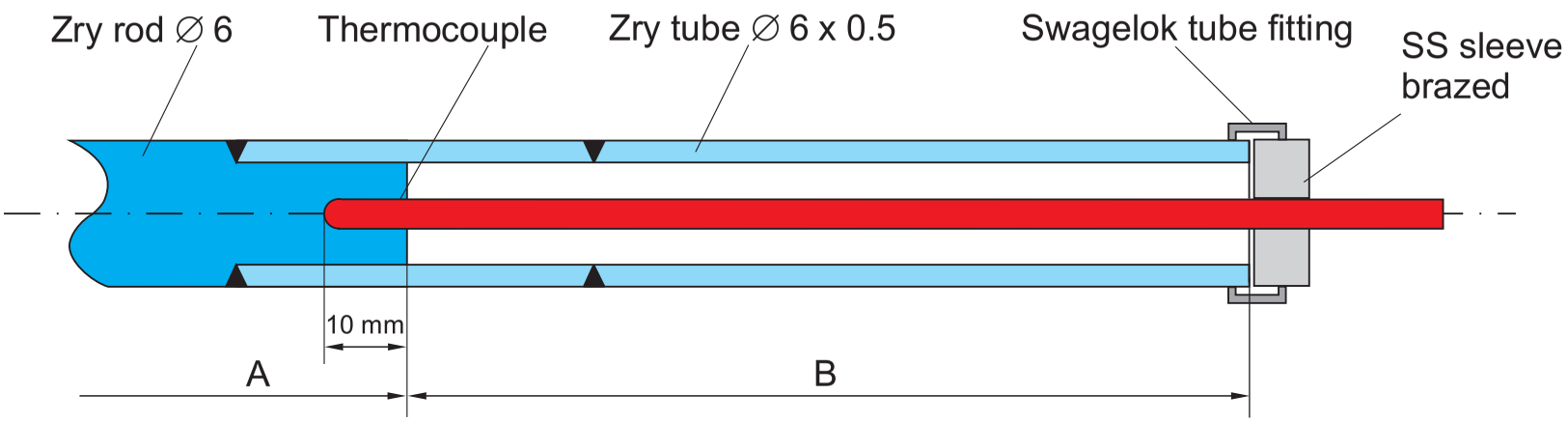

Rod A: TIT A13 (950 mm), W/Re, ∅ 2.1 mm, A = 360 mm, B = 2080 mm

Rod D: TIT D12 (850 mm), W/Re, ∅ 2.1 mm, A = 460 mm, B = 1980 mm

Rod C: TIT C 9 (550 mm), NiCr/Ni, ∅ 1 mm, A = 760 mm, B = 1680 mm

Rod B: TIT B 7 (350 mm), NiCr/Ni, ∅ 1 mm, A = 960 mm, B = 1480 mm

Fig 14

QUENCH - Facility

H_2 - Measurement mass spectrometer

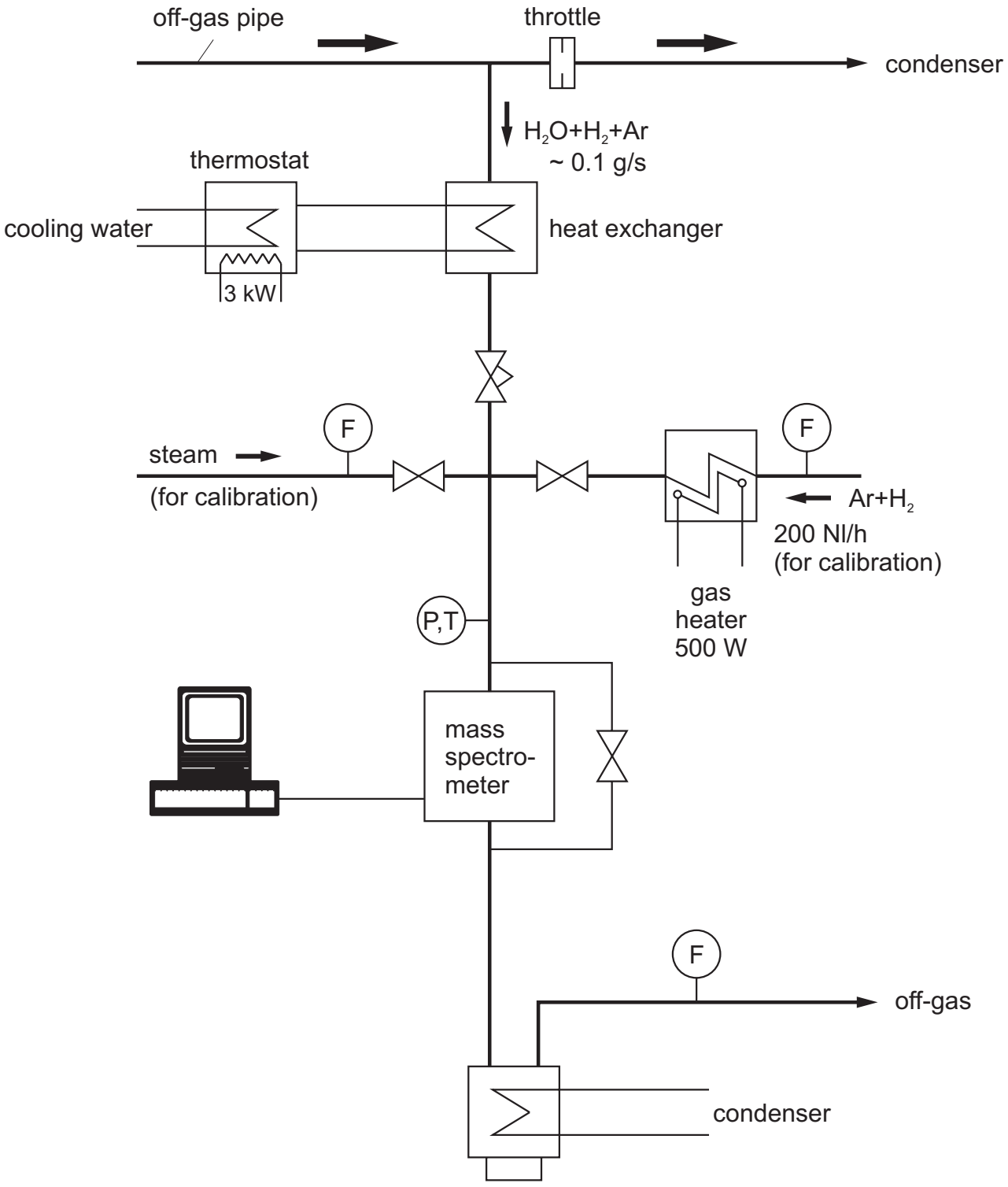

Fig 15

QUENCH Test Facility

Caldos device for the H_2 measurement

Fig 16

QUENCH

Hydrogen measurement with the CALDOS analyzer

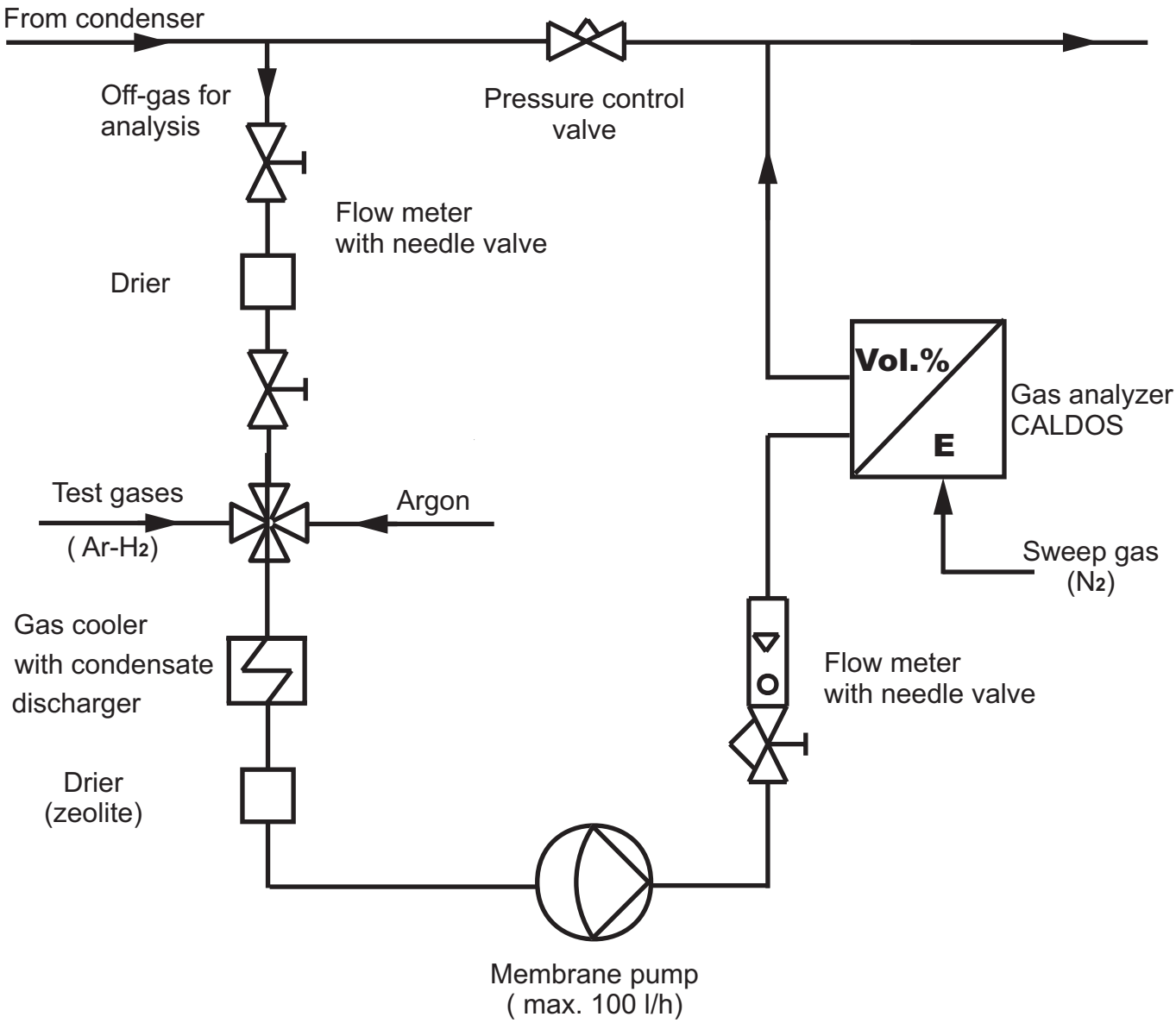

Fig 17

Figures to Experiment QUENCH-02

QUENCH-O2, Test Conduct (schematic)

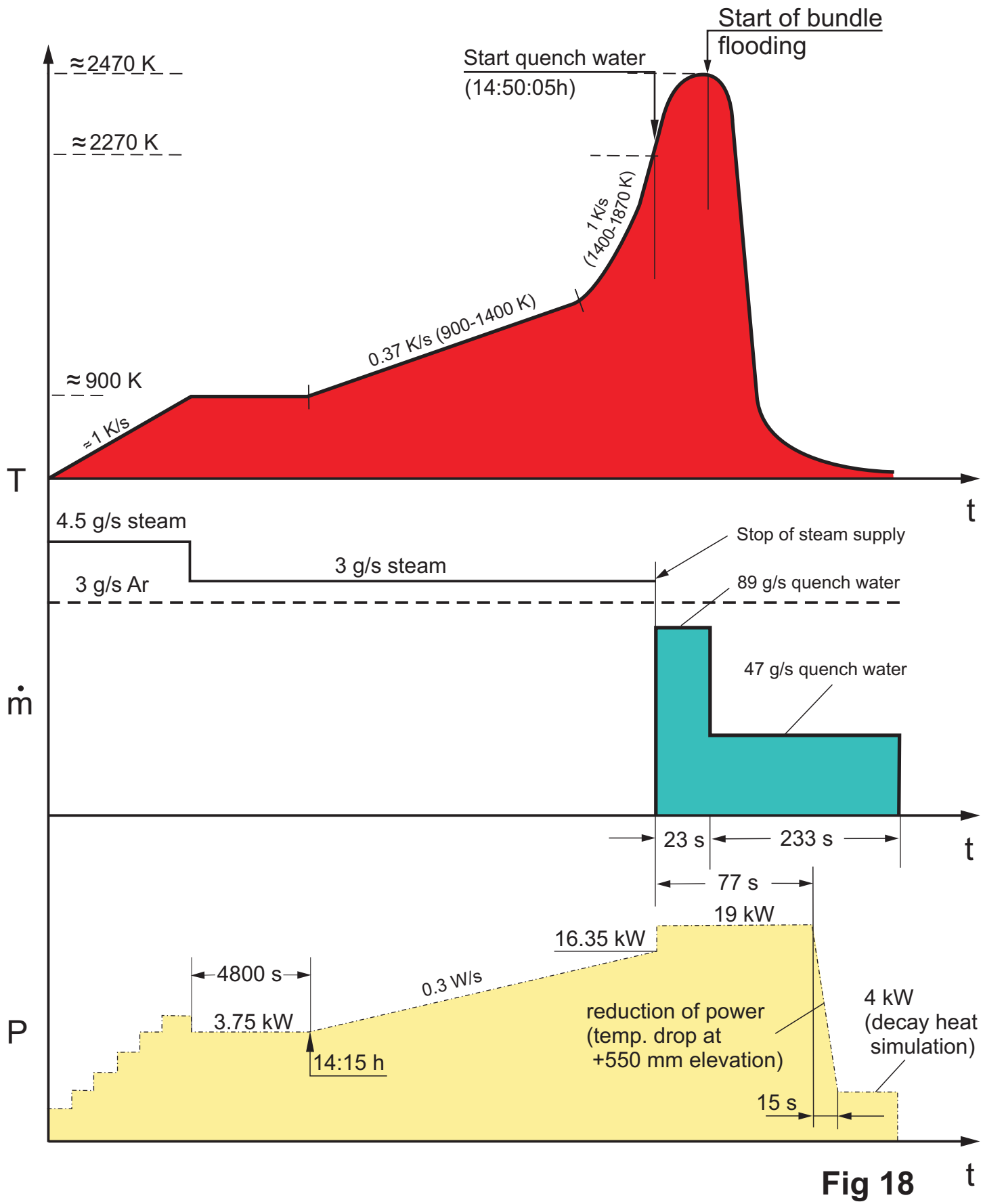

Fig 18

QUENCH-02

Temperature measured by the centerline thermocouple TCRC 14

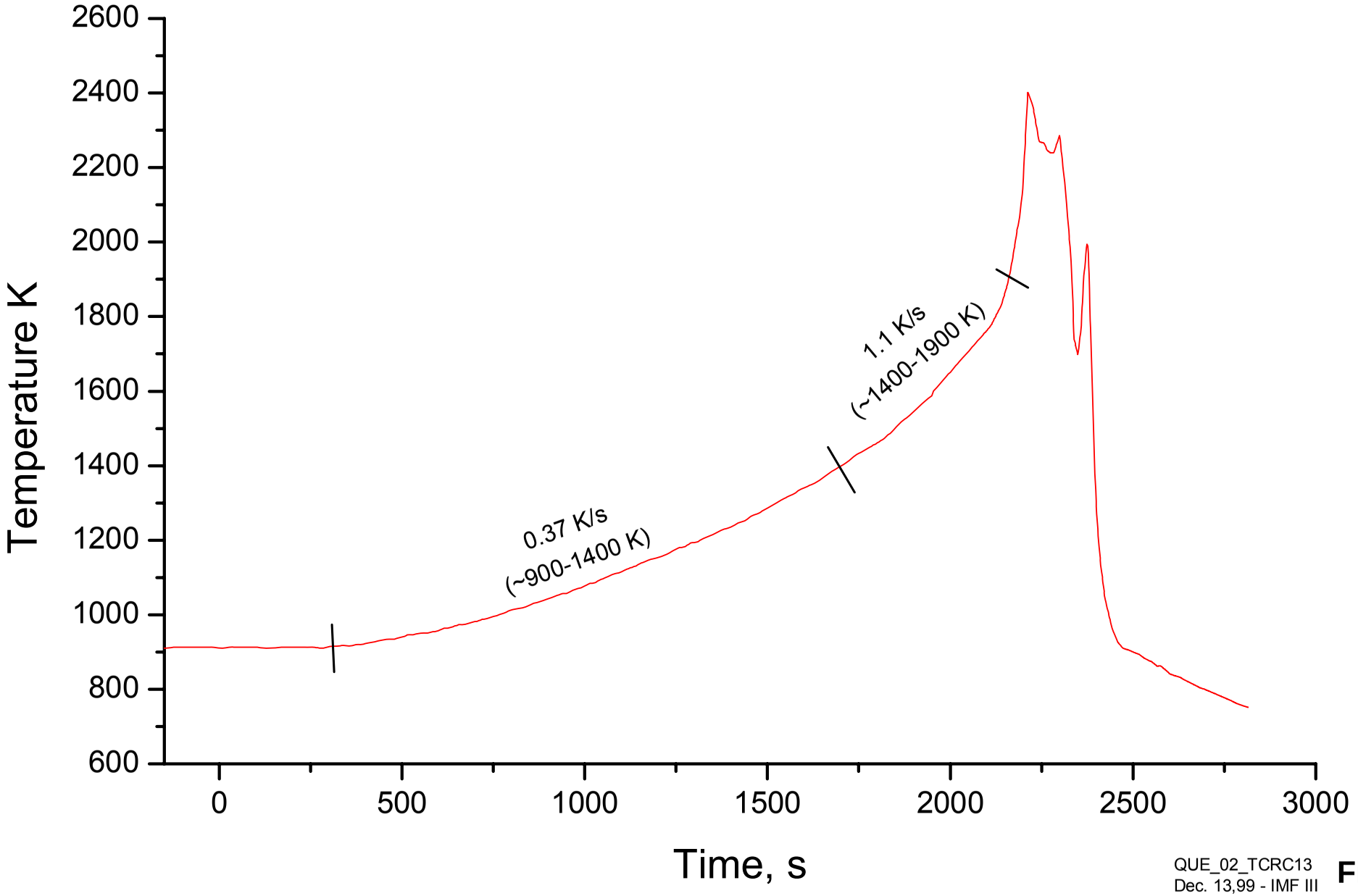

QUE_02_TCRC13
Dec. 13,99 - IMF III

Fig 19

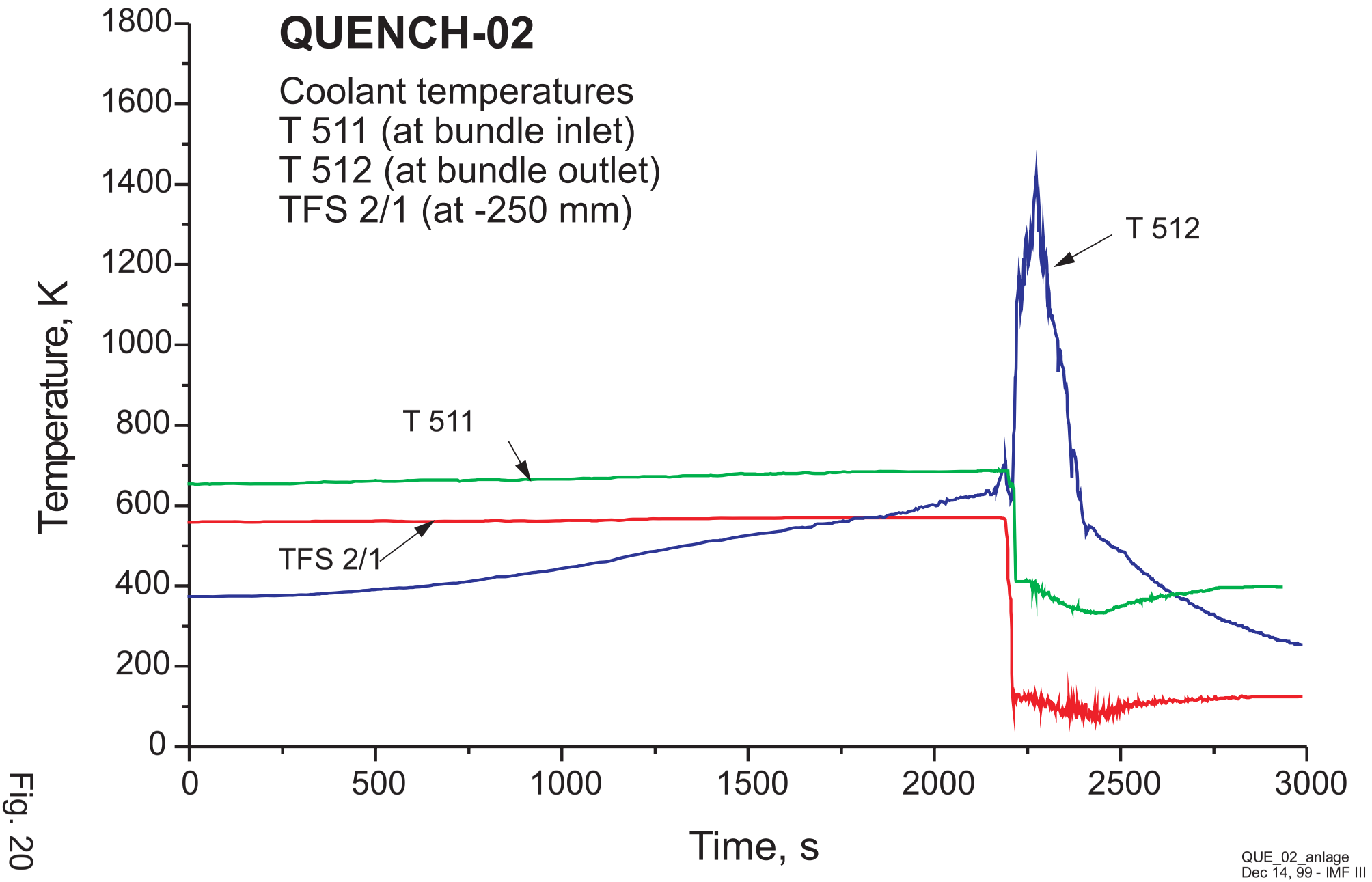
QUENCH-02
Coolant temperatures
T 511 (at bundle inlet)
T 512 (at bundle outlet)
TFS 2/1 (at -250 mm)
T 512
T 511
TFS 2/1
Temperature, K
Time, s
0
200
400
600
800
1000
1200
1400
1600
1800
0
500
1000
1500
2000
2500
3000
QUE_02_anlage
Dec 14, 99 - IMF III

Fig. 20

Definitions

- Onset of cooling
- Onset of quenching
- Max. cooldown rate

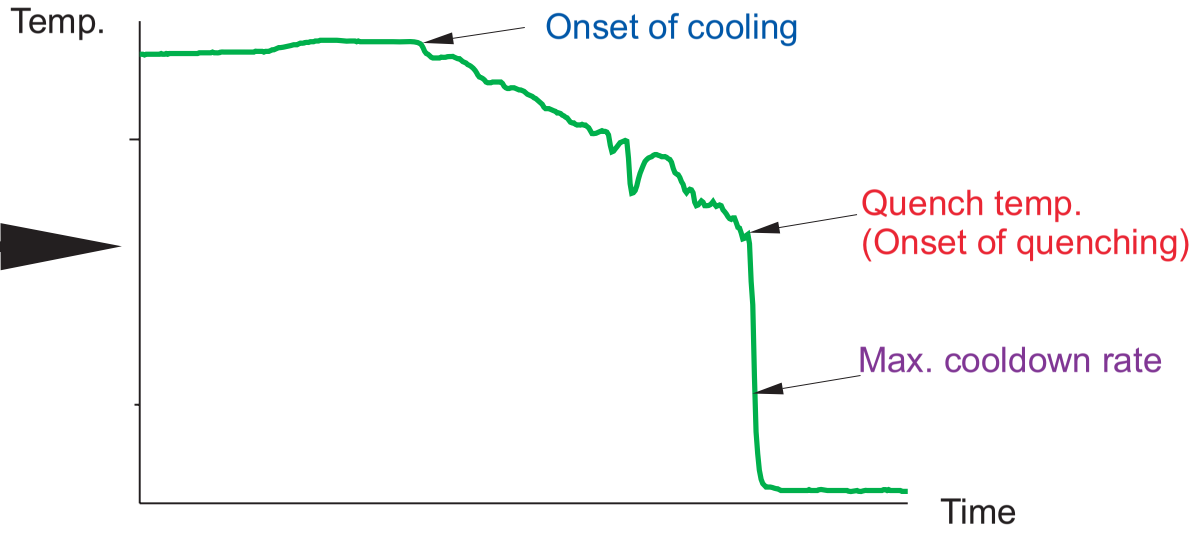

- Quench rate

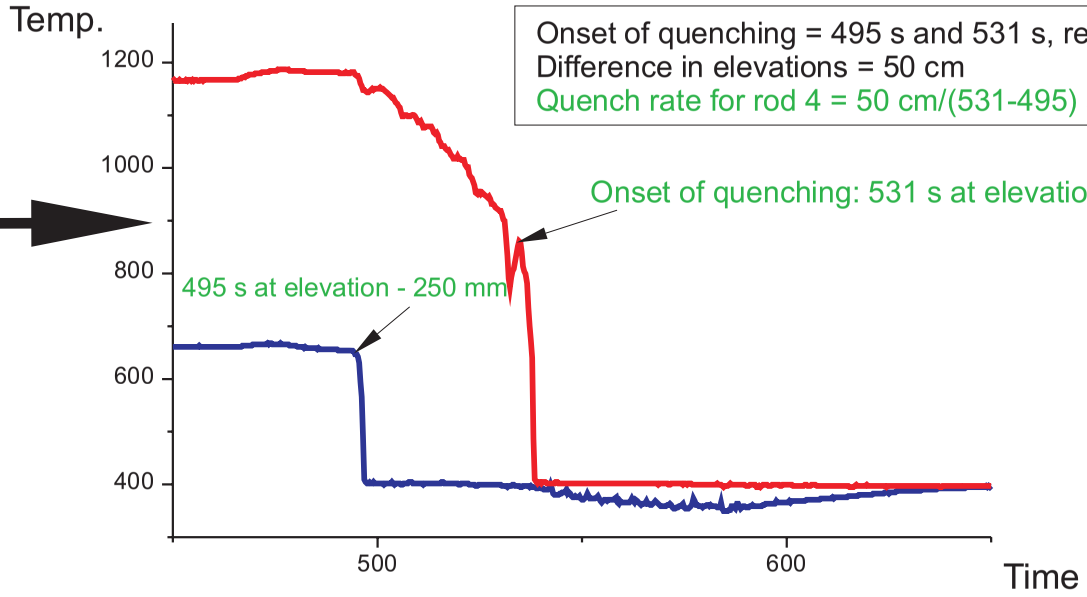

- Injection rate = Quench water flow entering the bottom of the test section determined by quench pump rate
- Flooding rate = Injection rate minus water evaporation in the test section; function of elevation

QUENCH-02 Quench Phase

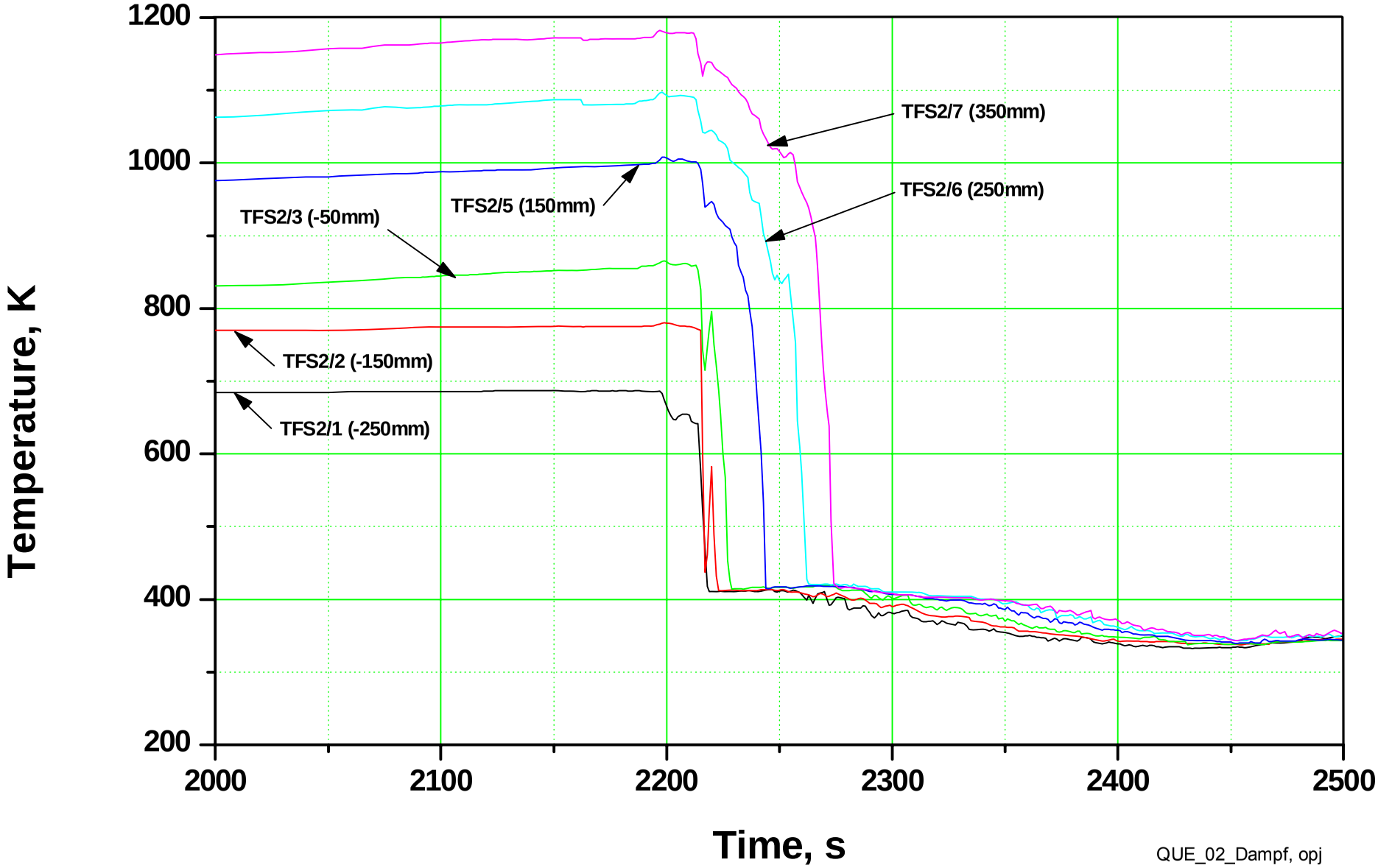

QUE_02_Dampf, opj
Nov 23,99 - IMF III

Fig 22

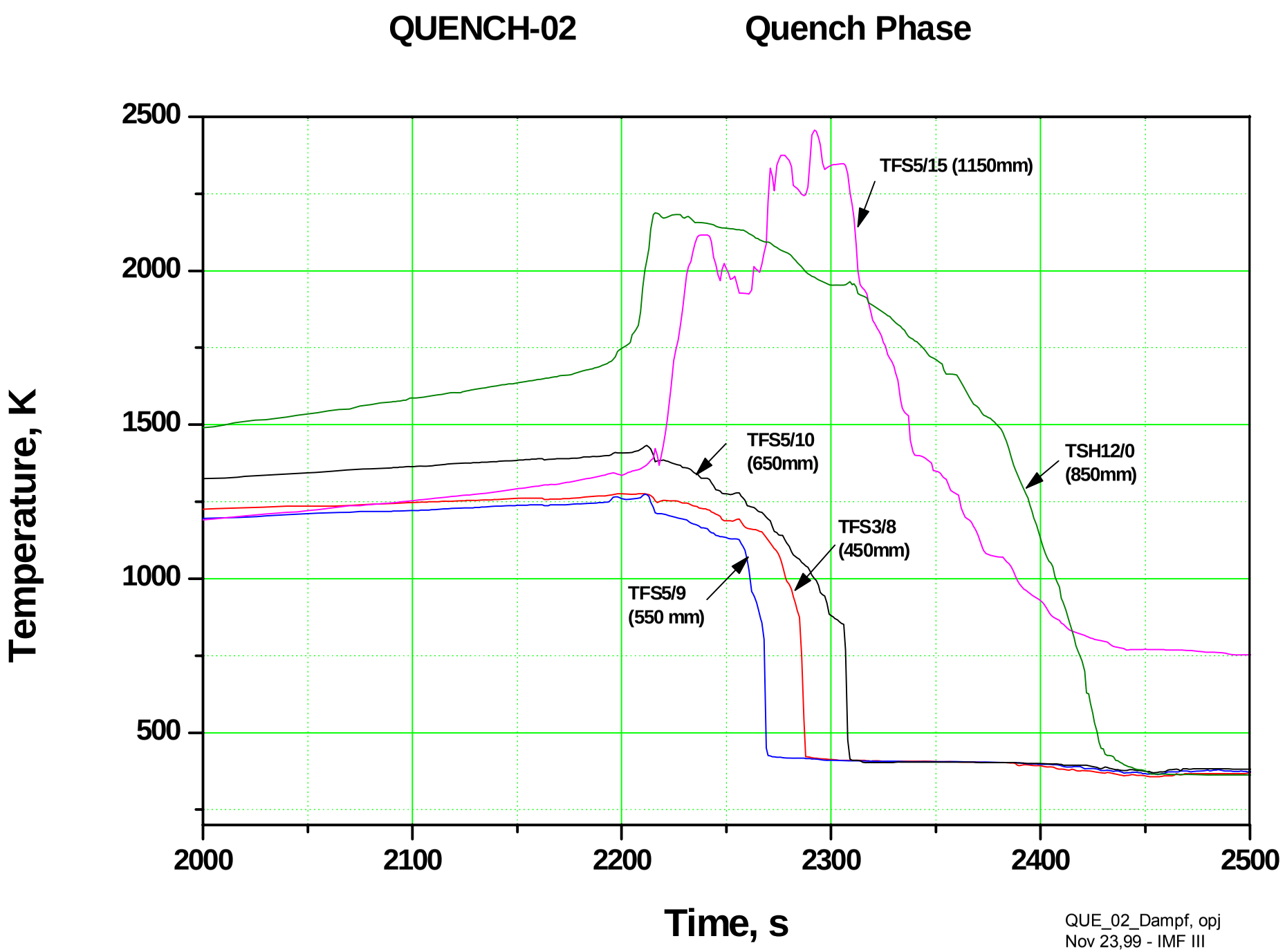
QUENCH-02
Quench Phase
Temperature, K
Time, s
2500
2000
1500
1000
500
2000
2100
2200
2300
2400
2500
TFS5/15 (1150mm)
TFS5/10
(650mm)
TSH12/0
(850mm)
TFS3/8
(450mm)
TFS5/9
(550 mm)
QUE_02_Dampf, opj
Nov 23,99 - IMF III

Fig 23

QUENCH-02, H_2O flow rates measured by MS and consumed by Zry oxidation

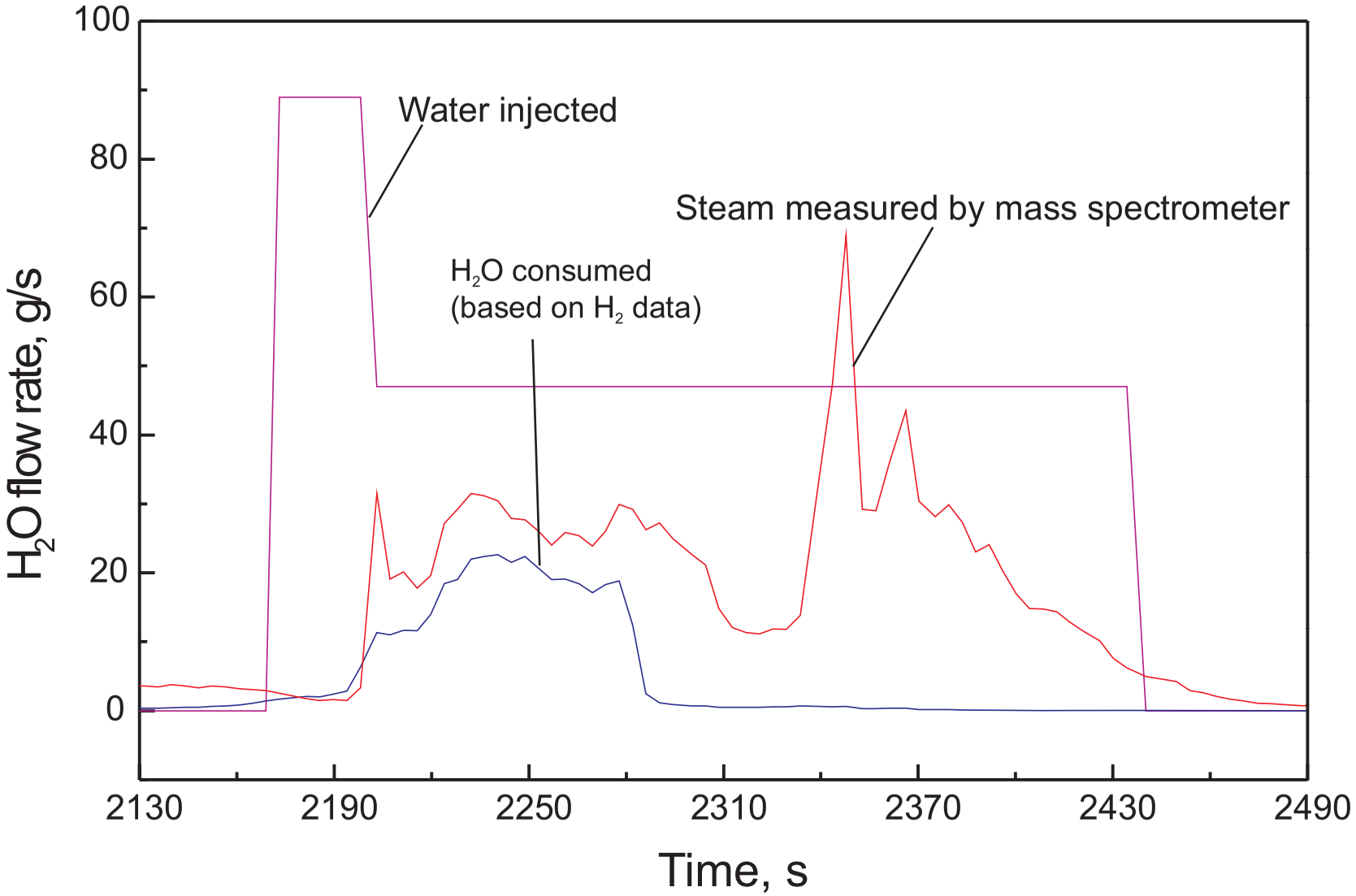

Fig 24

QUENCH-02

Axial Temperature Profile TFS 2, TFS 3, TFS 5
at 2250 s (Begin of quenching)

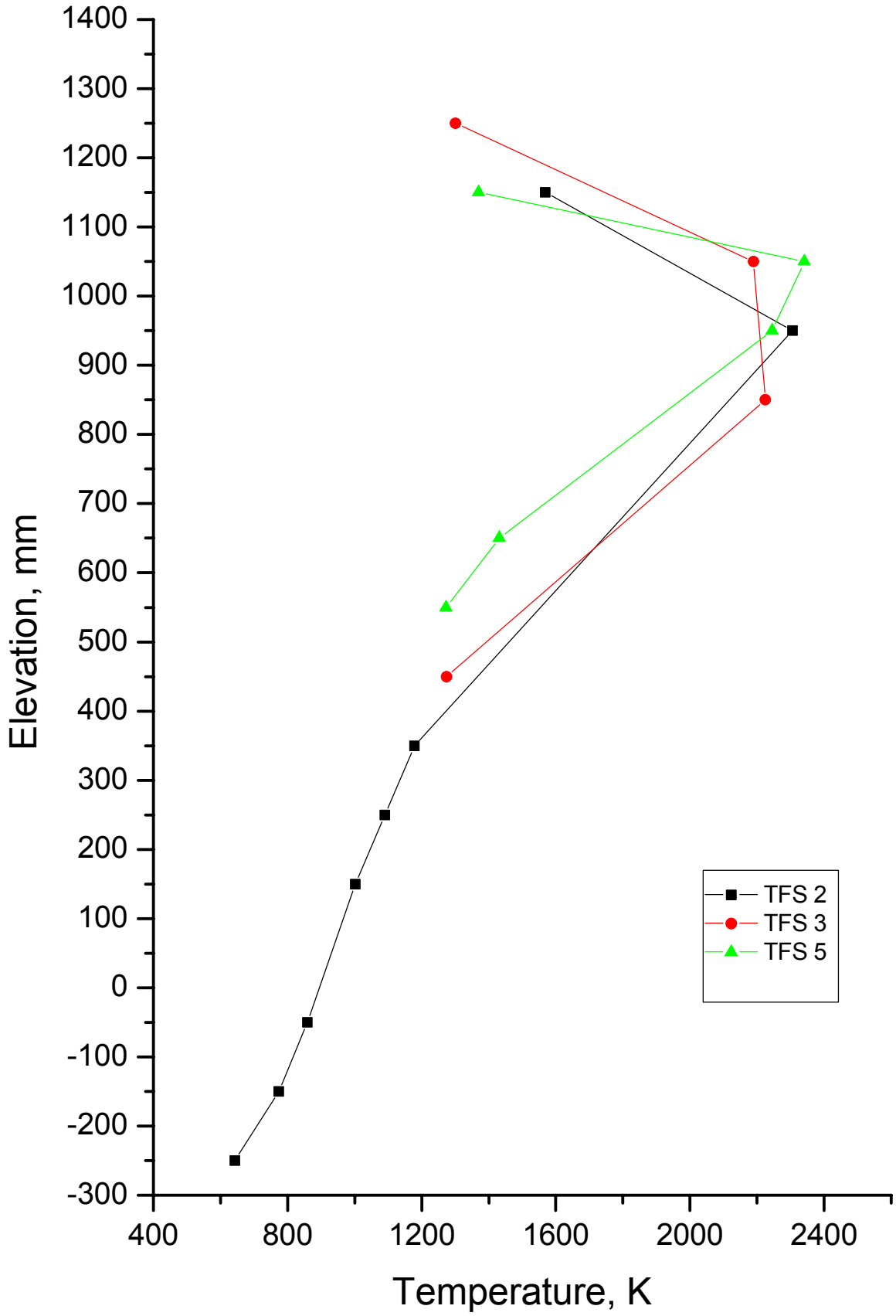

QUE02 Axial-Temp-Profil
dec 13,99 - IMF III

Fig 25

QUENCH-02

Axial Temperature Profile TFS 2, TFS 3, TFS 5
at 2275 s (Quenching phase)

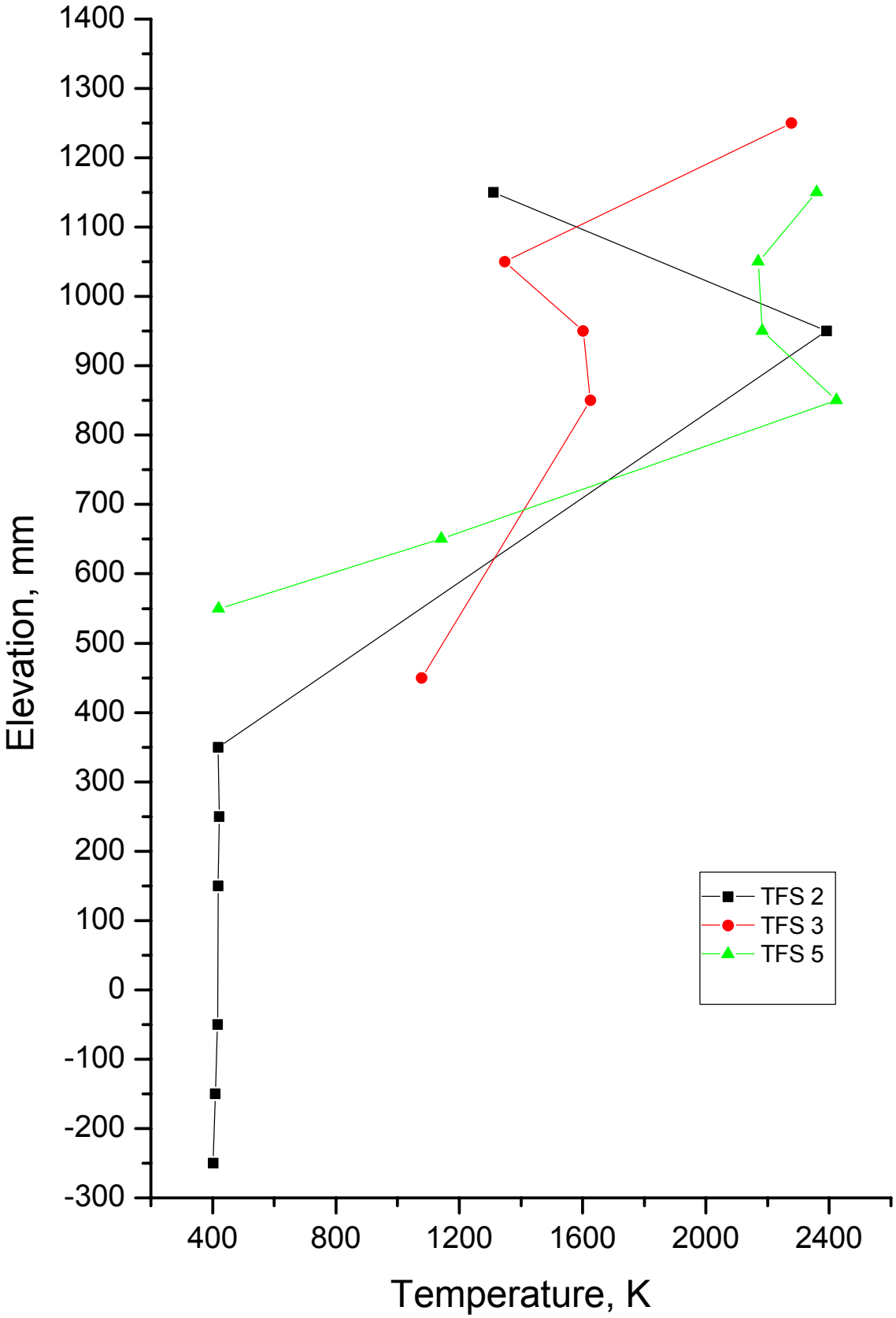

QUE02 Axial-Temp-Profil
dec 13,99 - IMF III

Fig 26

QUENCH-02

Hydrogen measurement by the mass spectrometer

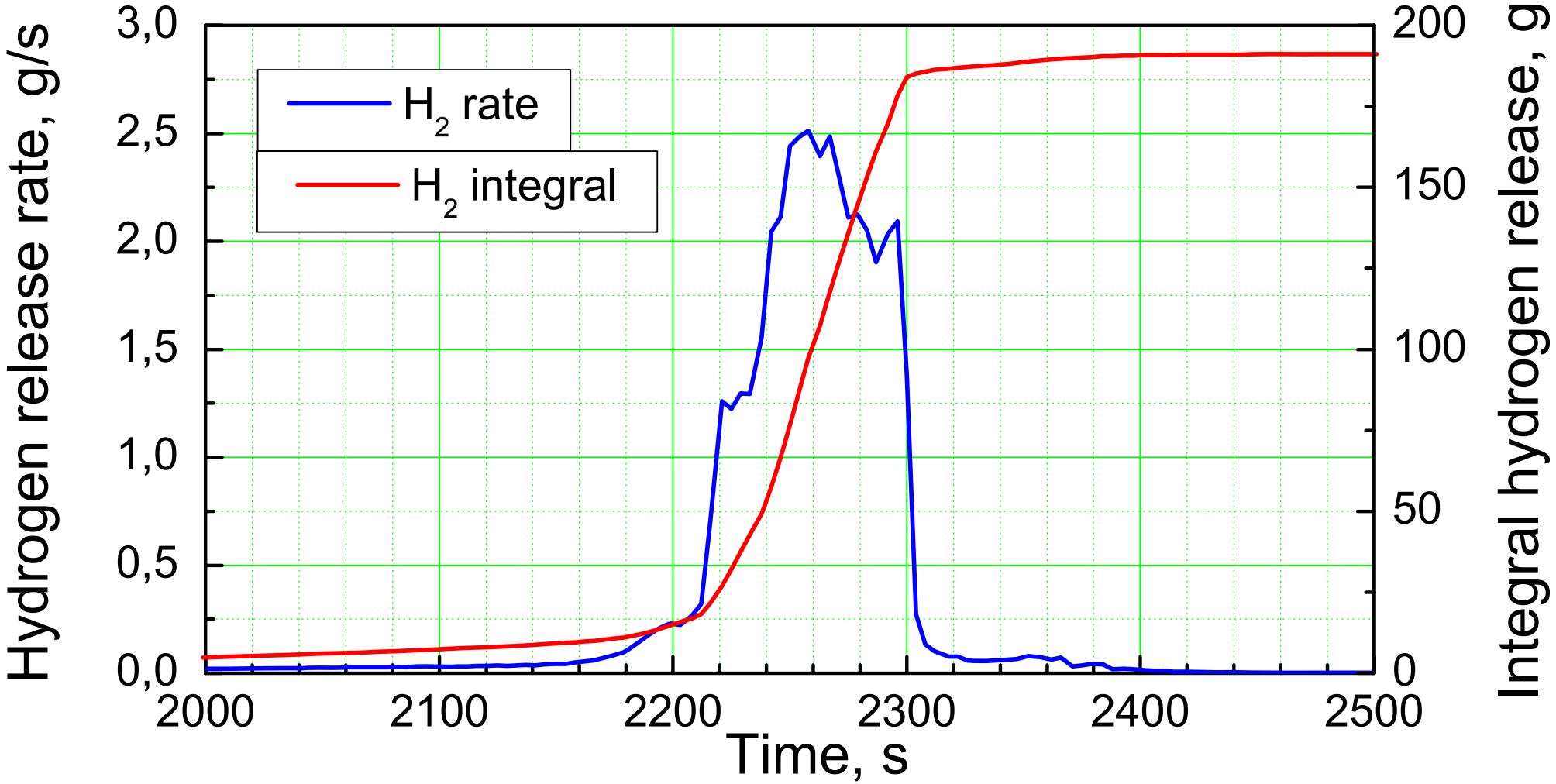

Fig 27

QUENCH-02

Influence of power input, rod temperature, and quench water injection on hydrogen generation

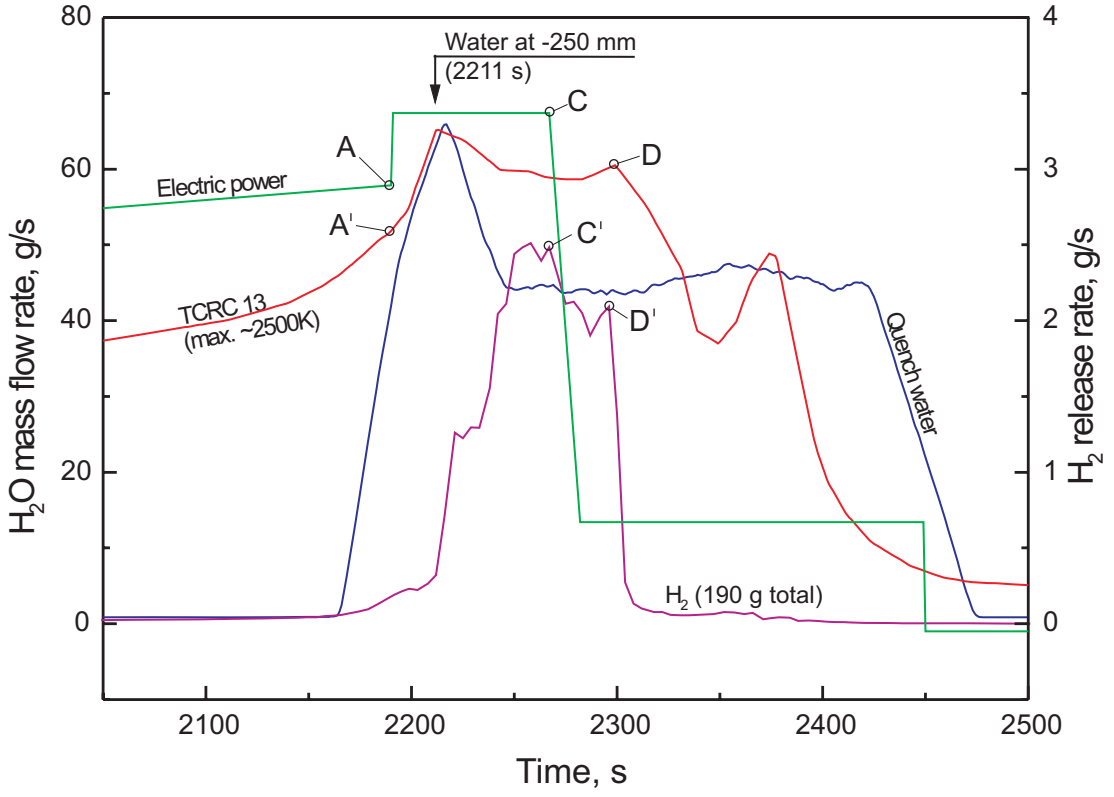

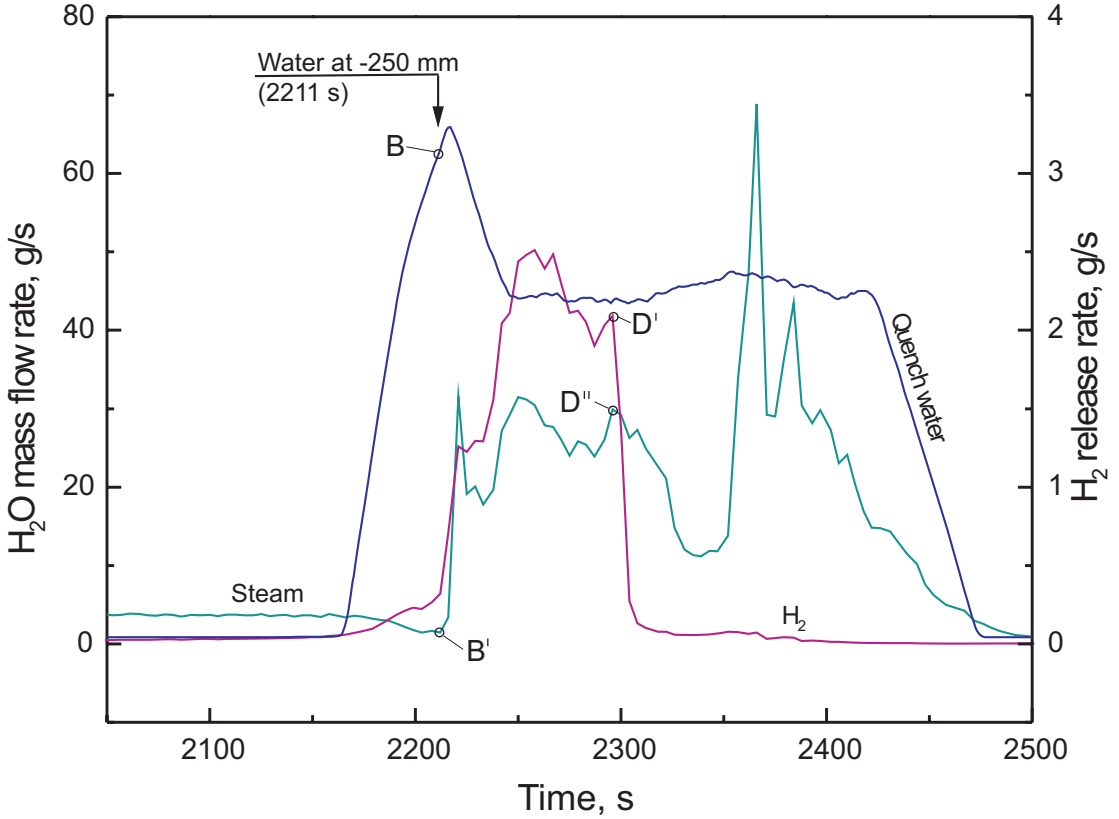

Fig 28

QUENCH-02; Posttest View 720 - 1350 mm (~225°)

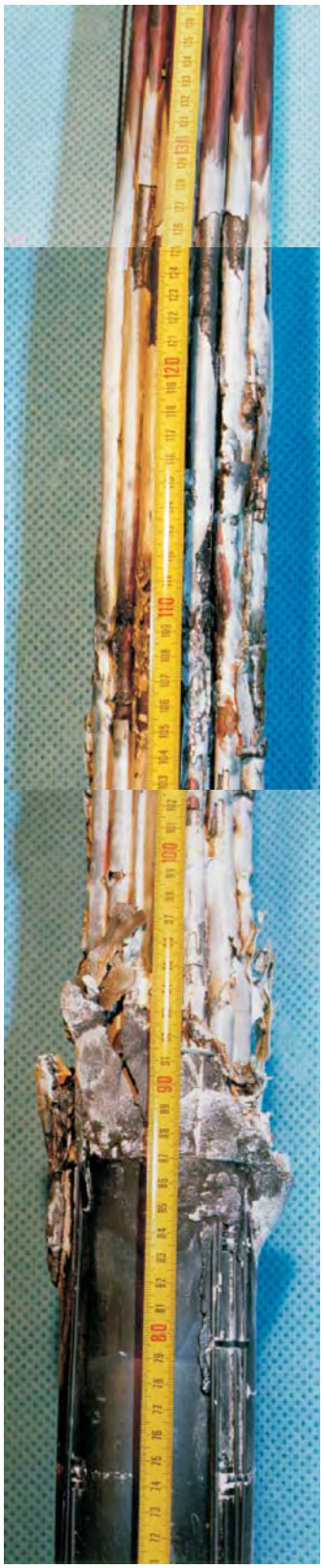

Fig 29

Post-test appearance of the bundle QUENCH-02

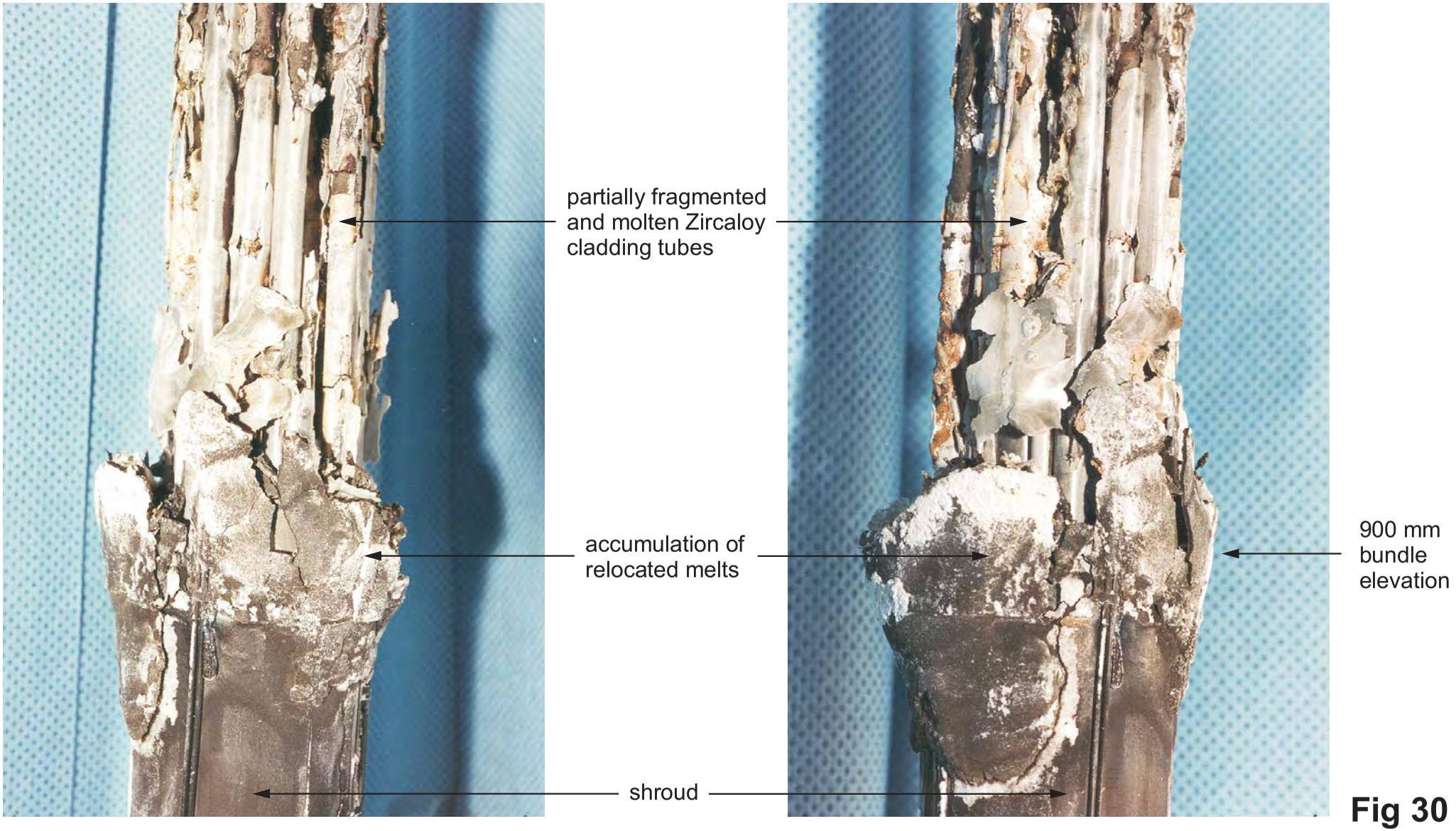

Fig 30

QUENCH-02; Posttest View of Shroud Upper End

Fig 31

Sectioning of Test Bundle QUENCH-02

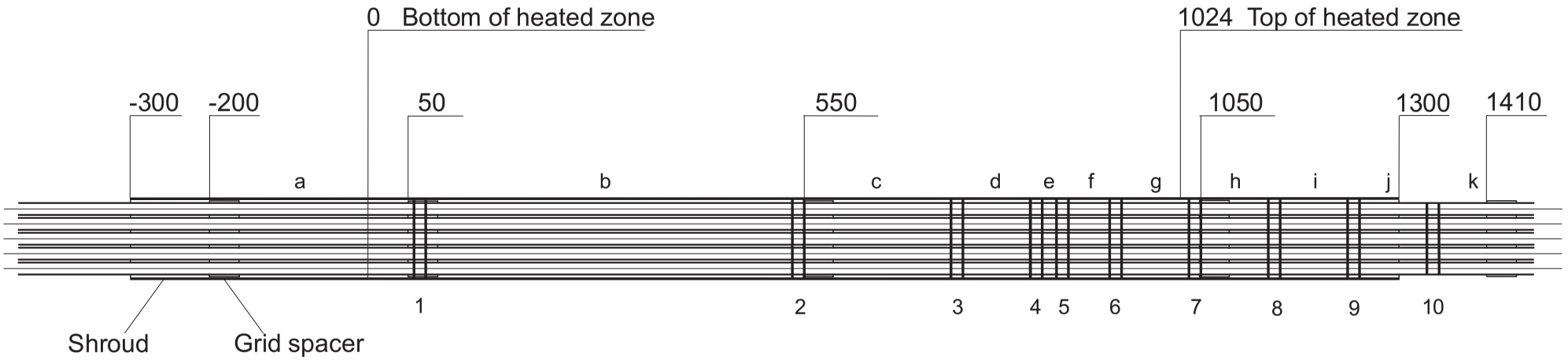

Fig. 32

QUE-02_cross-sections.CDR
August 11, 98_HIT

QUENCH-02, Cross Sections

(unpolished)

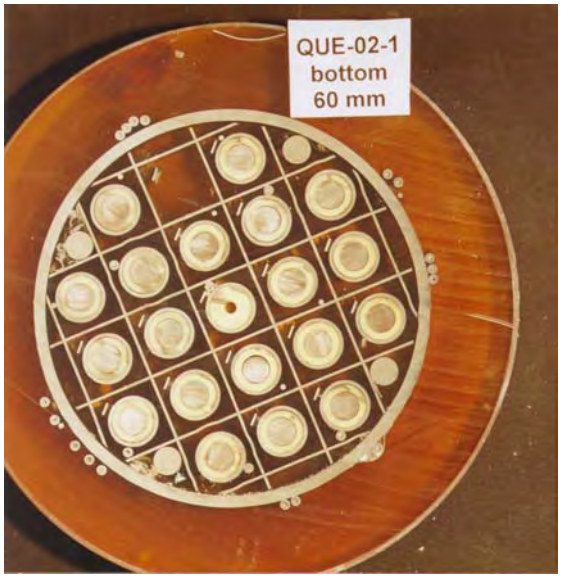

60 mm

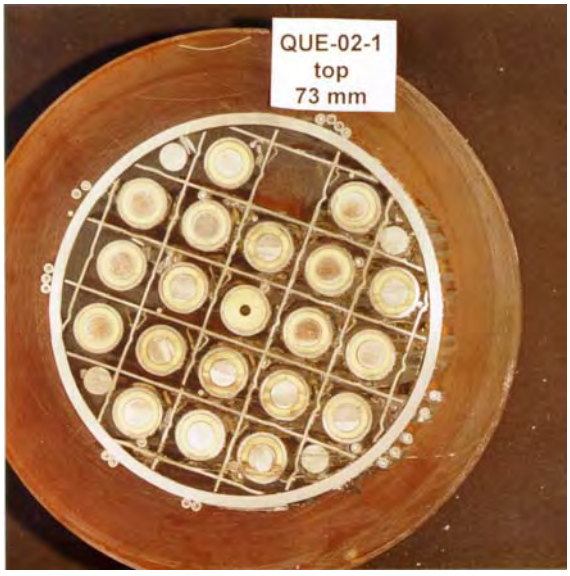

73 mm

537 mm

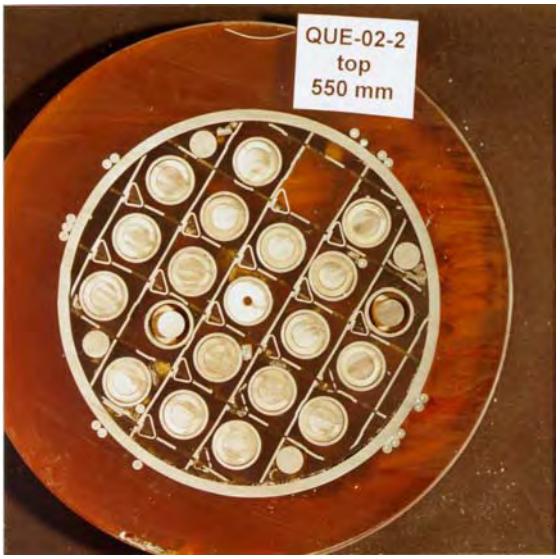

550 mm

Fig 33

QUENCH-02, Cross Sections

(unpolished)

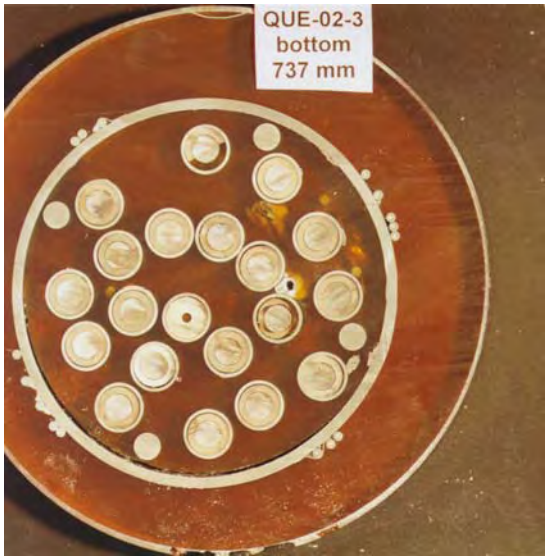

737 mm

750 mm

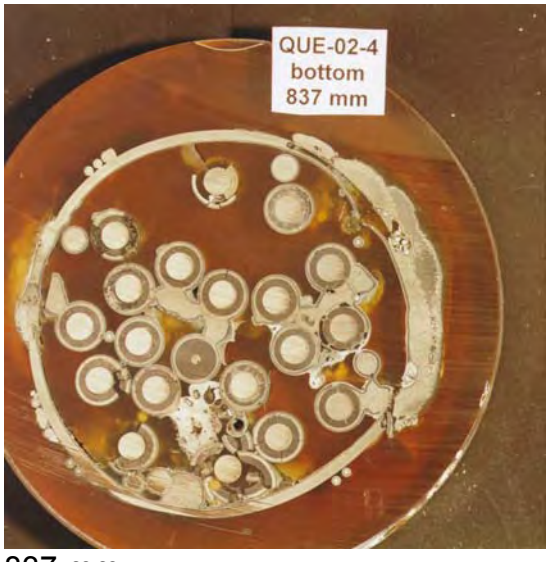

837 mm

850 mm

Fig 34

QUENCH-02, Cross Sections

(unpolished)

870 mm

883 mm

937 mm

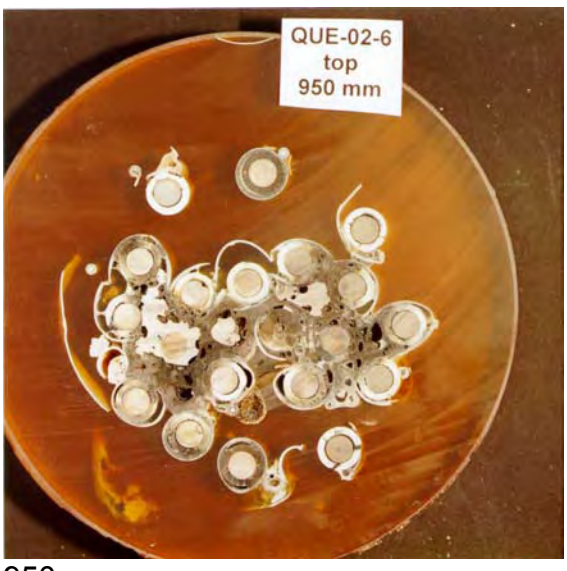

950 mm

Fig 35

QUENCH-02, Cross Sections

(unpolished)

1037 mm

1050 mm

1137 mm

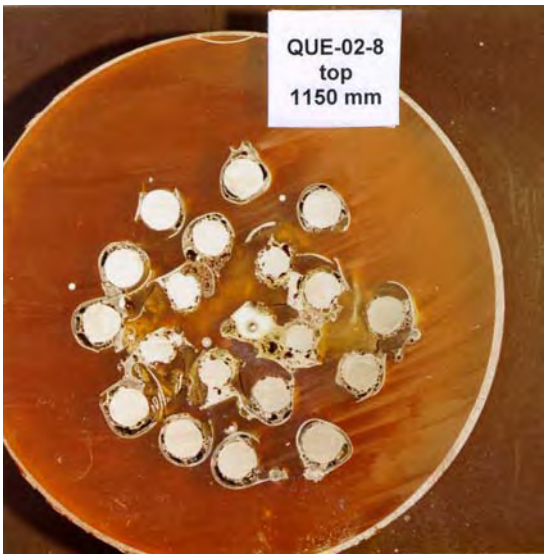

1150 mm

Fig 36

QUENCH-02, Cross Sections

(unpolished)

1237 mm

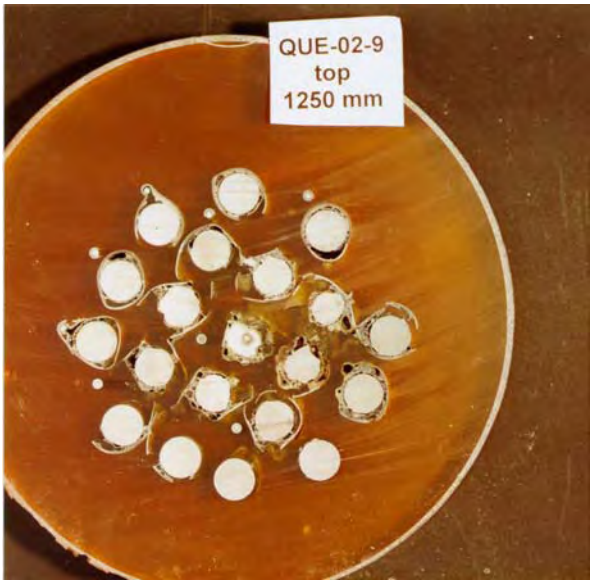

1250 mm

1337 mm

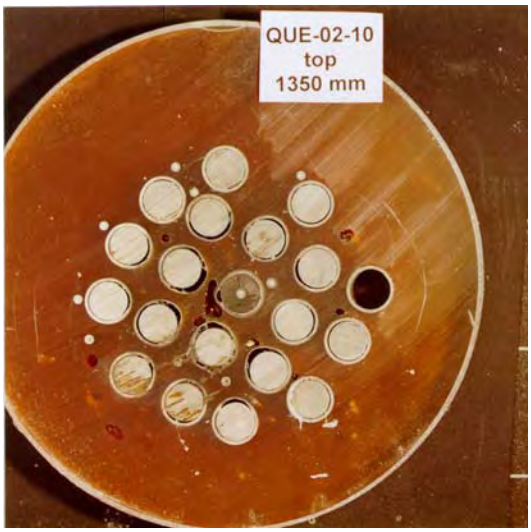

1350 mm

Fig 37

Physico-chemical behavior of the grid spacer and cladding tubes

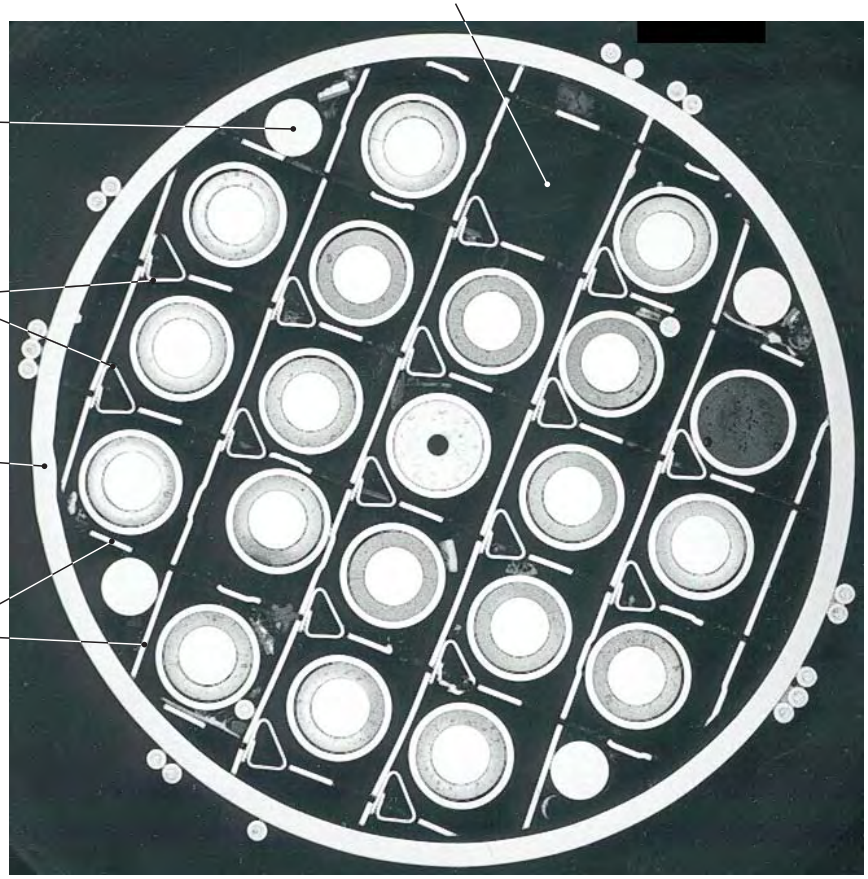

Total view of bundle cross section
at the Zircaloy grid spacer elevation

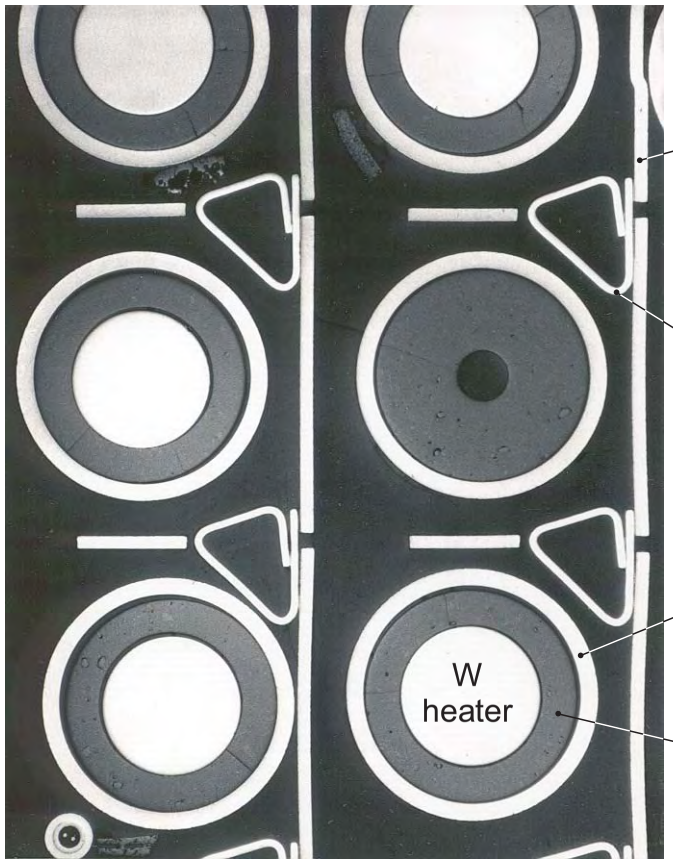

5 mm

Test QUENCH-02; bundle elevation 550 mm (QUE-02-2)

Fig 38

QUENCH-02: Oxidation of Zry-4 cladding tube at elevation 1350 mm

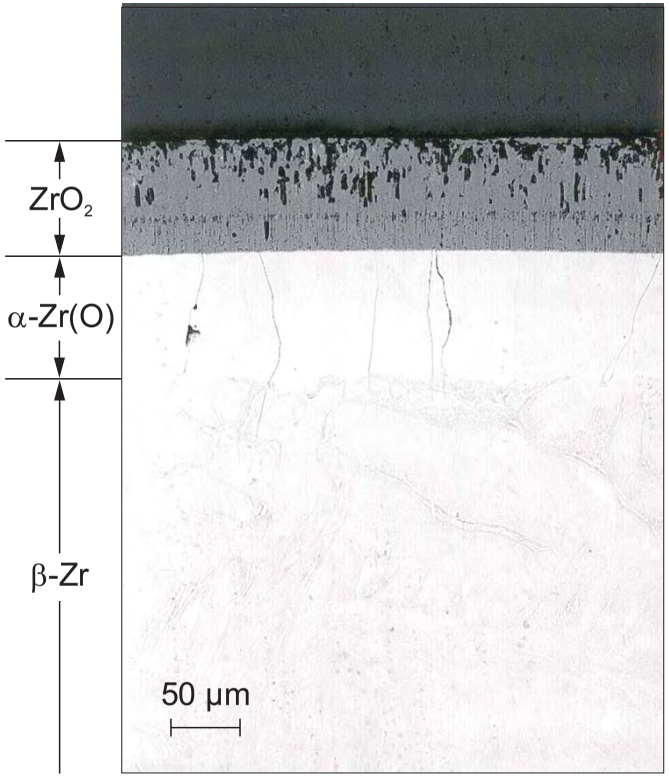

Thin oxide scale (85 µm) and cracks in the α-Zr(O) phase

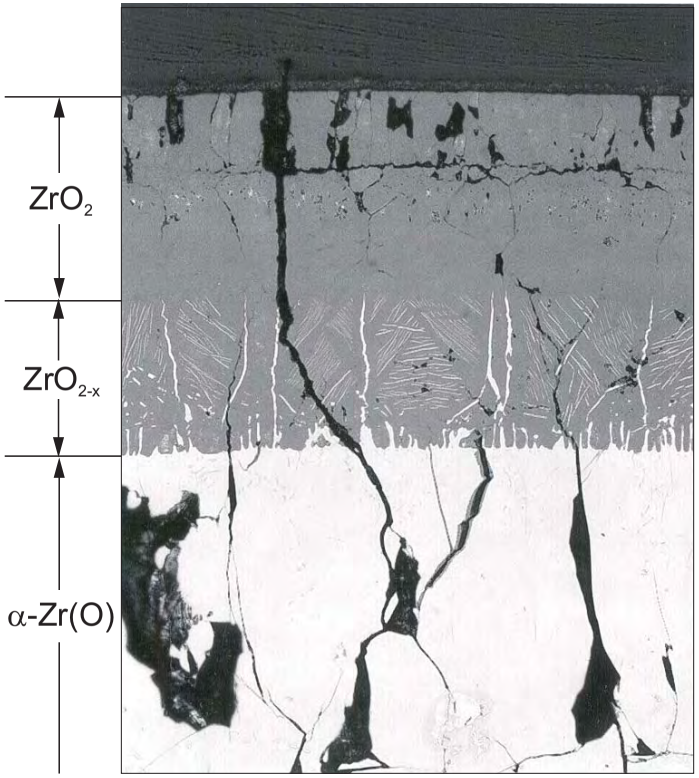

Thick oxide scale (250 µm) and through-wall cracks

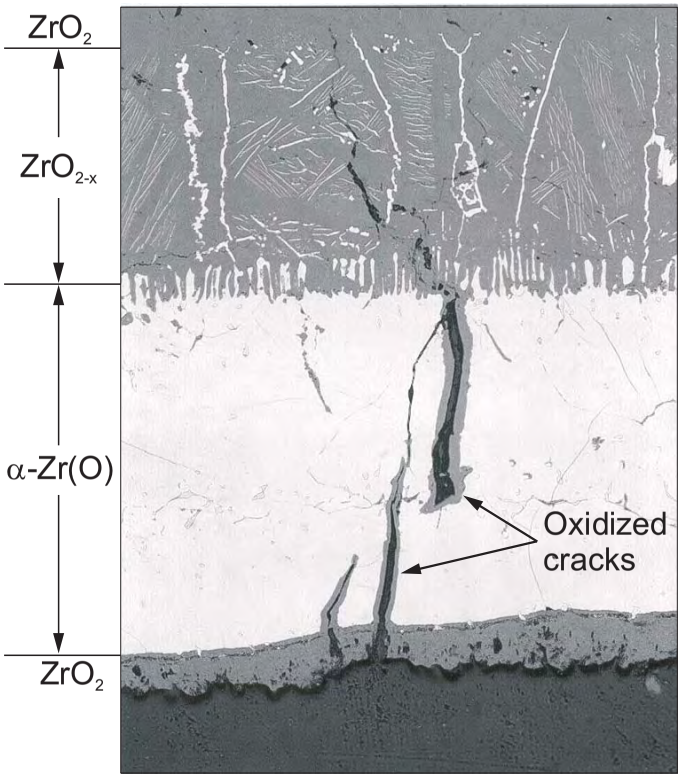

Oxidized crack surfaces in α-Zr(O) layer

Fig 39

QUENCH-02: Formation of substoichiometric oxide at high temperatures (> 1500 °C)

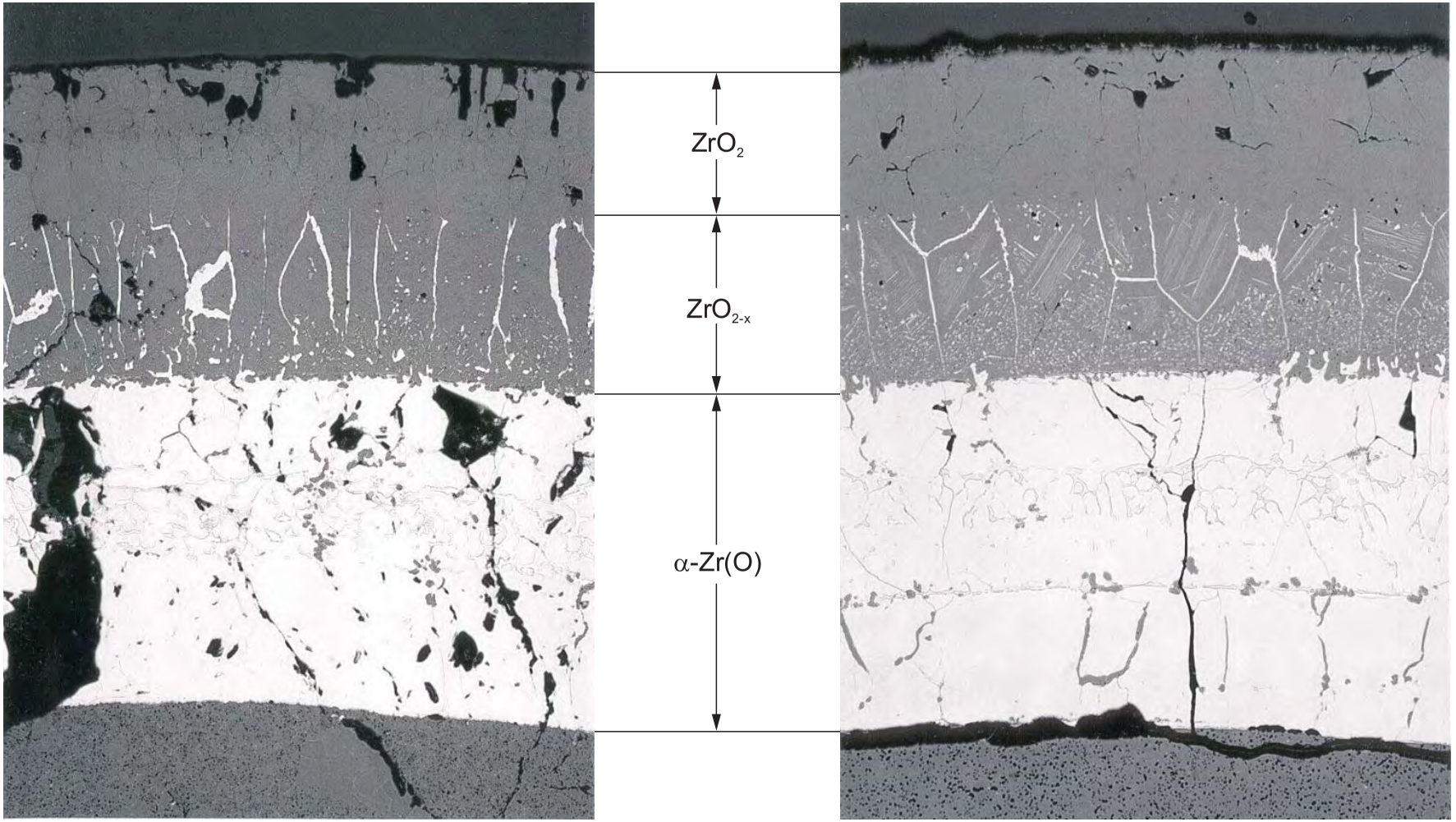

Axial bundle elevation 850 mm

Axial bundle elevation 1350 mm

Fig 40

QUENCH-02: Relocated melt at two axial bundle elevations

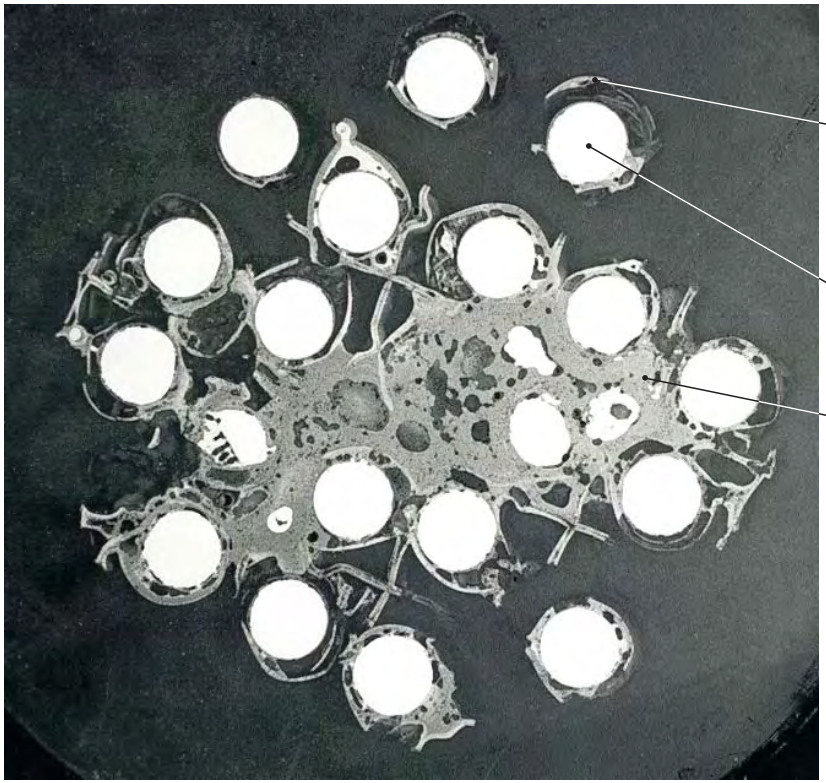

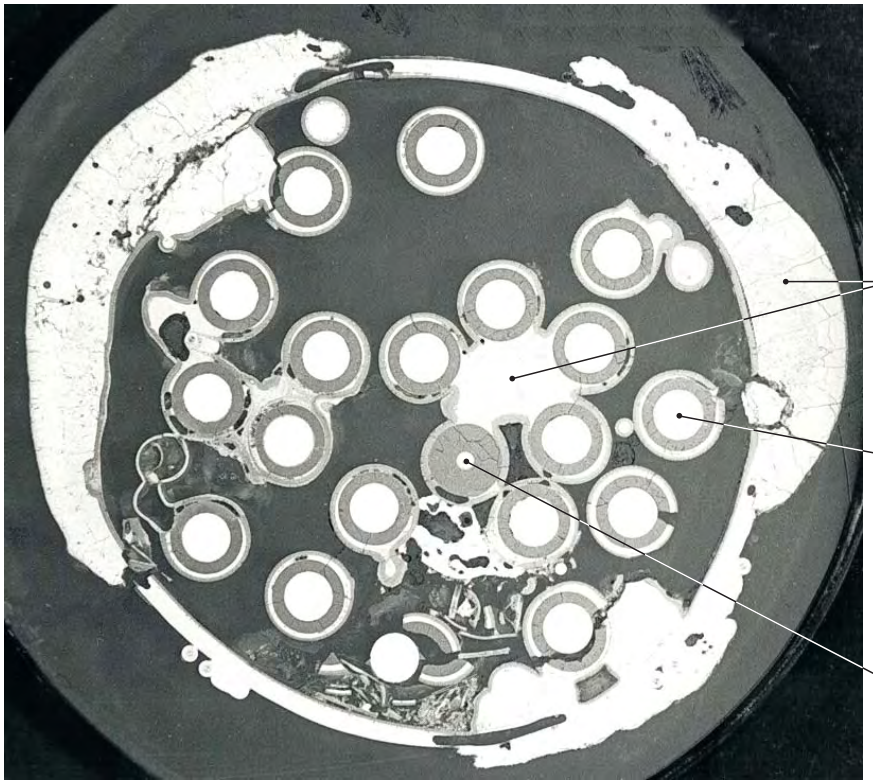

Fig 41

Almost completely oxidized melt at bundle elevation 1050 mm;
significant degradation of Mo electrodes

Metallic melt at axial bundle elevation 850 mm

QUENCH-02:
Dissolution of oxide scales by relocated Zr(O) melt

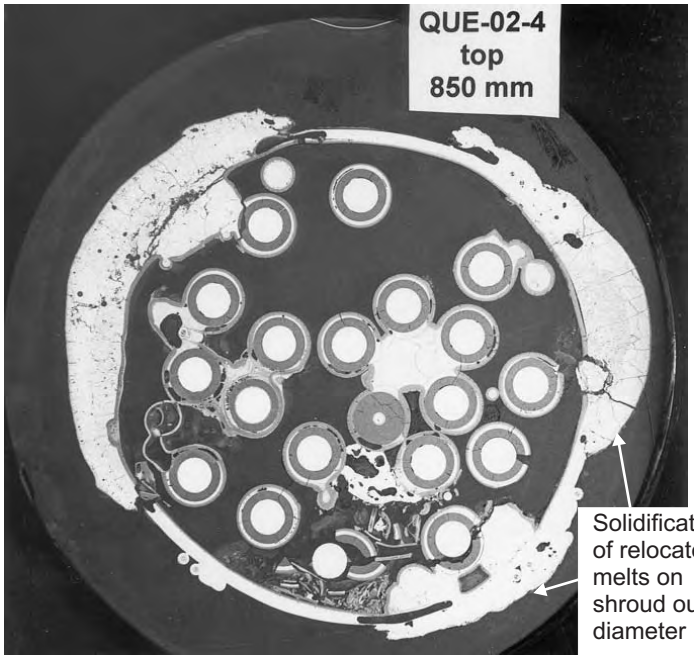

Cross section of the bundle at elevation 850 mm

Interaction of relocated melt with ZrO_2 shells

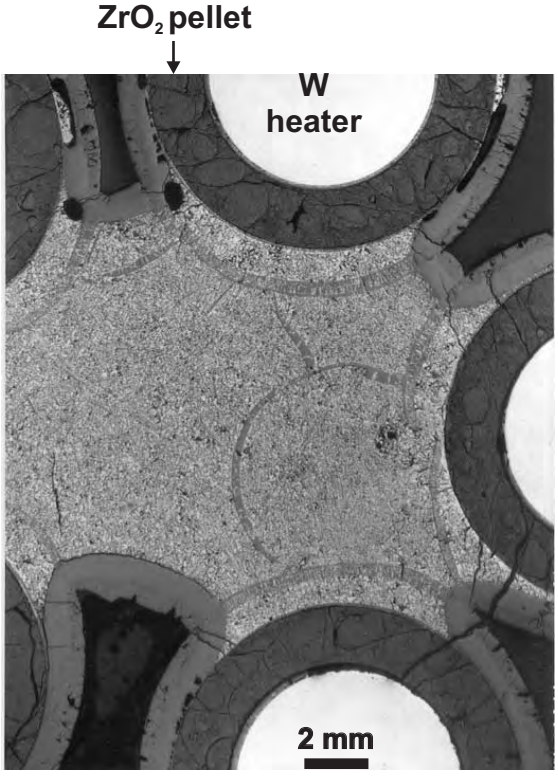

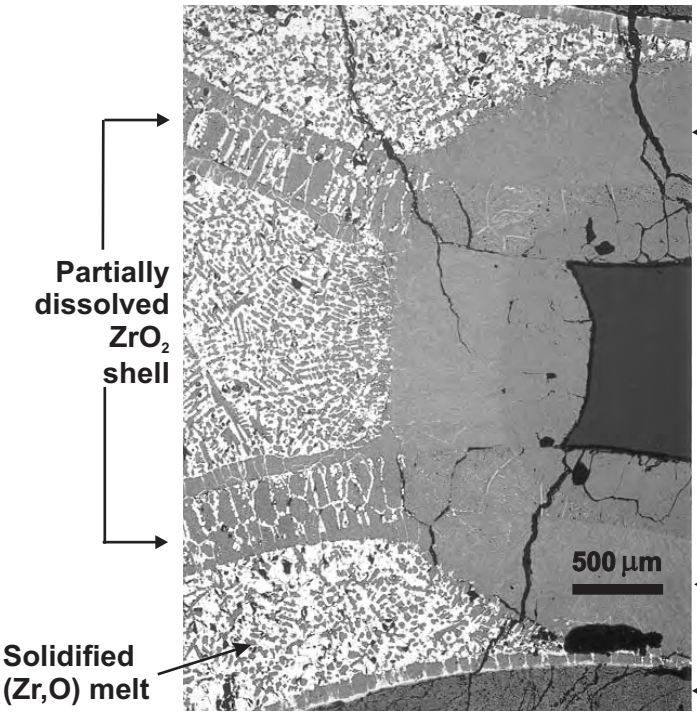

Oxide layer thicknesses at bundle elevation 73 mm

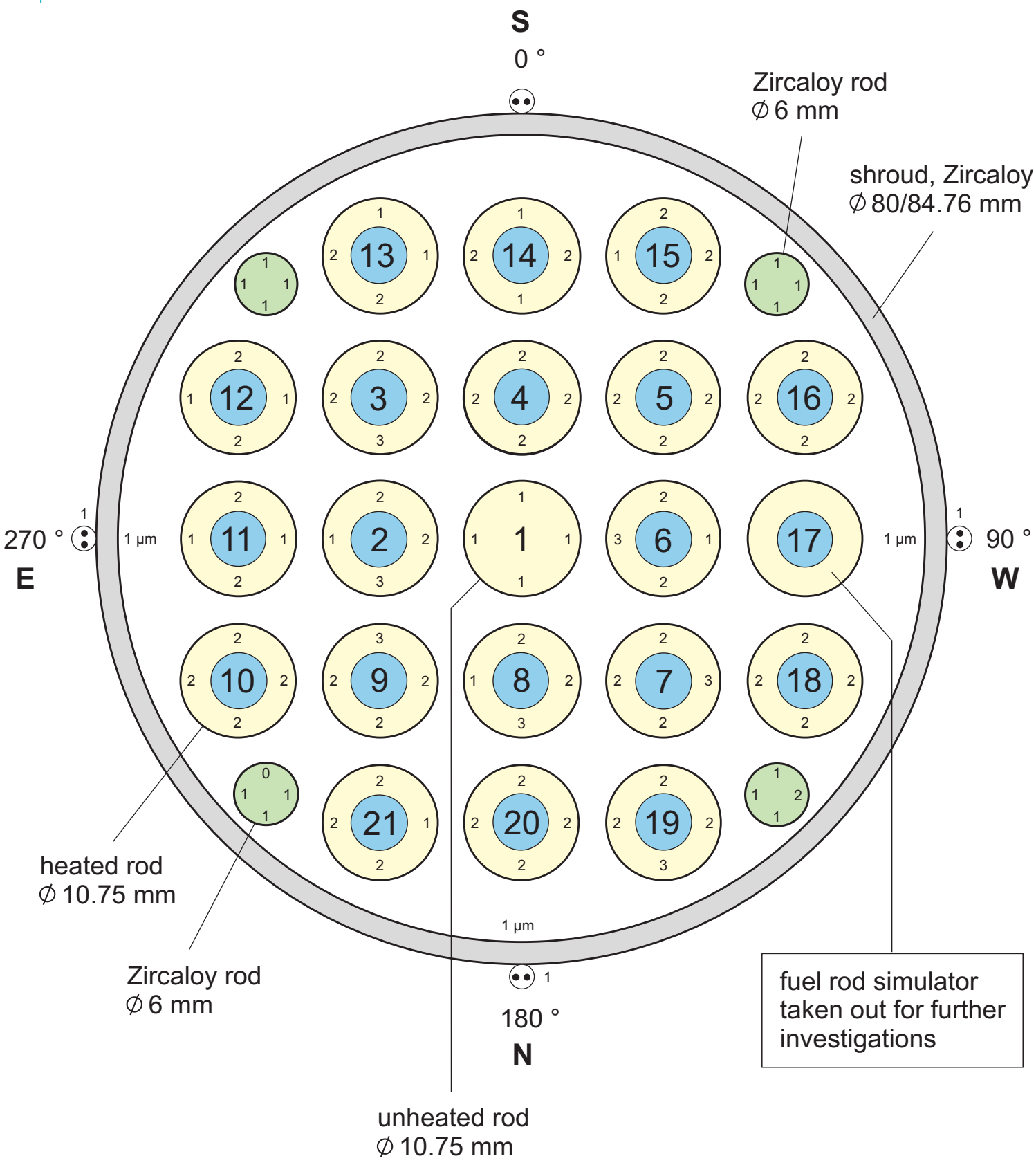

Test QUENCH-02; Cross section QUE-02-1 **Fig 43**

Oxide layer thicknesses at bundle elevation 550 mm

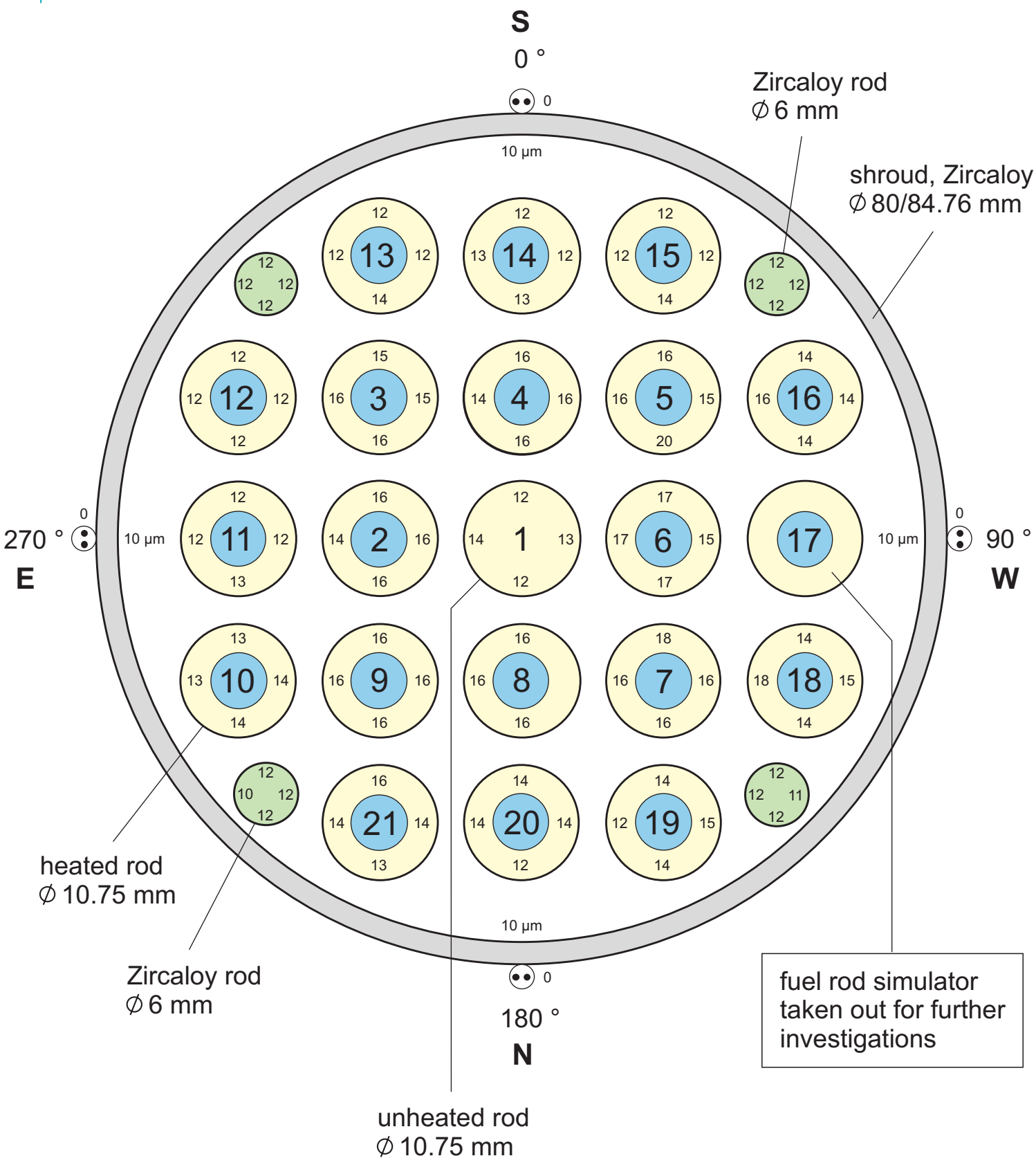

Test QUENCH-02; Cross section QUE-02-2 **Fig 44**

Oxide layer thicknesses at bundle elevation 750 mm

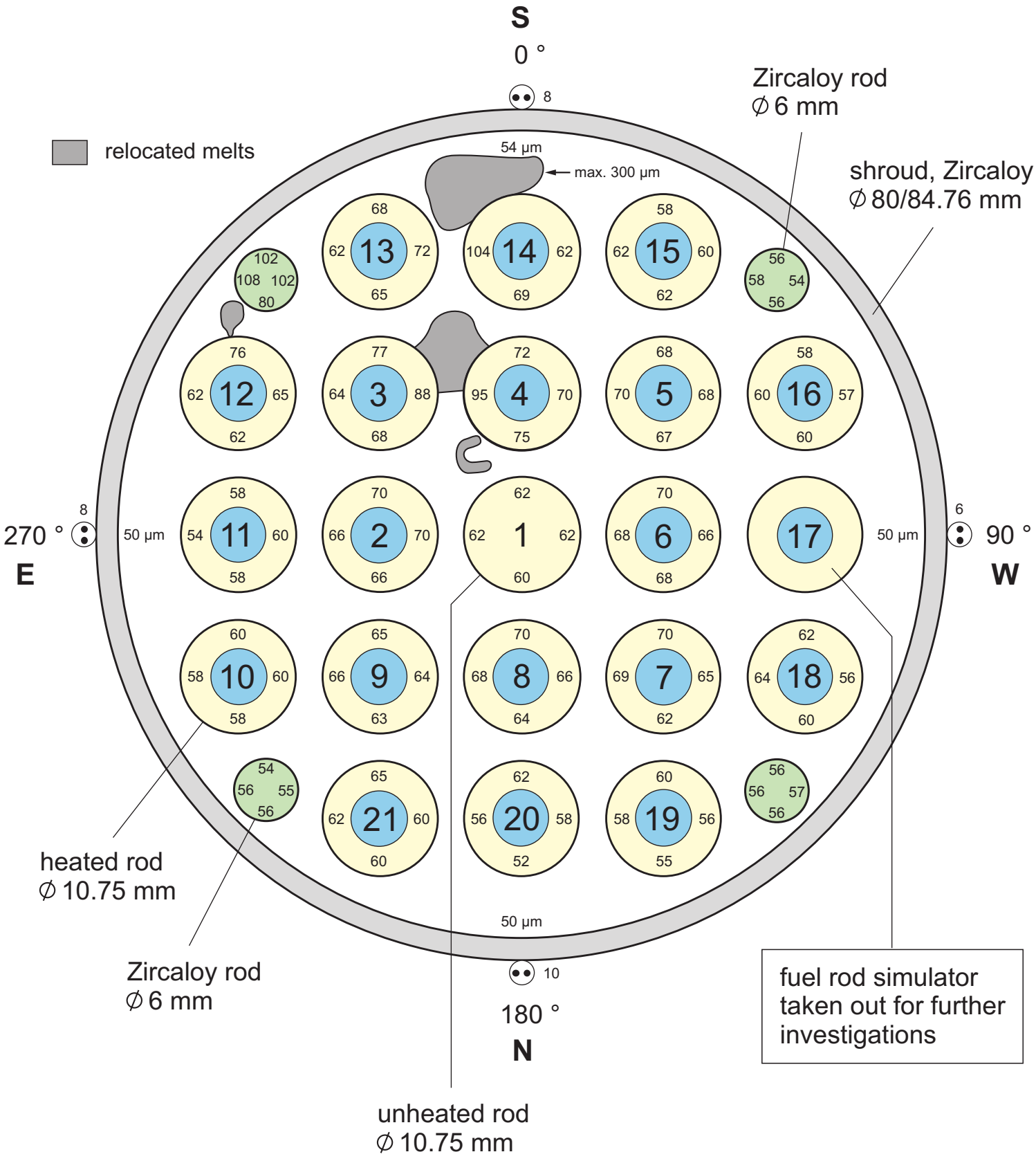

Test QUENCH-02; Cross section QUE-02-3 **Fig 45**

Oxide layer thicknesses at bundle elevation 850 mm

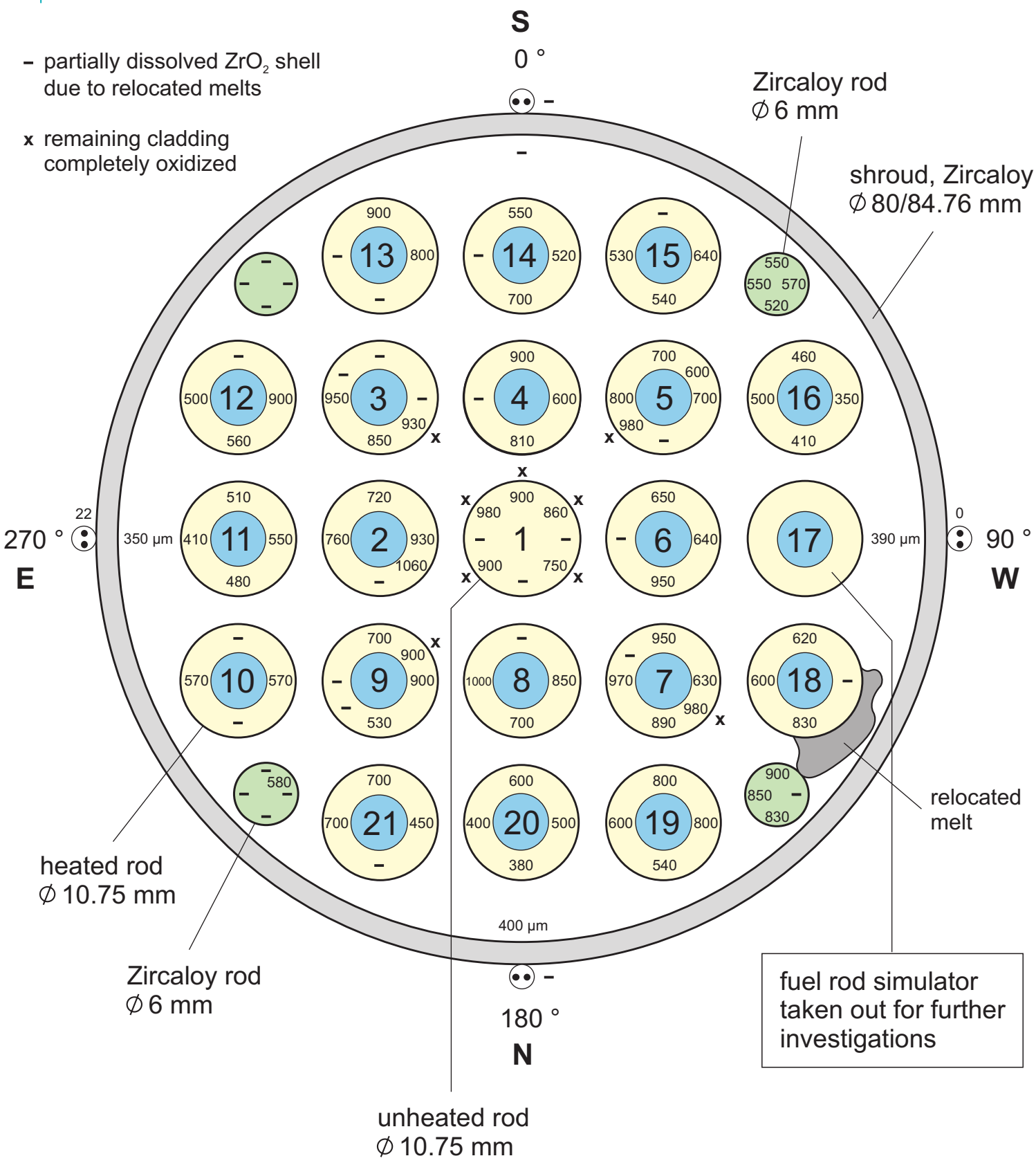

Test QUENCH-02; Cross section QUE-02-4 **Fig 46**

Oxide layer thicknesses at bundle elevation 868 mm

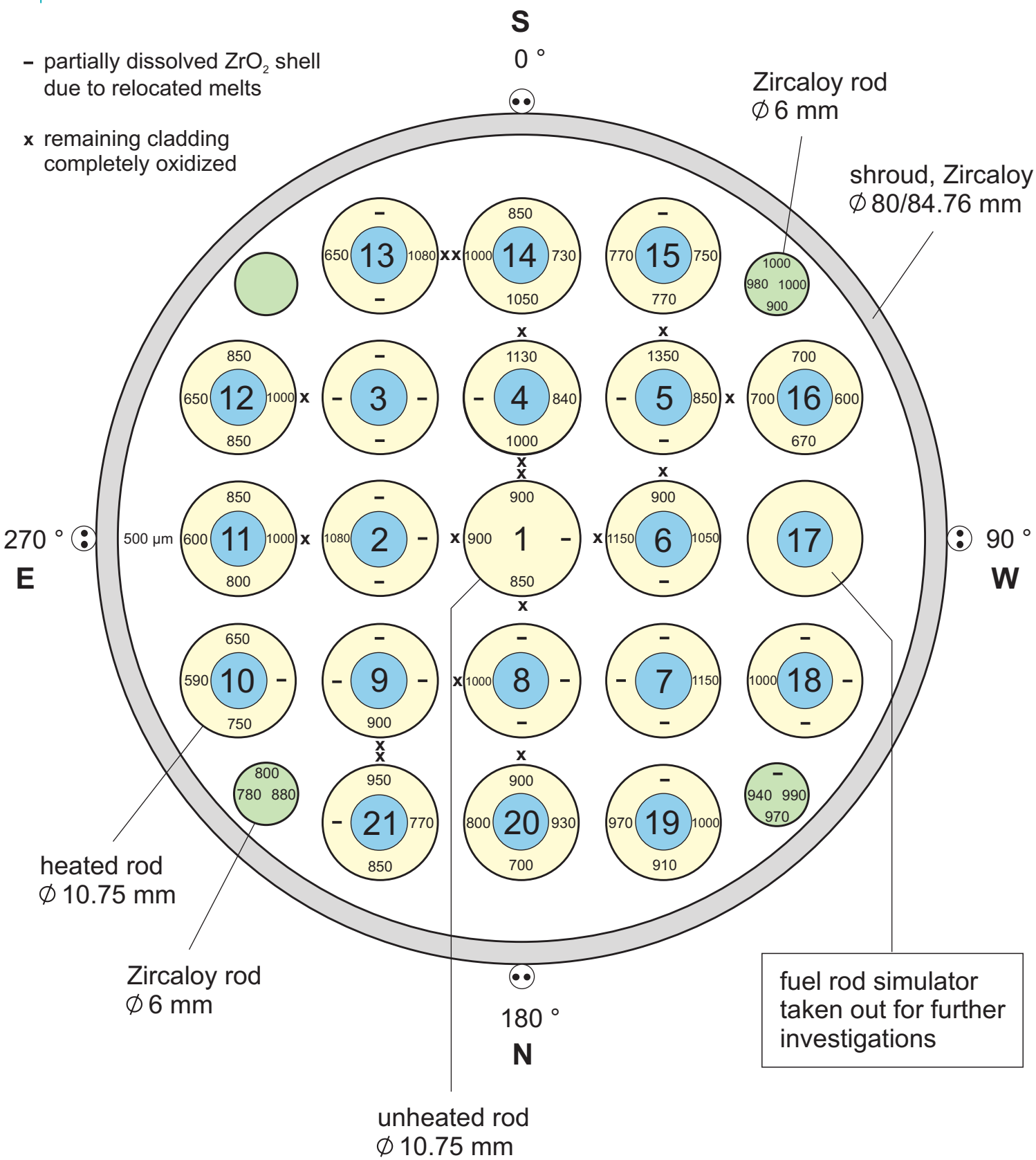

Test QUENCH-02; Cross section QUE-02-e **Fig 47**

Oxide layer thicknesses at bundle elevation 883 mm

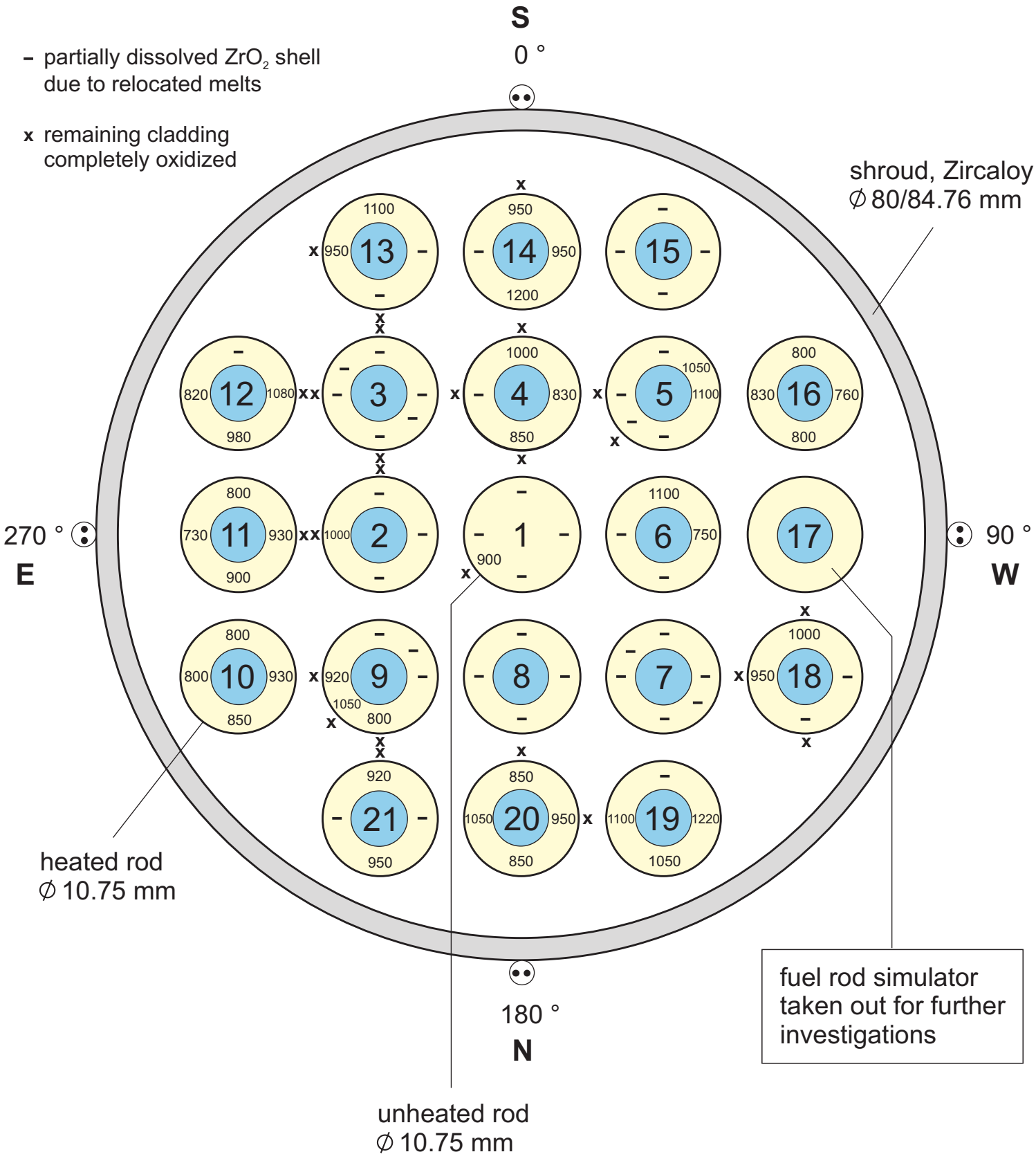

Test QUENCH-02; Cross section QUE-02-5 **Fig 48**

Oxide layer thicknesses at bundle elevation 950 mm

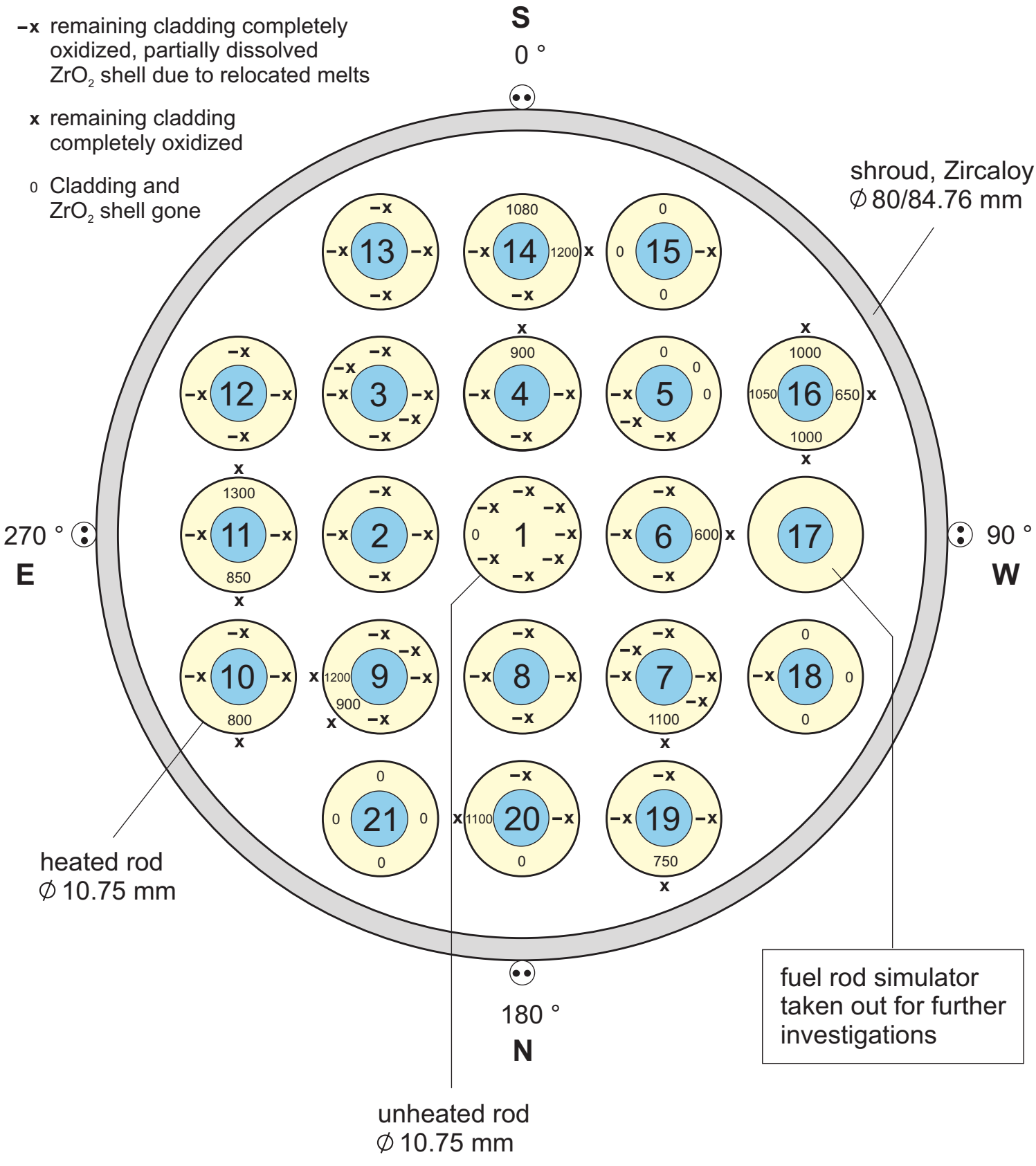

Test QUENCH-02; Cross section QUE-02-6 **Fig 49**

Oxide layer thicknesses at bundle elevation 1050 mm

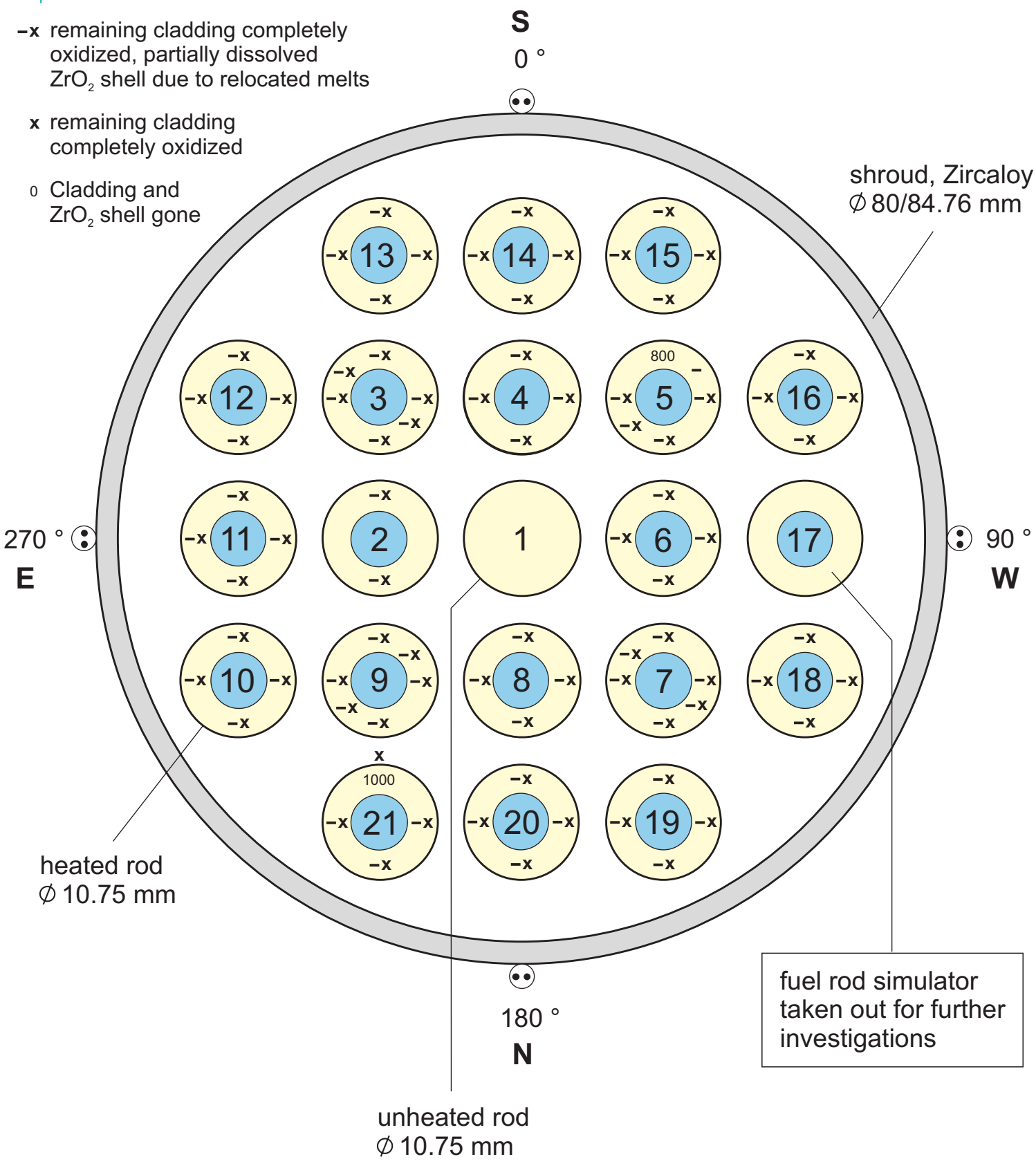

Test QUENCH-02; Cross section QUE-02-7 **Fig 50**

Oxide layer thicknesses at bundle elevation 1150 mm

–x remaining cladding completely oxidized, partially dissolved ZrO_2 shell due to relocated melts

x remaining cladding completely oxidized

0 Cladding and ZrO_2 shell gone

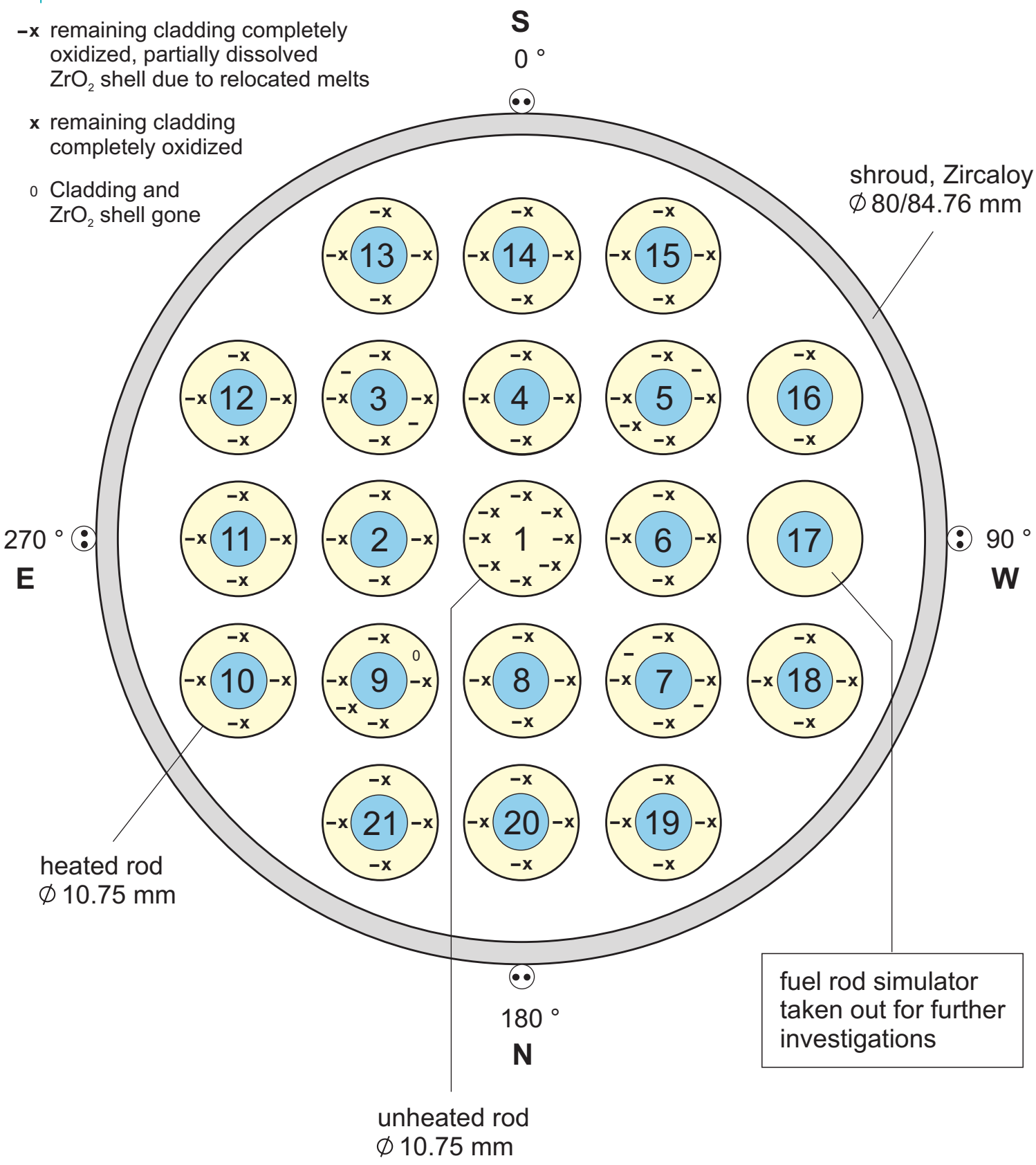

Test QUENCH-02; Cross section QUE-02-8 **Fig 51**

Oxide layer thicknesses at bundle elevation 1350 mm

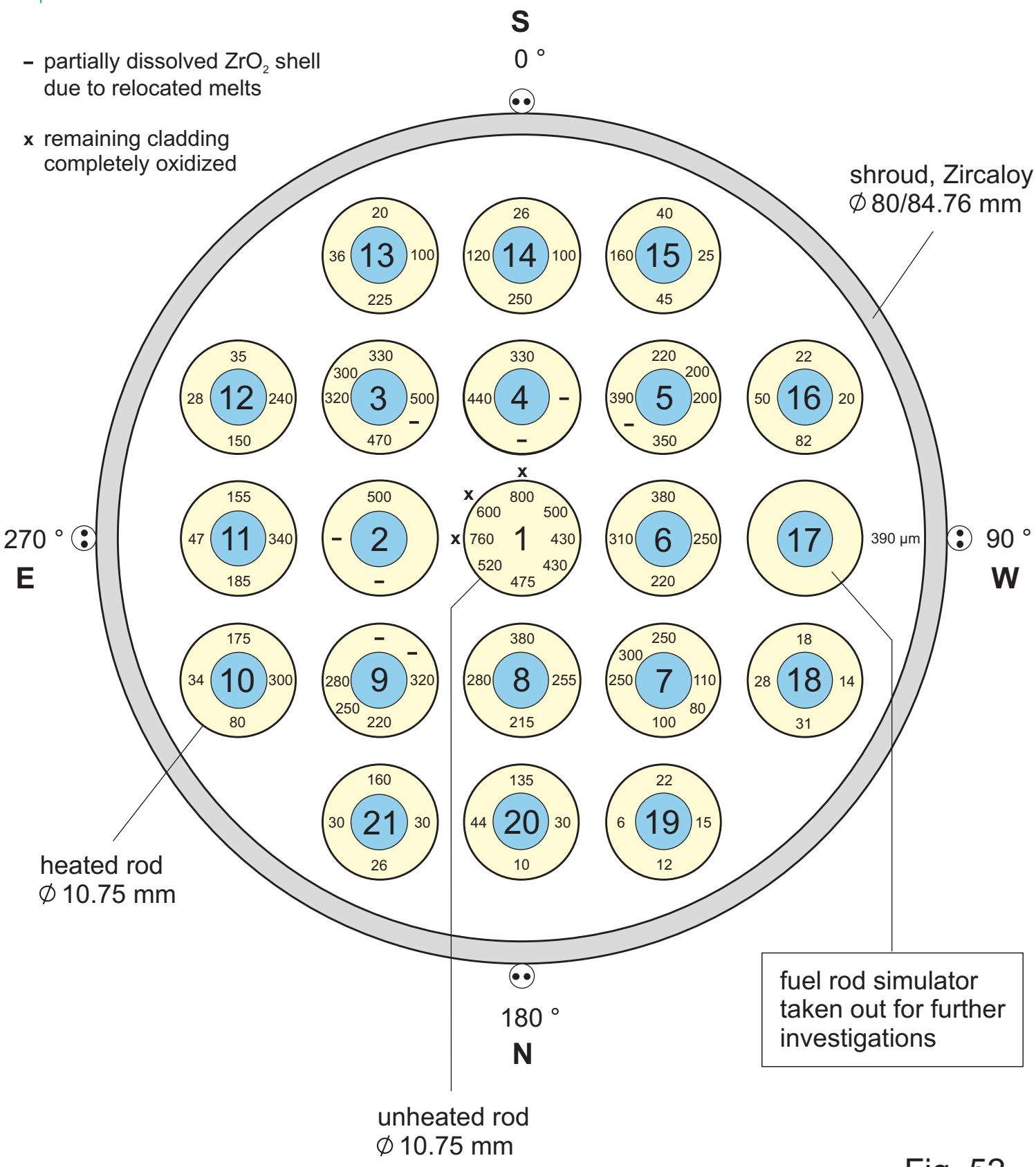

Fig. 52

Test QUENCH-02; Cross section QUE-02-10

QUENCH-02: **Axial oxide scale thickness distribution of heated and unheated fuel rod simulators, corner rods and shroud inner surface**

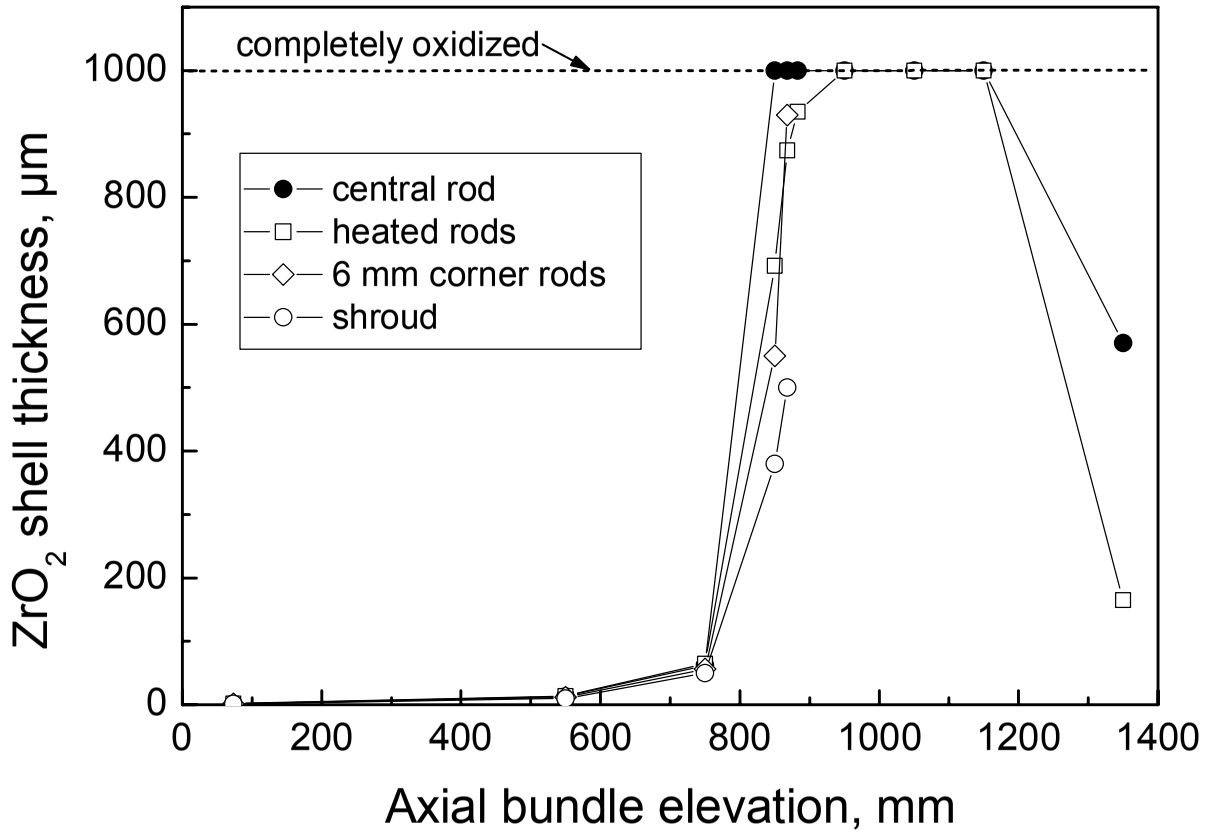

Fig. 53

QUENCH-02: Axial oxide layer thickness distribution

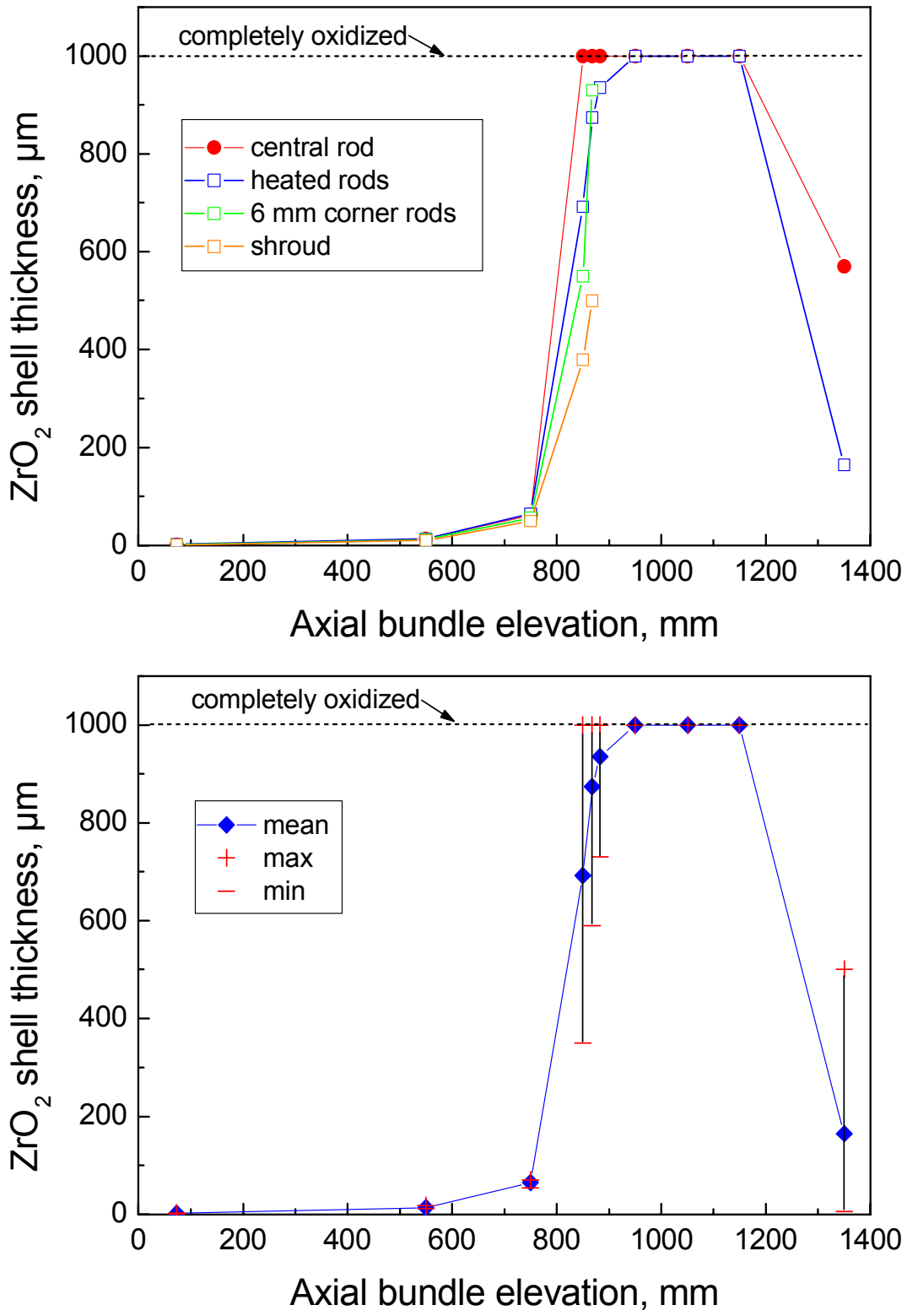

Fig. 54

Figures to Experiment QUENCH-03

QUENCH-02: Oxidation and partial melting of cladding tubes at axial bundle elevation 1350 mm

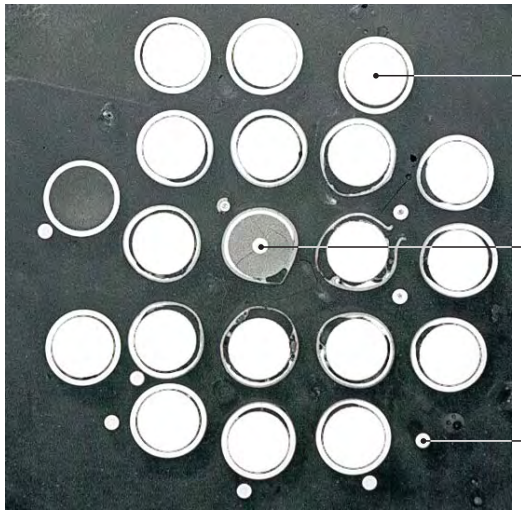

Heated rod with Mo-electrode

Central, unheated rod with ZrO_2 pellet and HT thermocouple

High temperature thermocouple

Cross section at elevation 1350 mm

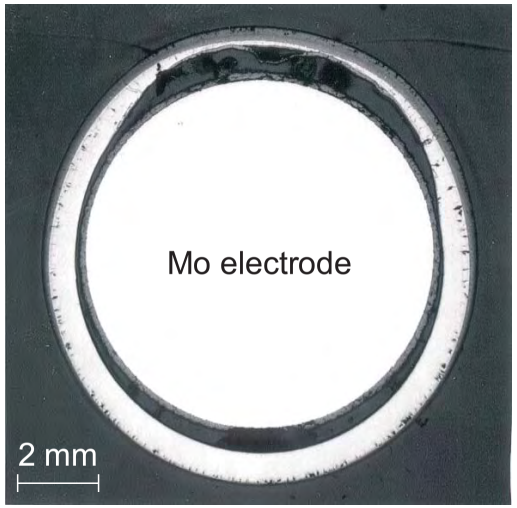

Pronounced circumferencial gradient in oxide scale thickness

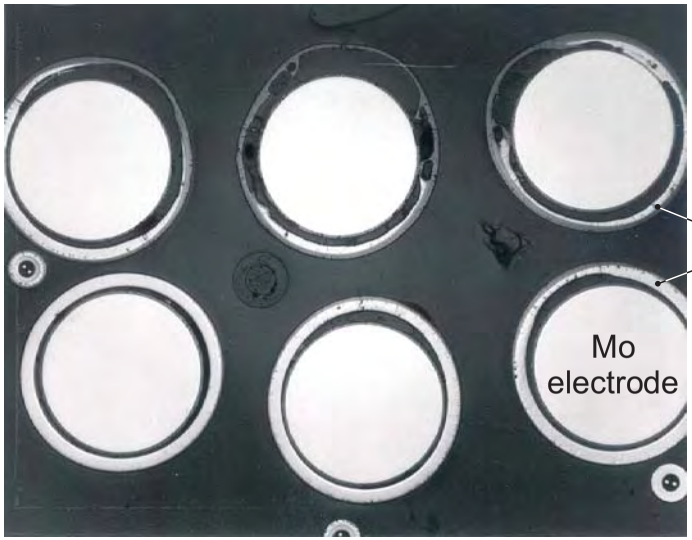

Partially oxidized Zry-4 cladding

Thinning of Zry clad by melt relocation

Melting and relocation of Zry-4 cladding

Fig 55

QUENCH-02

Axial ZrO_2 layer profile of cladding tube of rod # 17 and axial profile of the maximum temperature

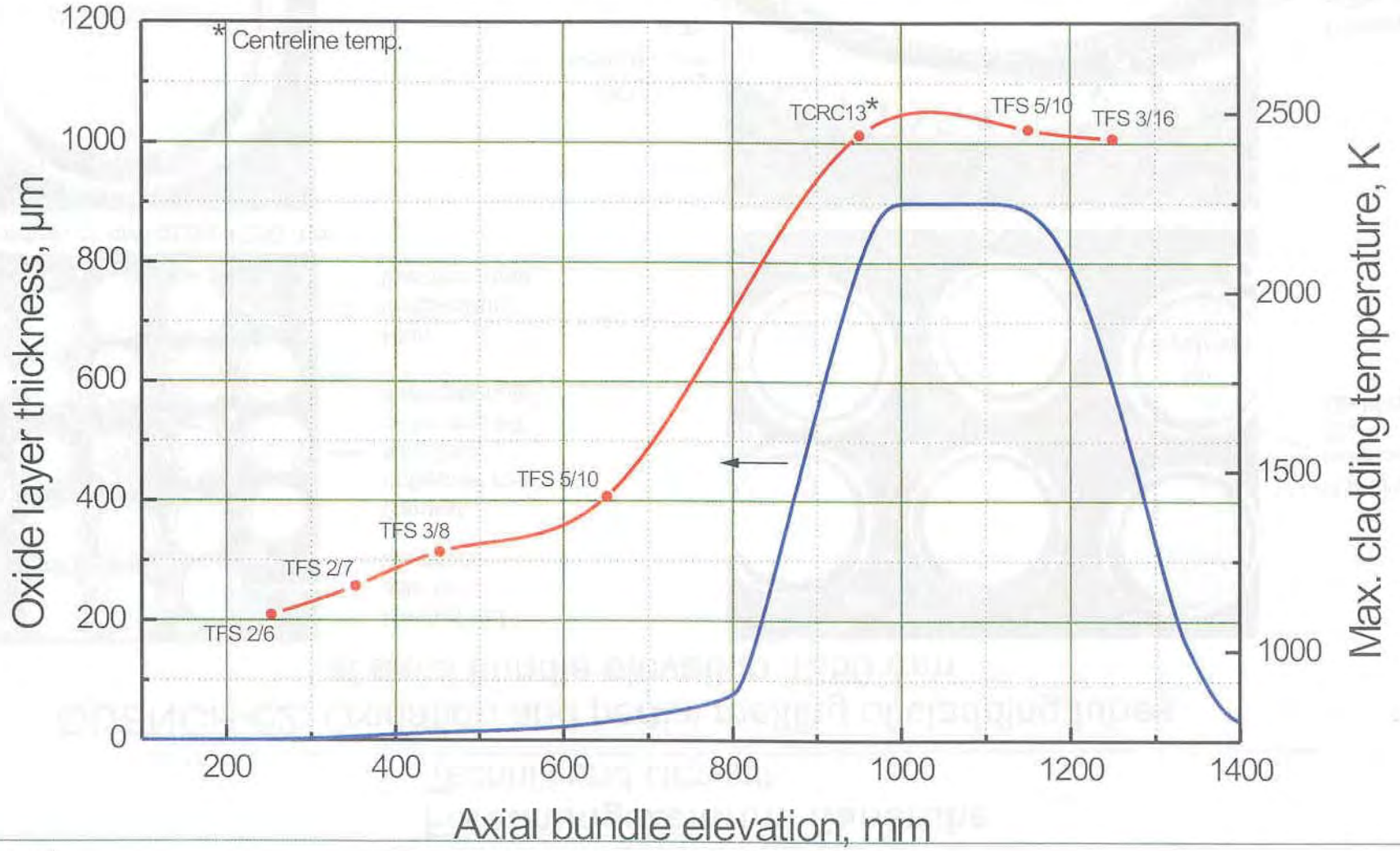

Fig. 56

Test QUENCH-02:
Absorbed hydrogen in the remaining Zry-4 metal
of cladding, shroud and corner rod and oxide layer

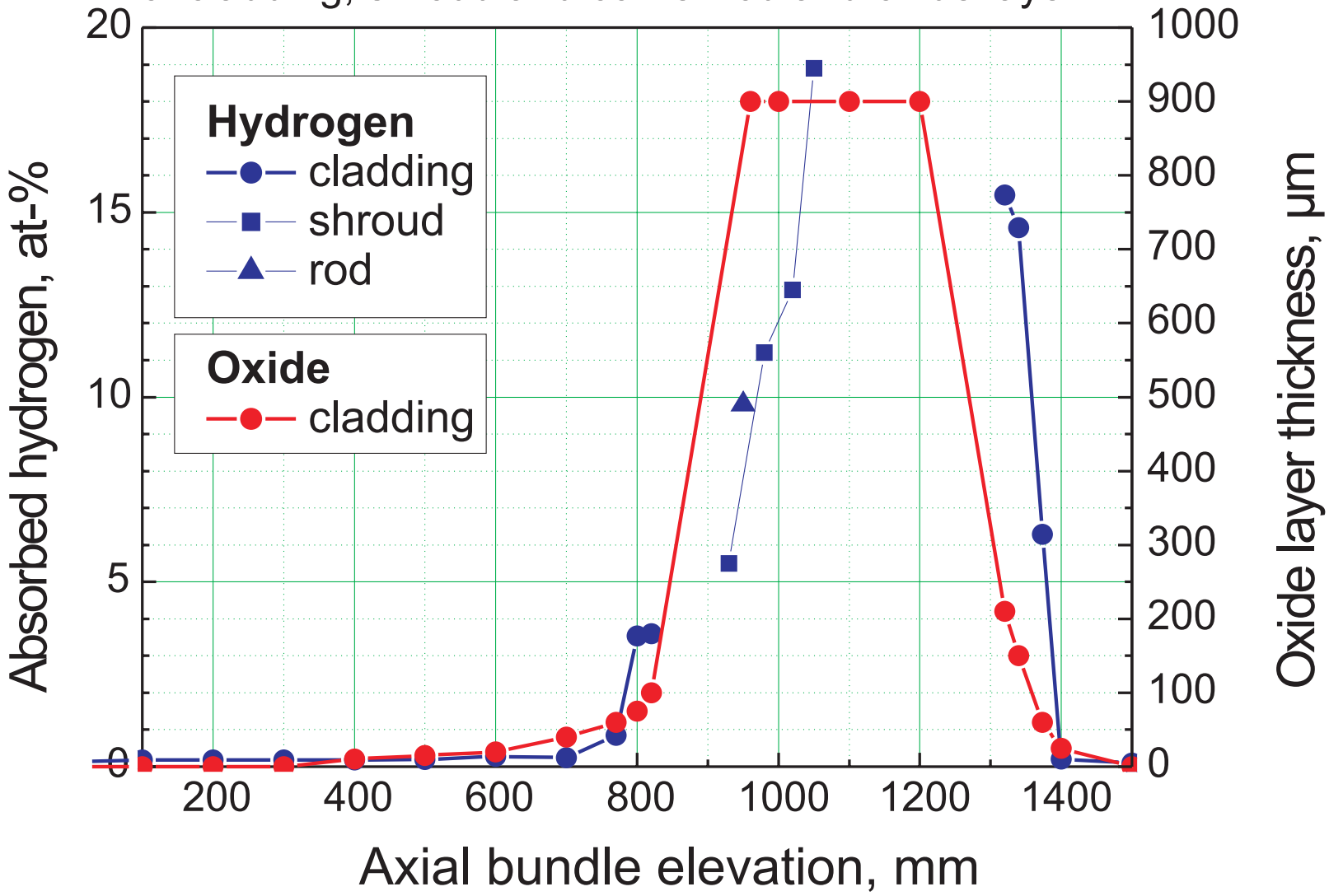

Fig 57

Test Conduct QUENCH-O3 (schematic)

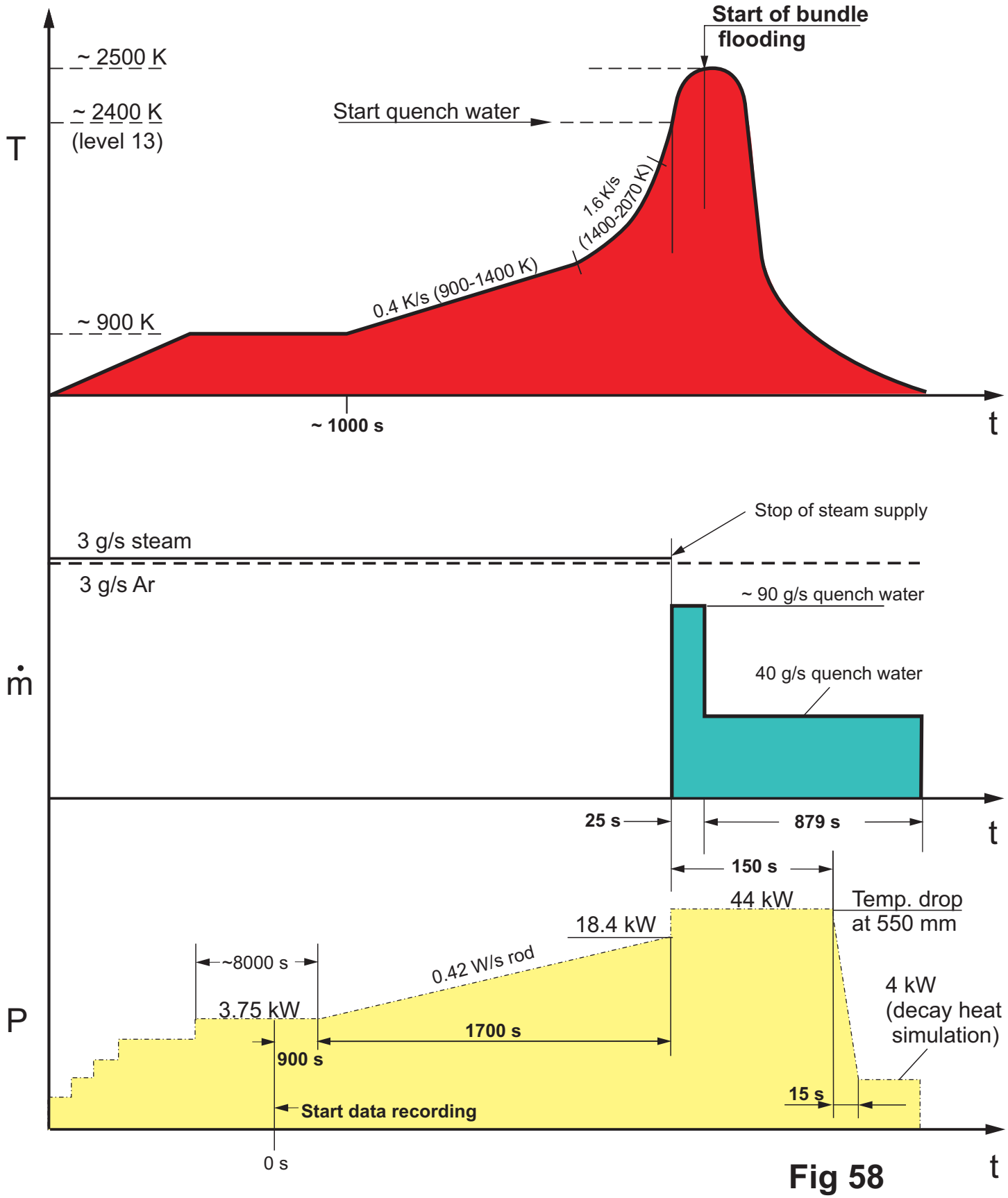

Fig 58

QUENCH-3

Temperatures measured by the centerline thermoxouples TCRC12 and TCRC13

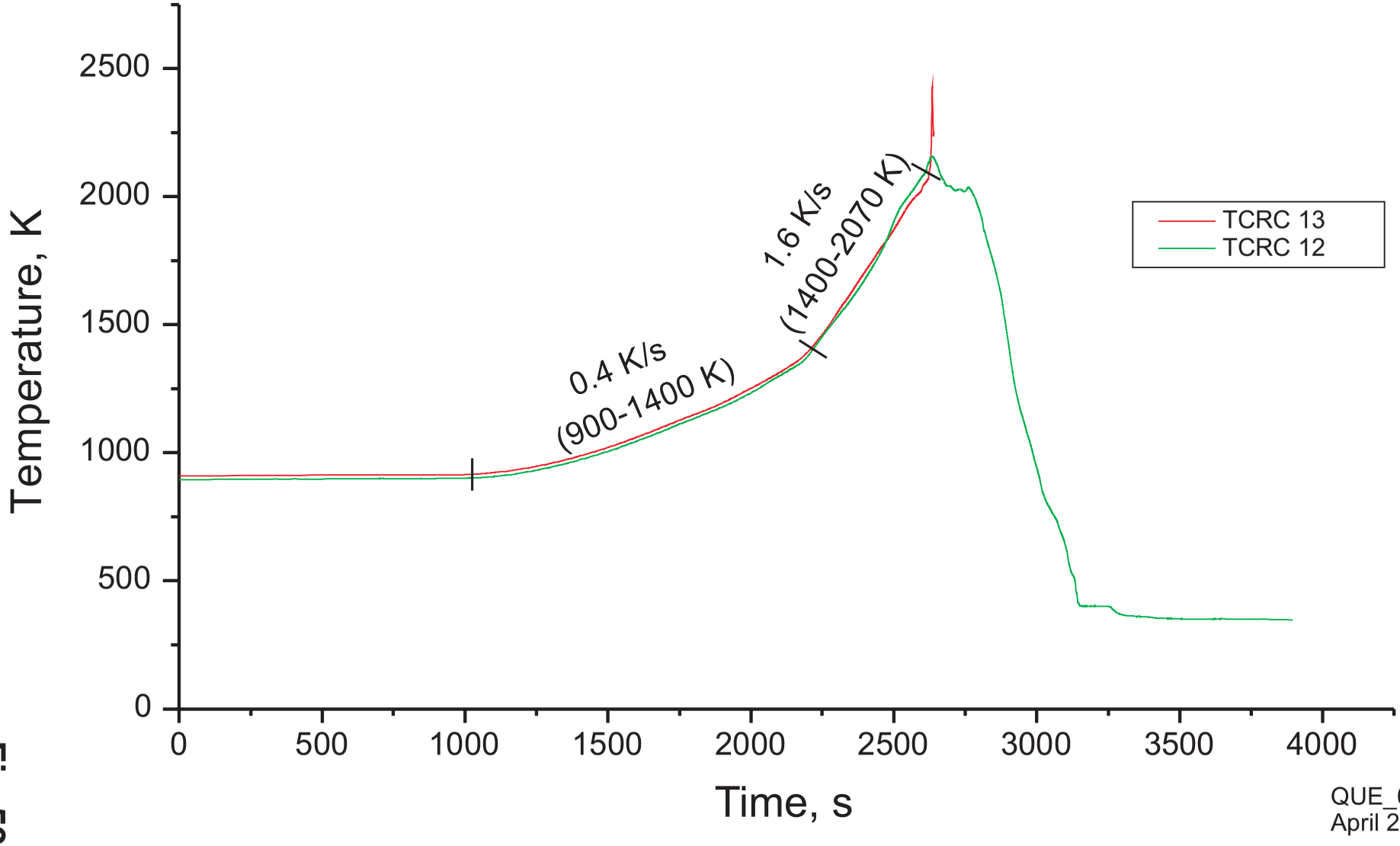

Fig 59

QUE_03_TCRC
April 26, 99 - HIT

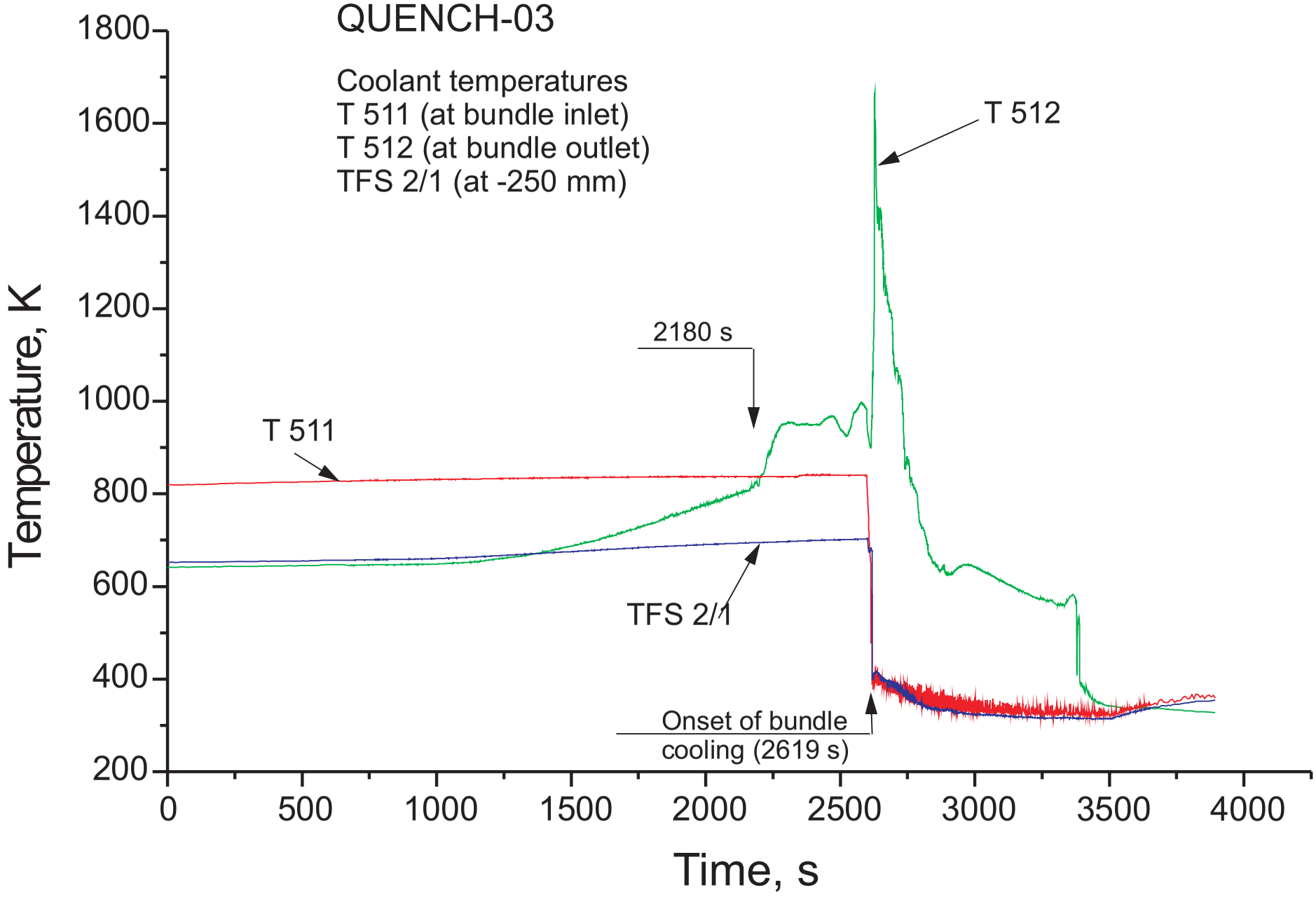
QUENCH-03
Coolant temperatures
T 511 (at bundle inlet)
T 512 (at bundle outlet)
TFS 2/1 (at -250 mm)
T 512
2180 s
T 511
TFS 2/1
Onset of bundle
cooling (2619 s)
Temperature, K
Time, s
1800
1600
1400
1200
1000
800
600
400
200
0
500
1000
1500
2000
2500
3000
3500
4000

Fig 60

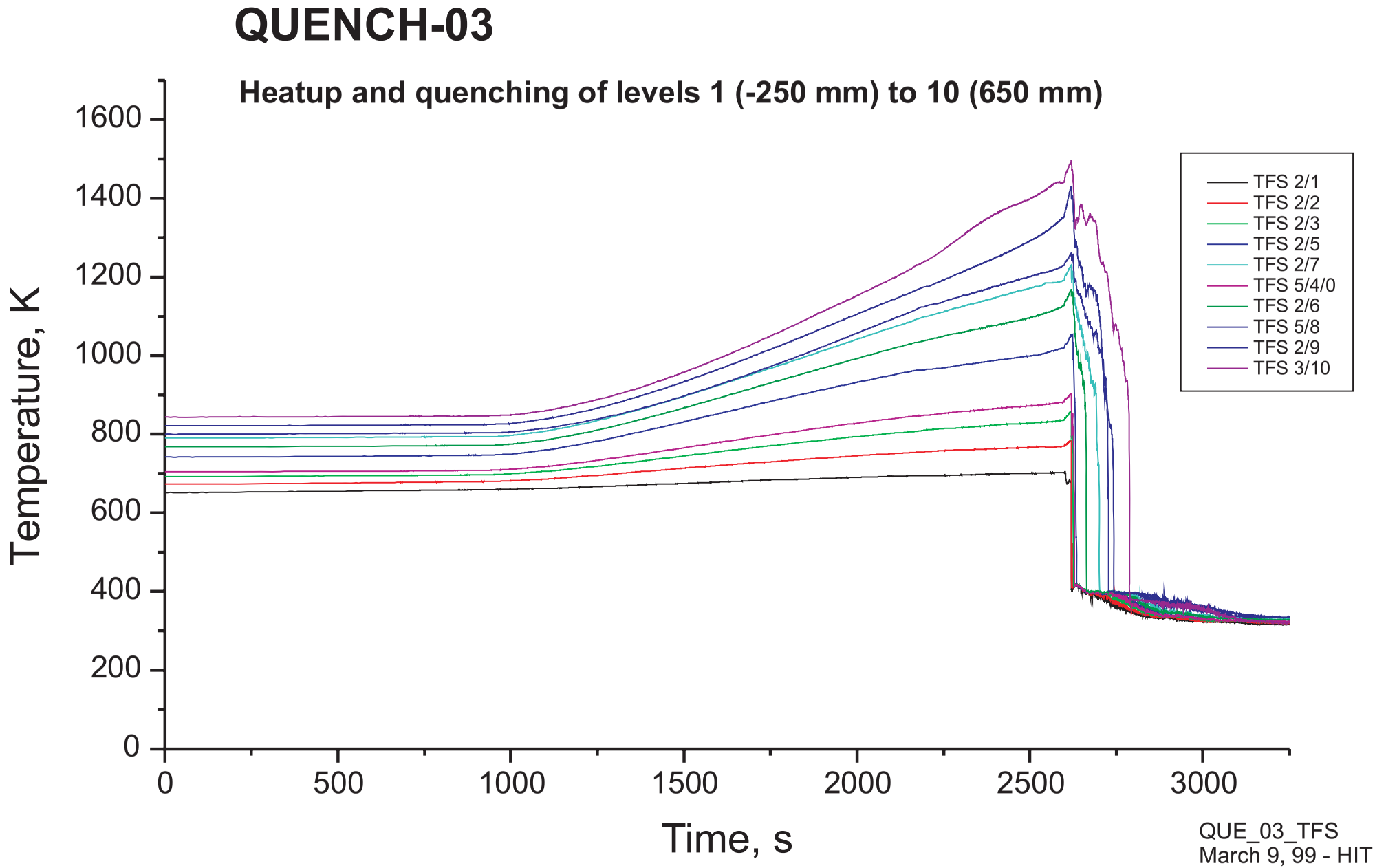
QUENCH-03
Heatup and quenching of levels 1 (-250 mm) to 10 (650 mm)
Temperature, K
Time, s
0
200
400
600
800
1000
1200
1400
1600
0
500
1000
1500
2000
2500
3000
TFS 2/1
TFS 2/2
TFS 2/3
TFS 2/5
TFS 2/7
TFS 5/4/0
TFS 2/6
TFS 5/8
TFS 2/9
TFS 3/10
QUE_03_TFS
March 9, 99 - HIT

Fig 61

QUENCH-03

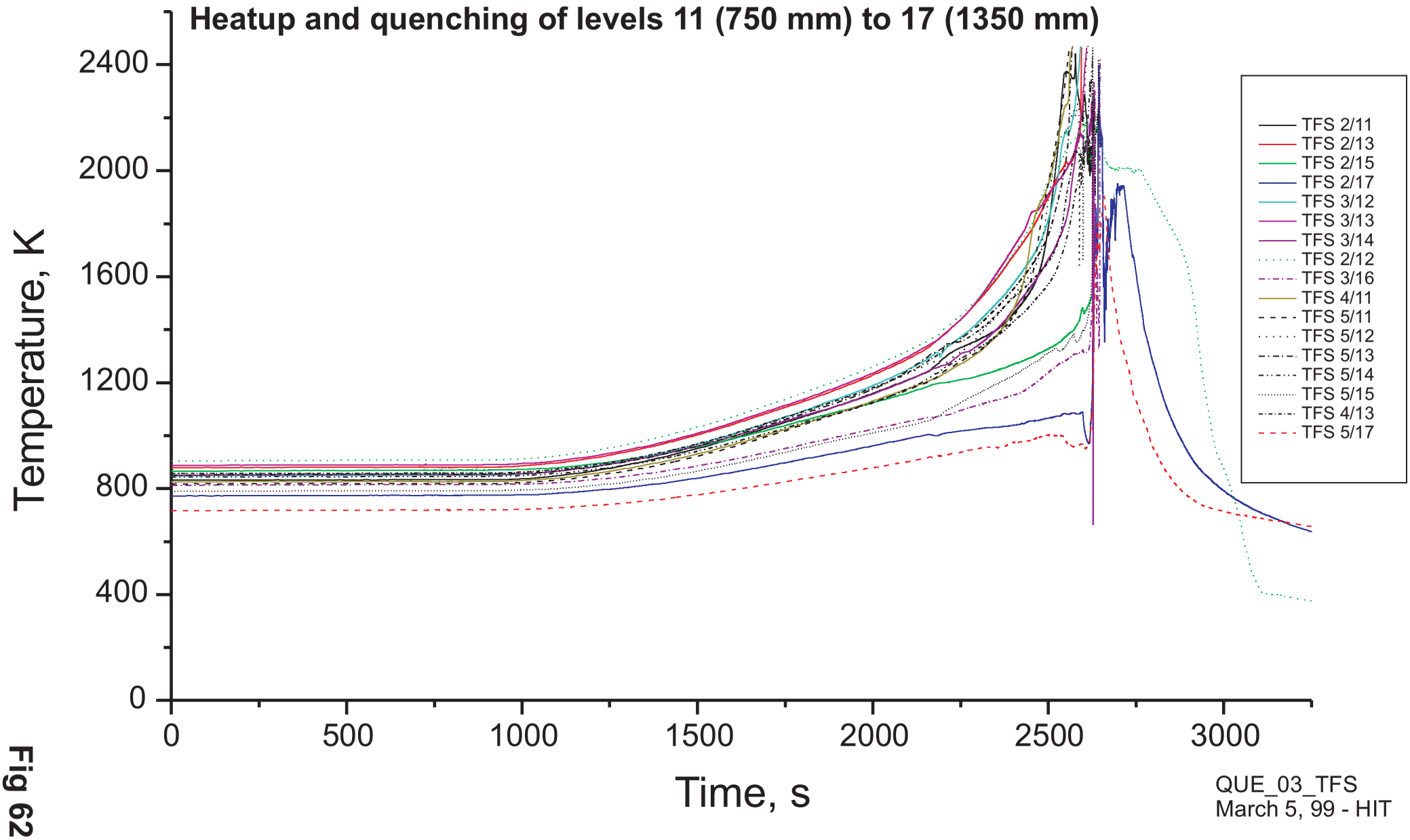

Fig 62

QUENCH-03

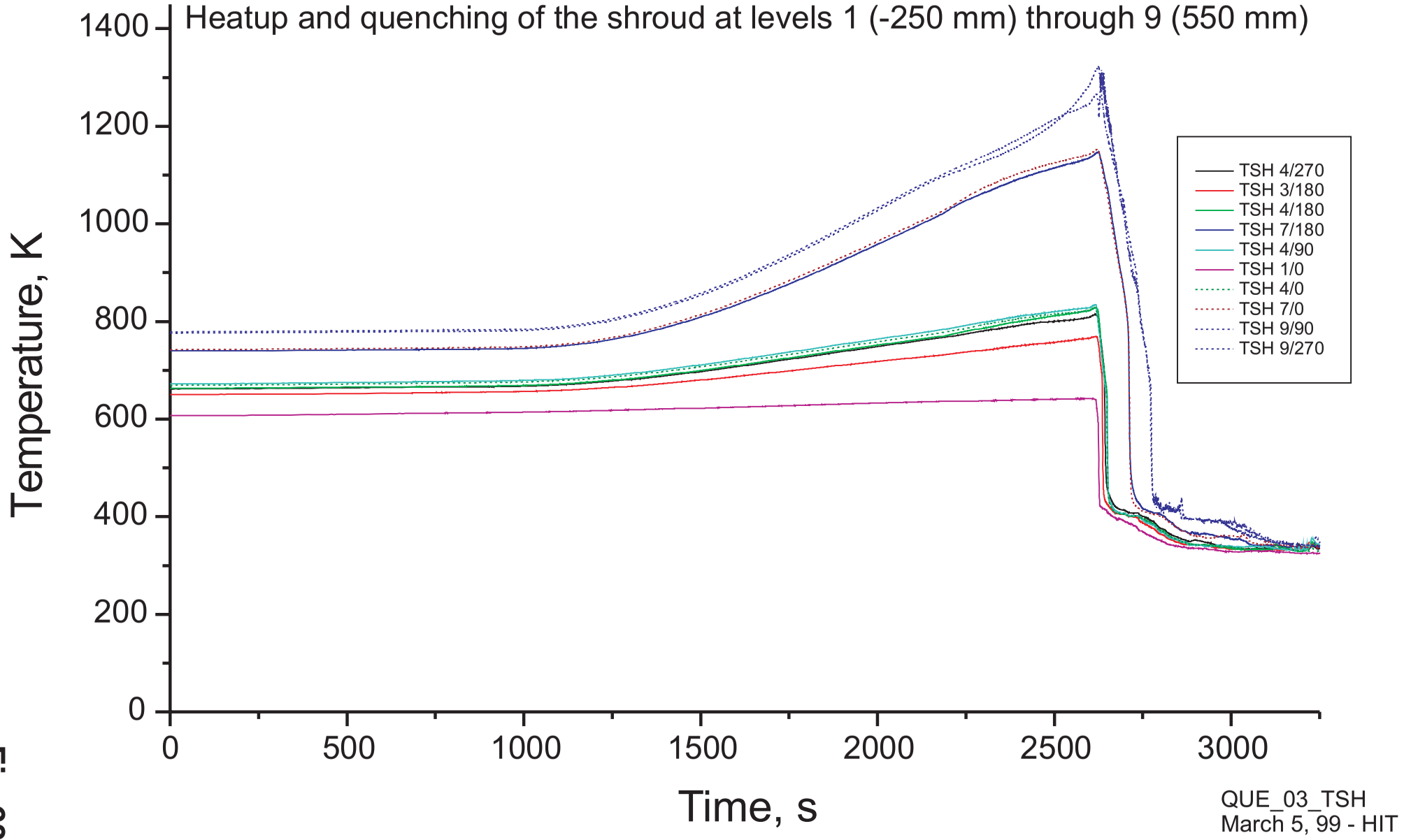

QUE_03_TSH
March 5, 99 - HIT

Fig 63

QUENCH-03

Heatup and quenching of the shroud at levels 11 (750 mm) through 16 (1250 mm)

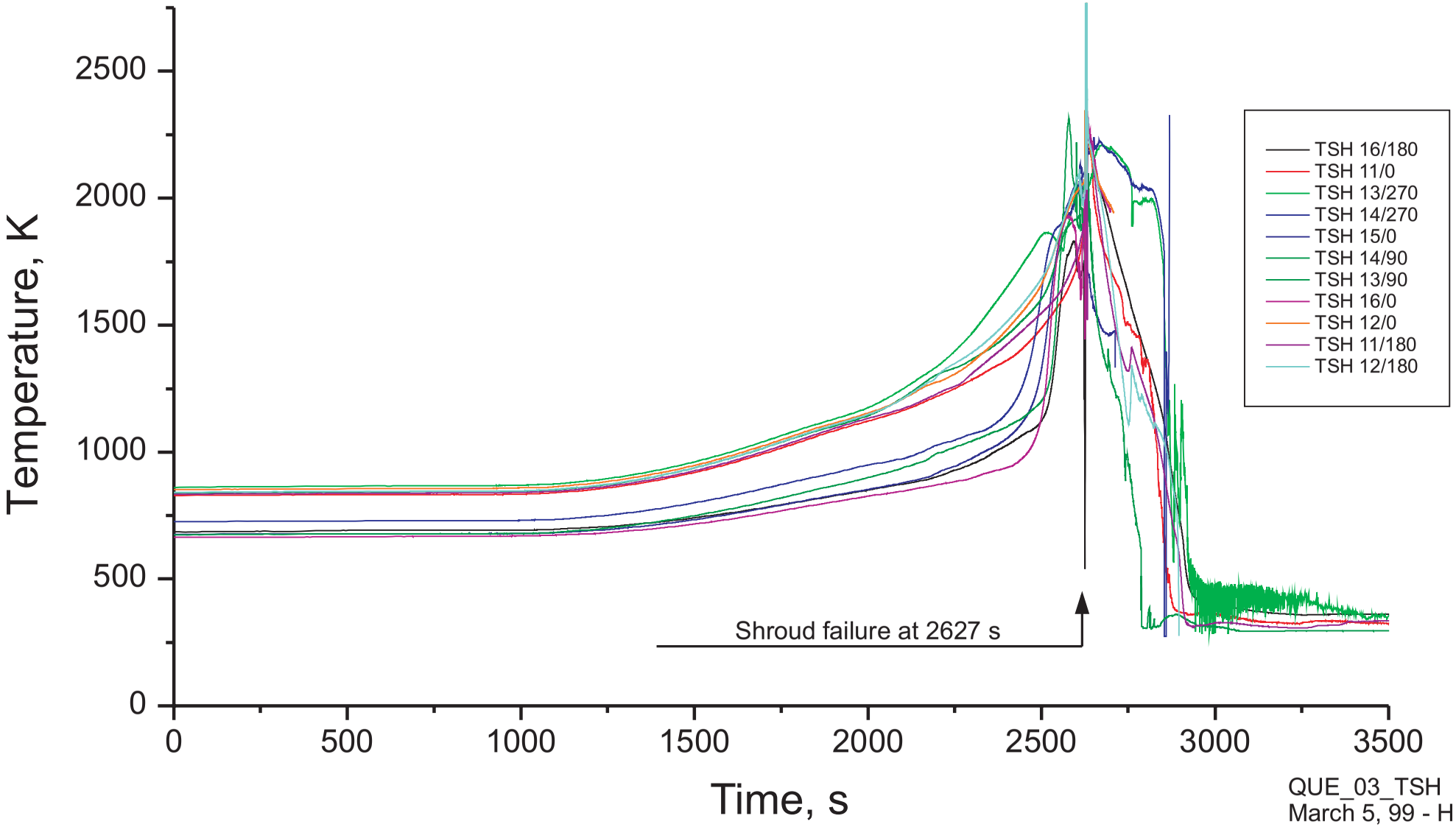

Fig 64

QUENCH-03

Temperature of escalation as a function of time

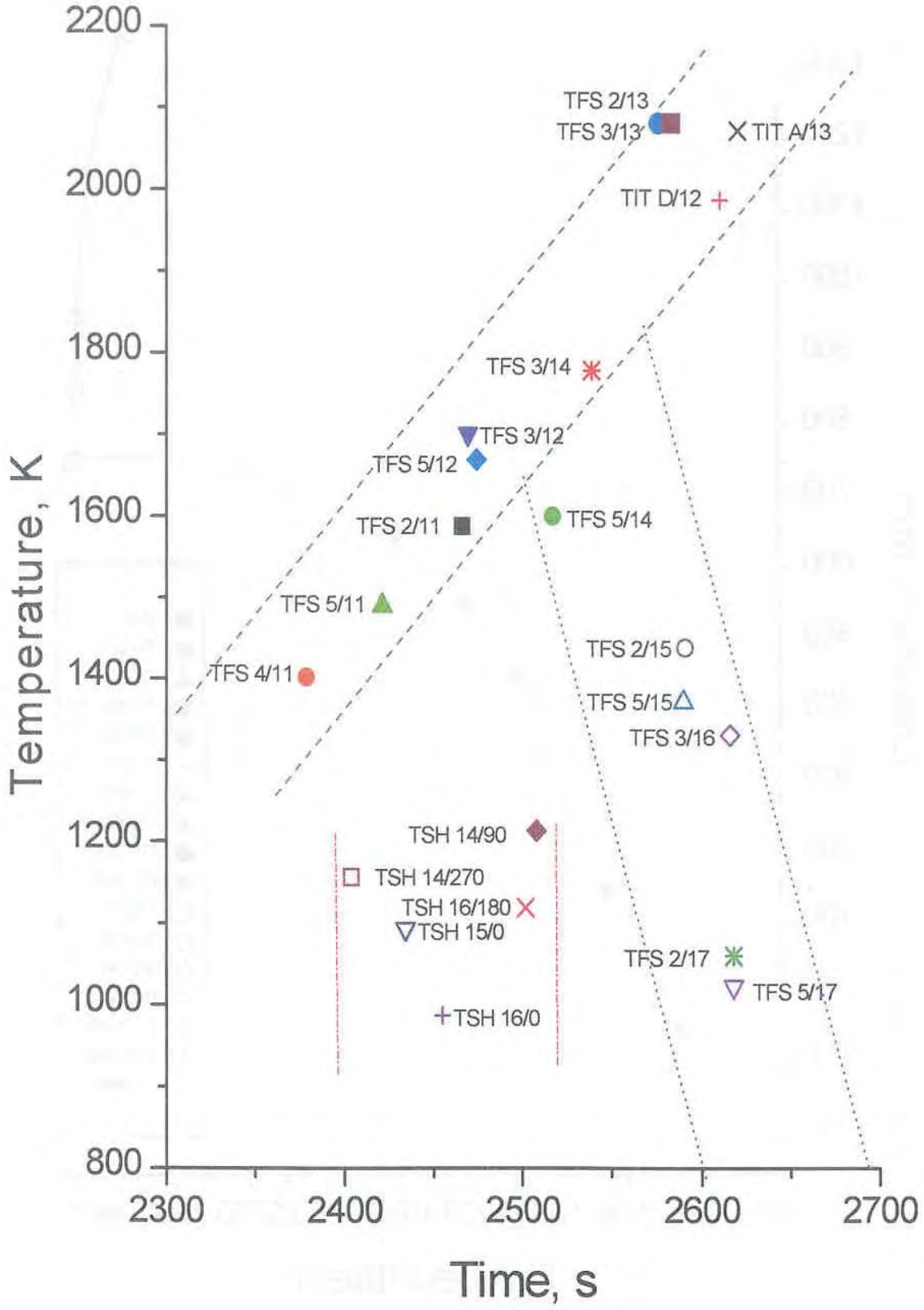

QUE_03_escalation_time
March 5,99 _ HIT

Fig. 65

QUENCH-03

Maximum temperature of each elevation

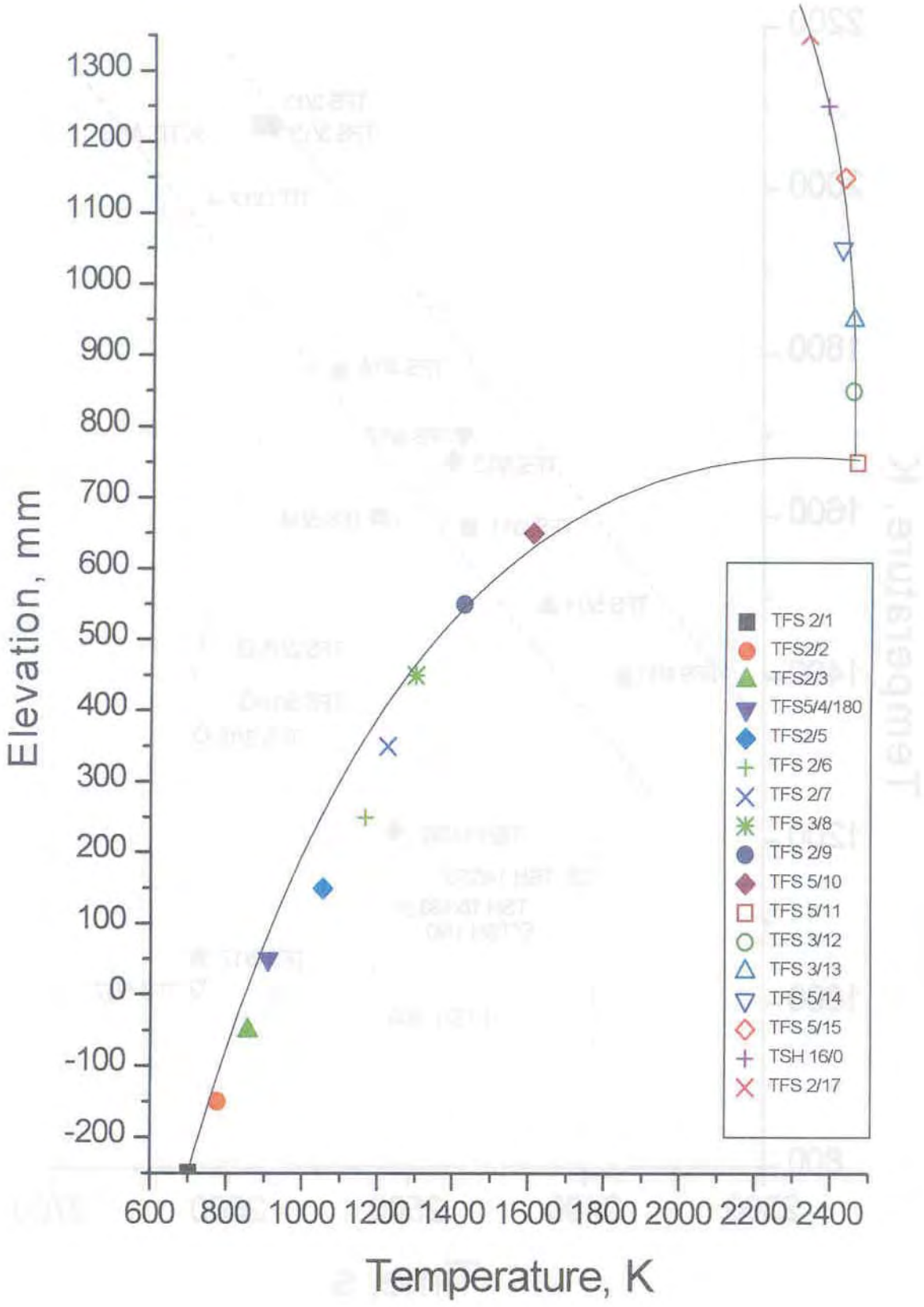

QUE_03_elevation_maxTk
March 3,99 -HIT

Fig. 66

QUENCH-03

Axial Temperature Profile TFS2
at 2250 s, 2550 s, 2570 s, 2619 s, 2625 s

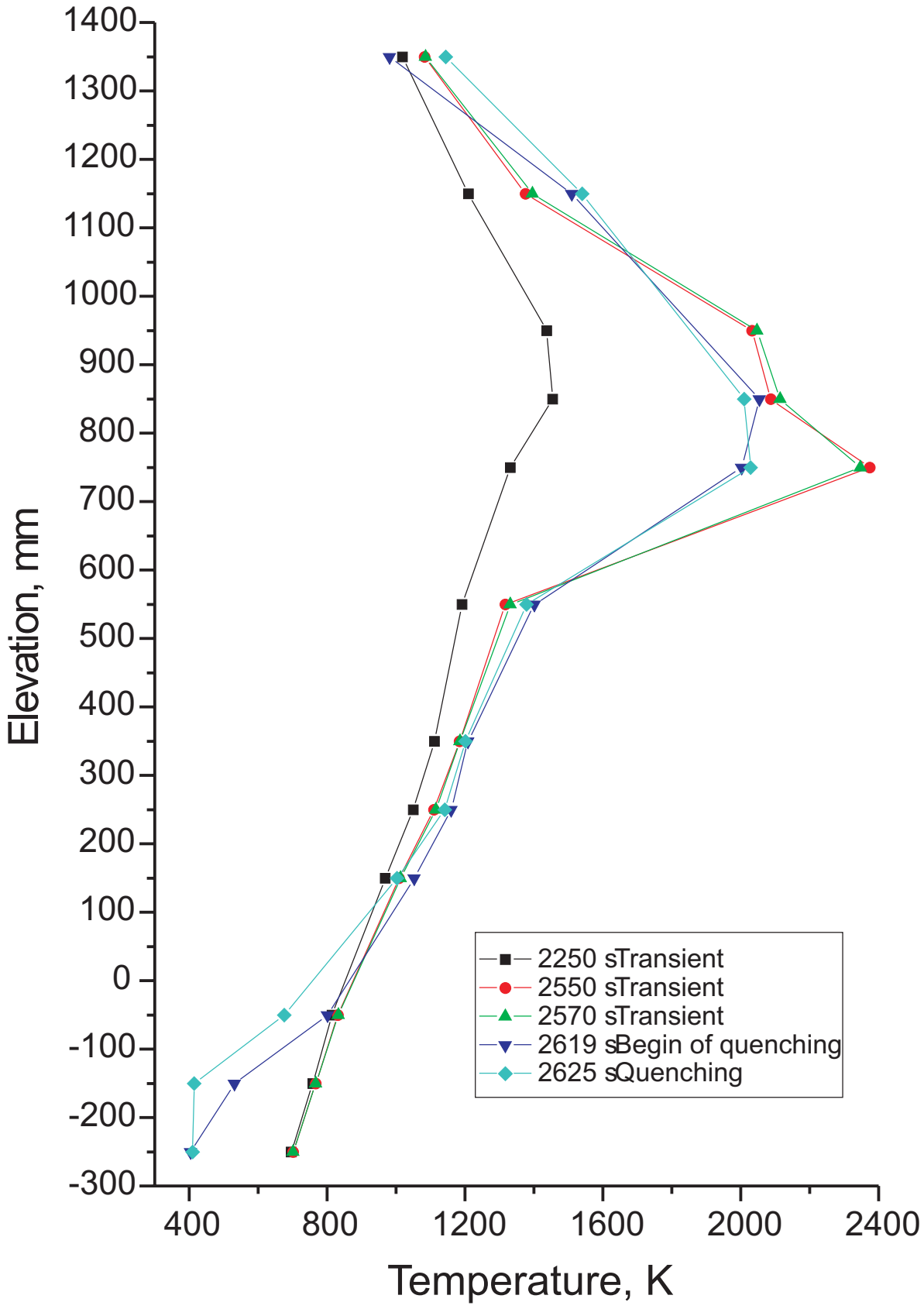

QUE_03_Axialprofil
Sep 27,99 - IMF III

Fig 67

QUENCH-03

Axial Temperature Profile TFS5
at 2250 s, 2550 s, 2570 s, 2619 s, 2625 s

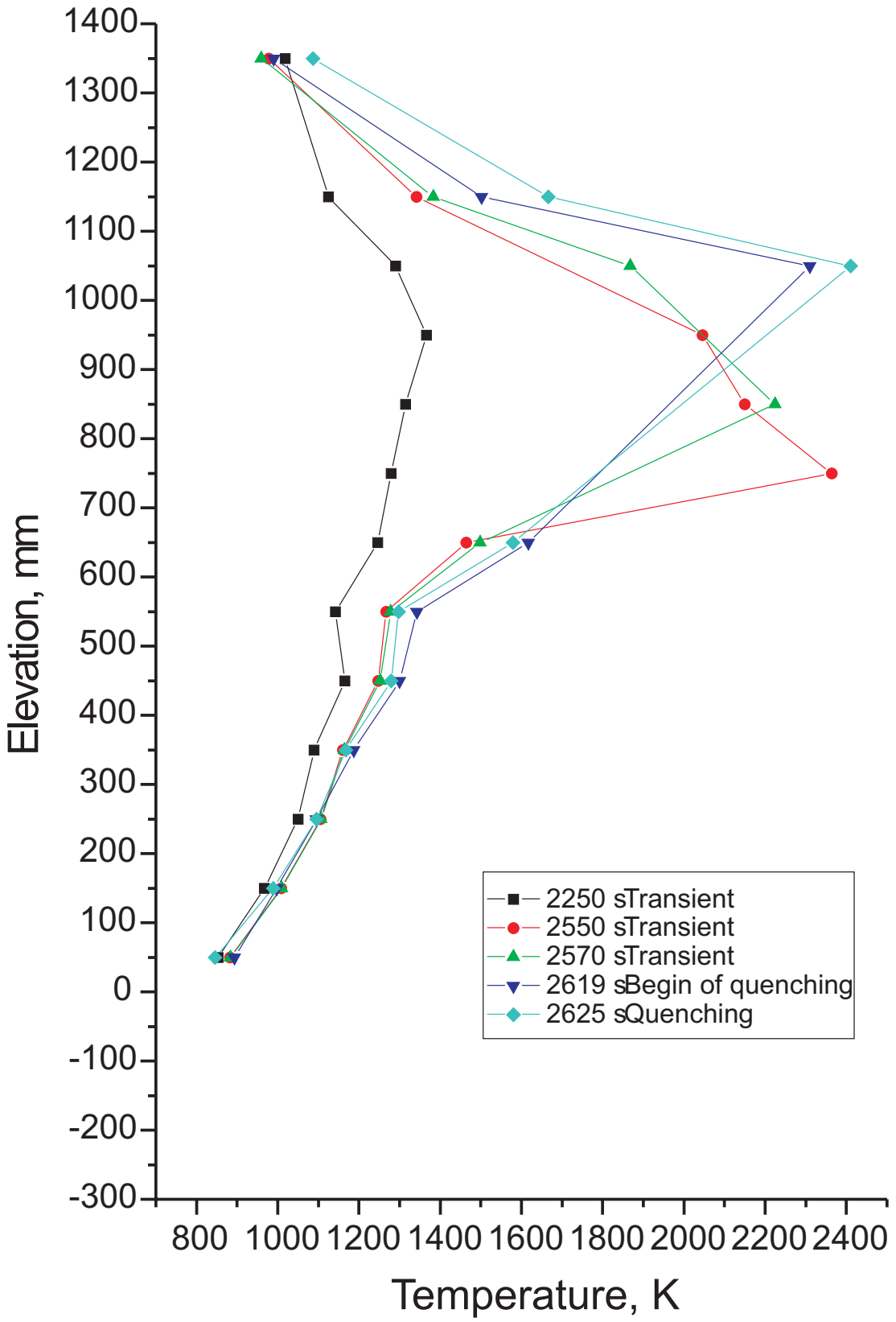

QUE_03_Axialprofil
Sep 27,99 - IMF III

Fig 68

QUENCH-03

Axial Temperature Profile TSH
at 2250 s, 2550 s, 2570 s, 2619 s, 2625 s

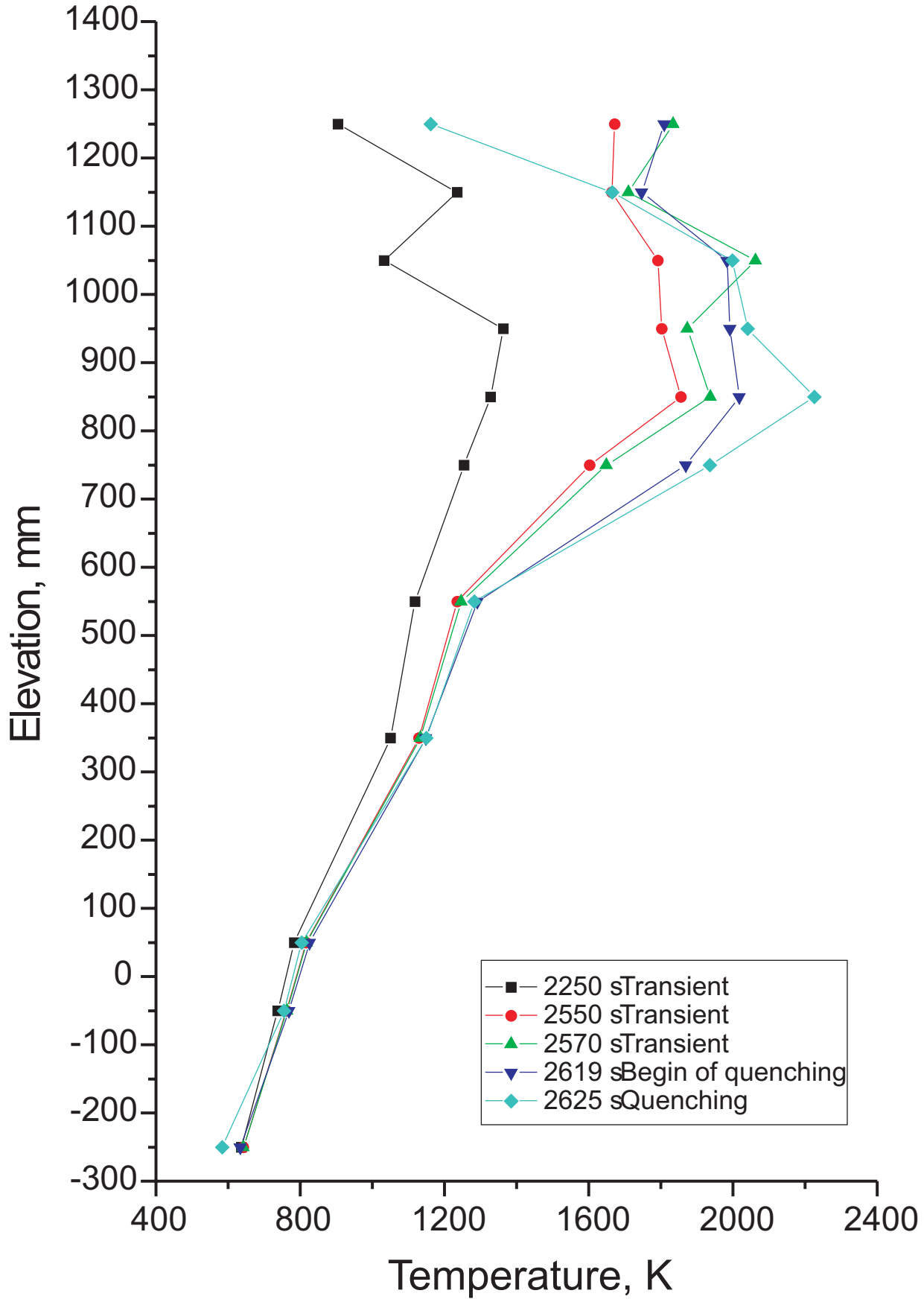

QUE_03_Axialprofil
Sep 27,99 - IMF III

Fig 69

QUENCH-03

Axial Temperature Profile TIT
at 2250 s, 2550 s, 2570 s, 2619 s, 2625 s

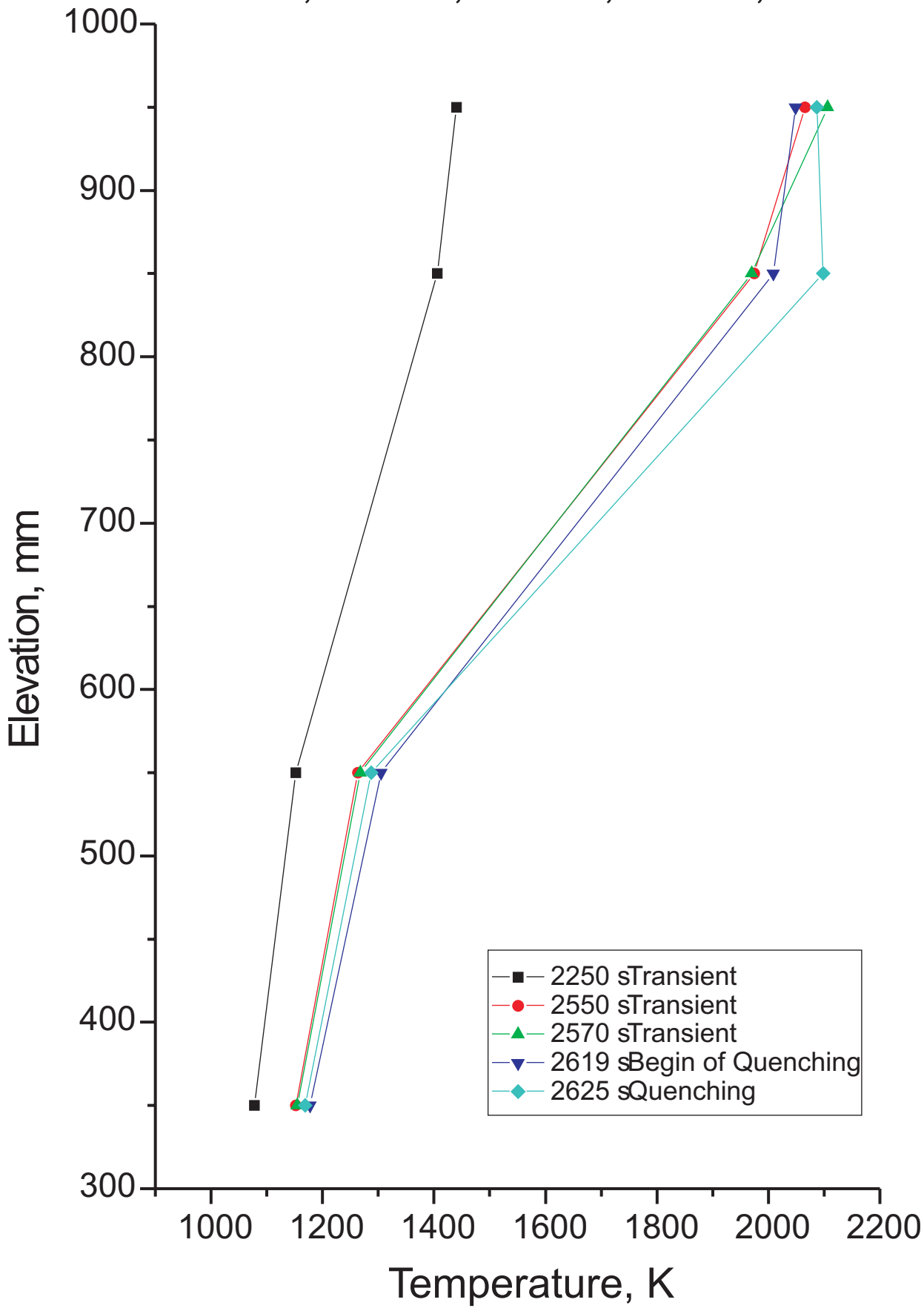

QUE_03_Axialprofil
Sep 27,99 - IMF III

Fig 70

QUENCH-03

Axial Temperature Profile TFS2, TFS 5, TSH, TIT at 2250 s (Transient)

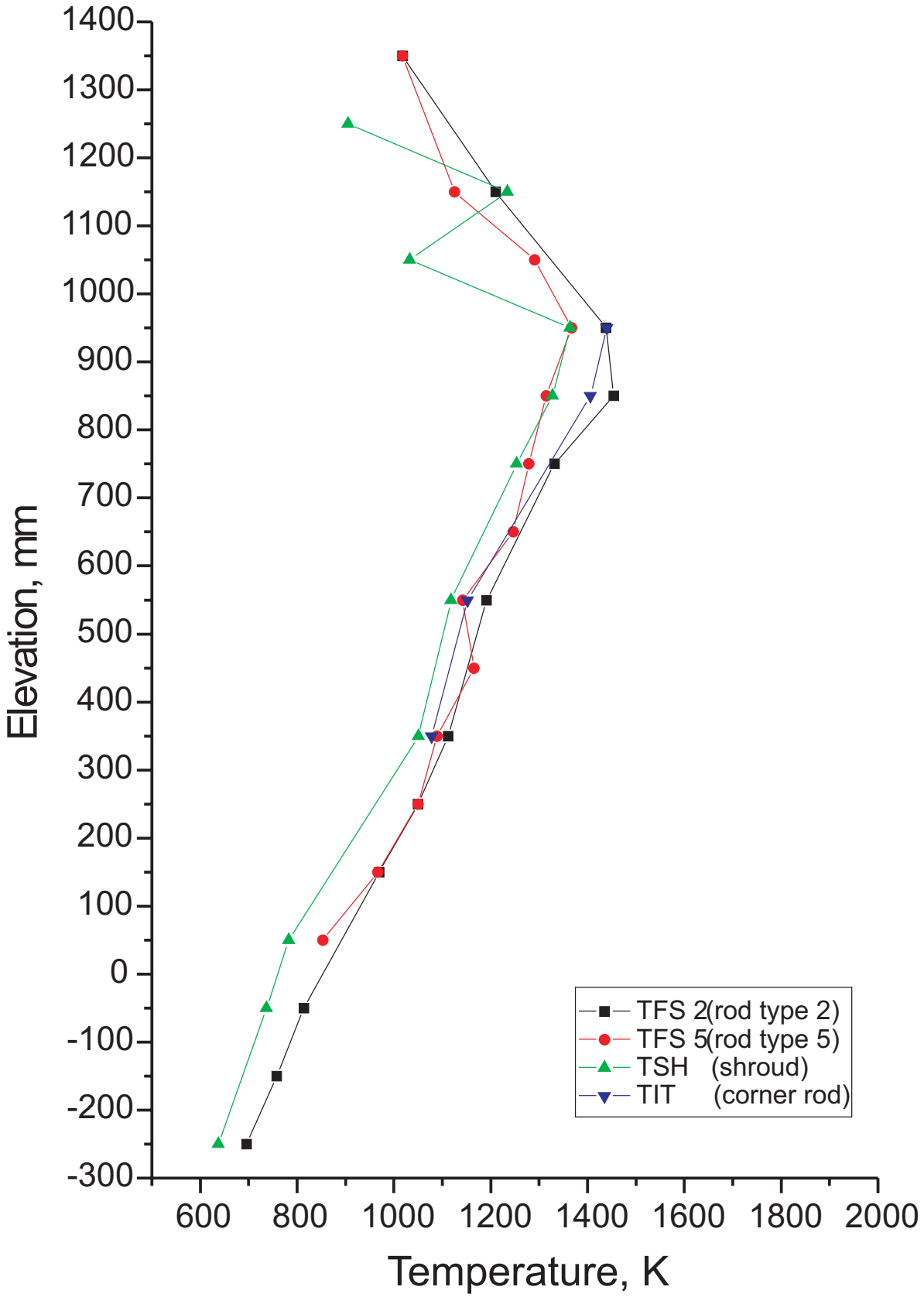

QUE_03_Axial-Temp-Profil
Sep 27,99 - IMF III

Fig 71

QUENCH-03

Axial Temperature Profile TFS2, TFS 5, TSH, TIT at 2550 s (Transient)

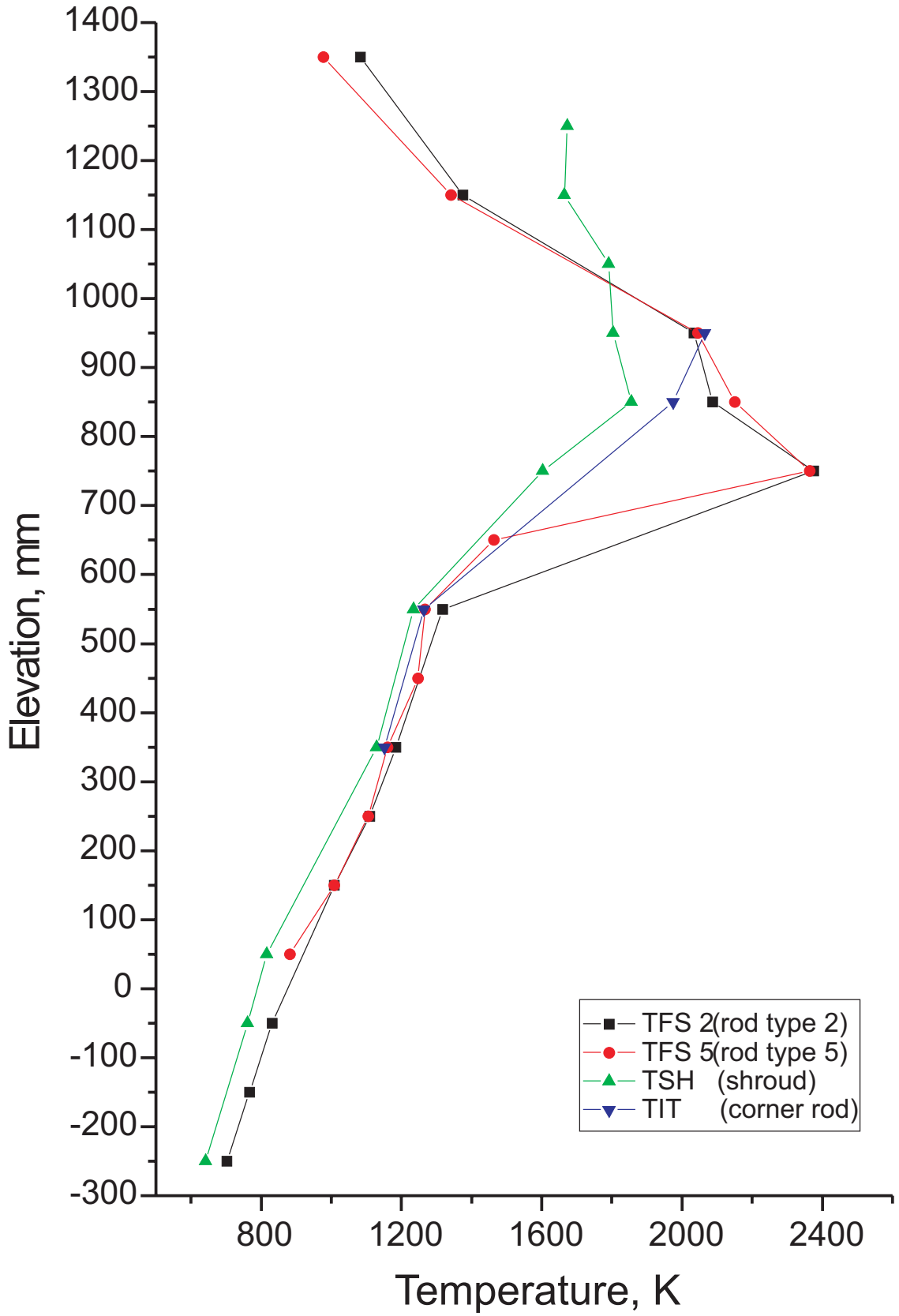

QUE_03_Axial-Temp-Profil
Sep 27,99 - IMF III

Fig 72

QUENCH-03

Axial Temperature Profile TFS2, TFS 5, TSH, TIT at 2570 s (Transient)

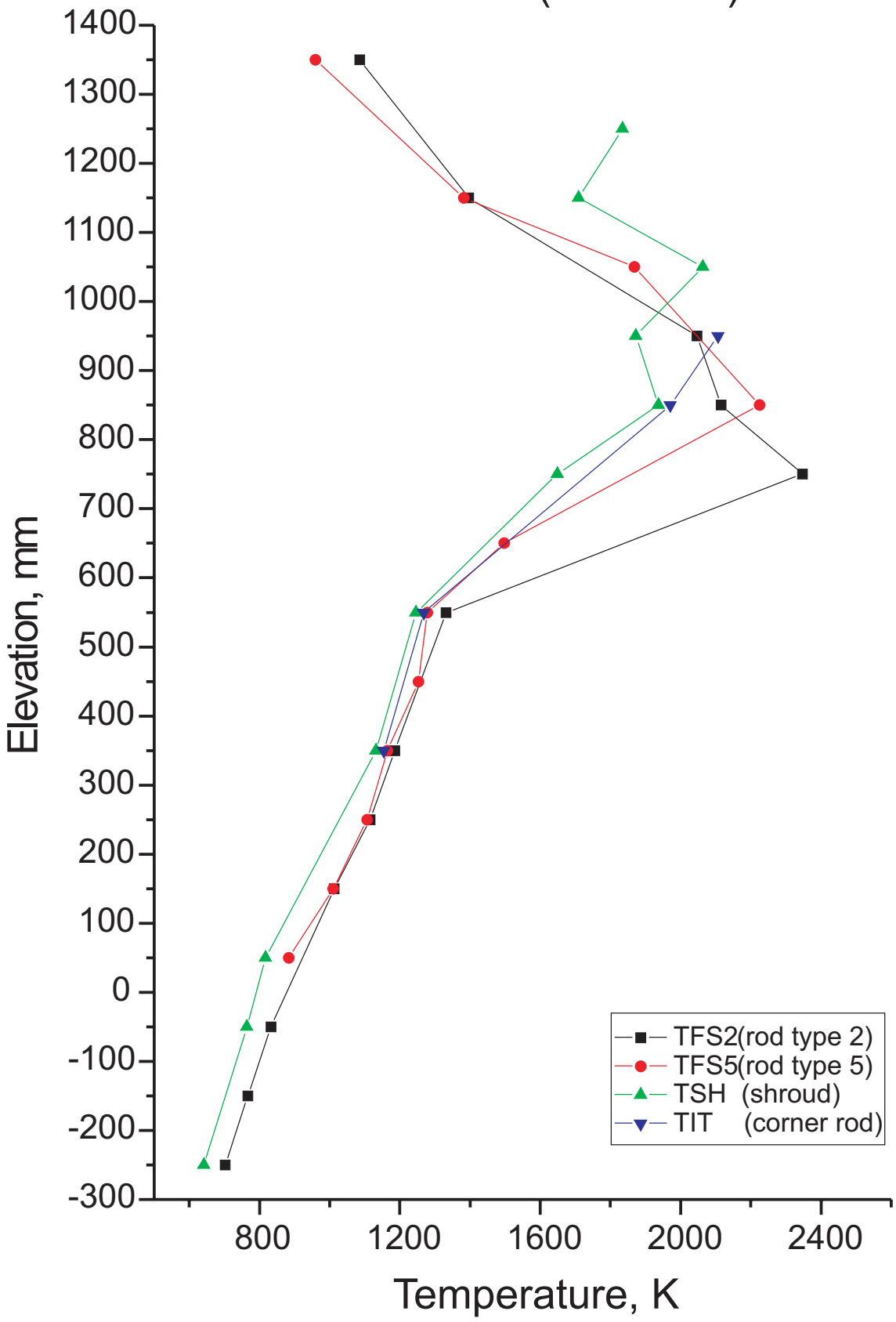

QUE_03_Axial-Temp-Profil
Sep 27,99 - IMF III

Fig 73

QUENCH-03

Axial Temperature Profile TFS2, TFS 5, TSH, TIT at 2619 s (Begin of Quenching)

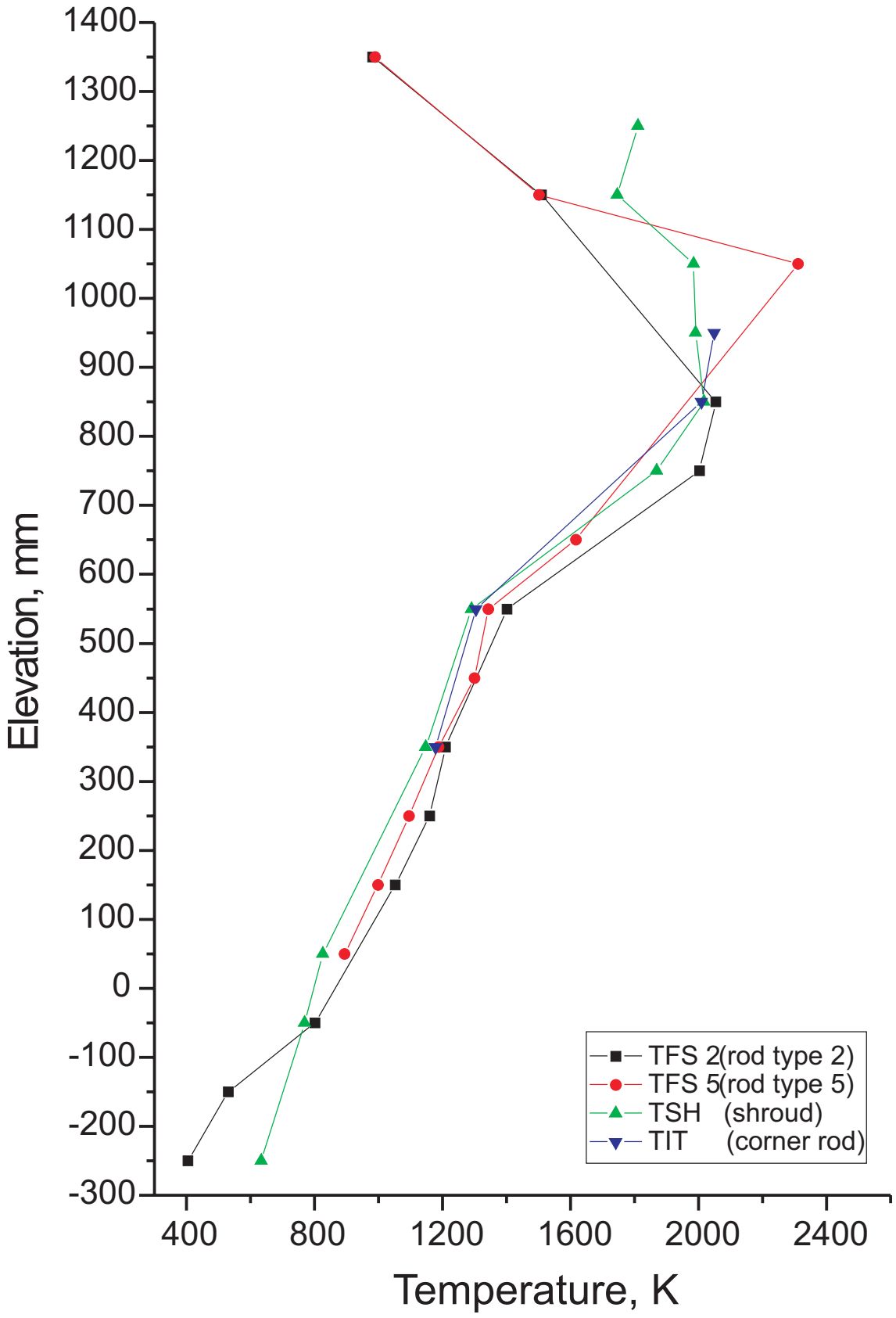

QUE_03_Axial-Temp-Profil
Sep 27,99 - IMF III

Fig 74

QUENCH-03

Axial Temperature Profile TFS2, TFS 5, TSH, TIT at 2625 s (Quenching)

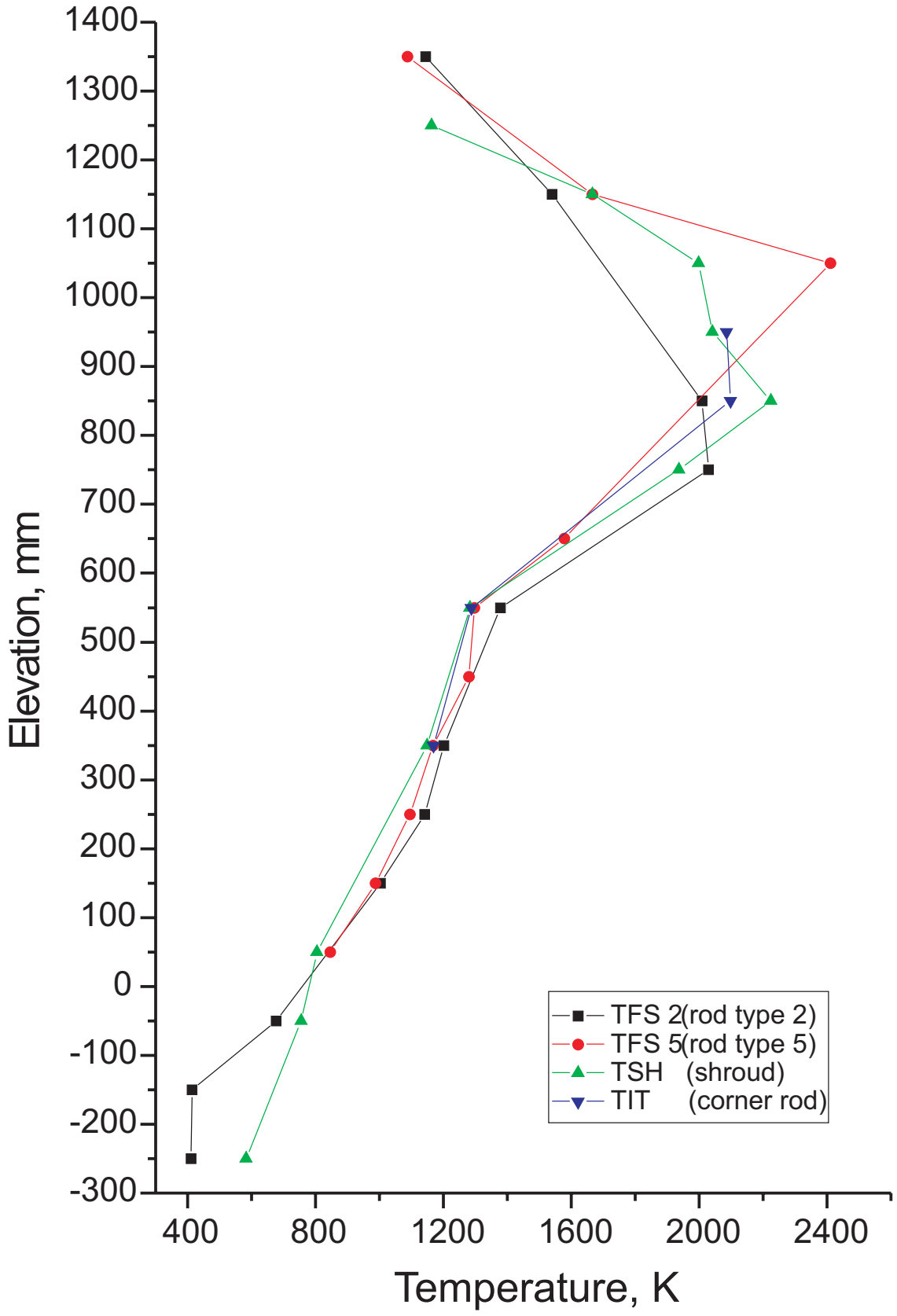

QUE_03_Axial-Temp-Profil
Sep 27,99 - IMF III

Fig 75

QUENCH-03

Temperature histories of the inner cooling jacket at 350 and 550 mm together with shroud temperature at 550 mm

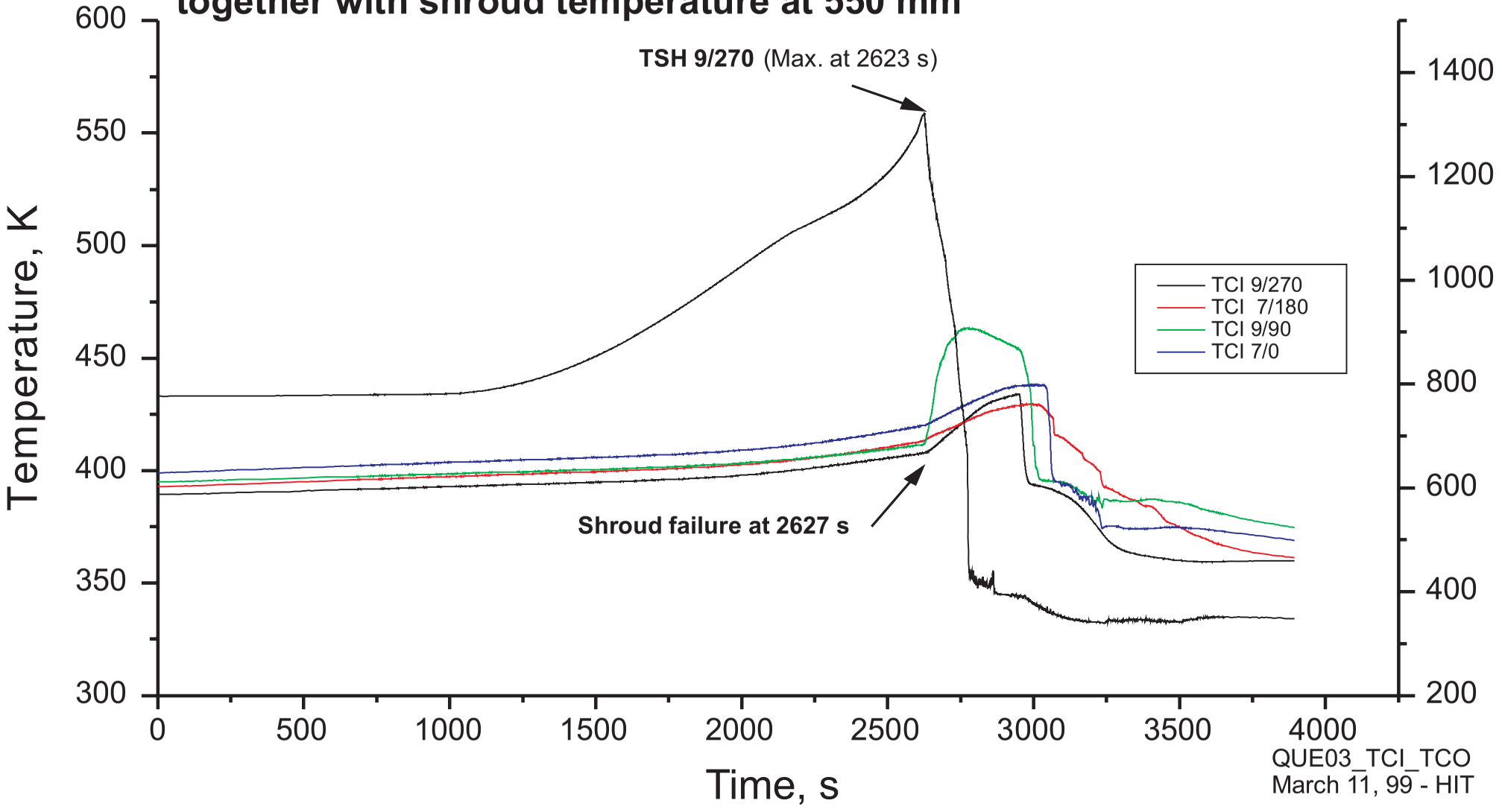

Fig 76

QUENCH-03

Temperature histories of the inner cooling jacket at 650 and 750 mm together with shroud temperature at 750 mm

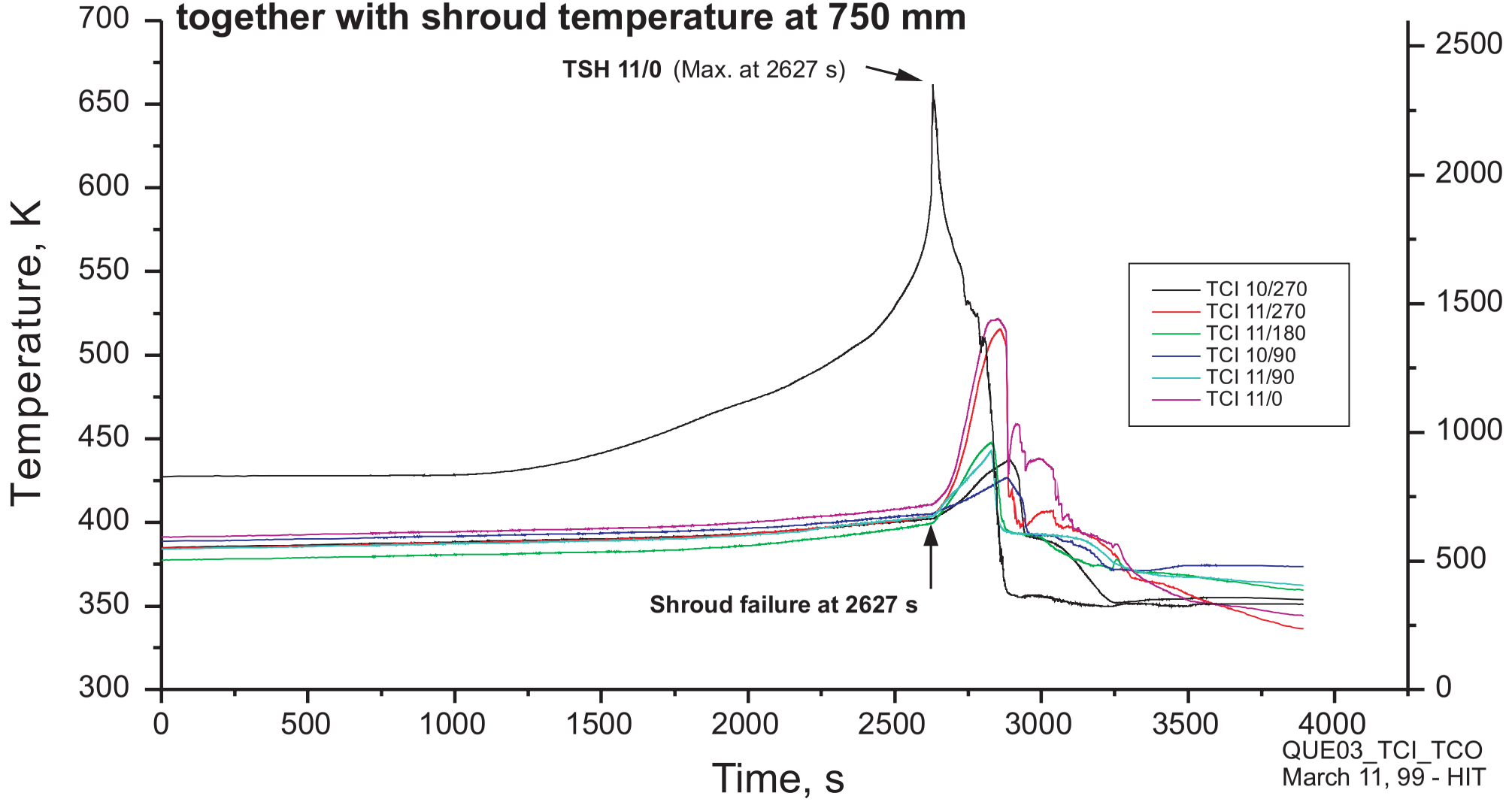

Fig 77

QUENCH-03

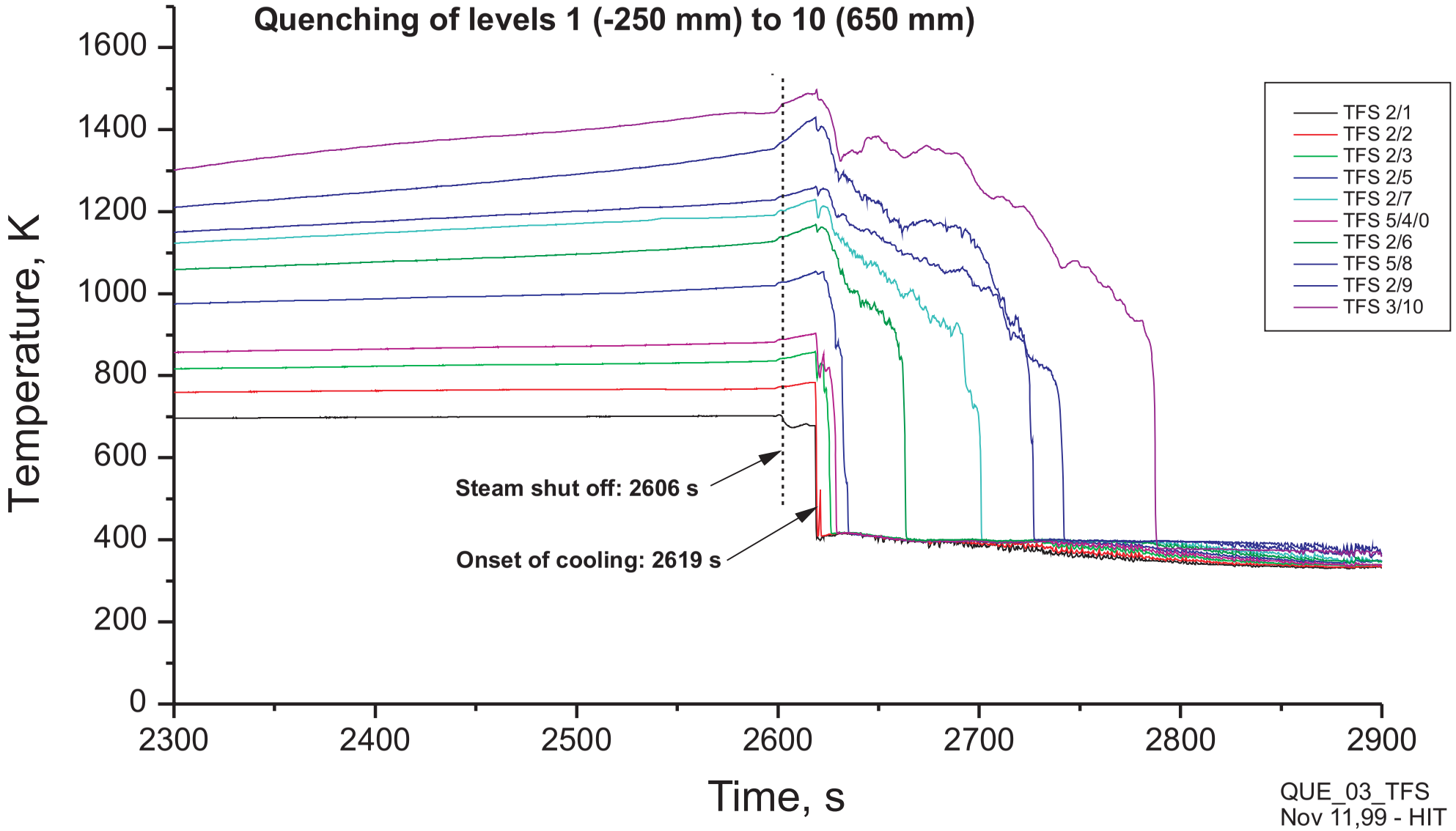

Fig 78

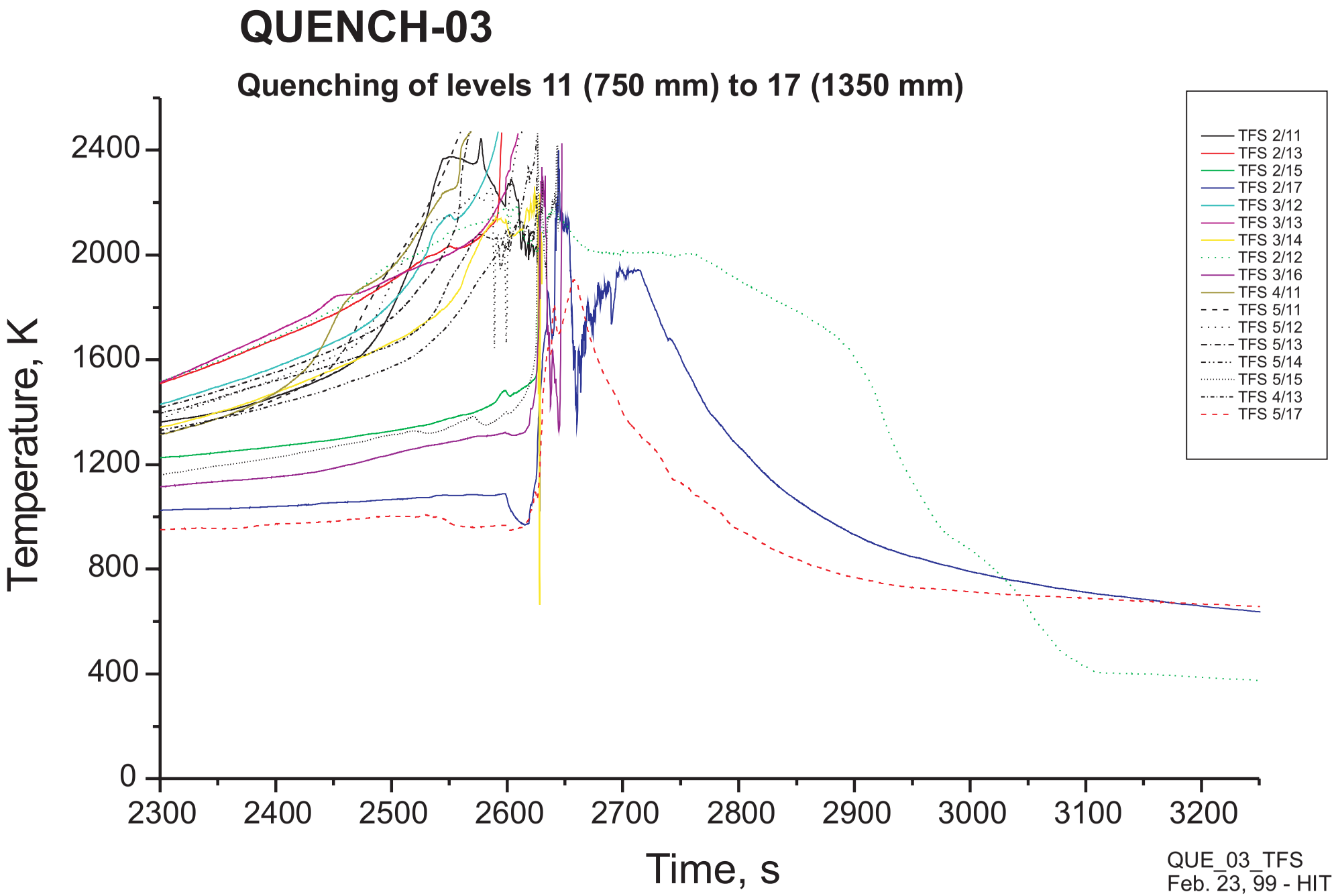
QUENCH-03
Quenching of levels 11 (750 mm) to 17 (1350 mm)
Temperature, K
Time, s
2400
2000
1600
1200
800
400
0
2300
2400
2500
2600
2700
2800
2900
3000
3100
3200
TFS 2/11
TFS 2/13
TFS 2/15
TFS 2/17
TFS 3/12
TFS 3/13
TFS 3/14
TFS 2/12
TFS 3/16
TFS 4/11
TFS 5/11
TFS 5/12
TFS 5/13
TFS 5/14
TFS 5/15
TFS 4/13
TFS 5/17
QUE_03_TFS
Feb. 23, 99 - HIT

Fig 79

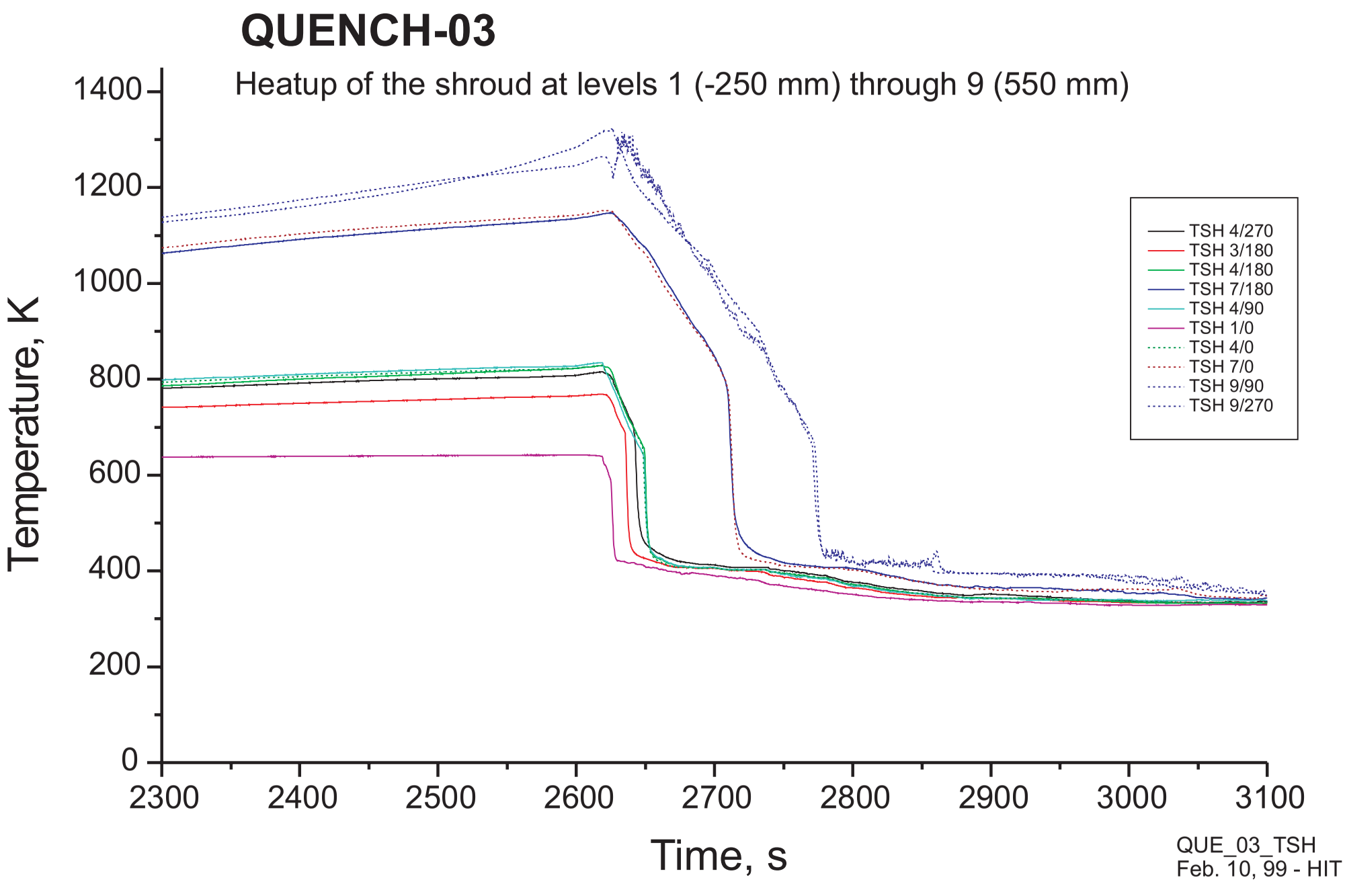
QUENCH-03
Heatup of the shroud at levels 1 (-250 mm) through 9 (550 mm)
Temperature, K
Time, s
0
200
400
600
800
1000
1200
1400
2300
2400
2500
2600
2700
2800
2900
3000
3100
TSH 4/270
TSH 3/180
TSH 4/180
TSH 7/180
TSH 4/90
TSH 1/0
TSH 4/0
TSH 7/0
TSH 9/90
TSH 9/270
QUE_03_TSH
Feb. 10, 99 - HIT

Fig 80

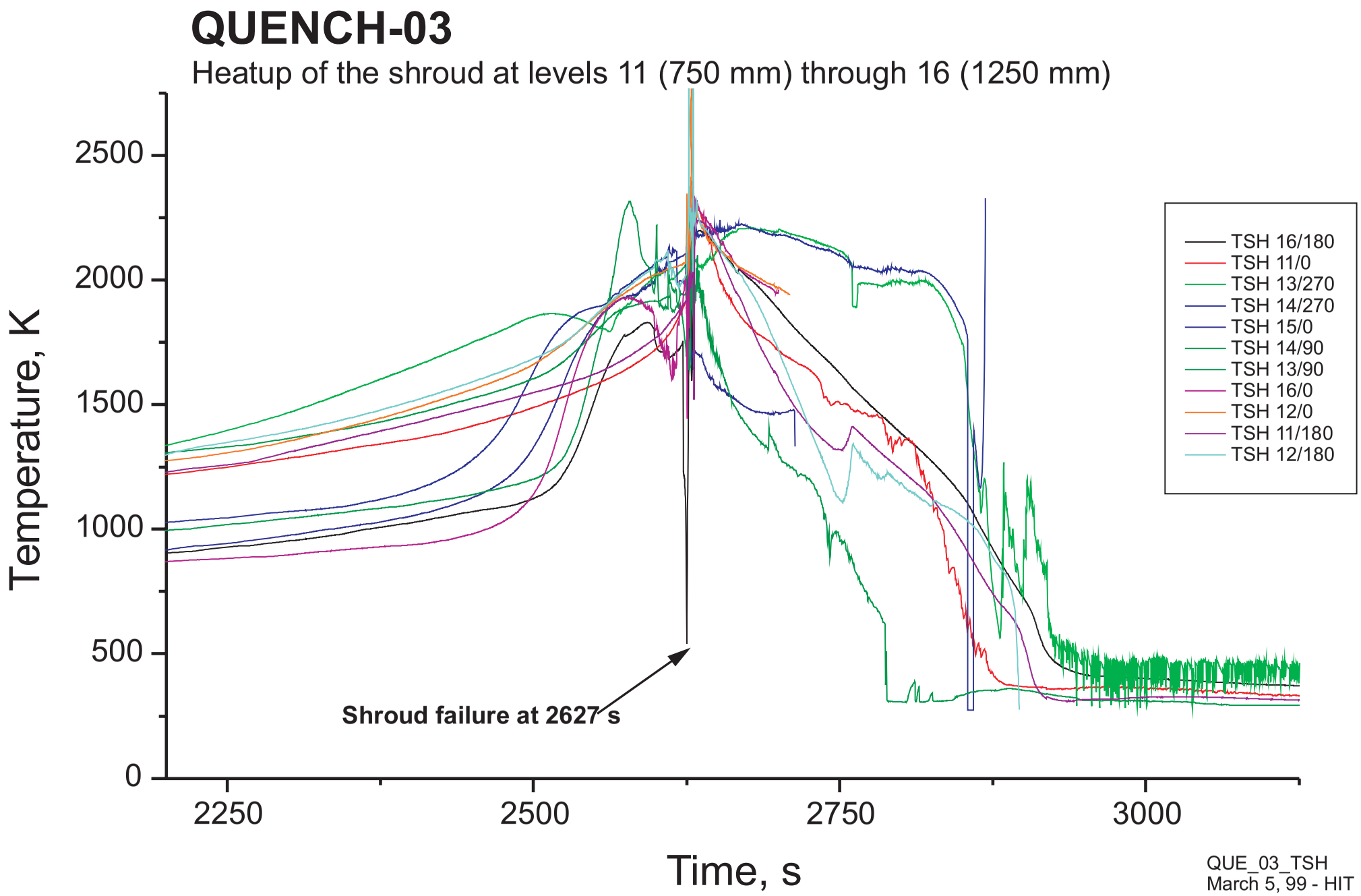
QUENCH-03
Heatup of the shroud at levels 11 (750 mm) through 16 (1250 mm)
Temperature, K
2500
2000
1500
1000
500
0
2250
2500
2750
3000
Time, s
Shroud failure at 2627 s
TSH 16/180
TSH 11/0
TSH 13/270
TSH 14/270
TSH 15/0
TSH 14/90
TSH 13/90
TSH 16/0
TSH 12/0
TSH 11/180
TSH 12/180
QUE_03_TSH
March 5, 99 - HIT

Fig 81

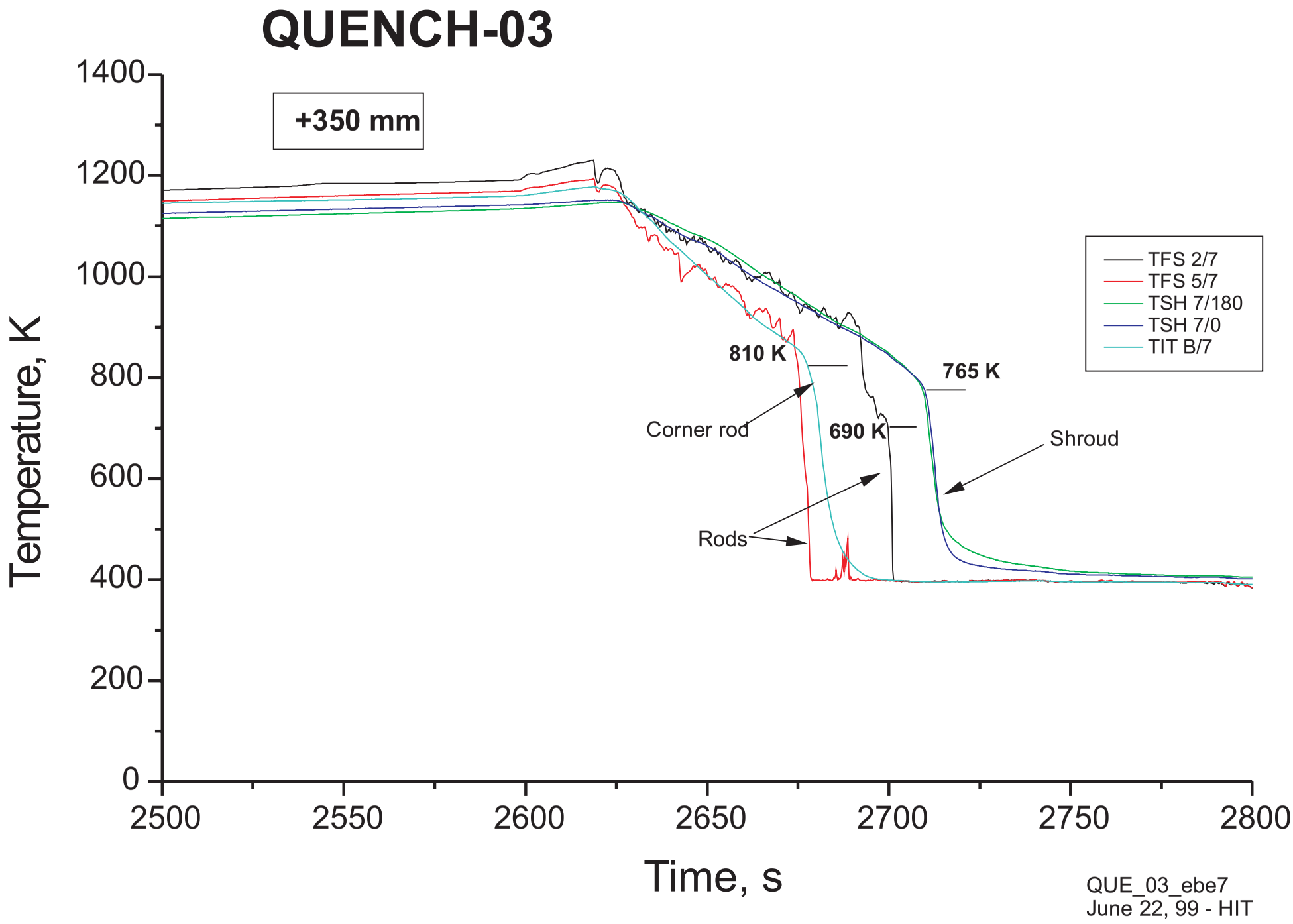
QUENCH-03
+350 mm
Temperature, K
Time, s
1400
1200
1000
800
600
400
200
0
2500
2550
2600
2650
2700
2750
2800
TFS 2/7
TFS 5/7
TSH 7/180
TSH 7/0
TIT B/7
810 K
765 K
690 K
Corner rod
Shroud
Rods
QUE_03_ebe7
June 22, 99 - HIT

Fig 82

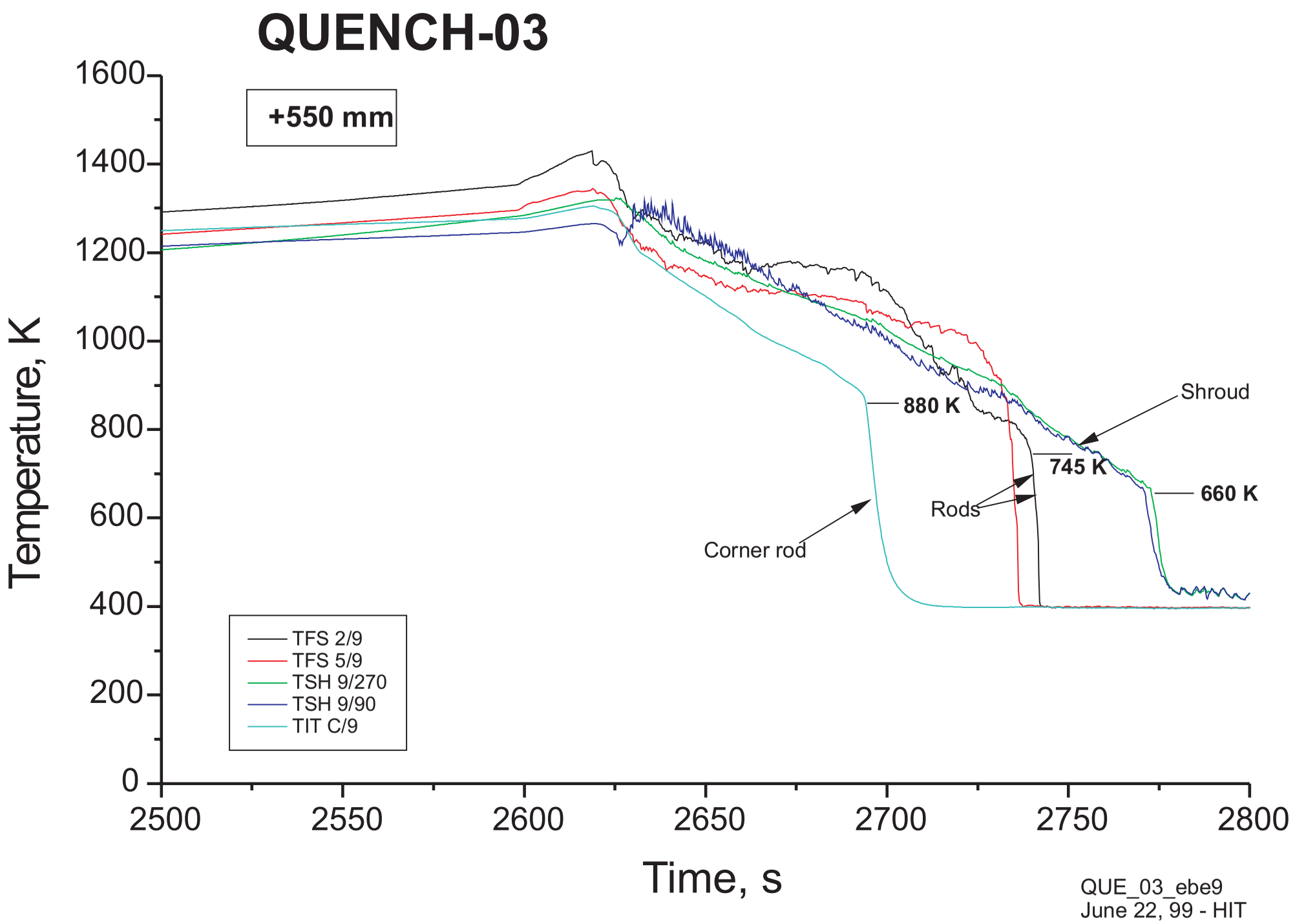
QUENCH-03
+550 mm
Temperature, K
Time, s
1600
1400
1200
1000
800
600
400
200
0
2500
2550
2600
2650
2700
2750
2800
TFS 2/9
TFS 5/9
TSH 9/270
TSH 9/90
TIT C/9
880 K
745 K
660 K
Shroud
Rods
Corner rod
QUE_03_ebe9
June 22, 99 - HIT

Fig 83

QUENCH-03

Influence of power input, rod temperature, and quench water injection on hydrogen generation

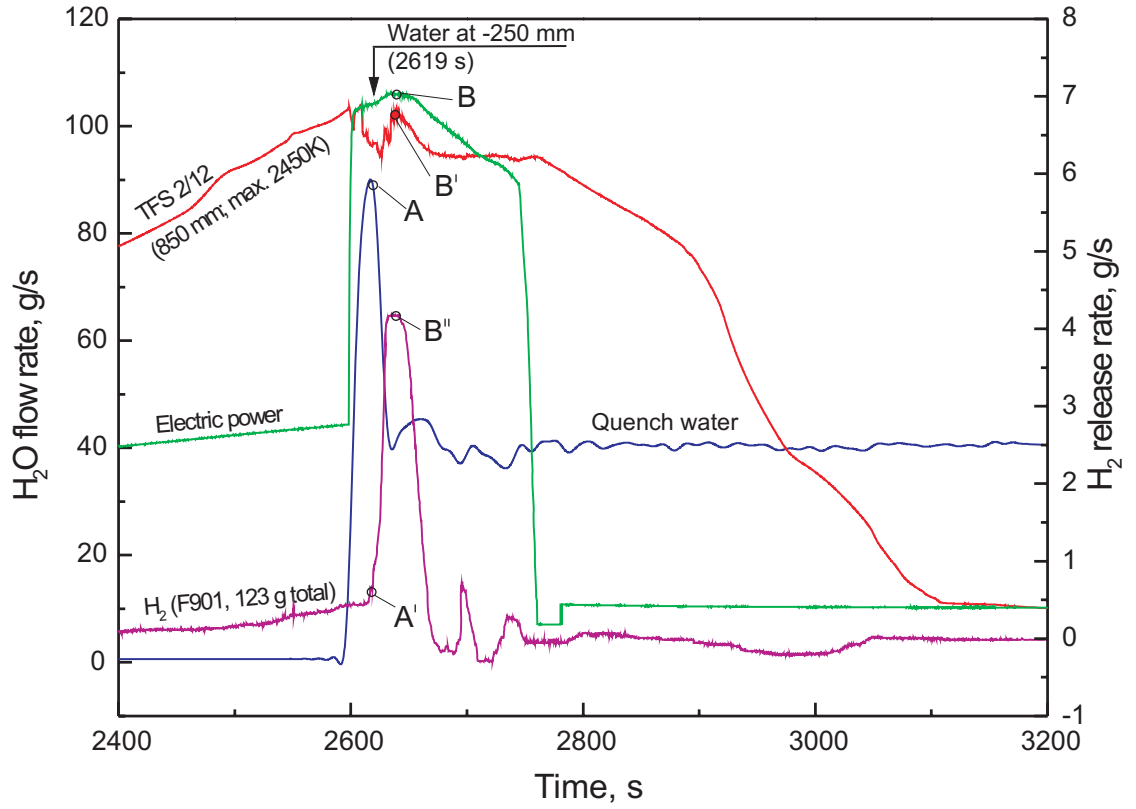

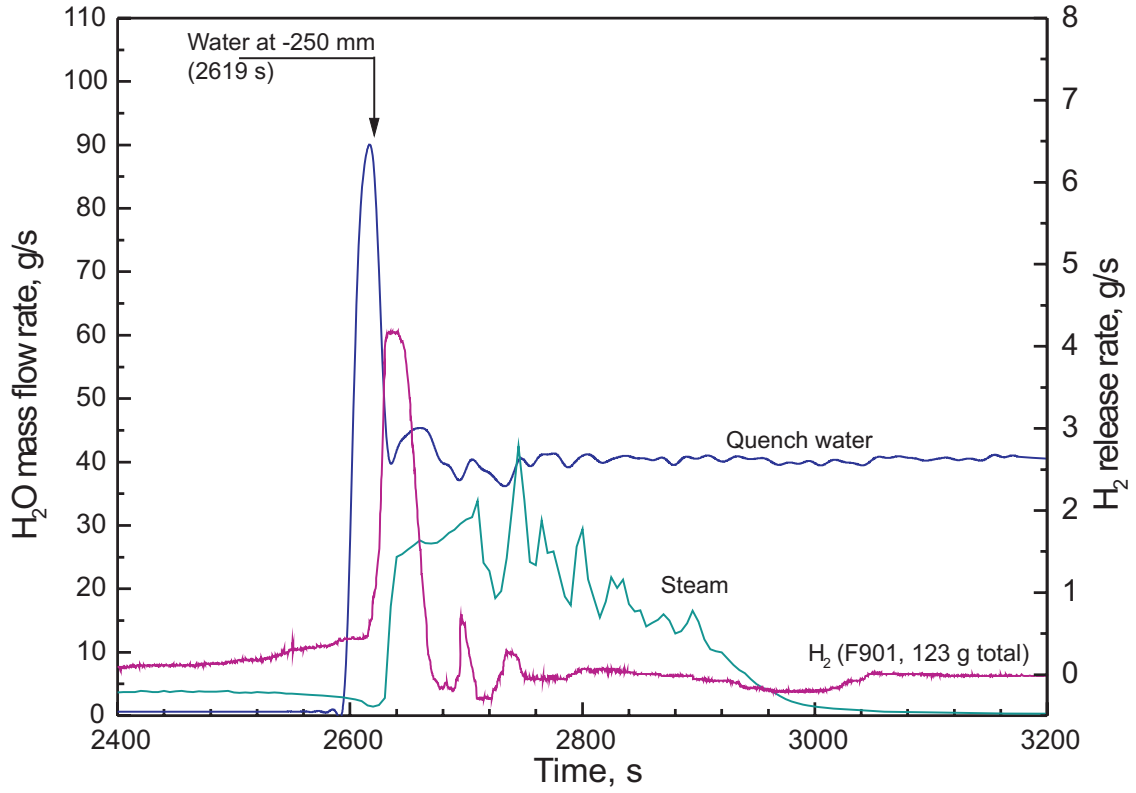

Fig 84

QUENCH-03

Hydrogen production measured by mass spectrometer (MS) and Caldos

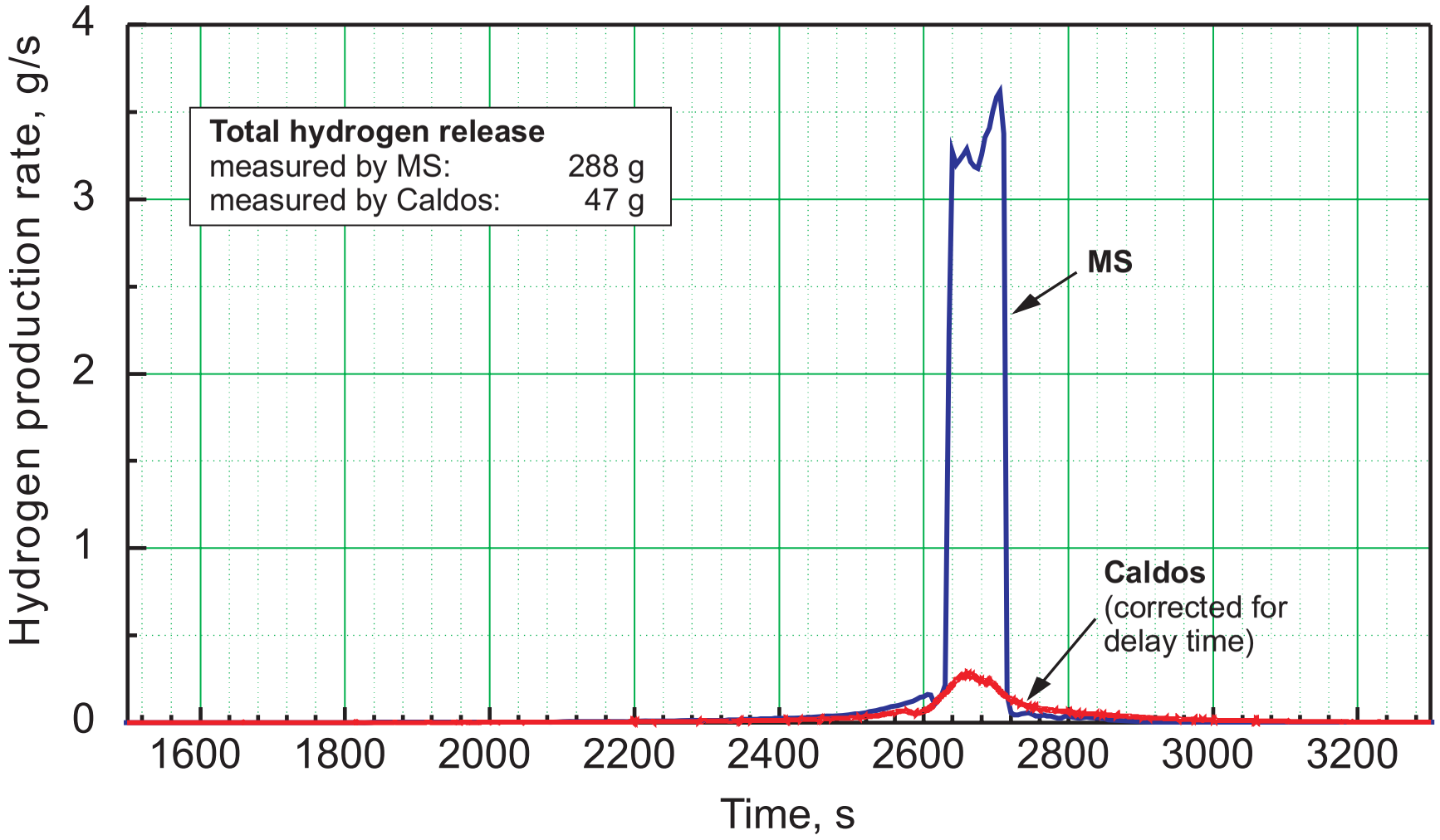

QUE_03_MS+Caldos
Feb. 23, 99

Fig 85

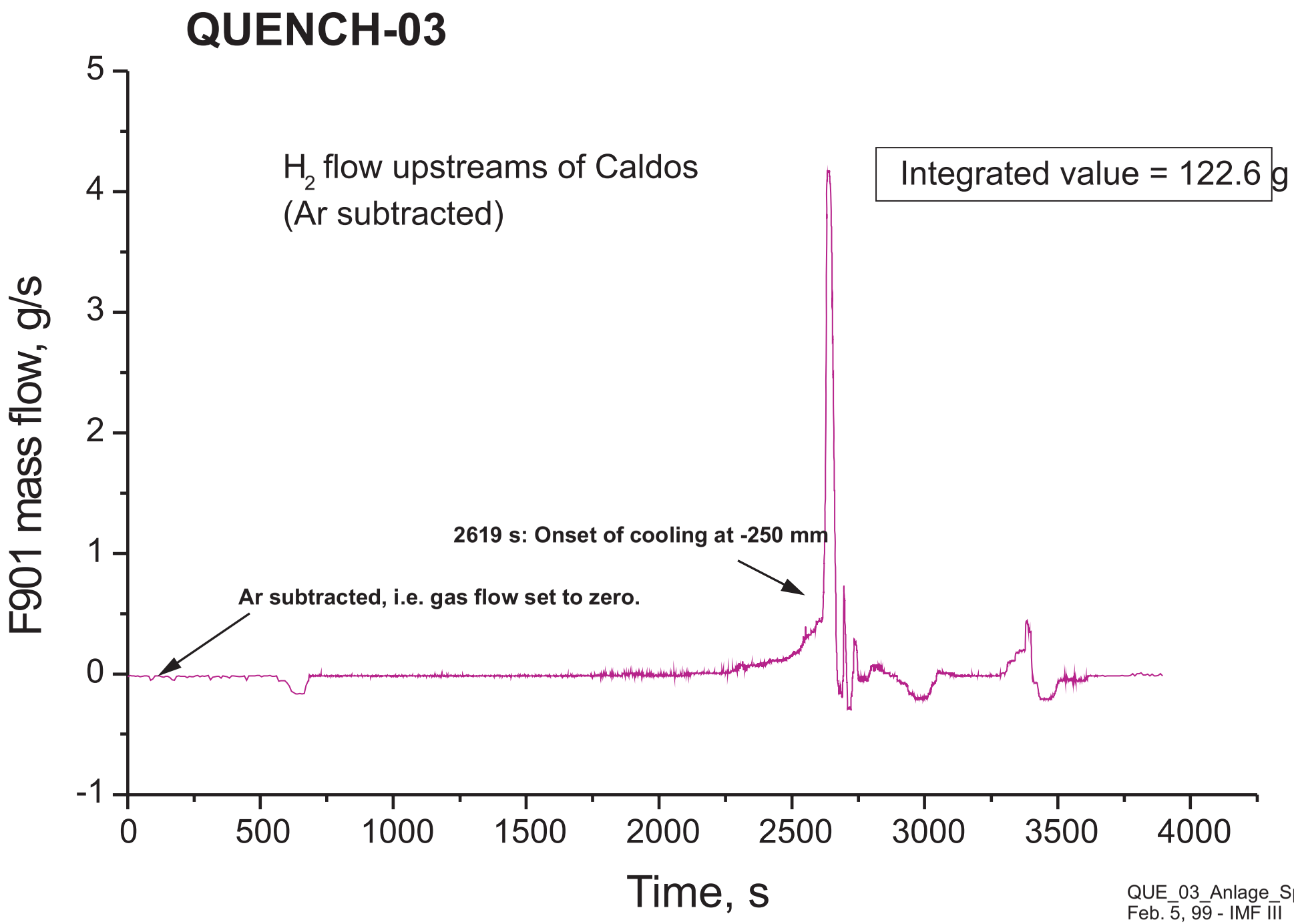

Fig 86

QUE_03_Anlage_Spezial
Feb. 5, 99 - IMF III

QUENCH-03

Posttest view of the bundle (540-1370 mm)

Fig 87

QUENCH-03

Solidified melt on the shroud surface (530 - 830 mm)

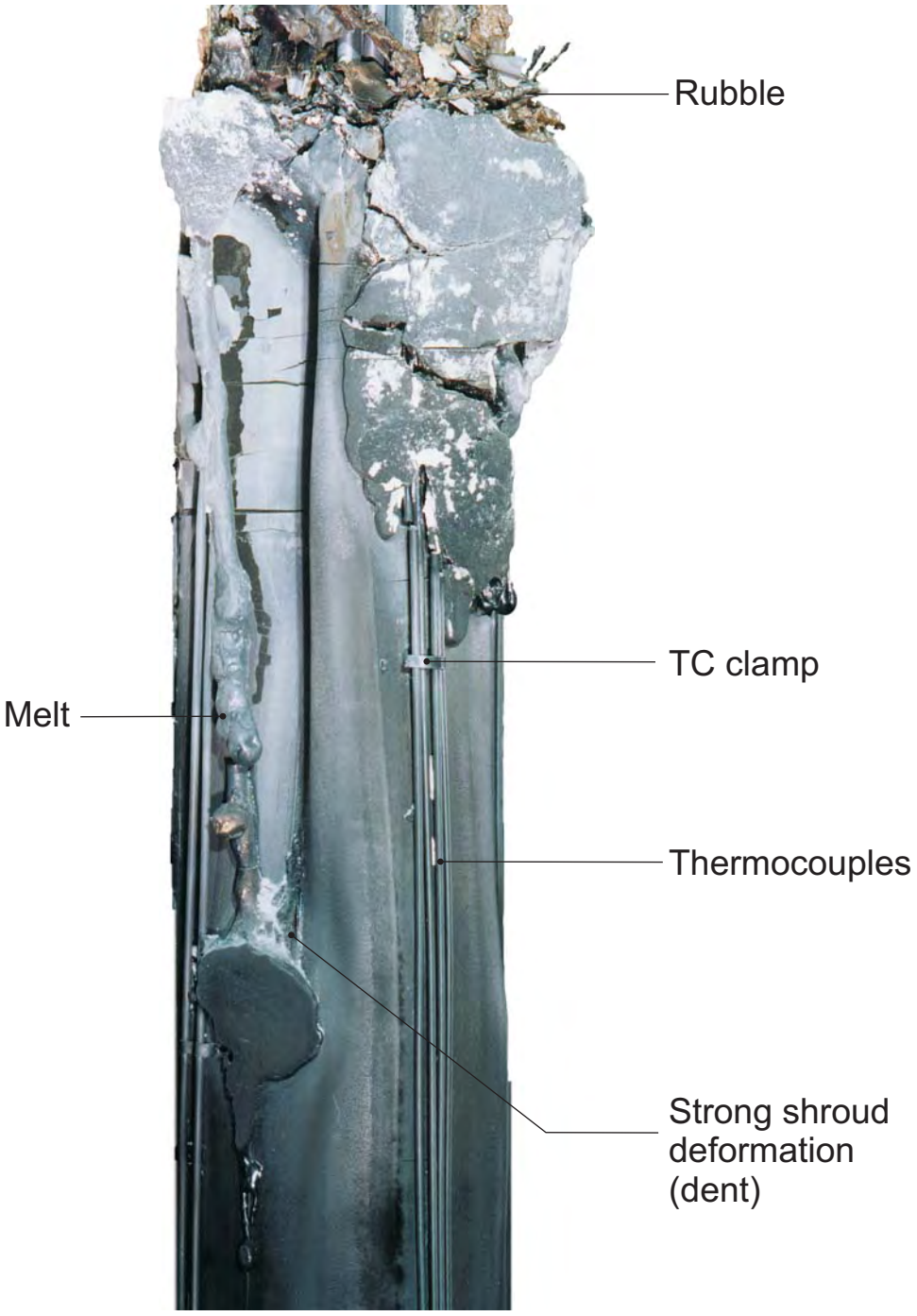

Fig 88

QUENCH-03

Posttest appearance of the bundle between 570 mm and 900 mm elevation

Fig 89

QUENCH-03

Posttest view of the region of total shroud destruction (770 -1070 mm)

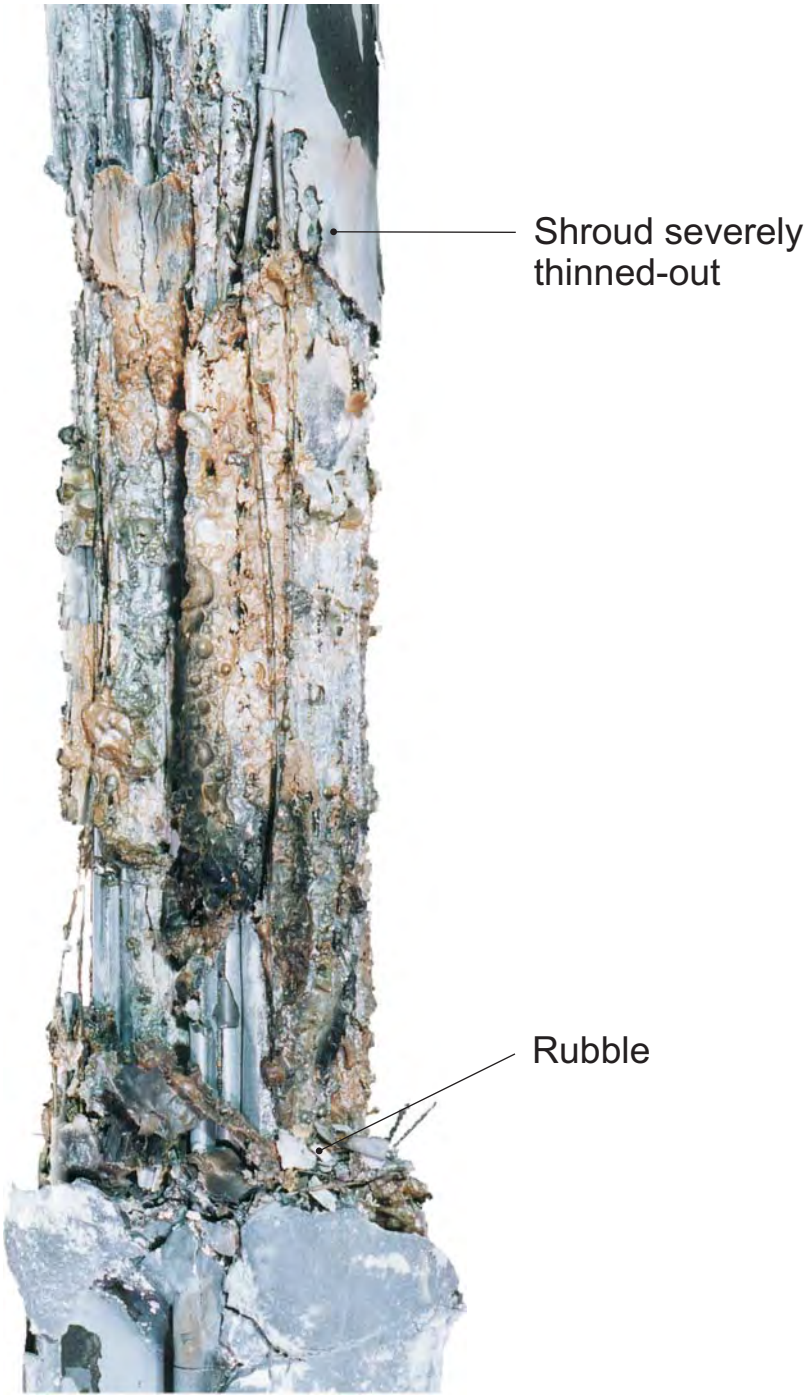

Fig 90

QUENCH-03

Bubble-like shroud and melt formation (720-930 mm)

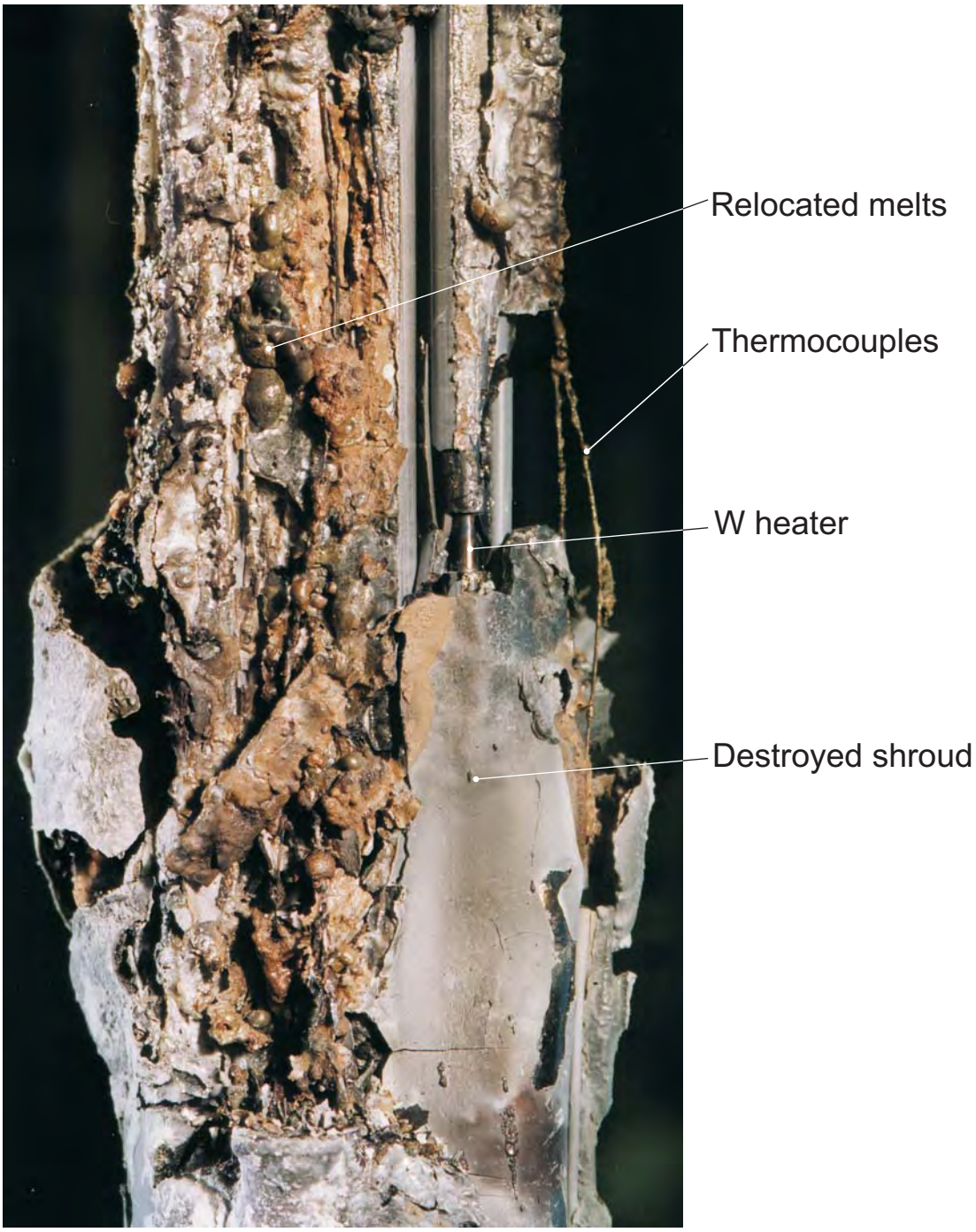

Fig 91

QUENCH-03

Posttest view of the upmost shroud region

Fig 92

QUENCH-03

Shroud and bundle fragments broken off the upper bundle region by posttest handling

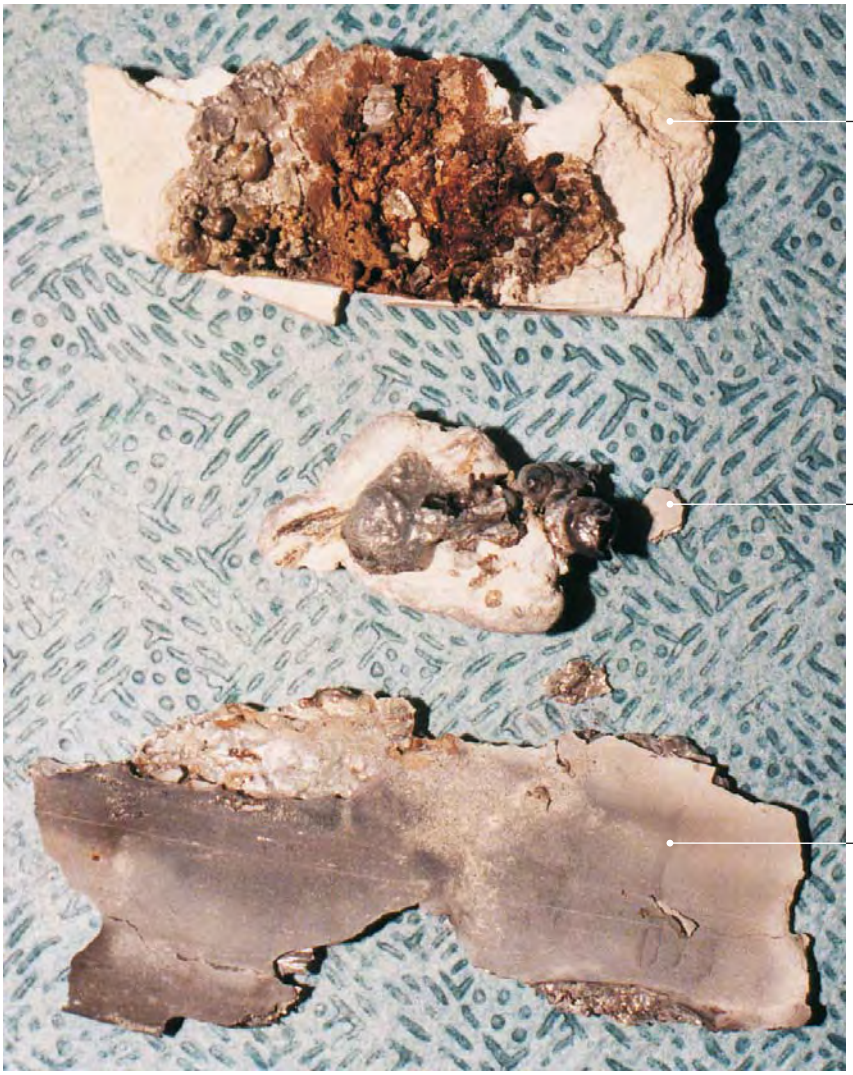

Fig 93

Sectioning of Test Bundle QUENCH-03

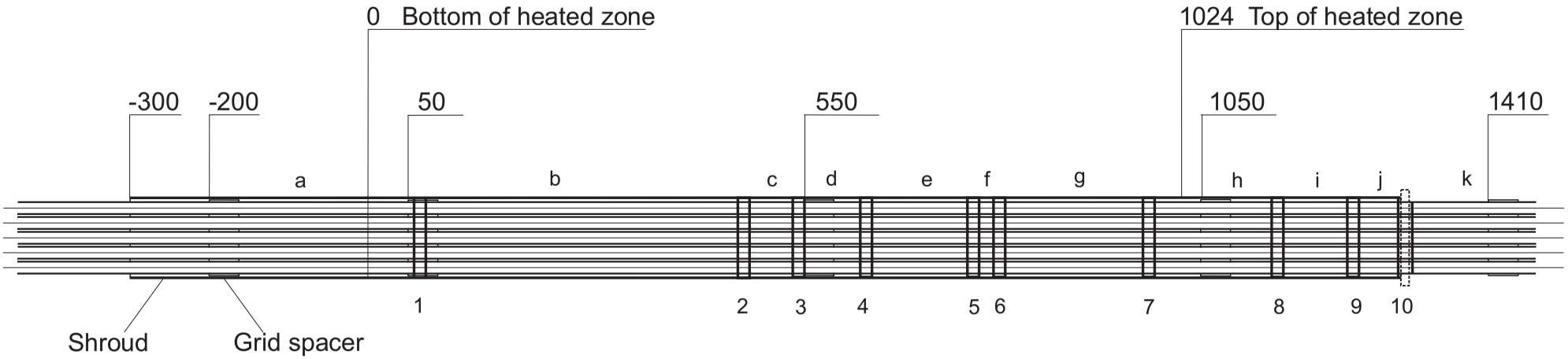

Fig 94

QUENCH-03, Cross Sections

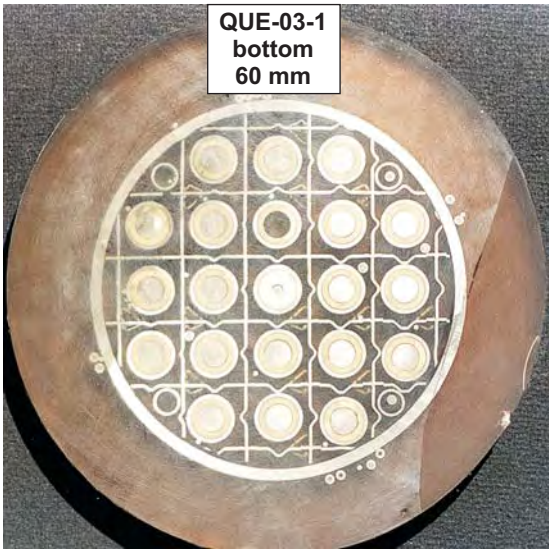

60 mm

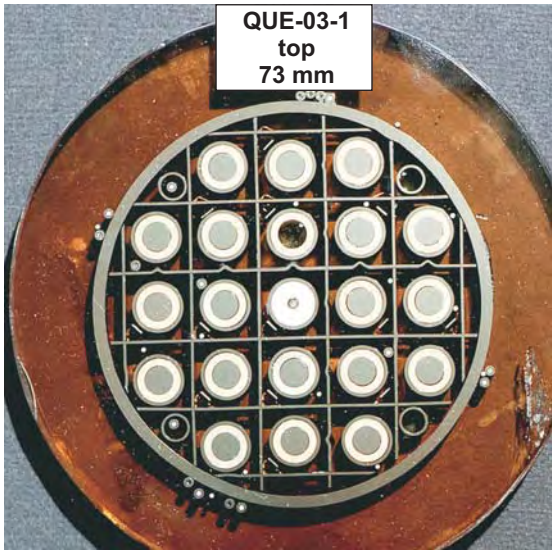

73 mm (polished)

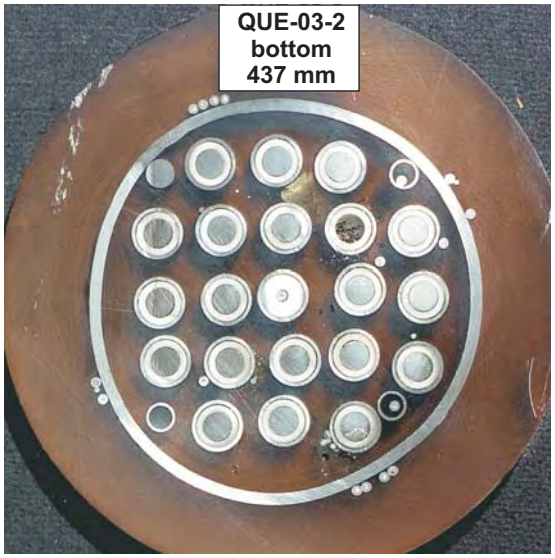

437 mm

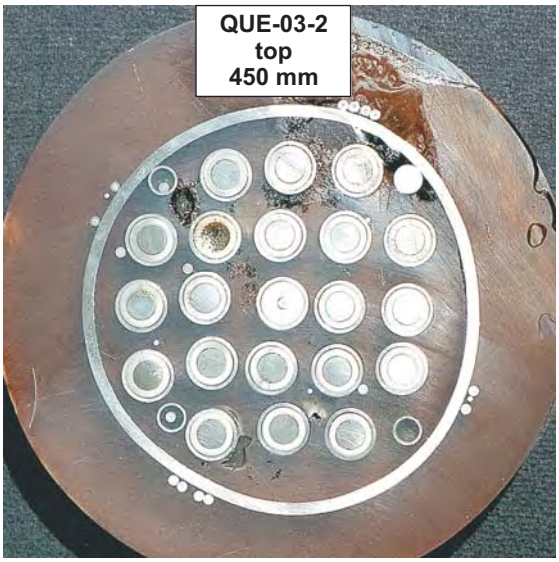

450 mm

537 mm

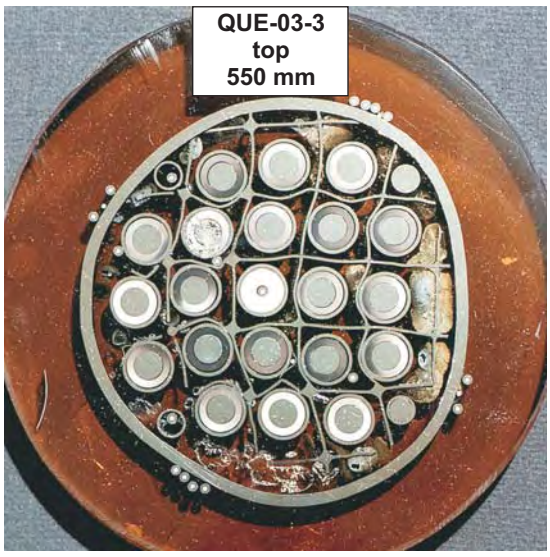

550 mm (polished)

QUENCH-03, Cross Sections

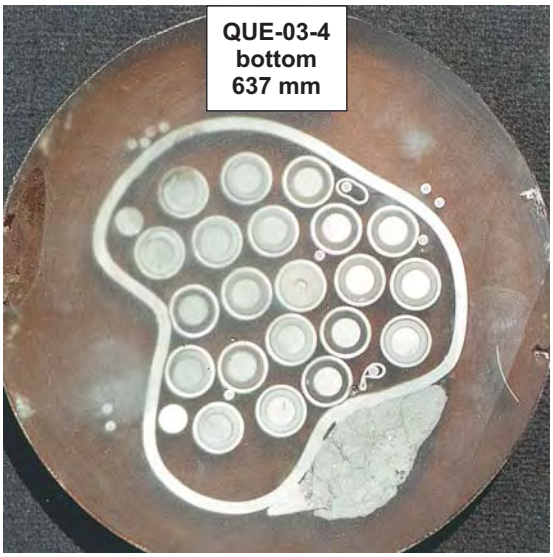

637 mm

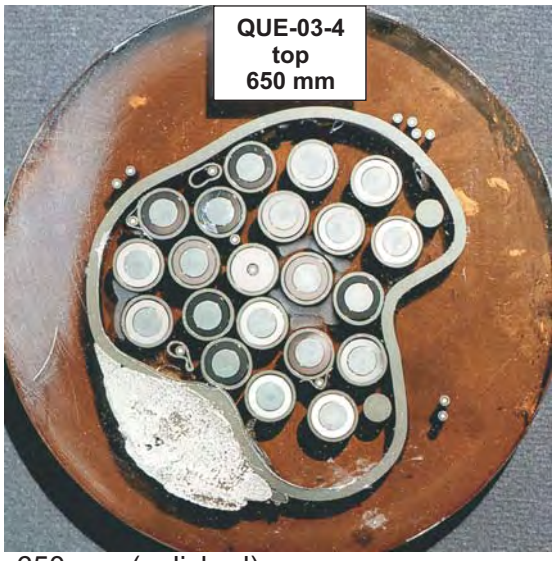

650 mm (polished)

737 mm

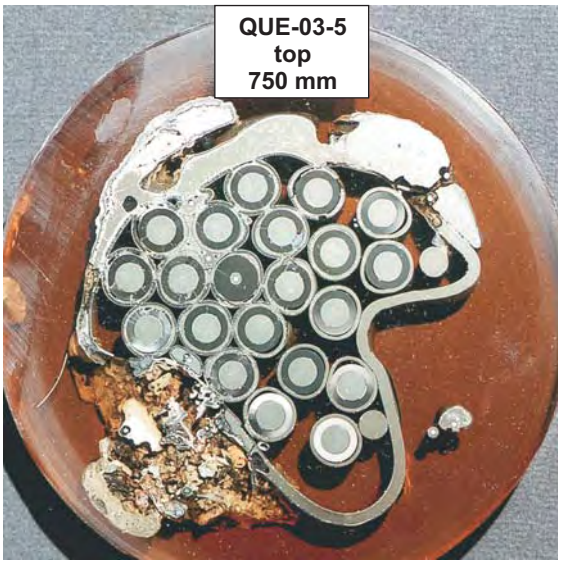

750 mm (polished)

787 mm

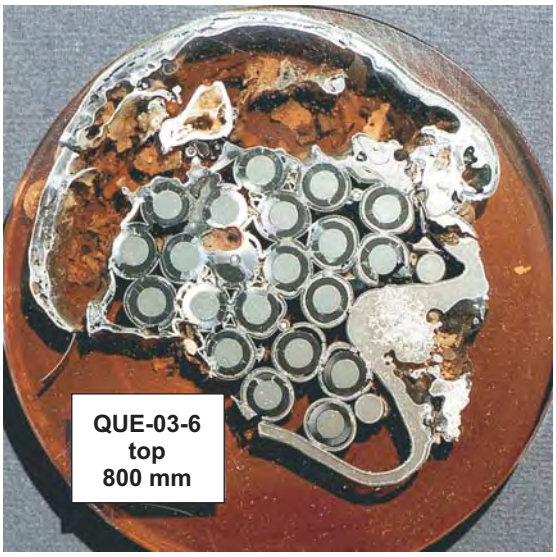

800 mm (polished)

QUENCH-03, Cross Sections

930 mm

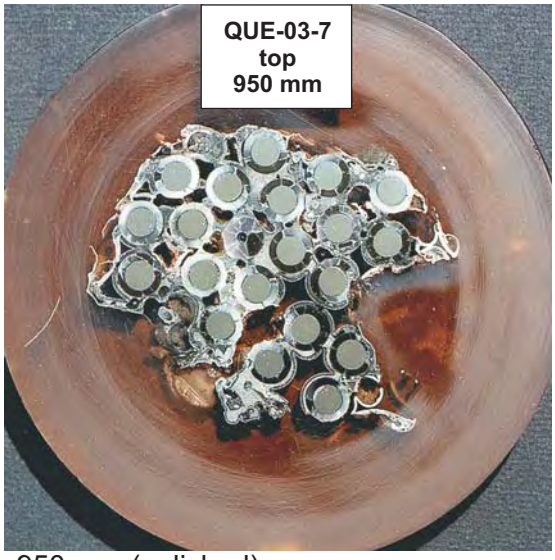

950 mm (polished)

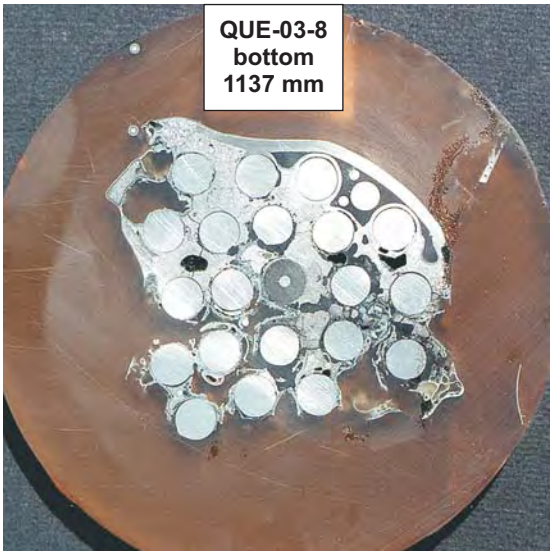

1137 mm

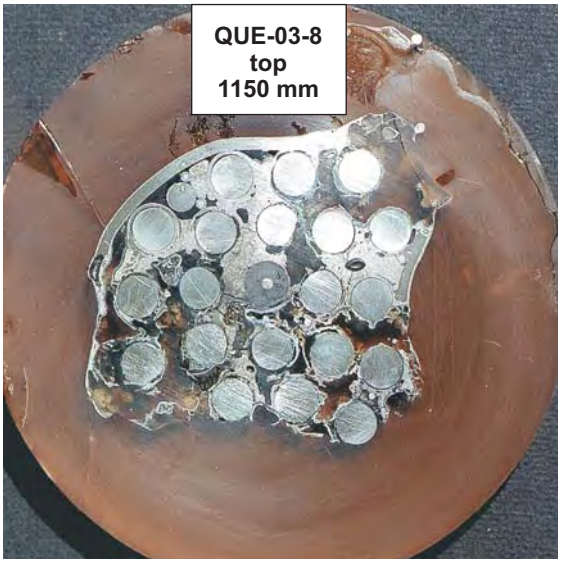

1150 mm

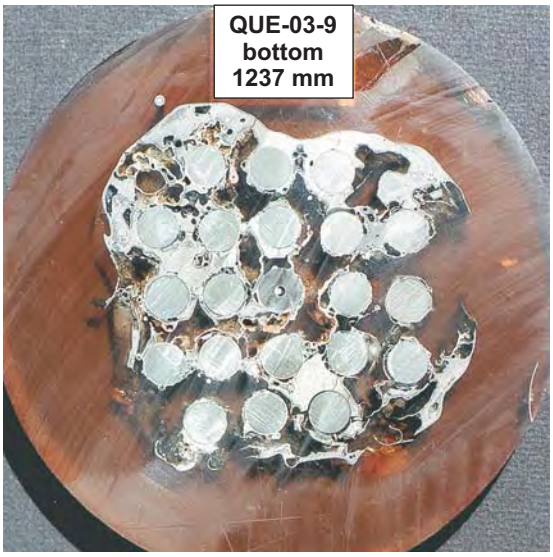

1237 mm

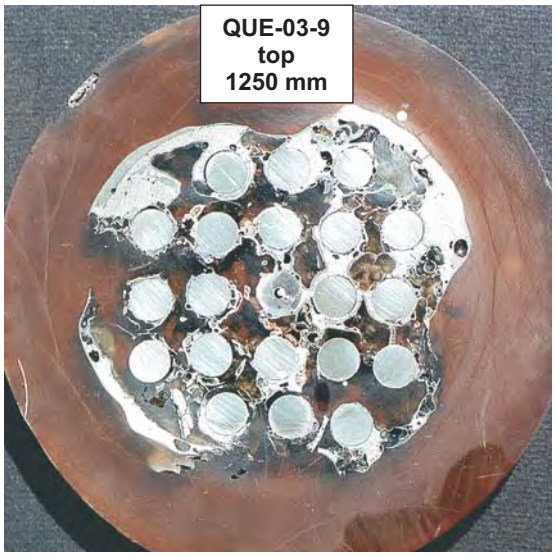

1250 mm

QUENCH-03, Cross Sections

1295 mm

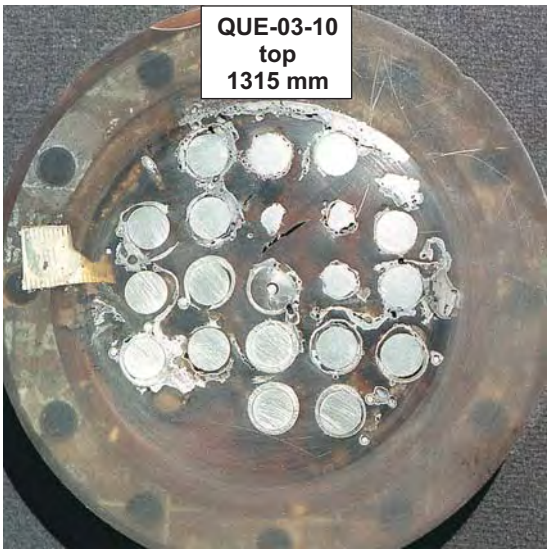

1315 mm

QUENCH-03: Polished cross section overview at bundle elevation 73 mm (QUE-03-1, top)

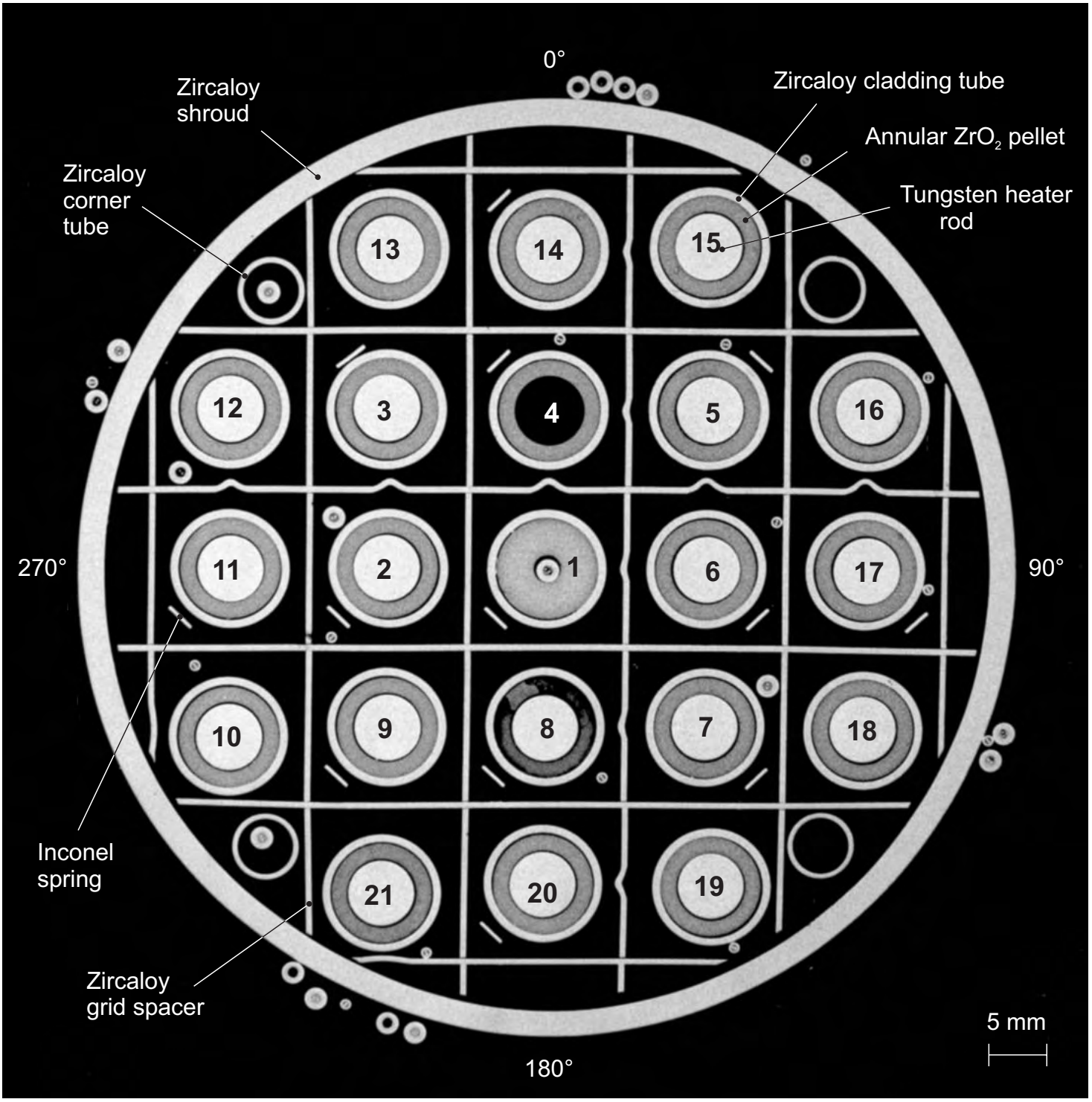

Reference for rod arrangement, spacer grid and shroud

Fig 99

QUENCH-03: Cross section at elevation 550 mm (QUE-03-3, top); spacer grid bulging due to rod bowing

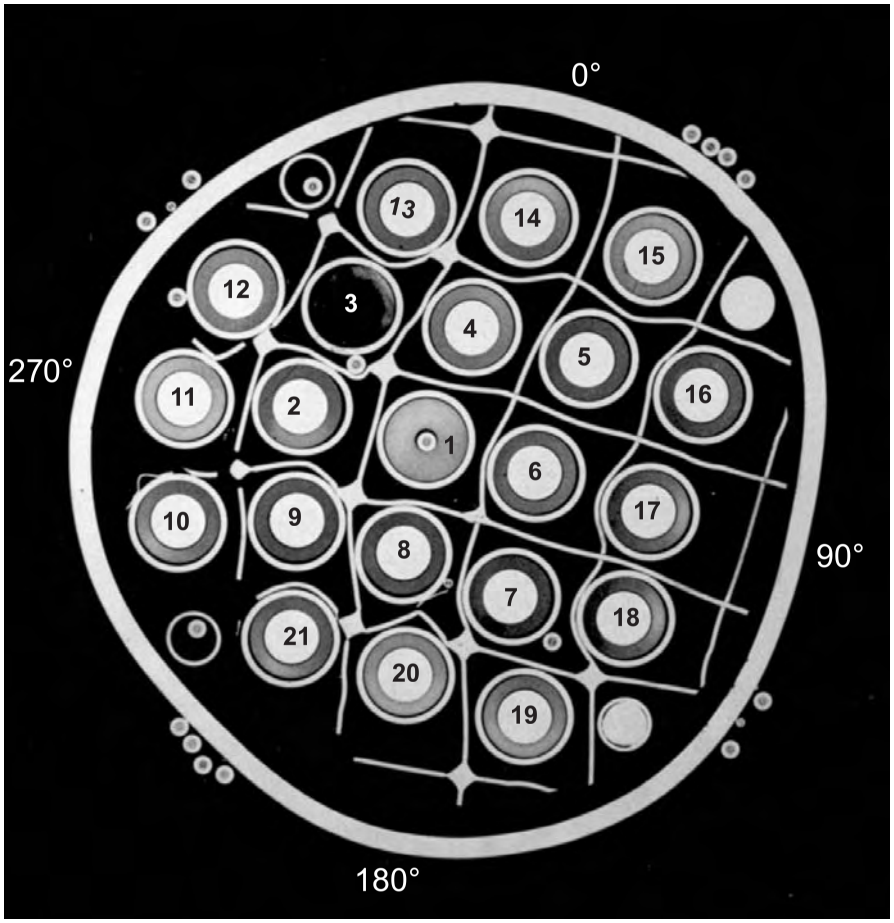

10 mm

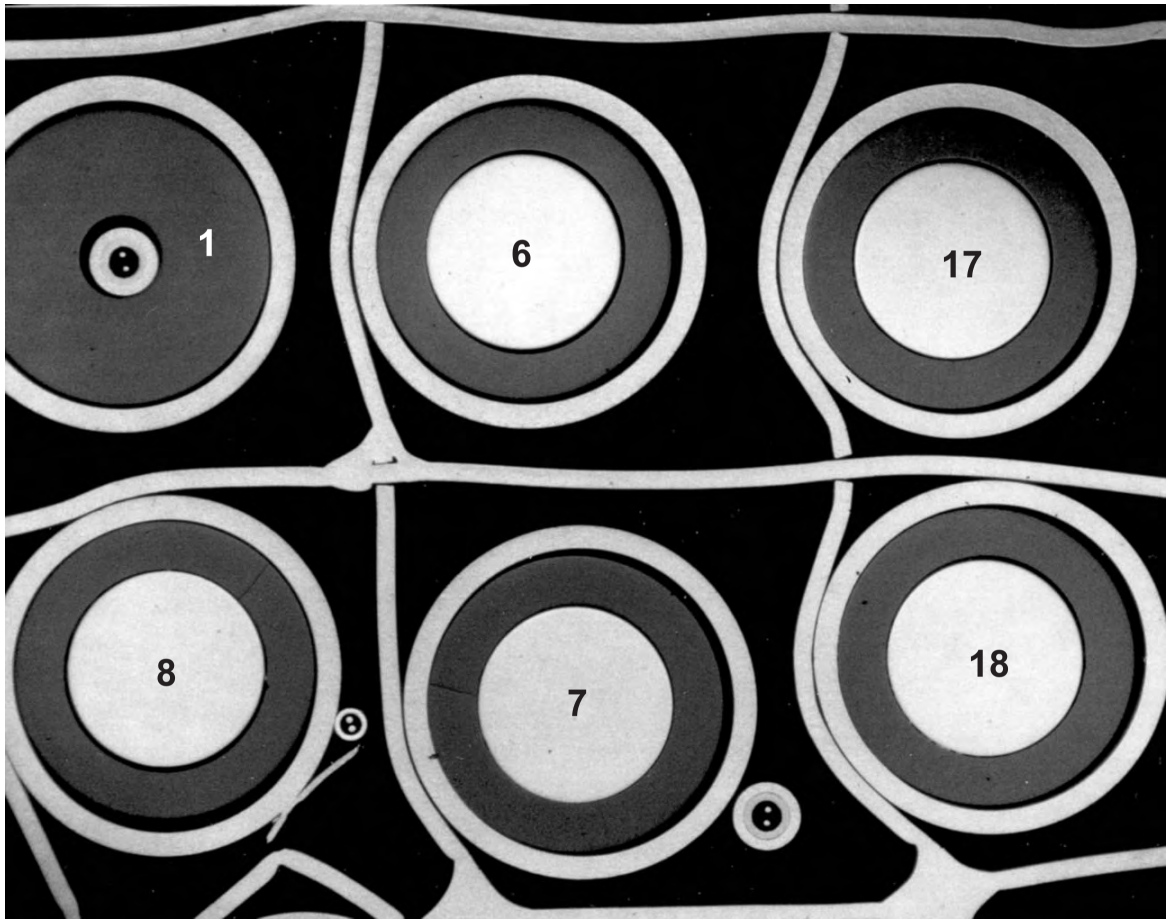

5 mm

Fig 100

QUENCH-03: Cross section at elevation 550 mm (QUE-03-3, top); cladding and spacer oxidation

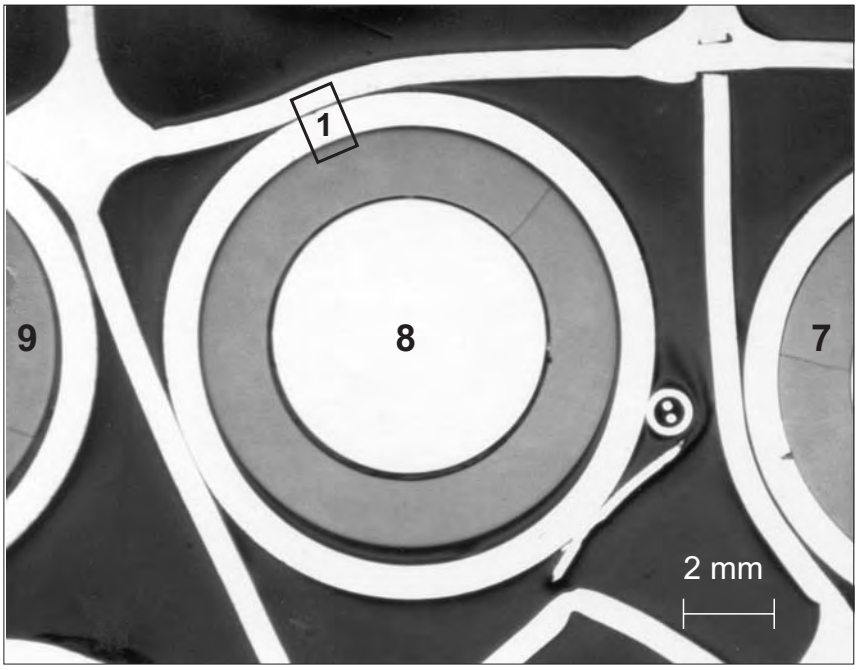

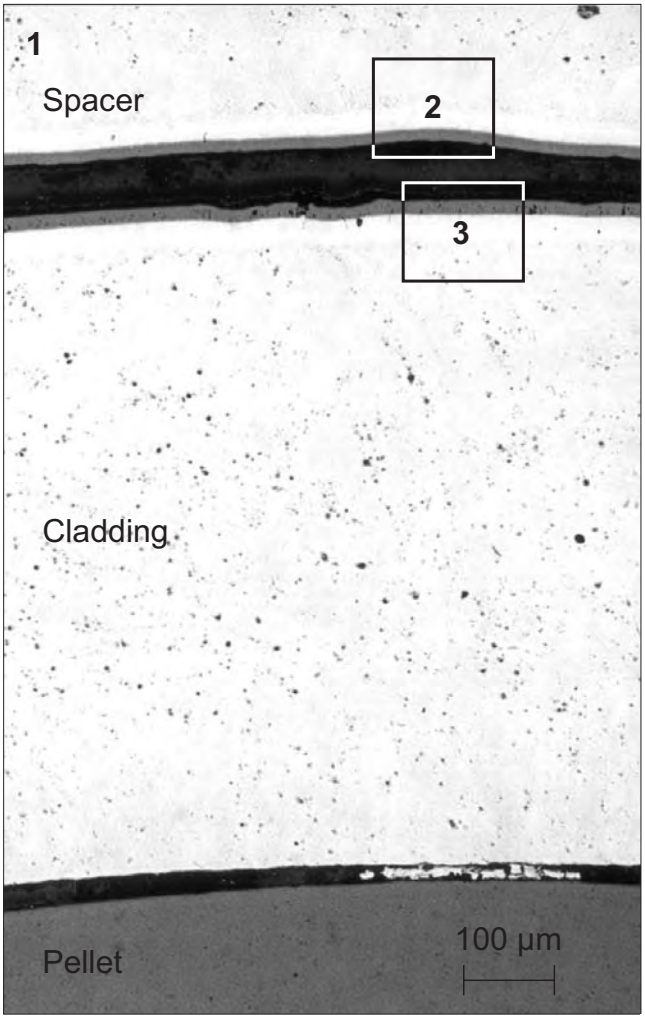

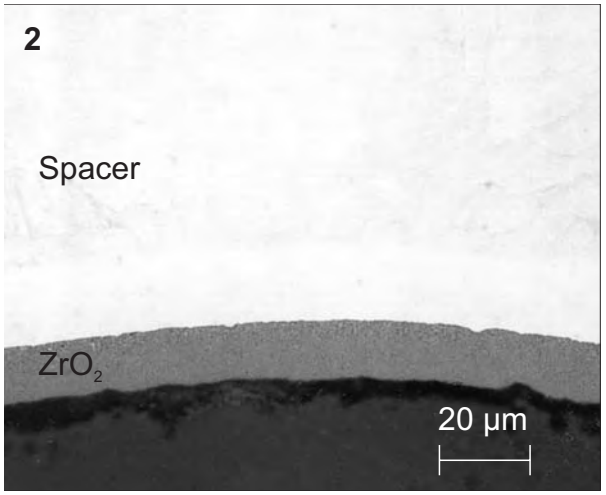

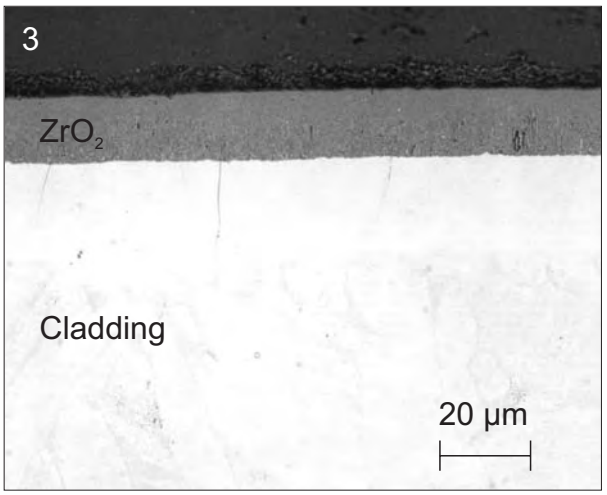

QUENCH-03: Cross section at elevation 650 mm (QUE-03-4, top)

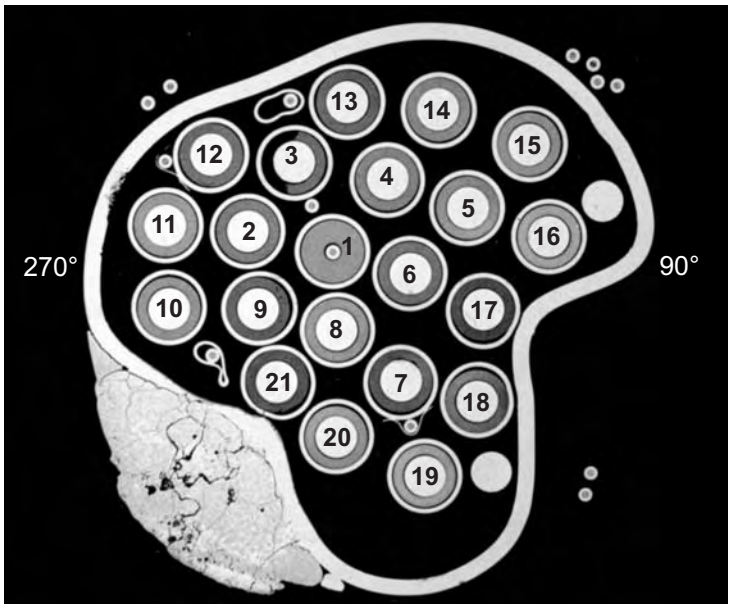

Overview

10 mm

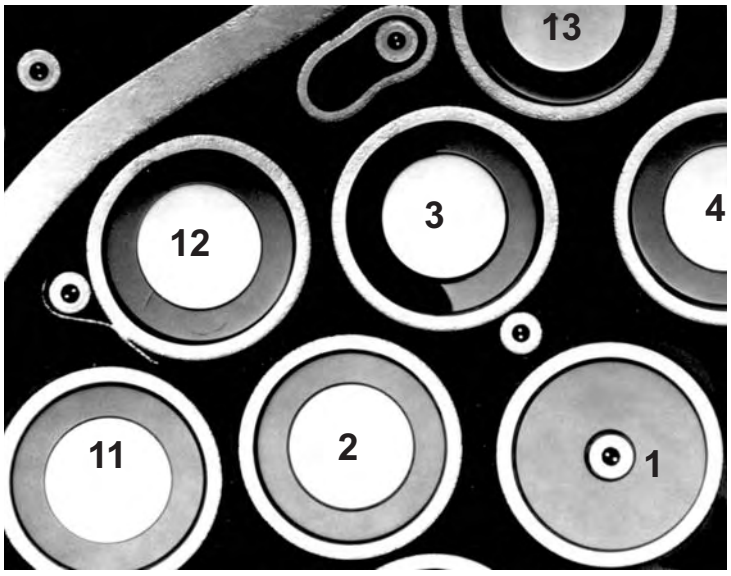

Rod arrangement

5 mm

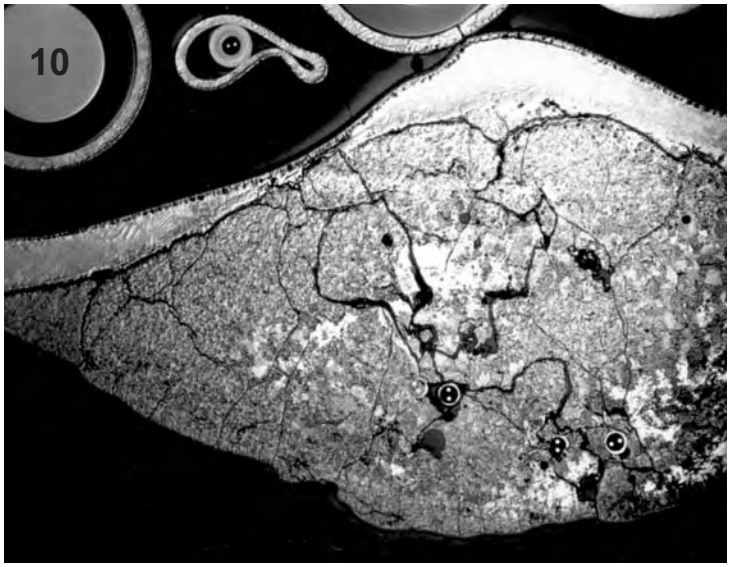

Melt accumulation at external side of shroud

5 mm

Fig 102

QUENCH-03: Cross section at elevation 650 mm (QUE-03-4, top); shroud in contact with externally relocated melt

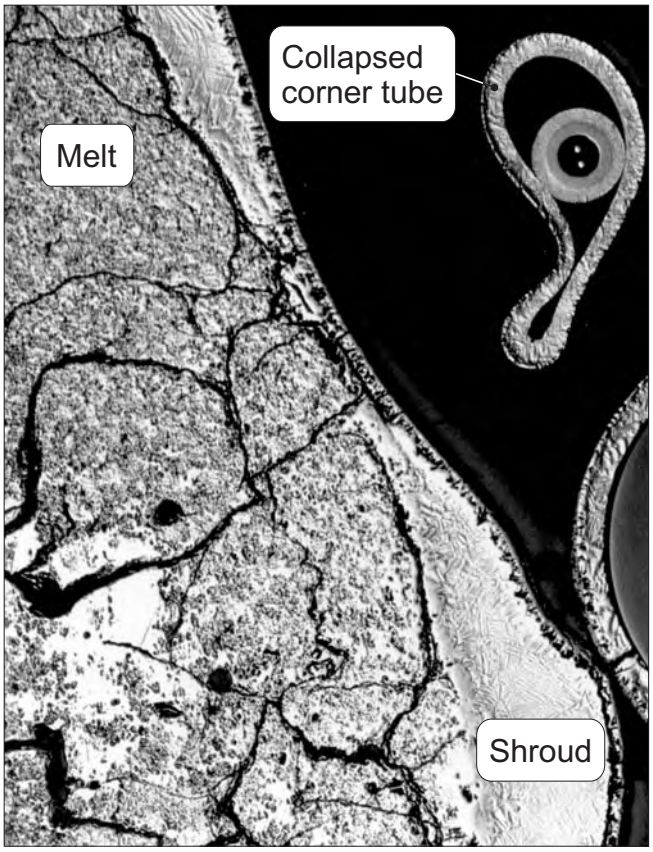

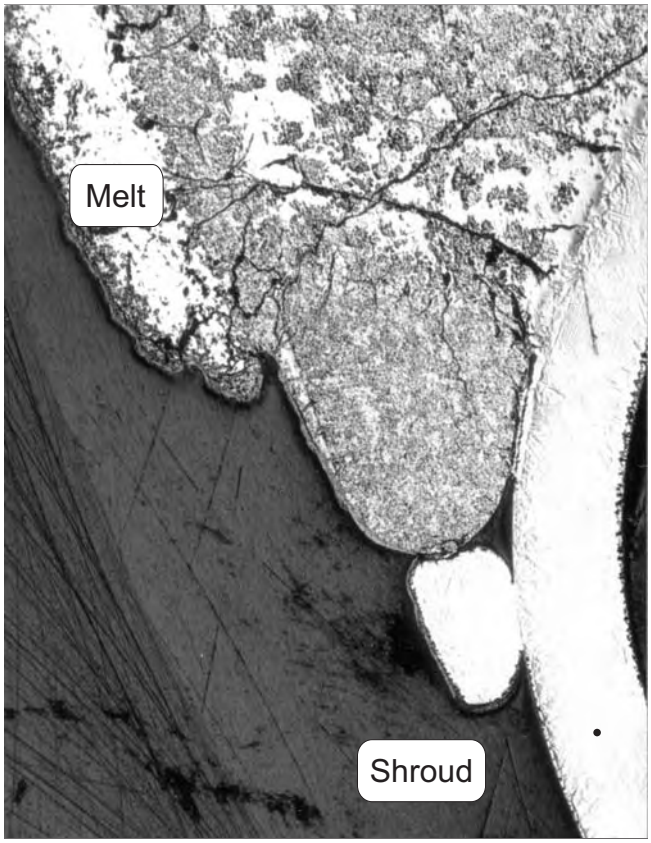

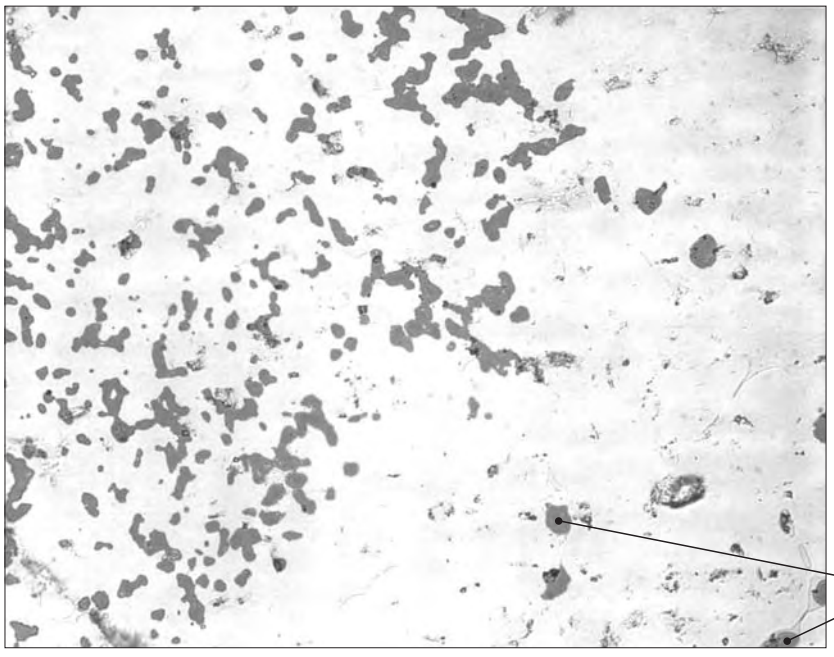

Microstructural details of a transition region between oxygen poor (right) and oxygen richer (left) melt

Fig 103

QUENCH-03: Cross section at elevation 650 mm (QUE-03-4, top); bundle oxidation status

Fuel rod oxidation

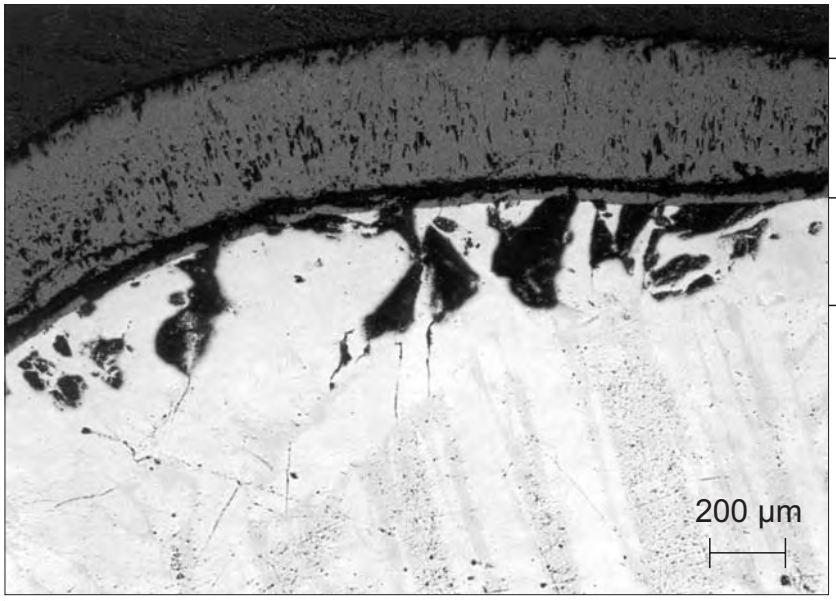

Oxidation of dense Zr rich melt type

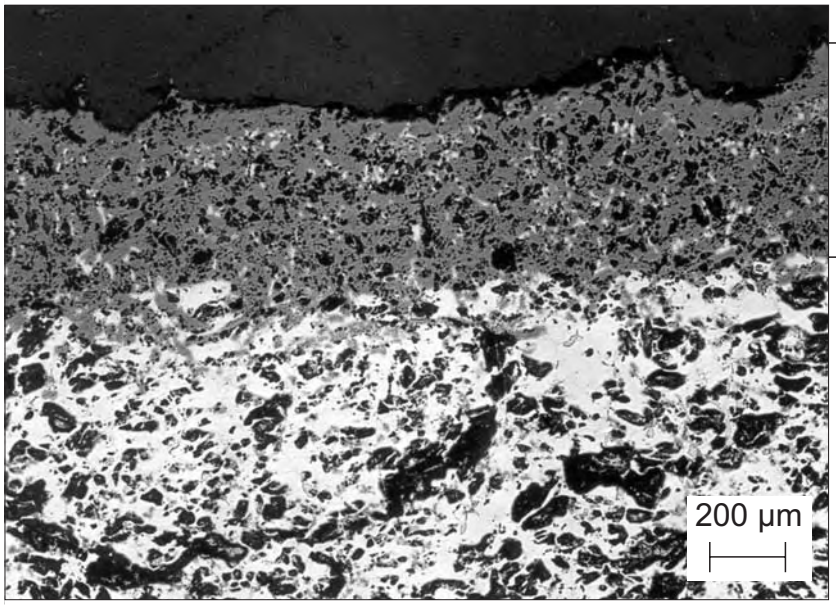

Oxidation of porous melt type

Fig 104

QUENCH-03: Cross section at elevation 750 mm (QUE-03-5, top)

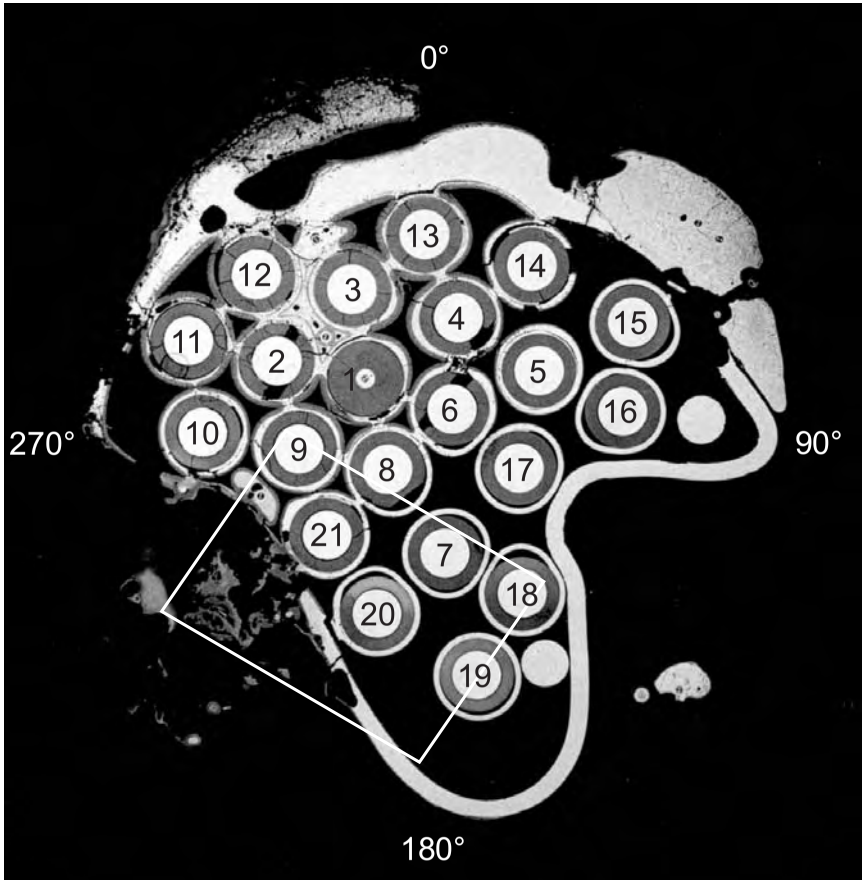

Global overview

10 mm

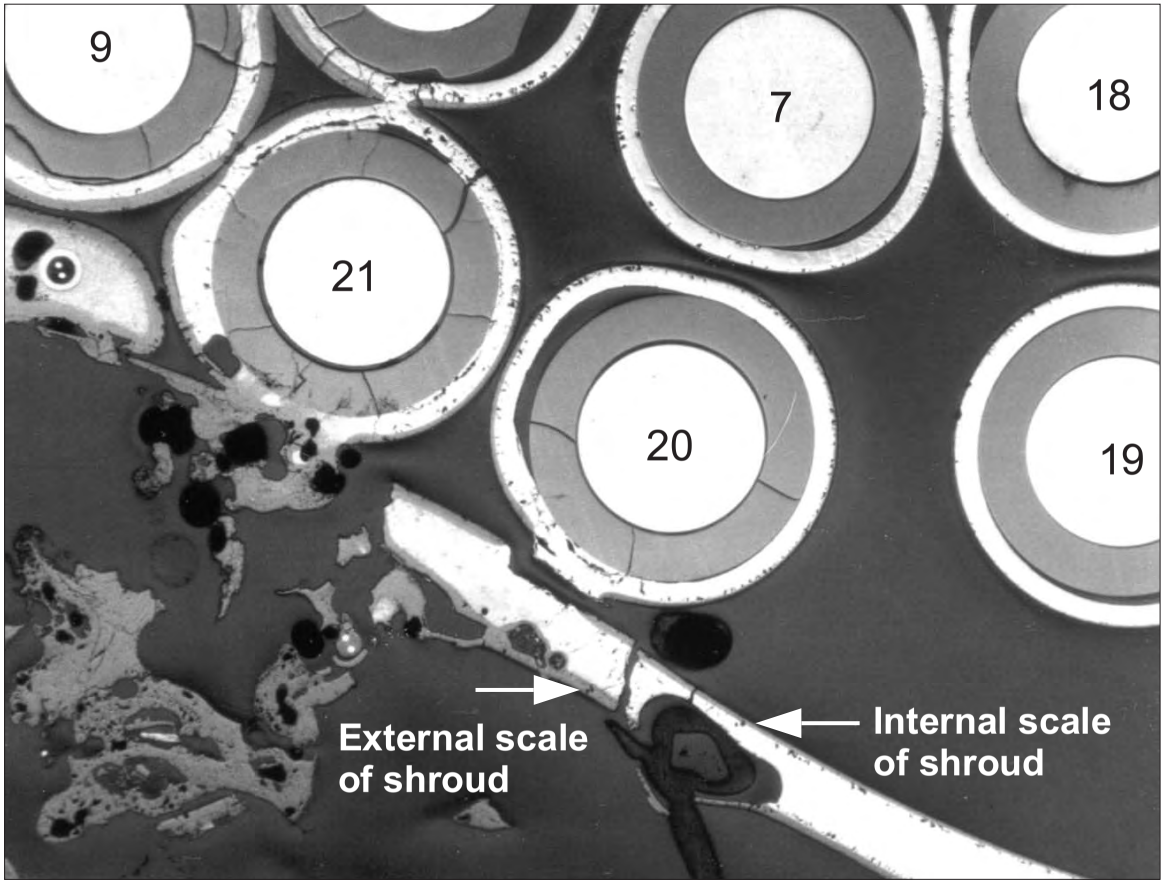

Shroud destruction

5 mm

Fig 105

QUENCH-03: Cross section at elevation 750 mm (QUE-03-5, top); shroud destruction, involving oxidation, melting, thickening from intrinsically relocated melt, interaction in contact with other relocated melts, dissolution and product melt relocation, interaction with rods and pellets

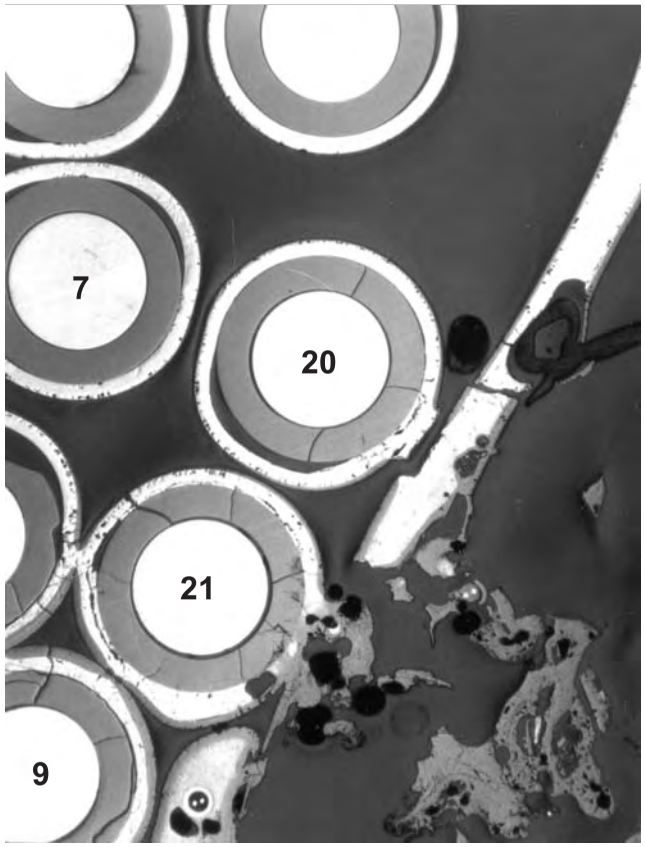

Overview on shroud destruction morphology

5 mm

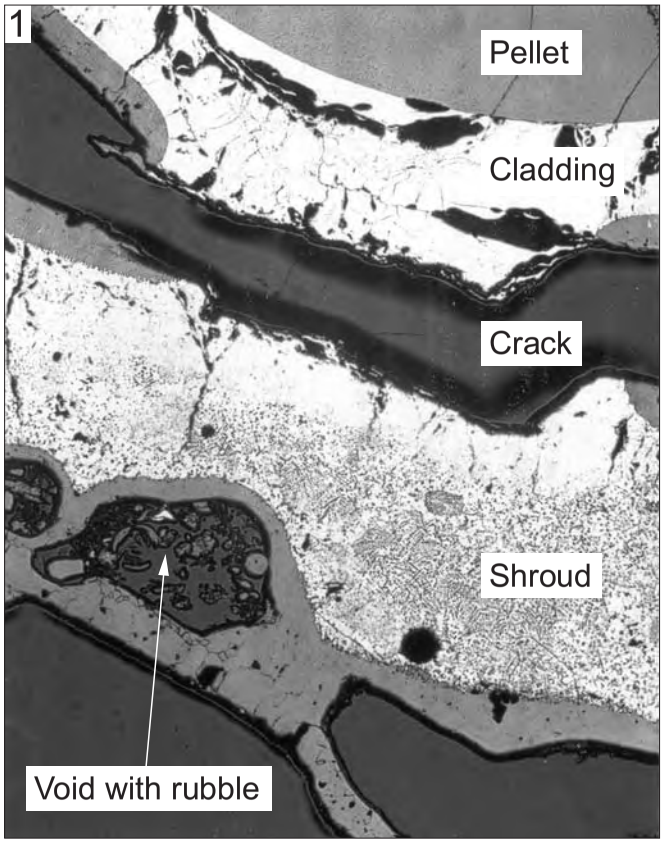

Rod after broken contact, thickened and oxidized shroud, oxidized external melt

500 µm

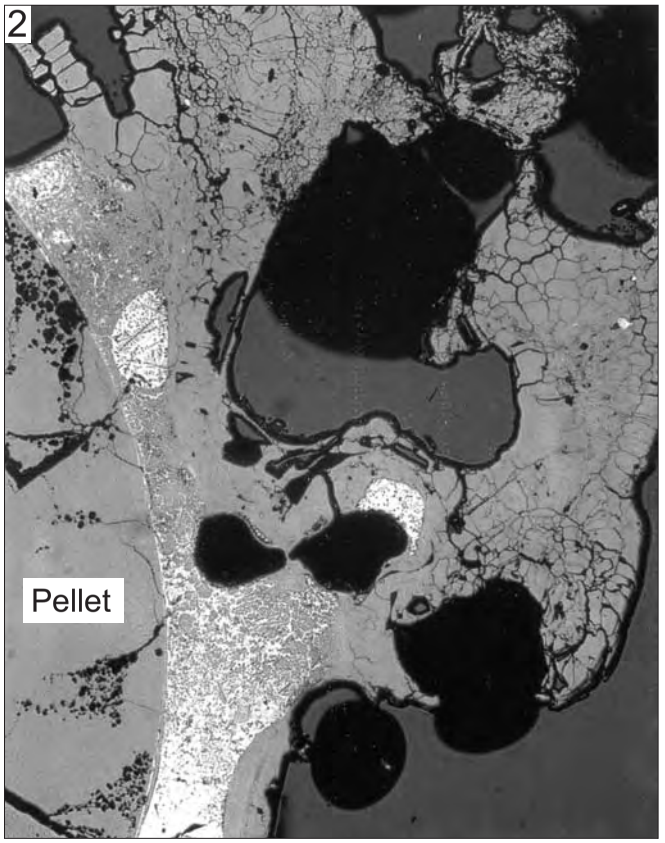

Pellet in close contact with shroud residues, mostly oxidized melt

500 µm

Fig 106

QUENCH-03: Cross section at elevation 750 mm (QUE-03-5, top); cladding oxidation

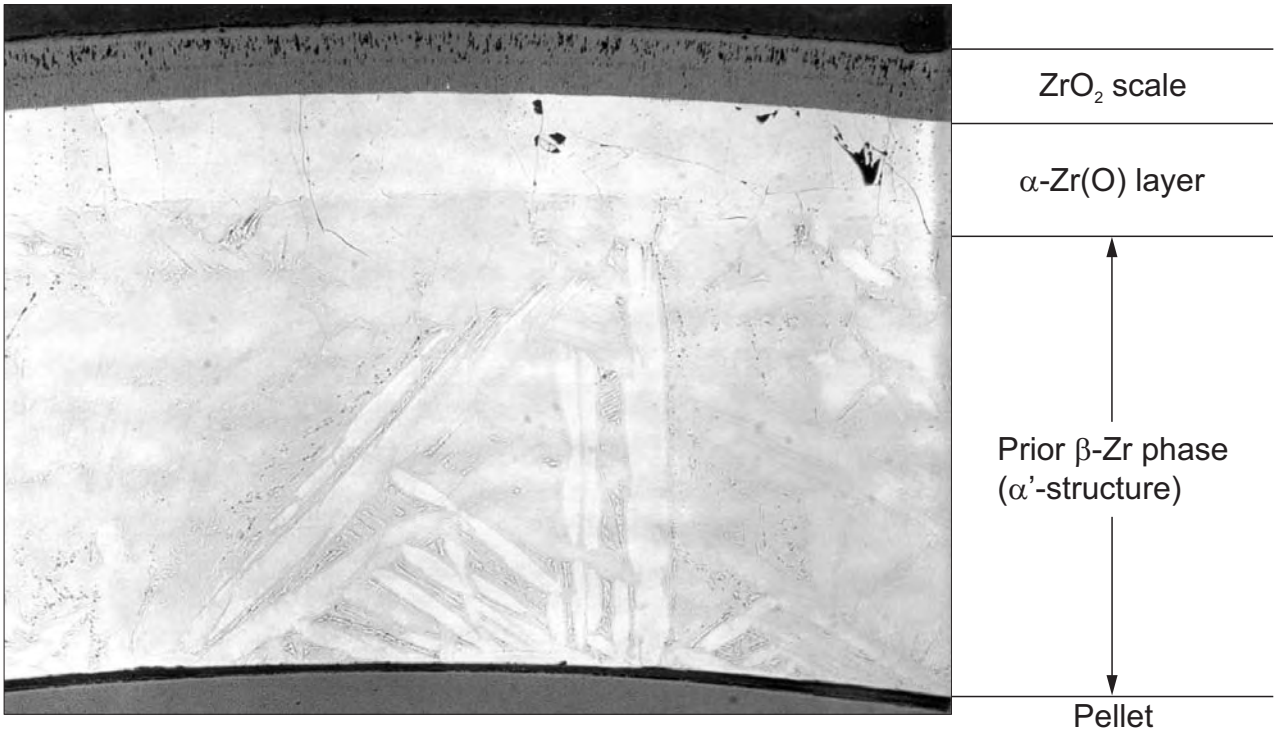

100 µm

External and internal oxidation

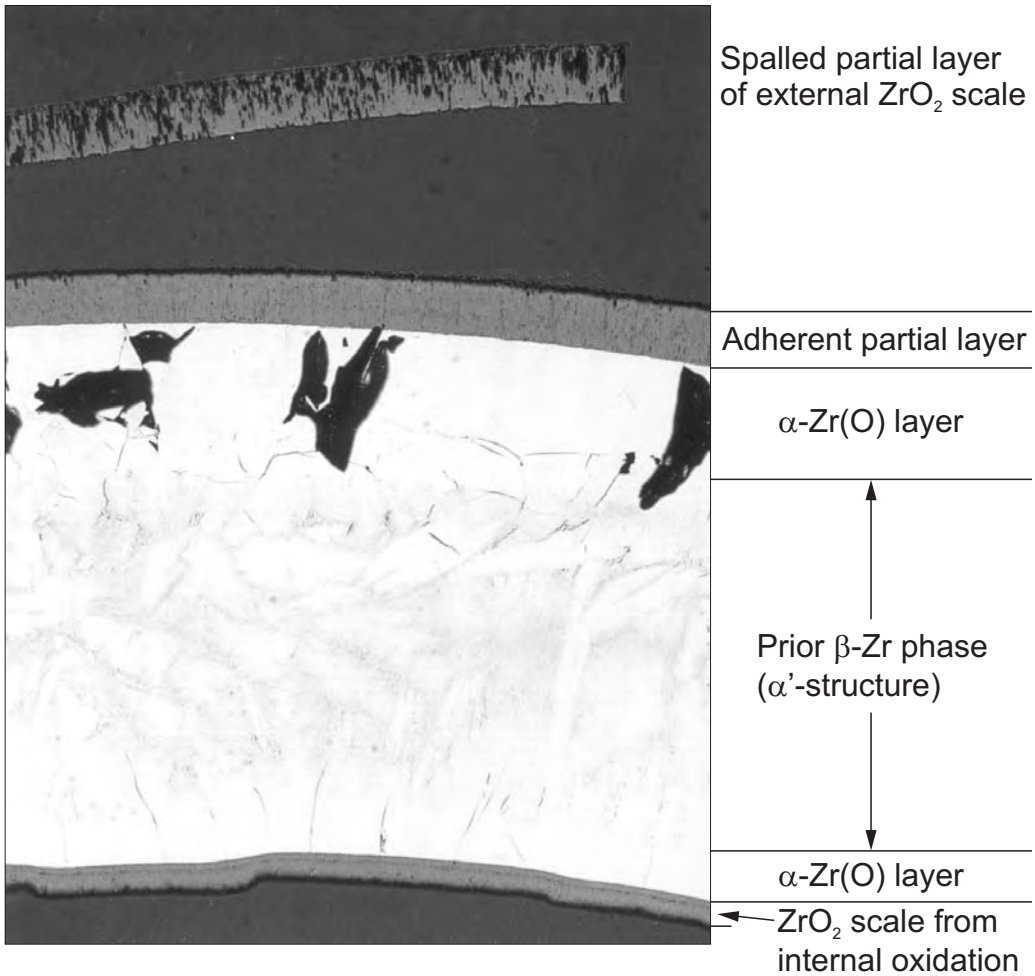

QUENCH-03: Cross section at elevation 750 mm (QUE-03-5, top); negligible internal cladding oxidation due to limited steam access after cladding fracture or late (low temperature) clad fragmentation

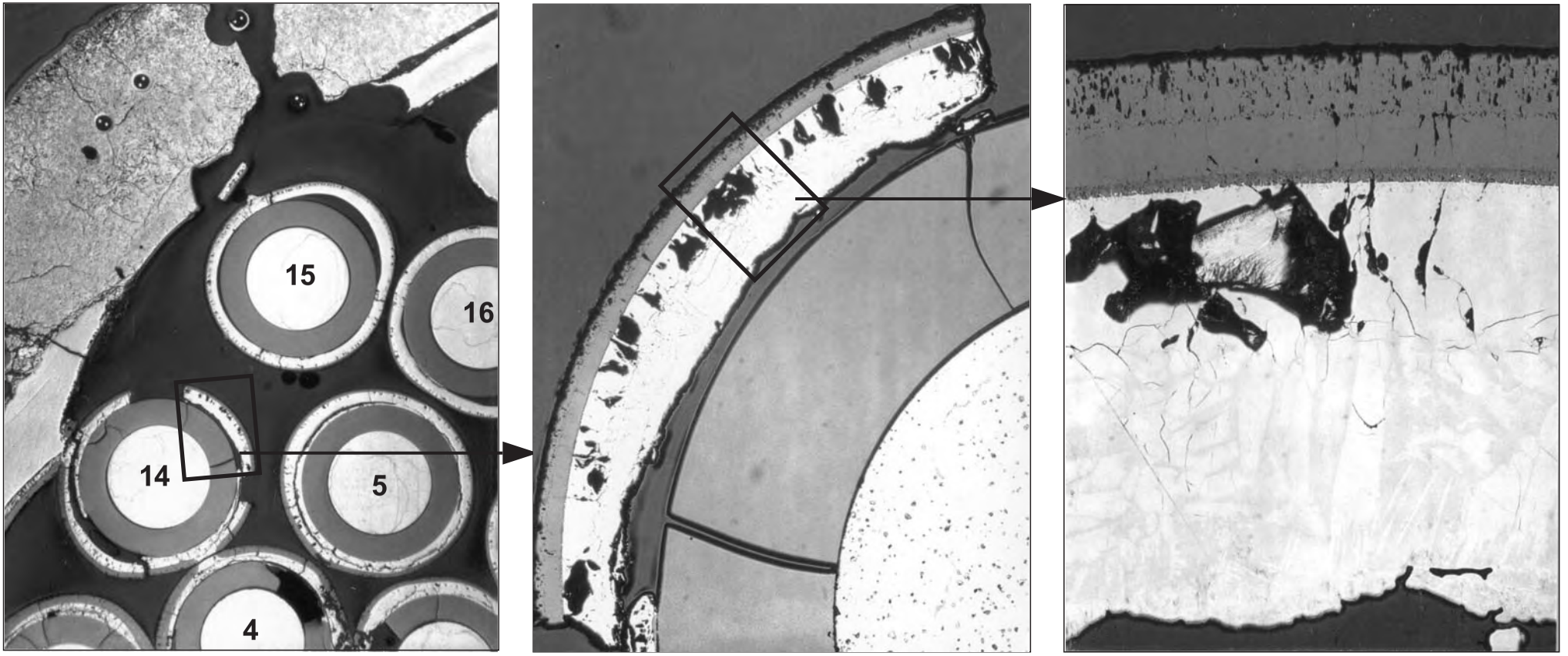

Fig 108

QUENCH-03: Cross section at elevation 750 mm (QUE-03-5, top); continued cladding oxidation after clad thickening by rod-internally relocated clad melt

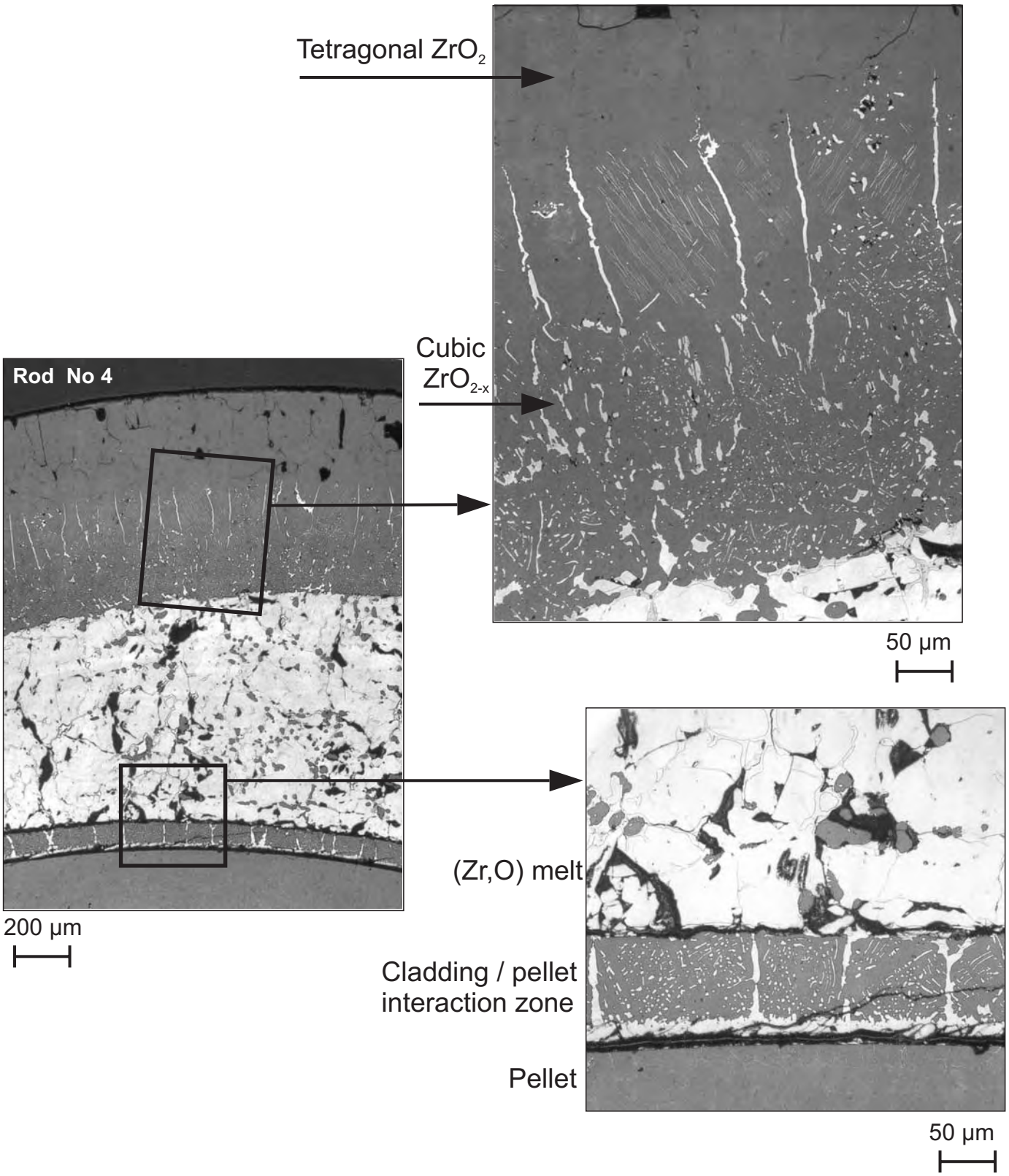

Fig 109

QUENCH-03: Cross section at elevation 750 mm (QUE-03-5, top); formation of necks between touching fuel rod simulators

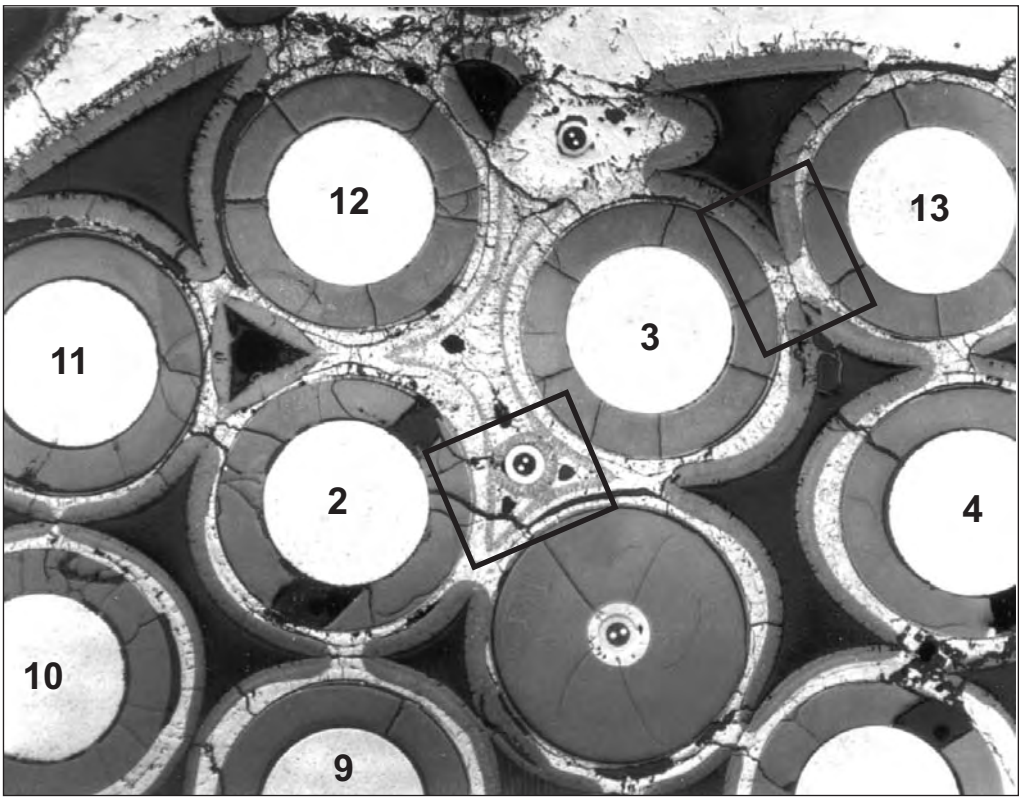

5 mm

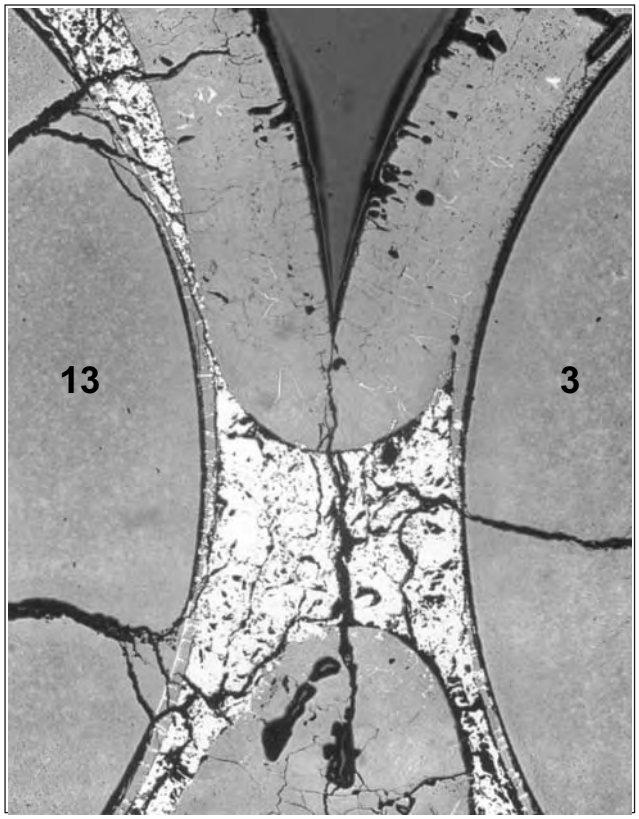

500 µm

Neck of once molten material, surrounded by ZrO_2 scale and adjacent pellets

Fig 110

QUENCH-03: Cross section at elevation 750 mm (QUE-03-5, top); region between three adjacent rods after necking and infiltration by relocated cladding melt

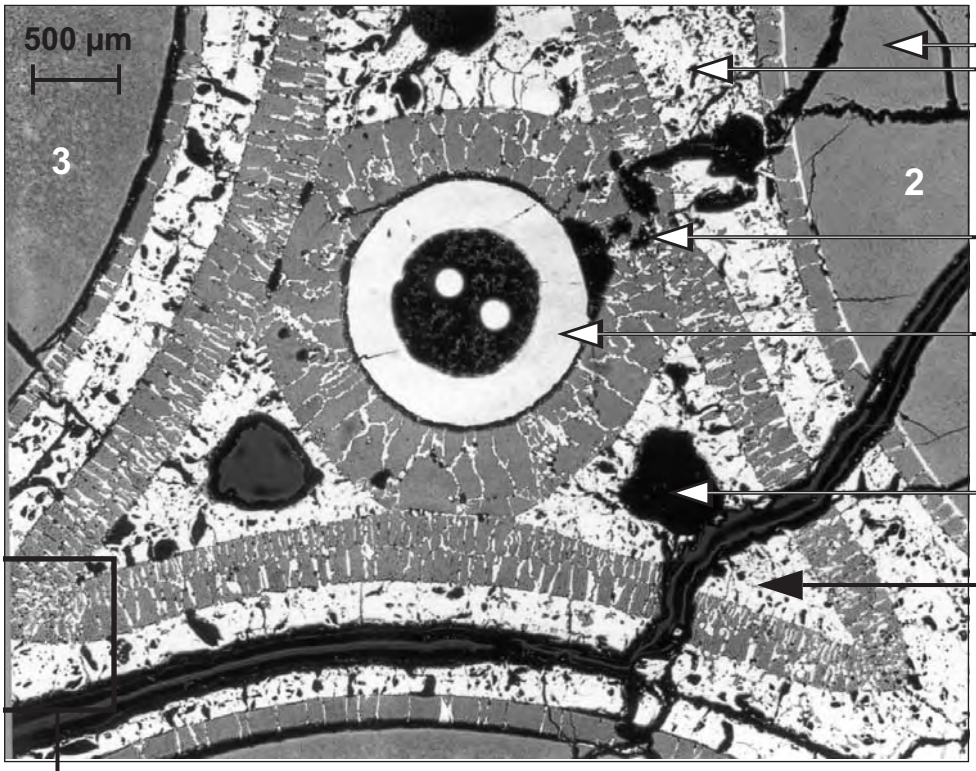

Pellet

Cladding

Cladding Scale

Thermocouple with oxidized Zircaloy part of duplex clad

Void

Relocated metallic melt

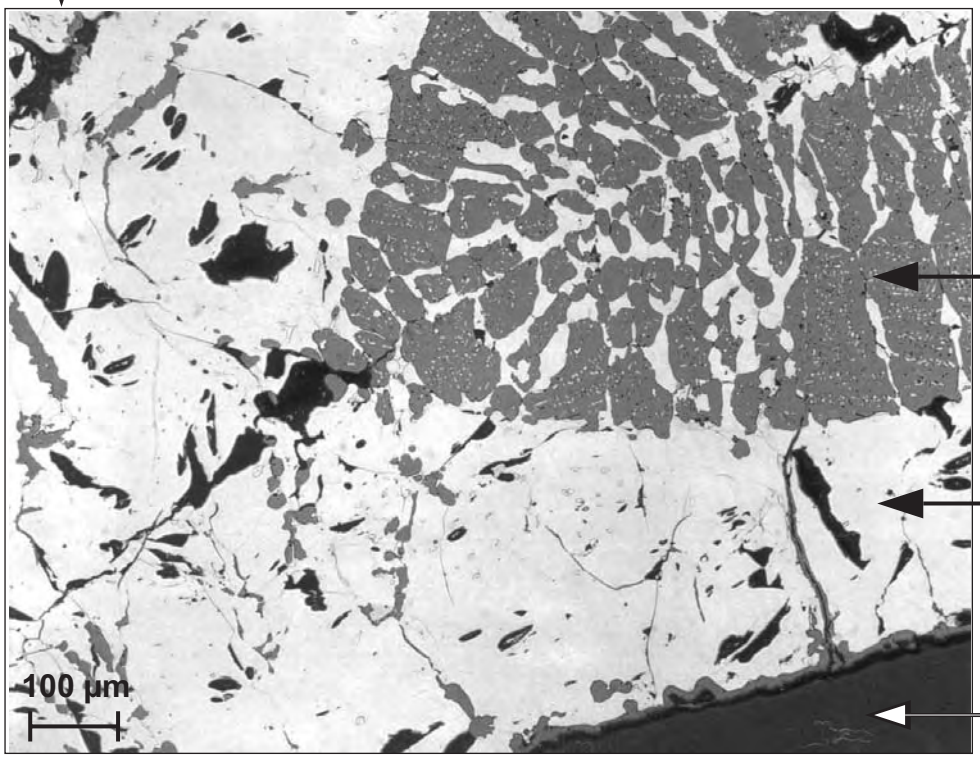

Details of once molten cladding and attacked scale

Scale

Cladding

Gap from fracture within cladding

Fig 111

QUENCH-03: Cross section at elevation 800 mm (QUE-03-6, top); overview

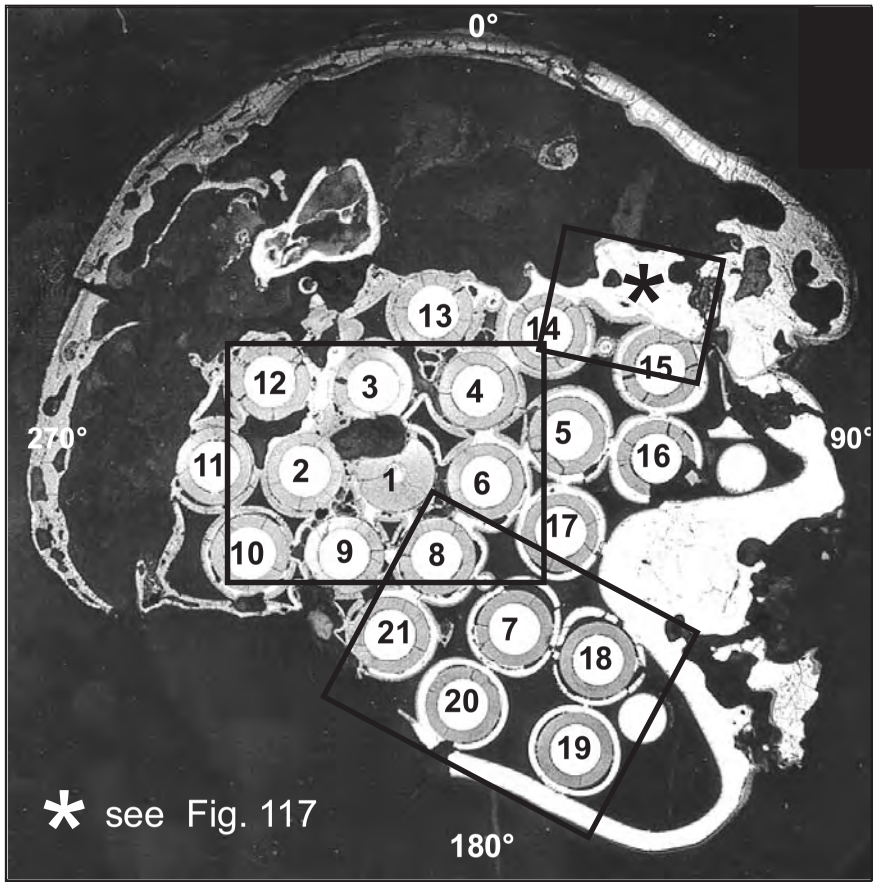

10 mm

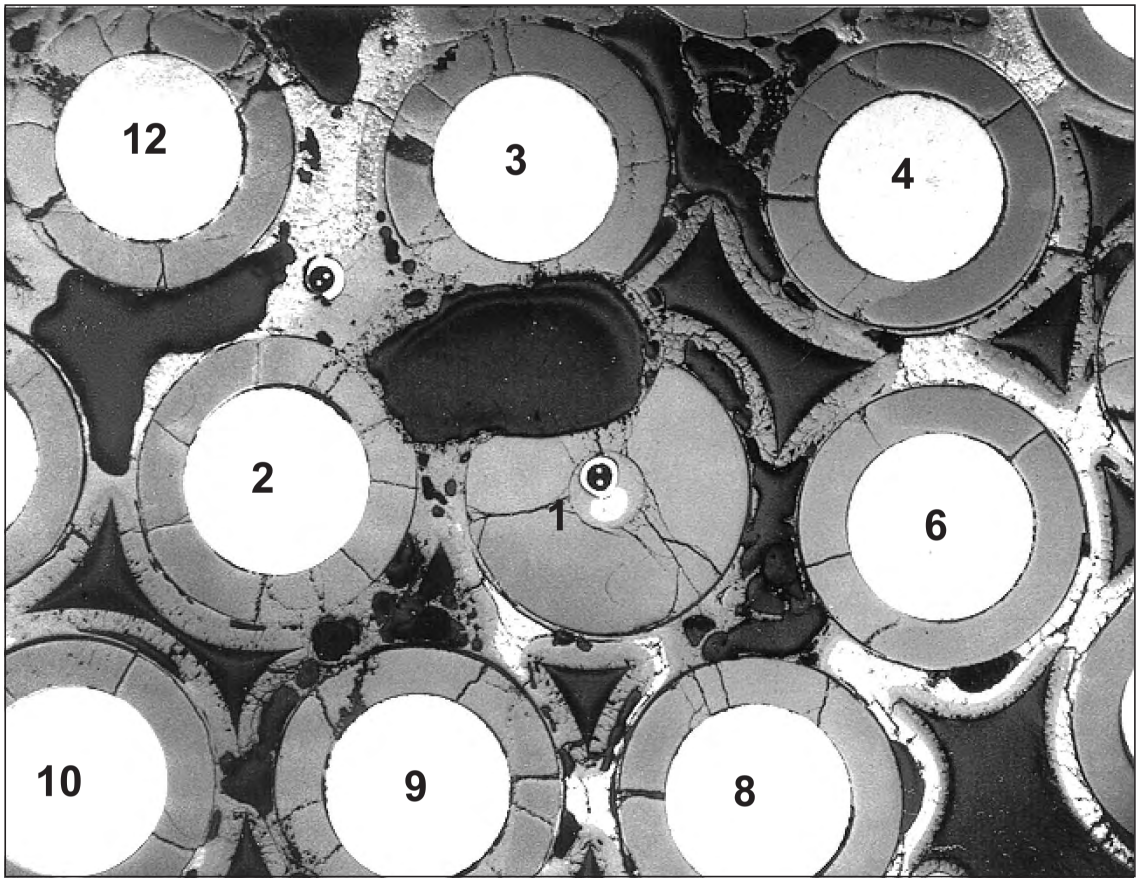

5 mm

Fig 112

QUENCH-03: Cross section at elevation 800 mm (QUE-03-6, top); necking between fuel rod simulator and shroud

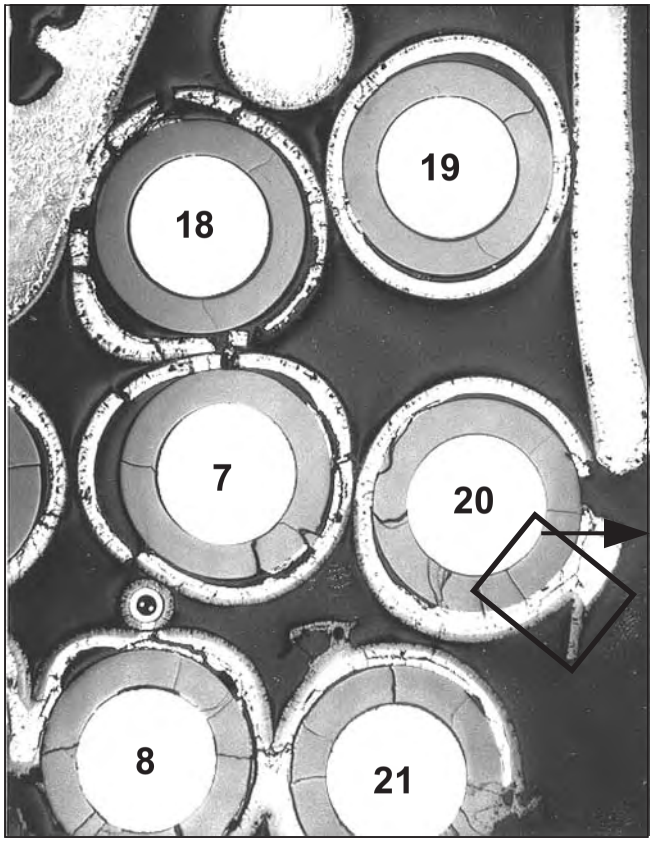

5 mm

Rod arrangement

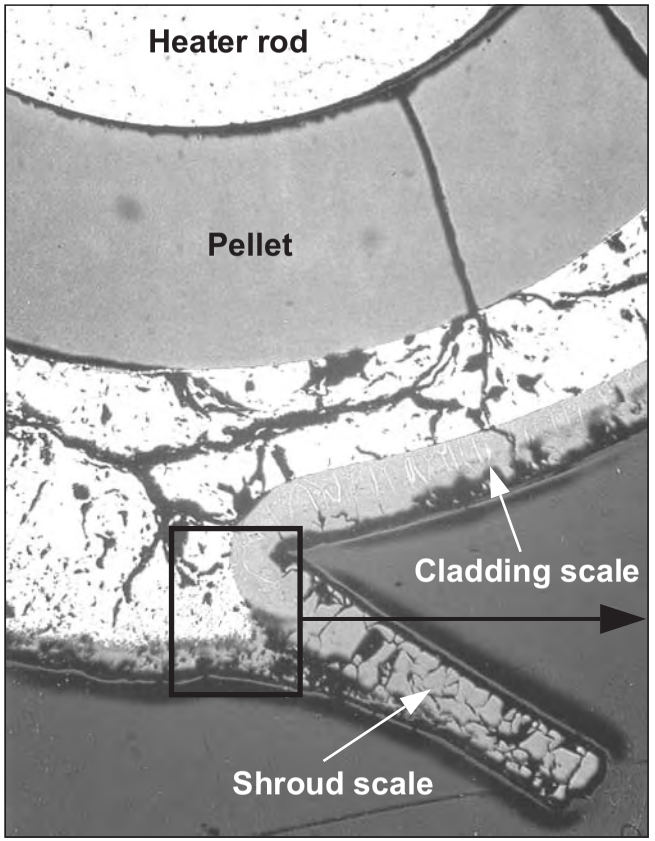

500 µm

Necking rod/shroud

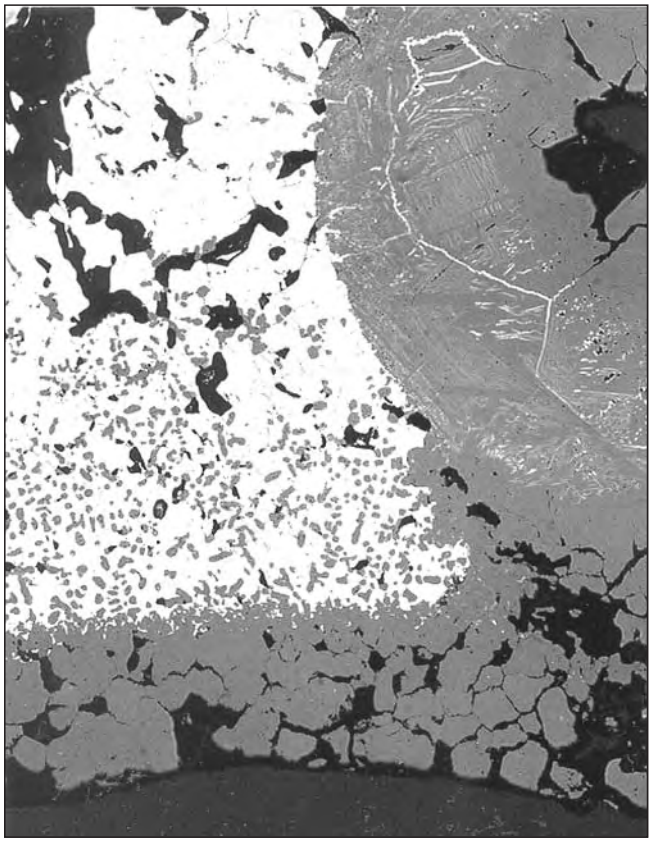

100 µm

Details of neck

Fig 113

QUENCH-03: Cross section at elevation 800 mm (QUE-03-6, top); neck formation, shroud oxidation

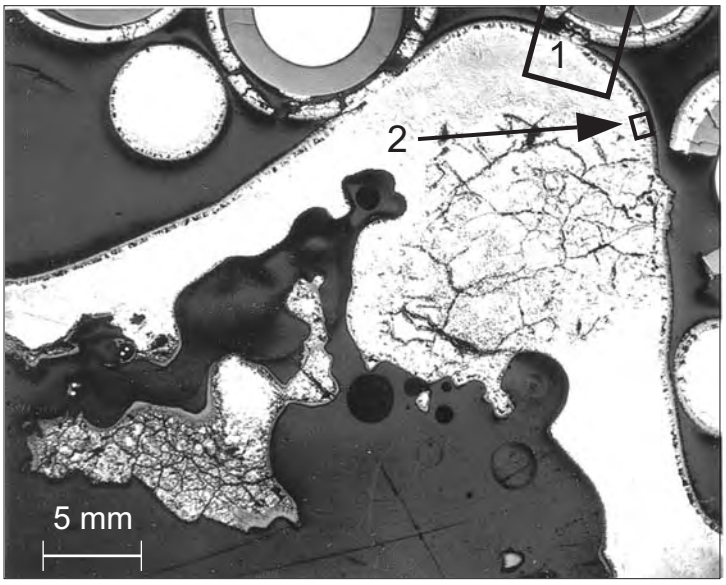

Bulged shroud with external melt

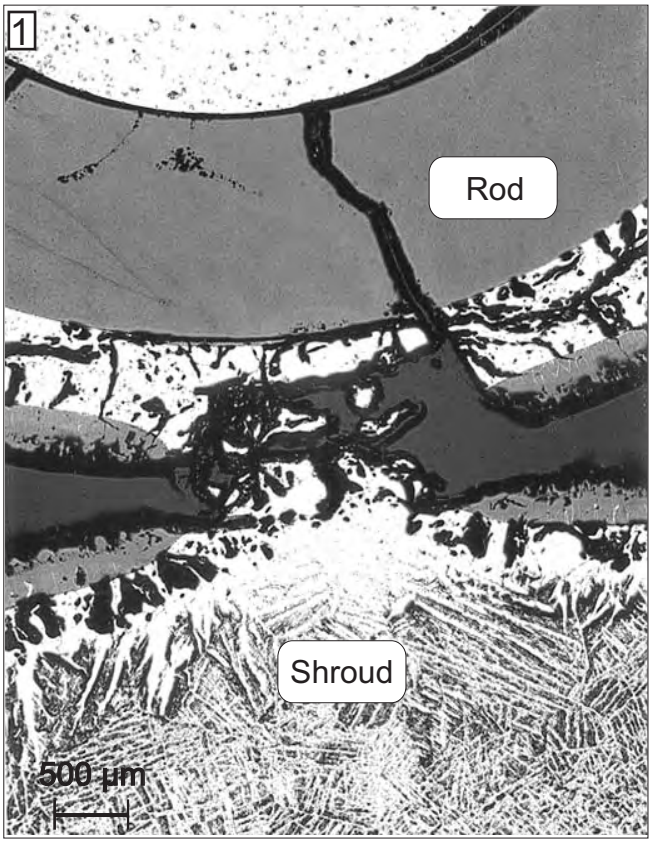

Necking between rod and shroud

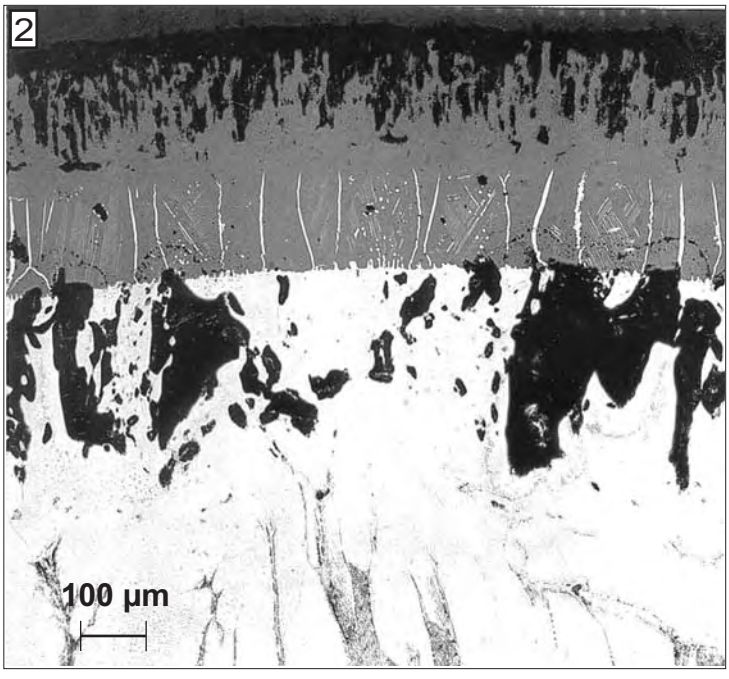

Internal oxidation of shroud

Fig 114

QUENCH-03: Cross section at elevation 800 mm(QUE-03-6, top); flow channel oxidation, interactions with residual metallic melt

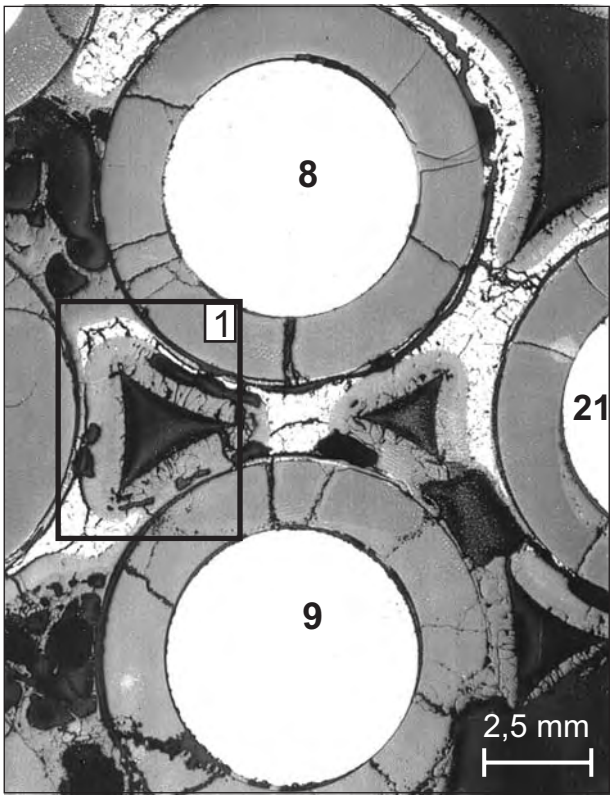

Flow channels

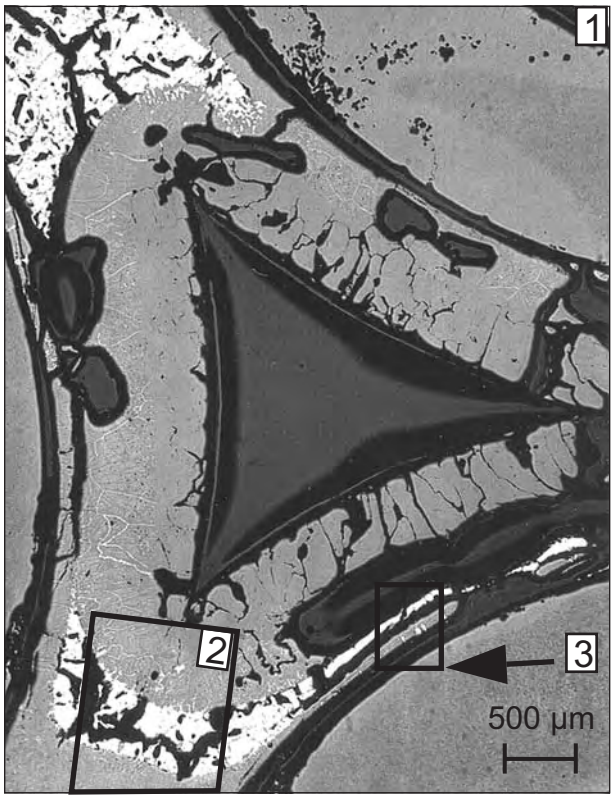

Flow channel and residual melt

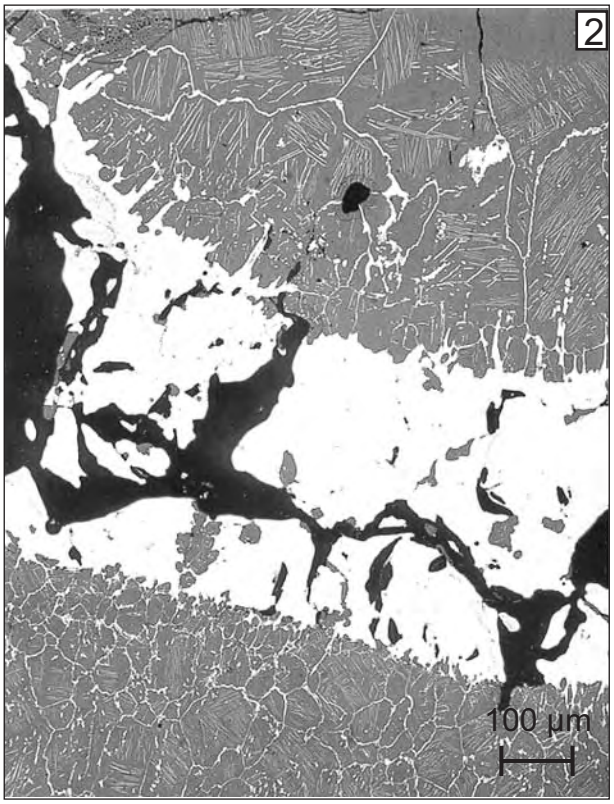

Residual melt between scales

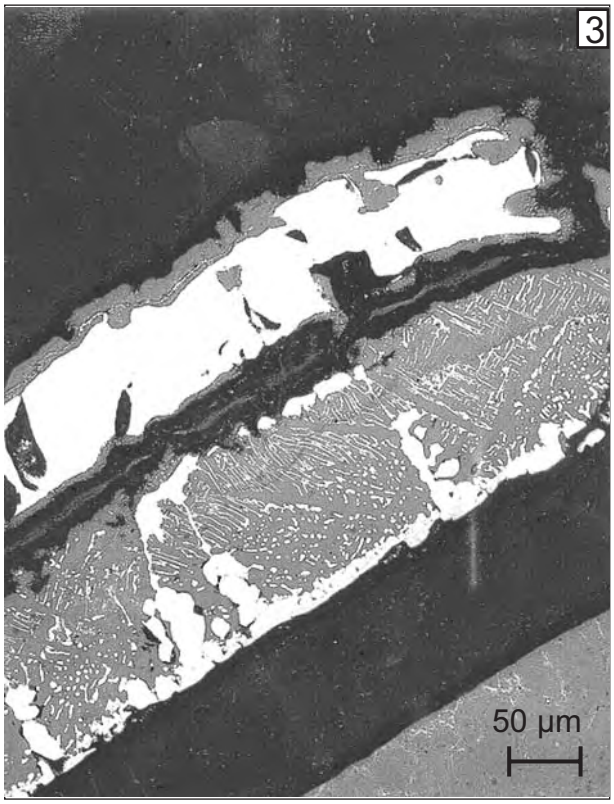

Residual melt and pellet/cladding interaction zone

QUENCH-03: Cross section at elevation 800 mm (QUE-03-6, top); scale microstructures indicating residual substoichiometry

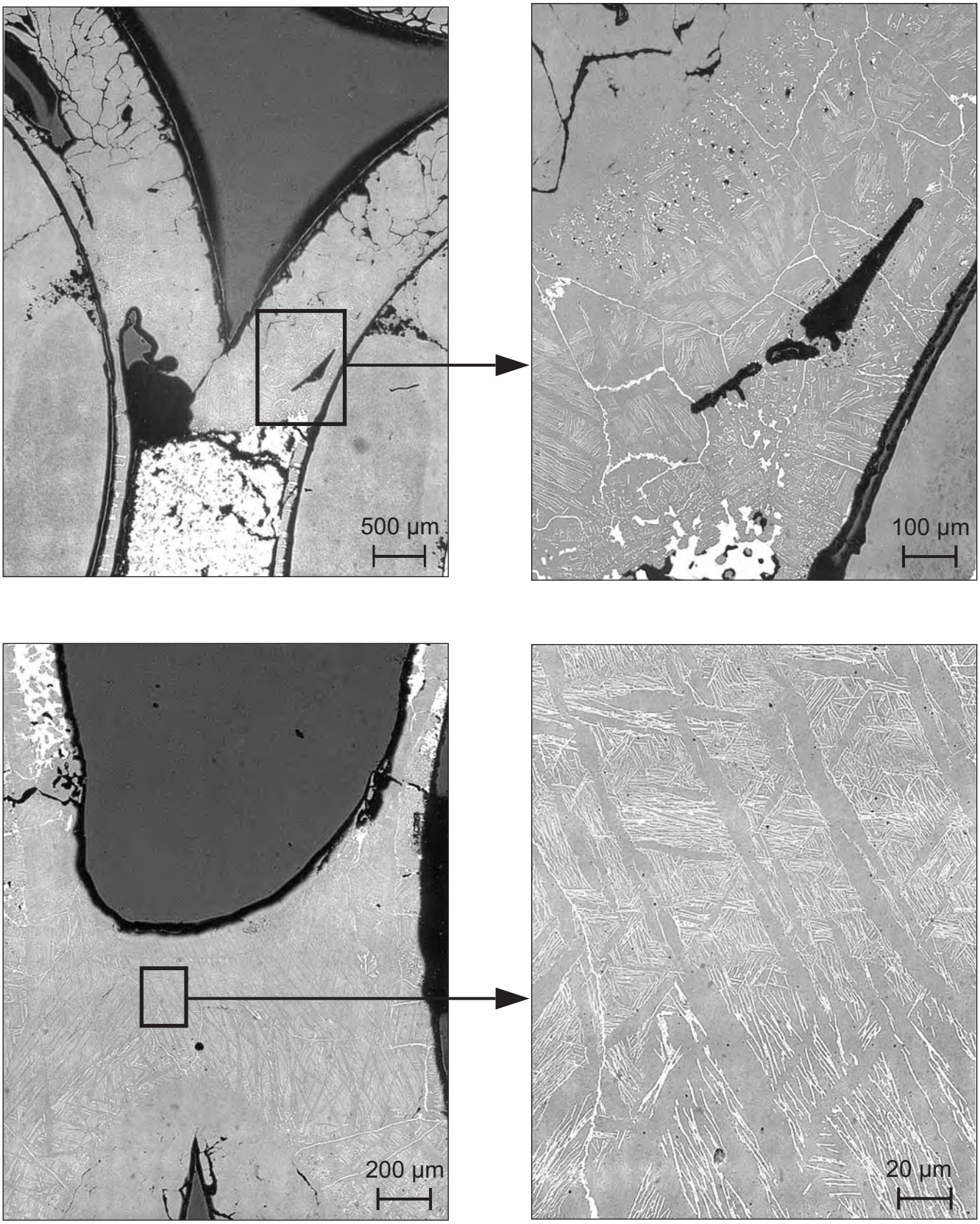

QUENCH-03: Cross section at elevation 800 mm (QUE-03-6, top); scale dissolution

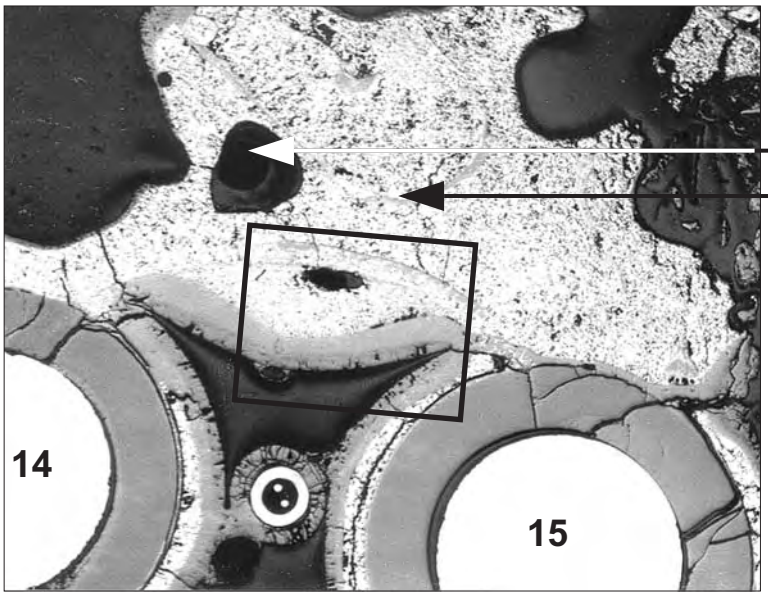

Pore
Melt

Melt of cladding/ shroud type

2,5 mm

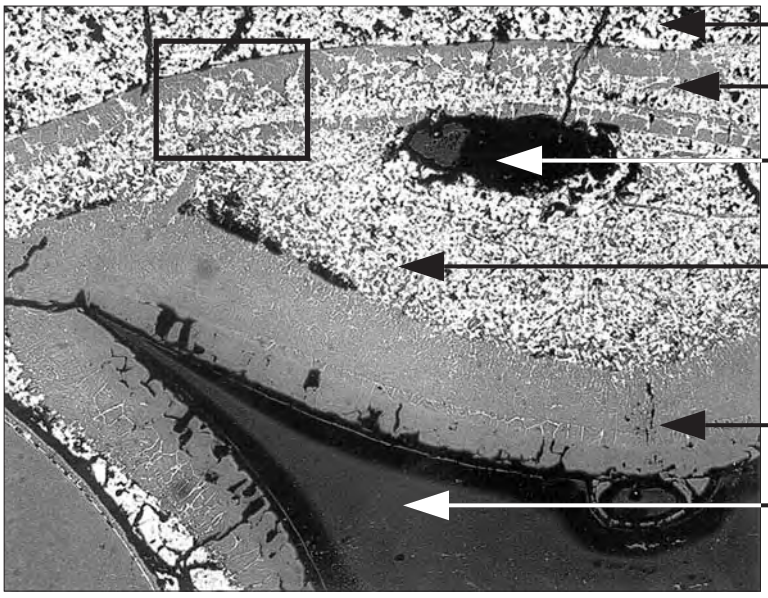

Melt
Scale
Pore
Melt
Scale
Flow channel

500 µm

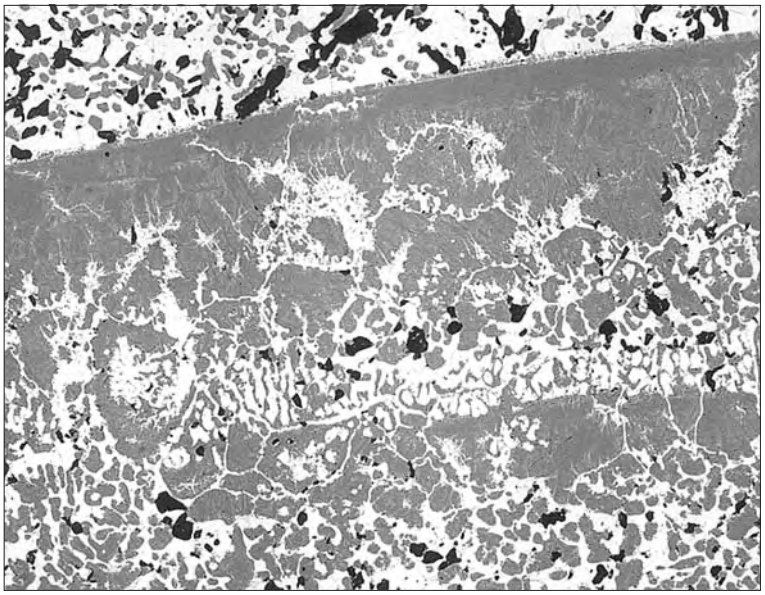

Scale in advanced dissolution

100 µm

Fig 117

QUENCH-03: Cross section at elevation 800 mm (QUE-03-6, top); pellet/cladding interaction

100 µm

Gap due to melt relocation

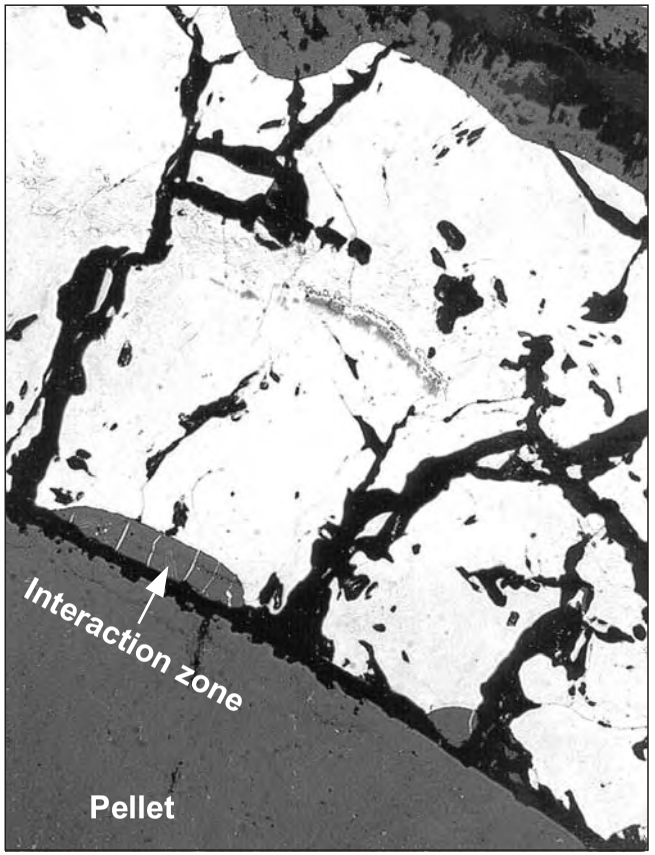

100 µm

Local pellet/cladding interaction

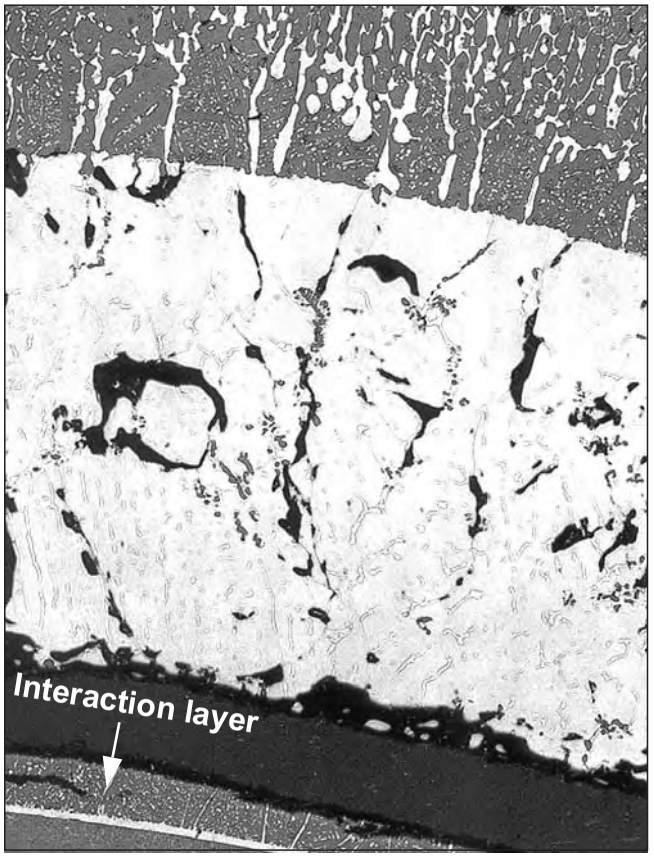

100 µm

Pellet/cladding interaction layer

Fig 118

QUENCH-03: Cross section at elevation 800 mm(QUE-03-6, top); pellet interaction with melt of cladding type

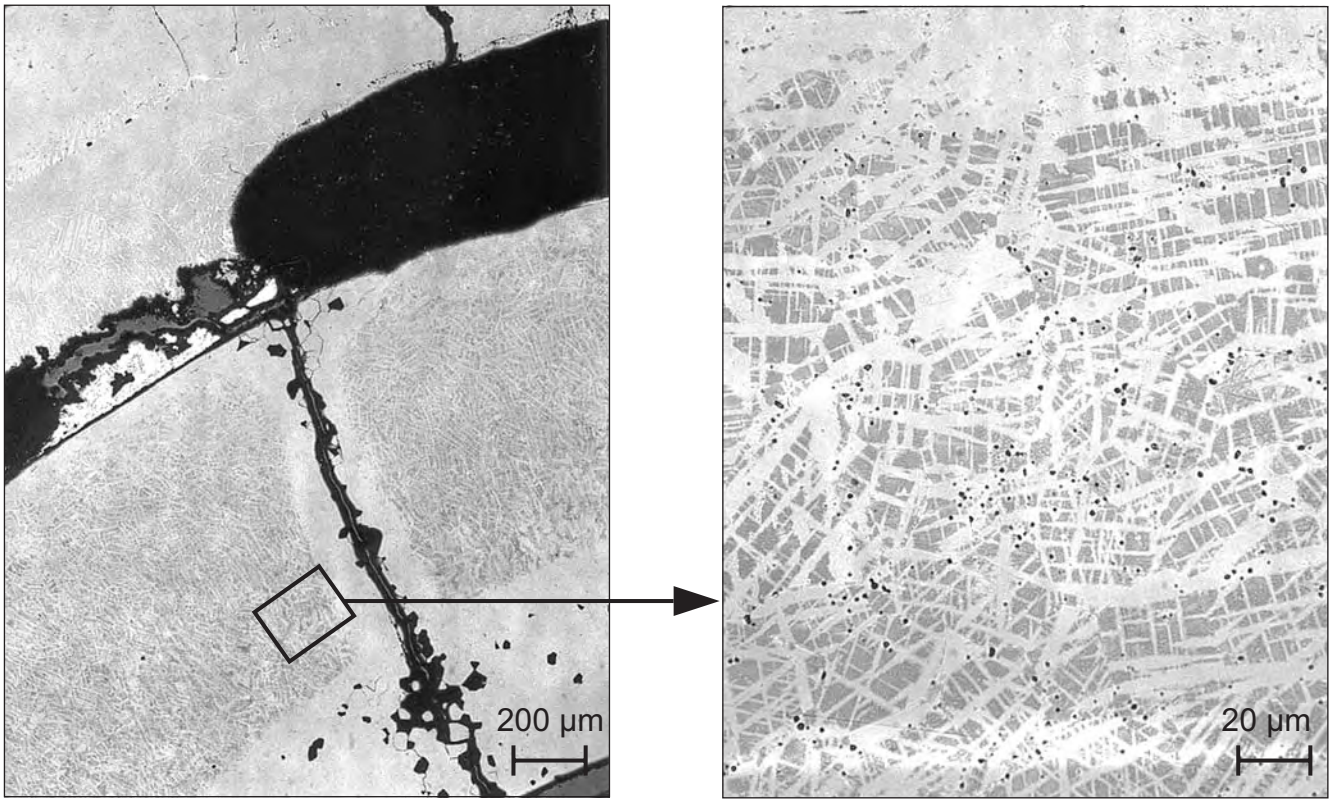

Modified pellet microstructure

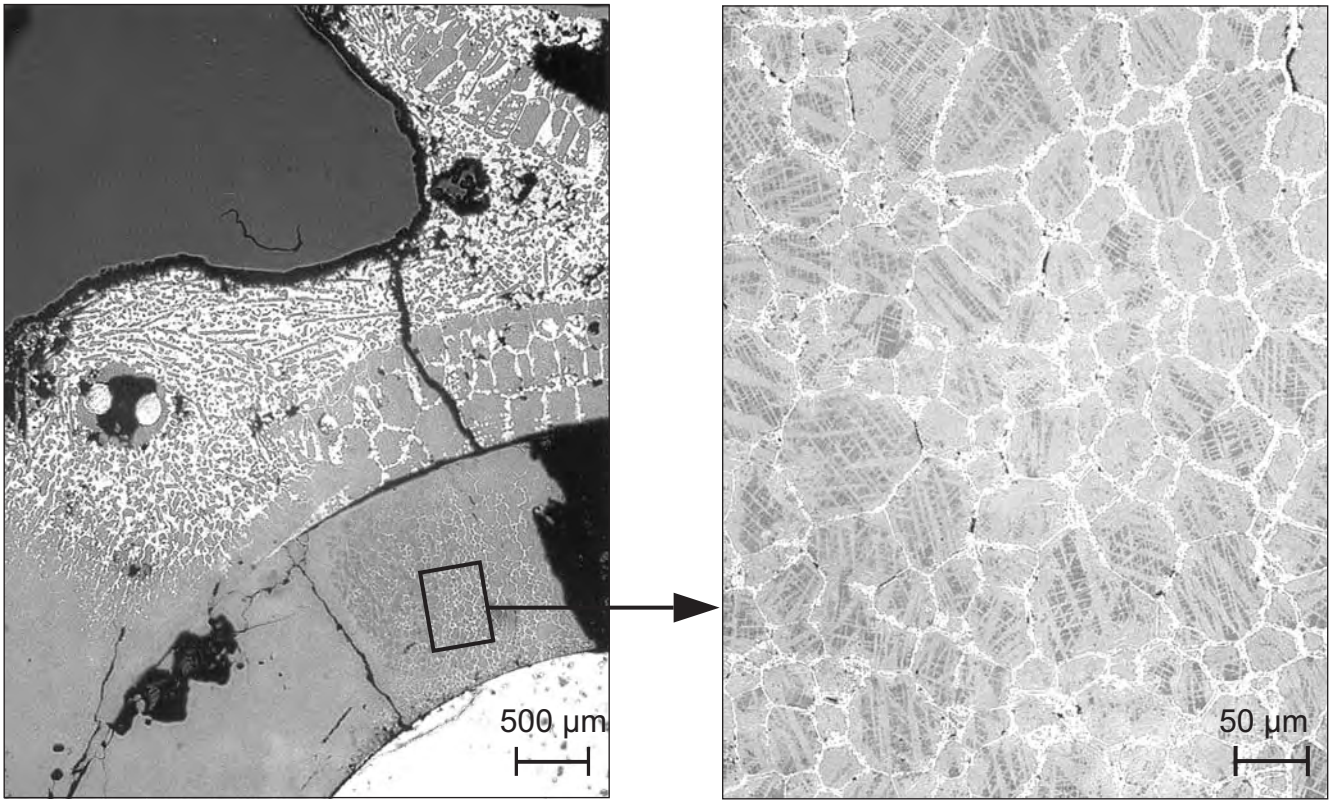

Advanced pellet reduction along grain boundaries

Fig 119

QUENCH-03: Cross section at elevation 800 mm (QUE-03-6, top); thermocouple status

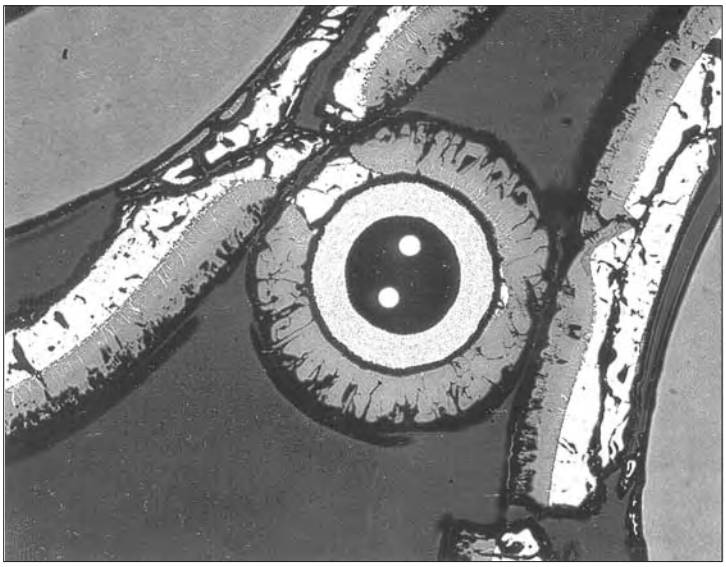

500 µm

Thermocouple with oxidized Zircaloy clad and still metallic neck

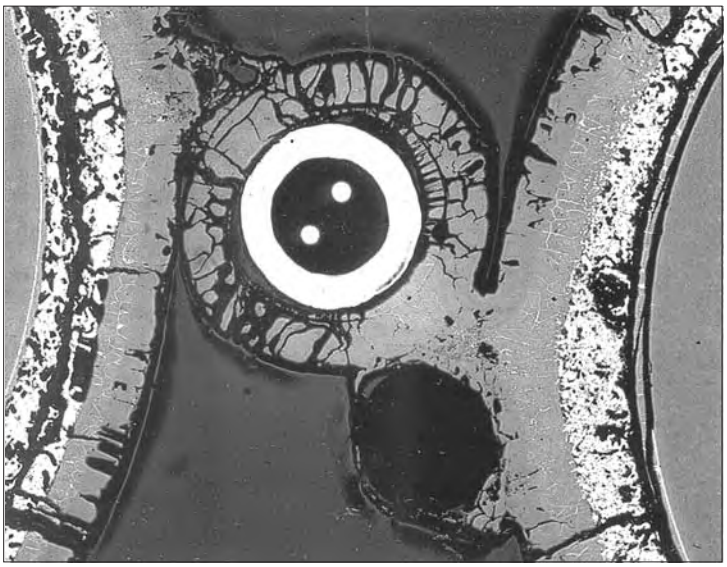

500 µm

Thermocouple with completely oxidized Zircaloy clad and necks

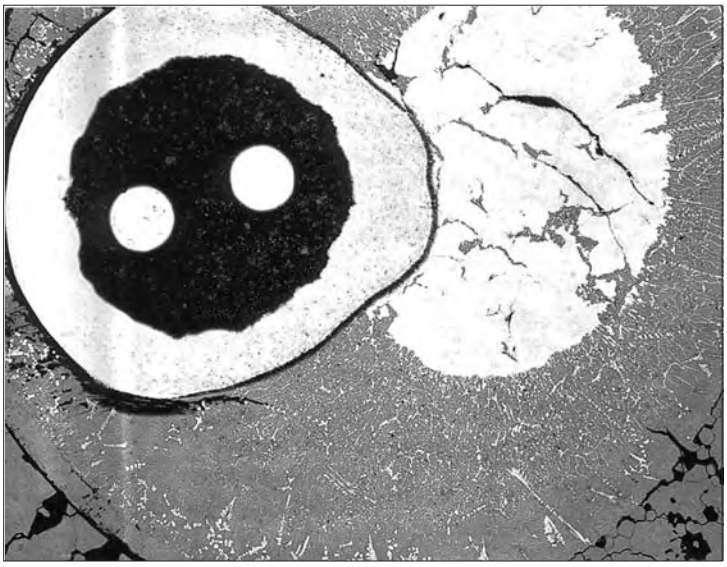

200 µm

Thermocouple within the unheated central fuel rod simulator with relocated metallic remnants of Zircaloy clad

Fig 120

QUENCH-03: Cross section at elevation 950 mm (QUE-03-7, top); overview

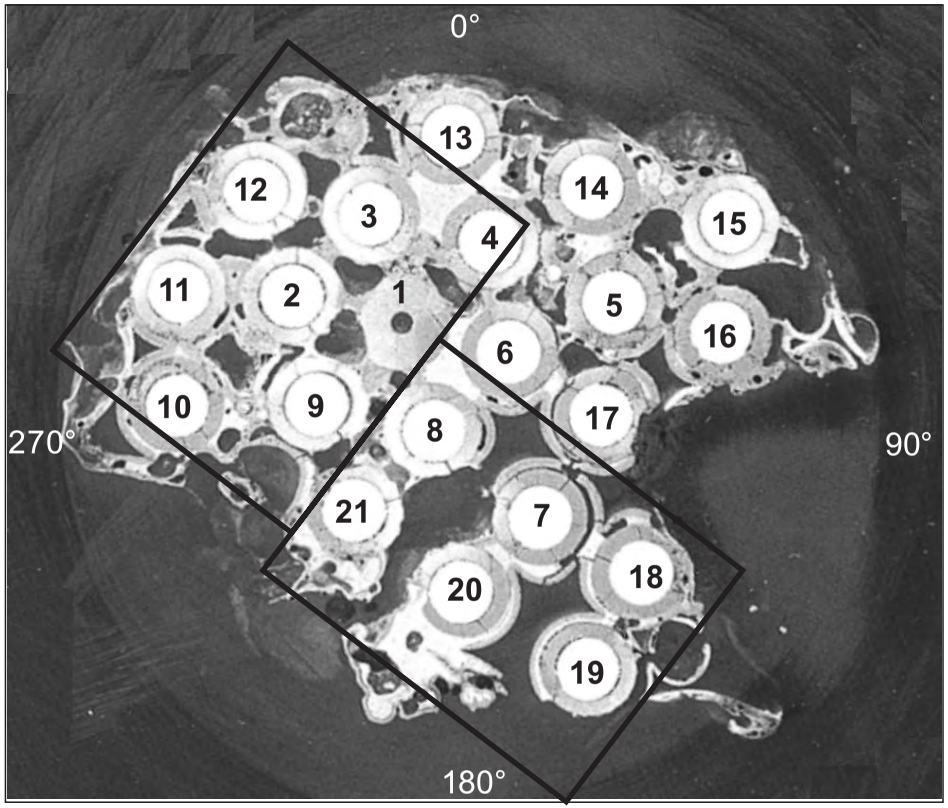

10 mm

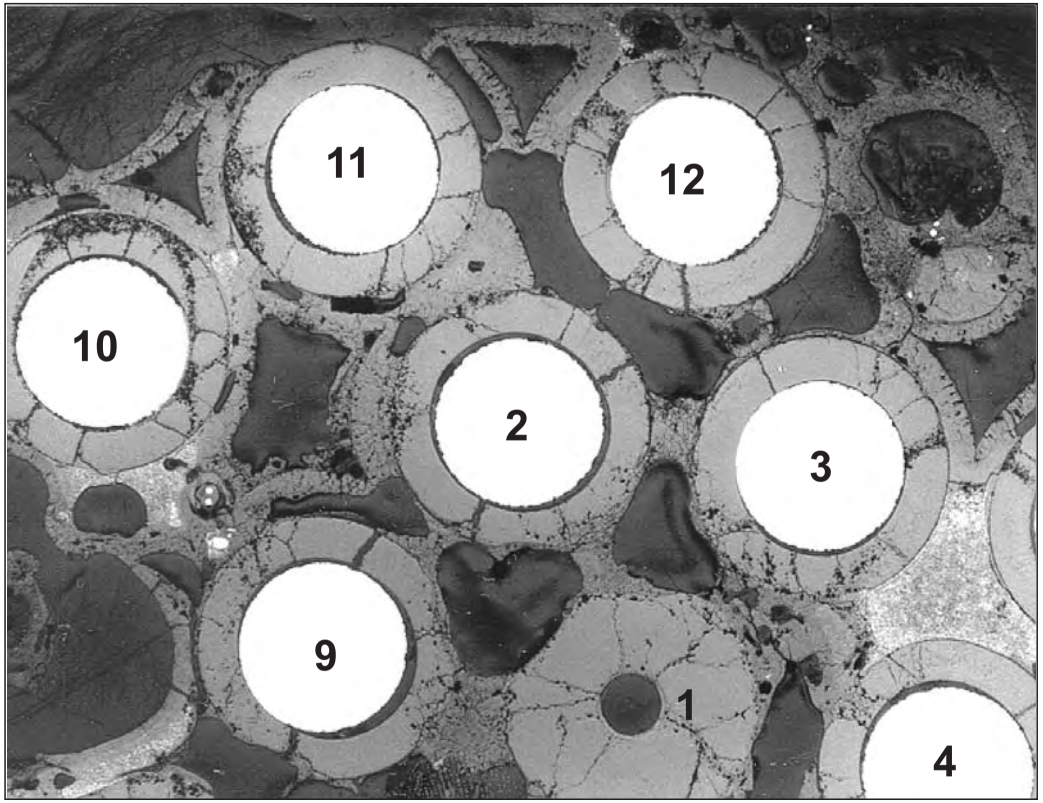

5 mm

Fig 121

QUENCH-03: Cross section at elevation 950 mm (QUE-03-7, top); status of a neck between neighbouring rods

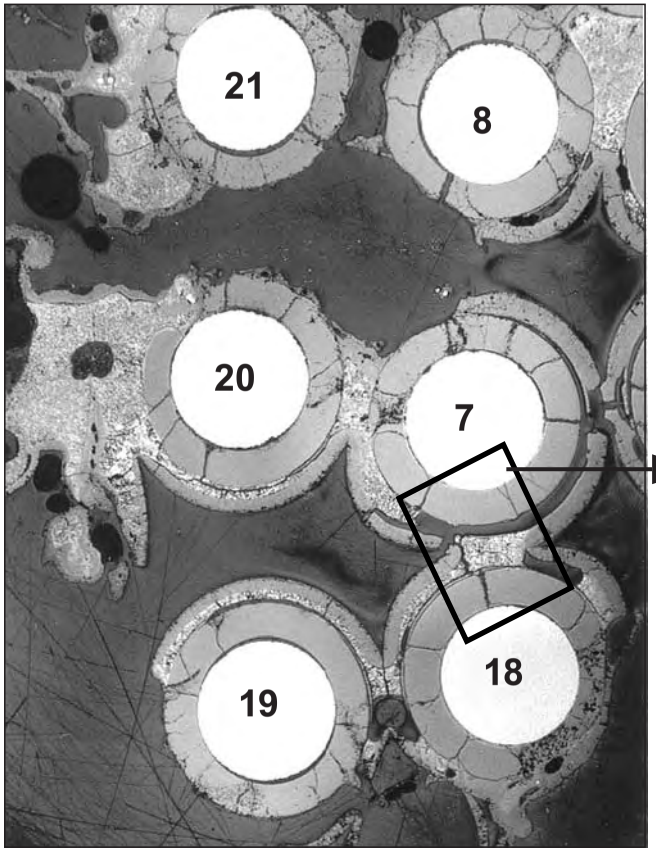

5 mm

Rod necking

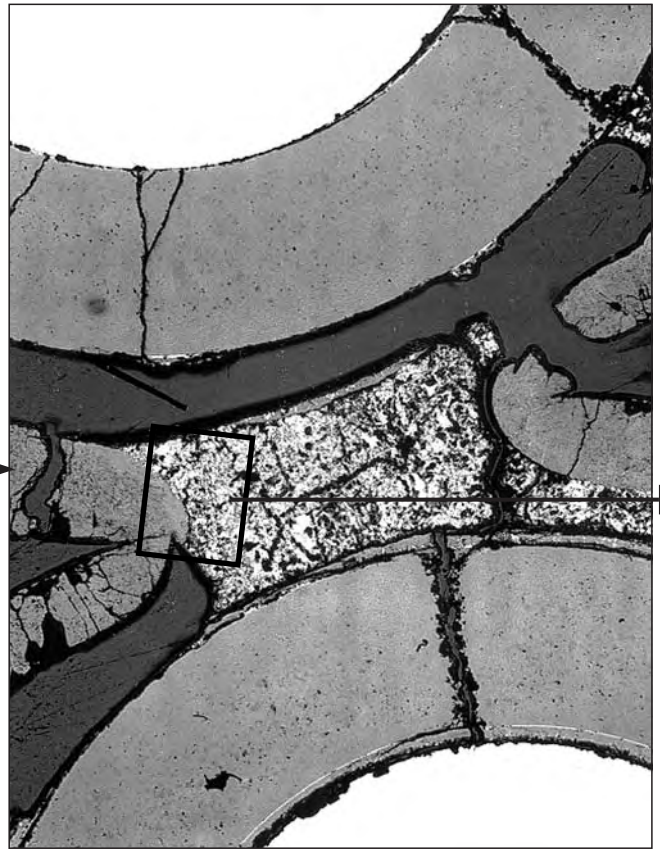

500 µm

Rod neck with residual metallic melt

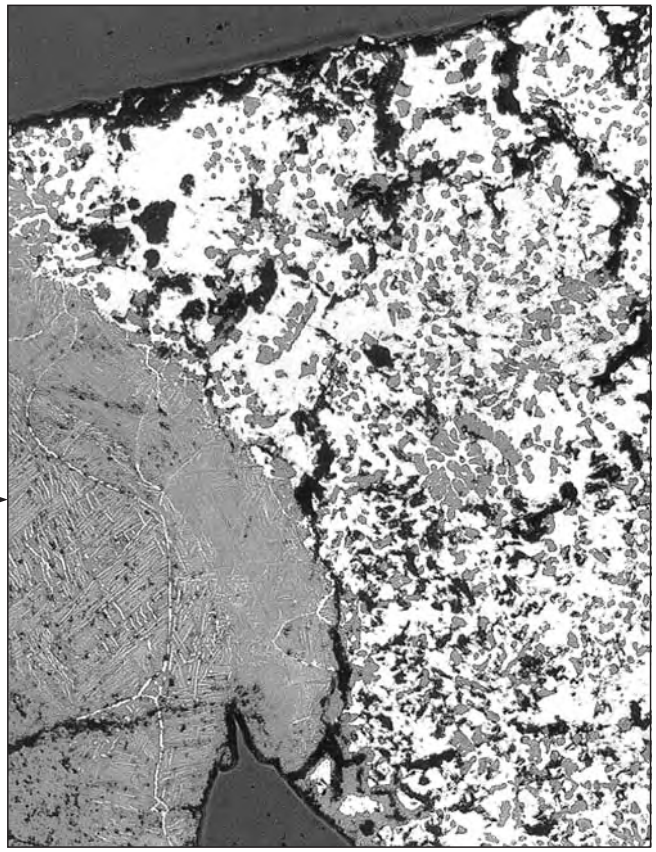

100 µm

Scale / melt contact zone

Fig 122

QUENCH-03: Cross section at elevation 950 mm (QUE-03-7, top); metallic cladding melt confined between scale and pellet, oxidation related microstructures

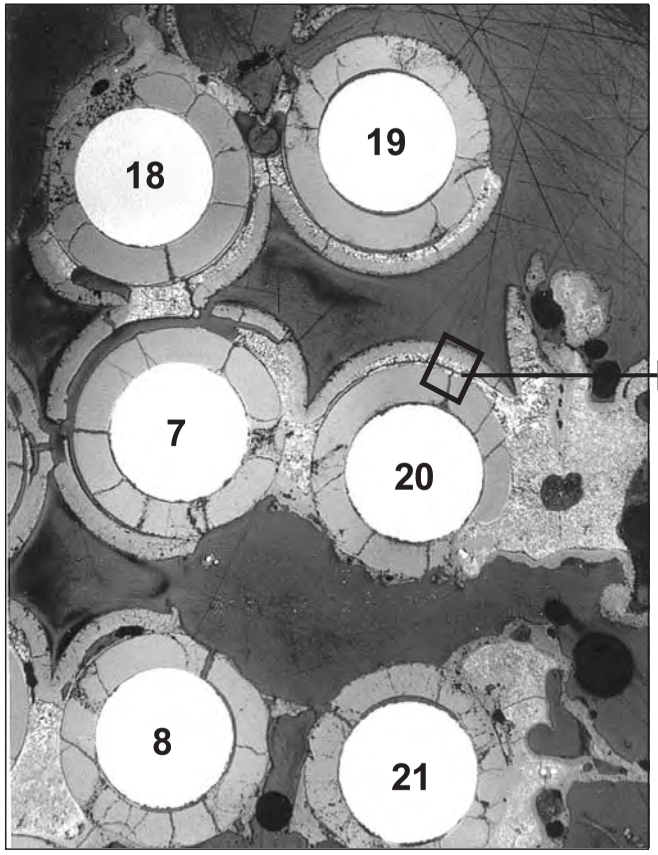

5 mm

Overview

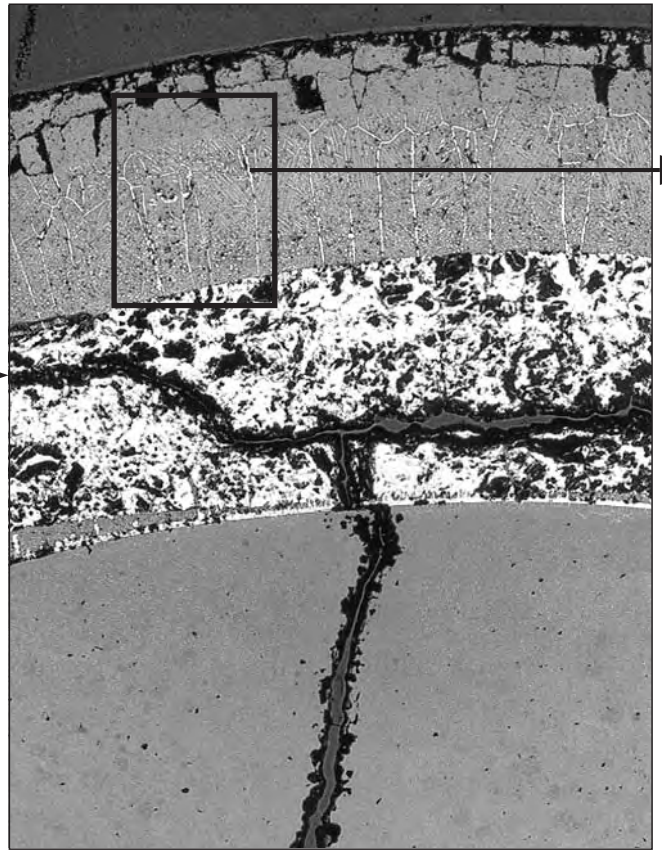

200 µm

Scale, molten metallic cladding, pellet

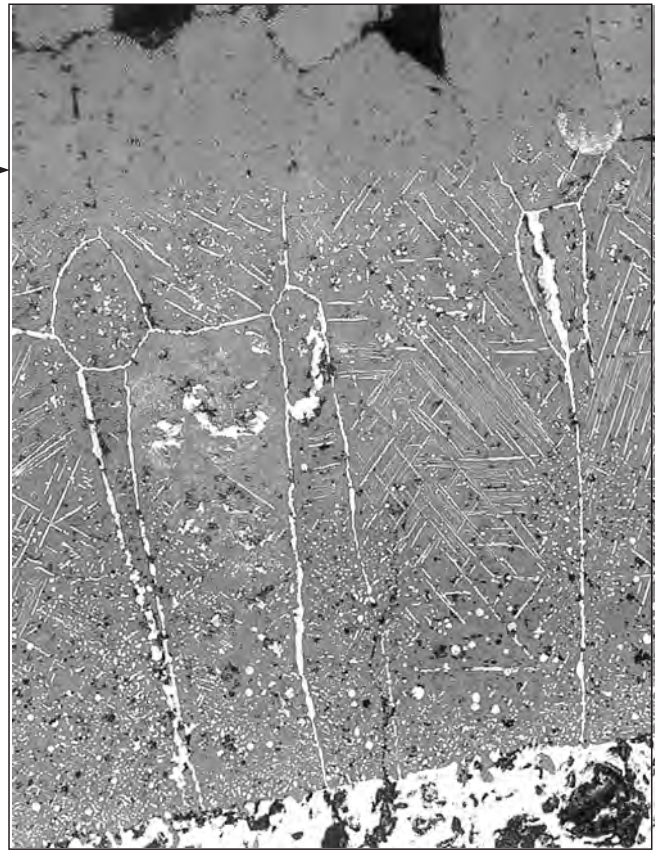

50 µm

Scale / melt contact

Fig 123

QUENCH-03: Cross section at elevation 950 mm (QUE-03-7, top); cladding expansion due to accumulated melt, oxidation-related microstructures

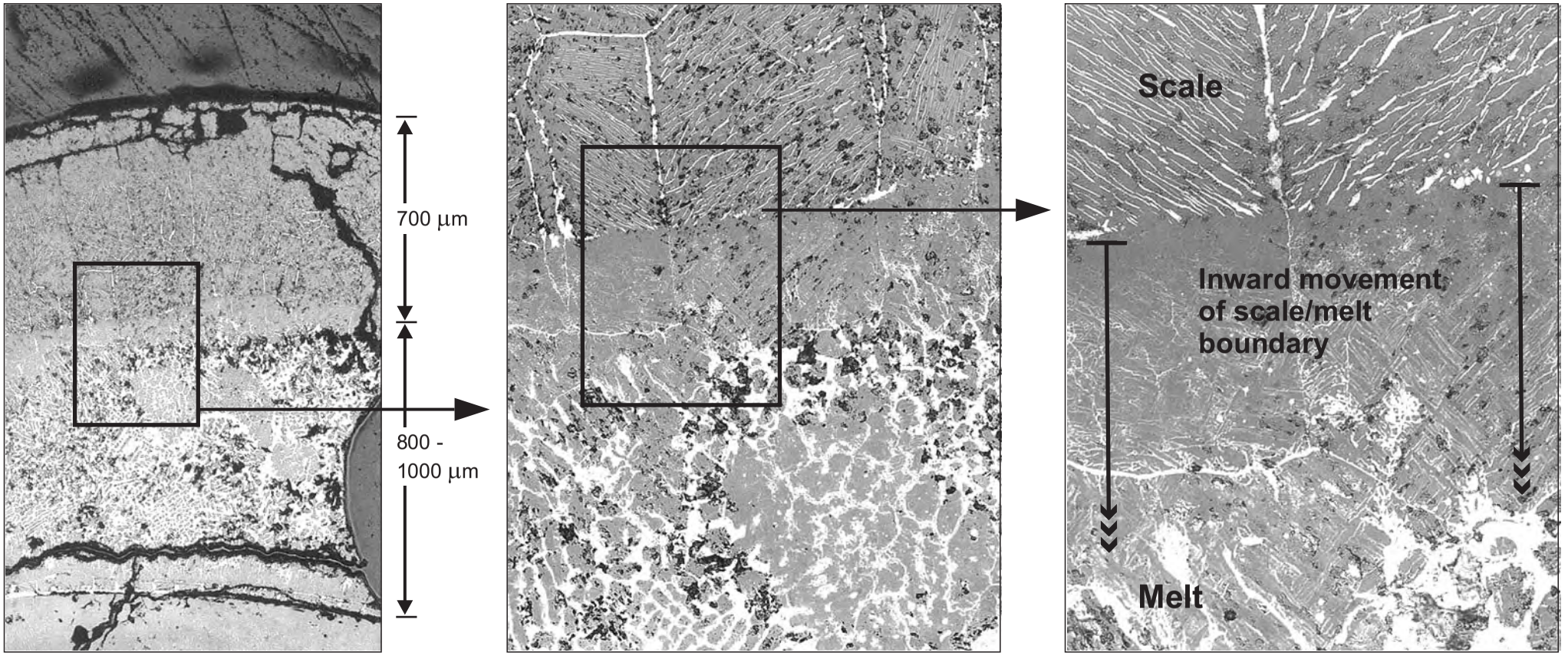

Overview

Transition region from scale to melt

Details of transition zone

Fig 124

QUENCH-03: Cross section at elevation 950 mm (QUE-03-7, top); pellet/melt interaction

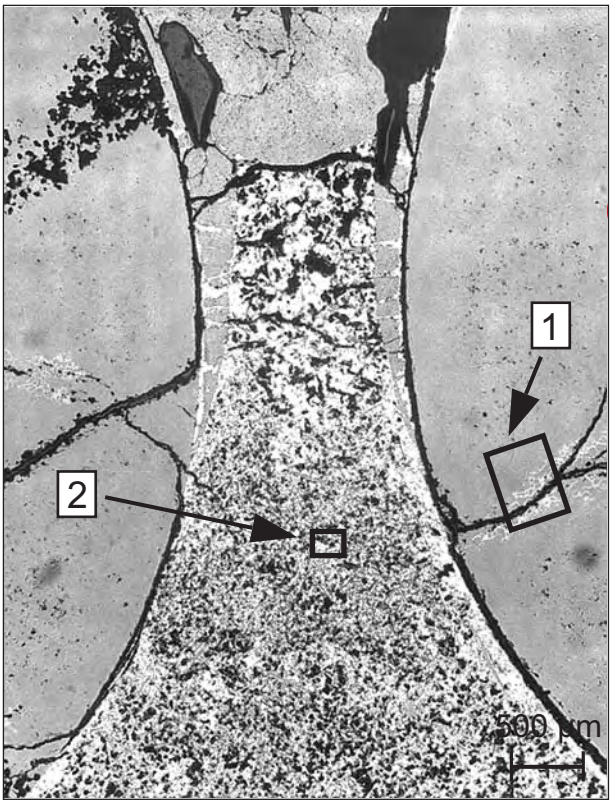

Melt in direct contact with pellets

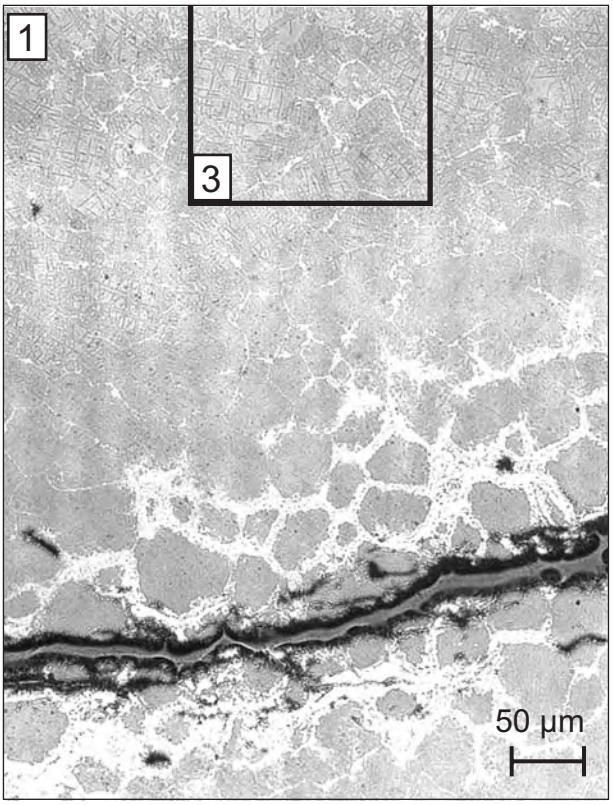

Cracked pellet

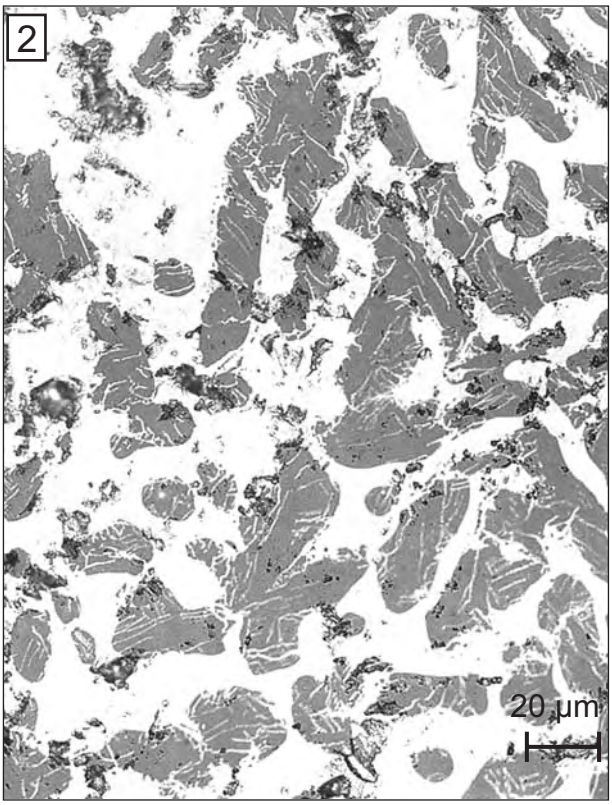

Melt microstructure

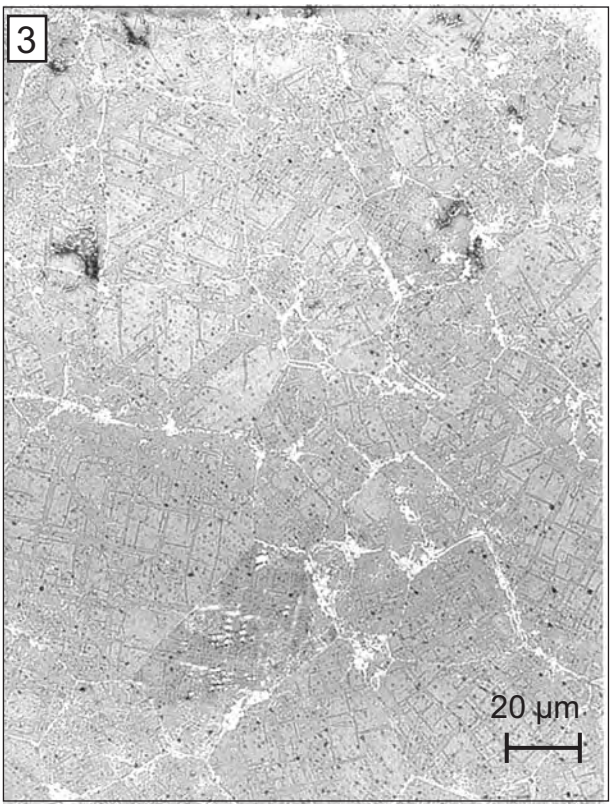

Pellet microstructure

Fig 125

QUENCH-03: Cross section at elevation 950 mm (QUE-03-7, top); thermocouple destruction status

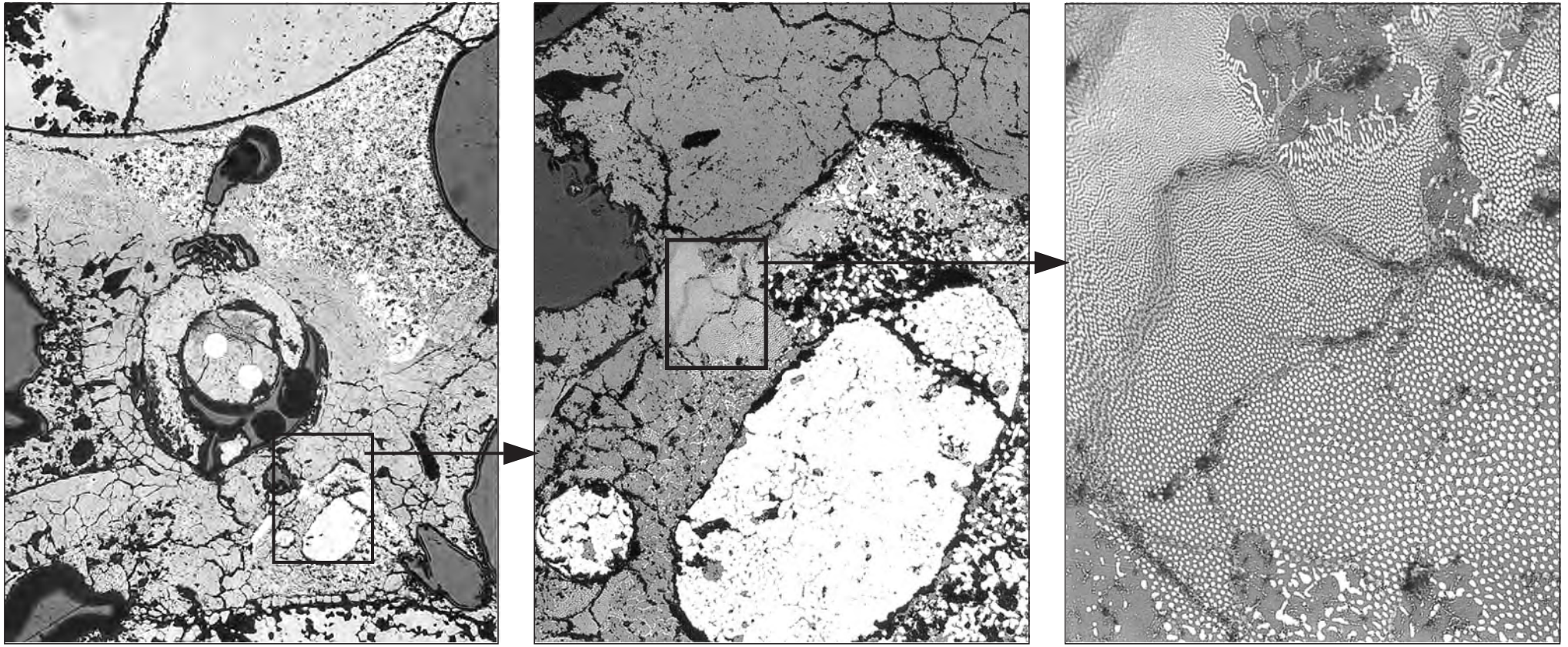

TC wires intact, duplex clad destroyed

Metallic residues containing TC components

Eutectic ceramic melt near to the TC

Fig 126

Oxide layer thicknesses at bundle elevation 73 mm

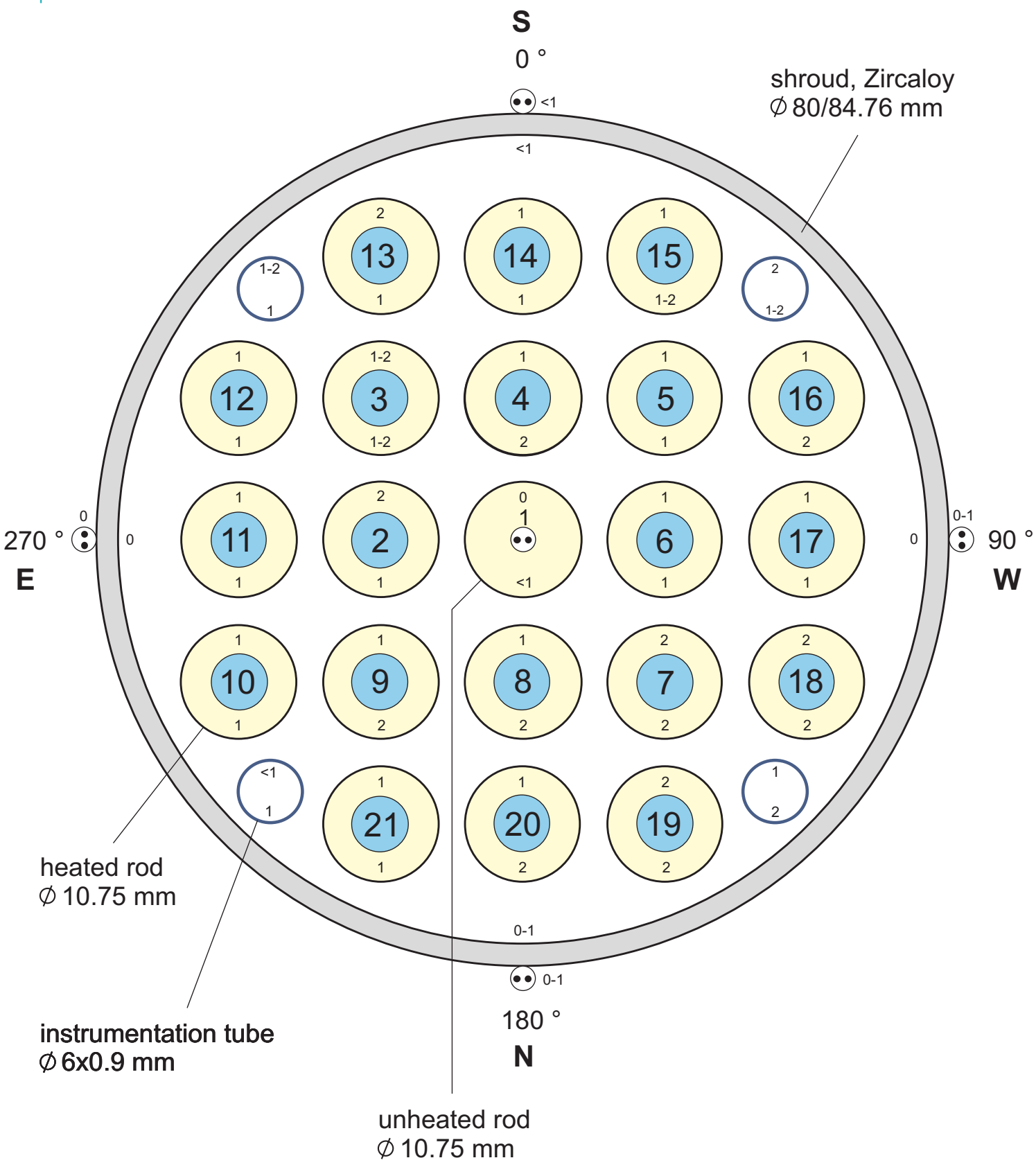

Test QUENCH-03; Cross section QUE-03-1 **Fig 127**

Oxide layer thicknesses at bundle elevation 550 mm

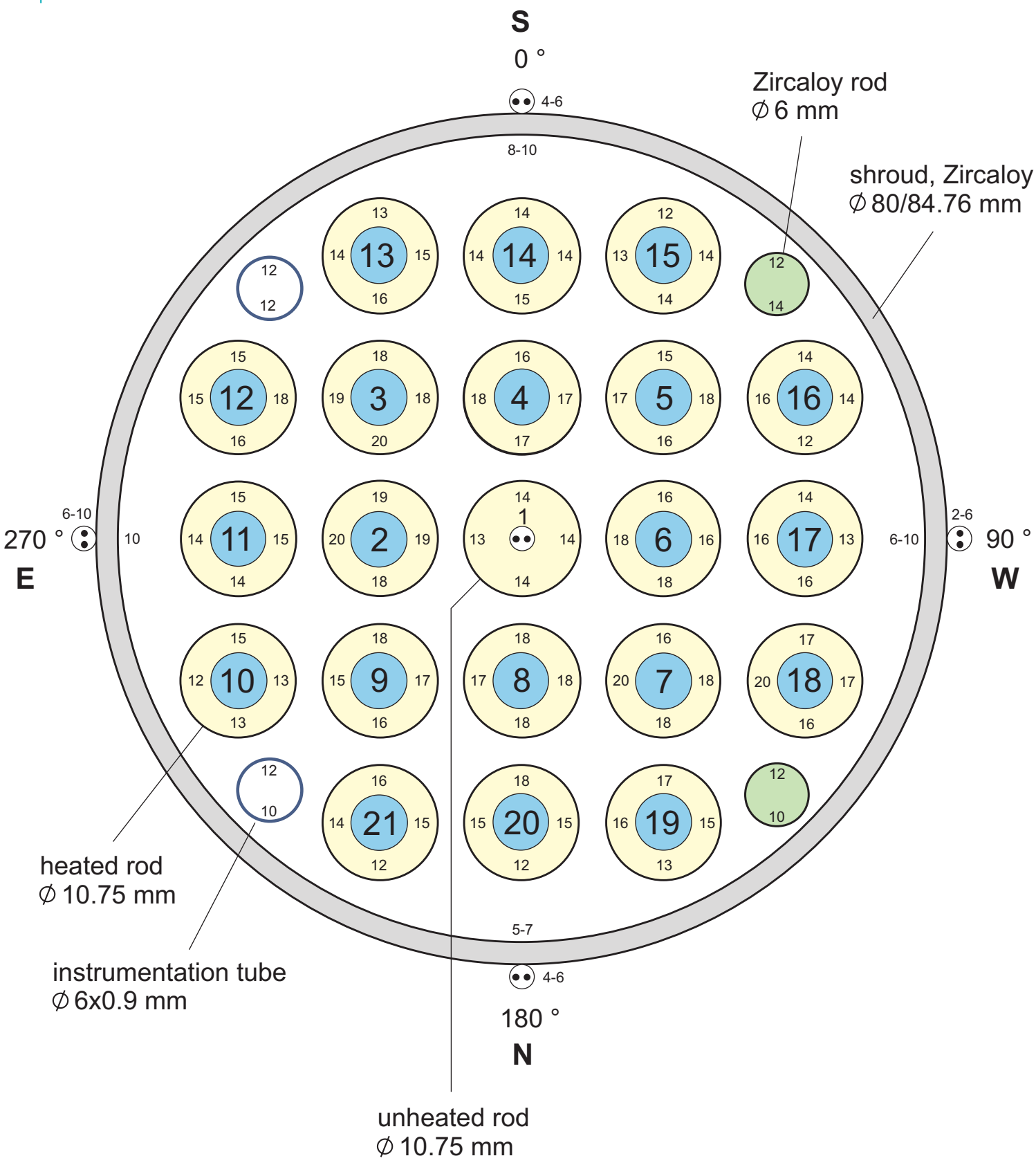

Test QUENCH-03; Cross section QUE-03-3 **Fig 128**

Oxide layer thicknesses at bundle elevation 650 mm

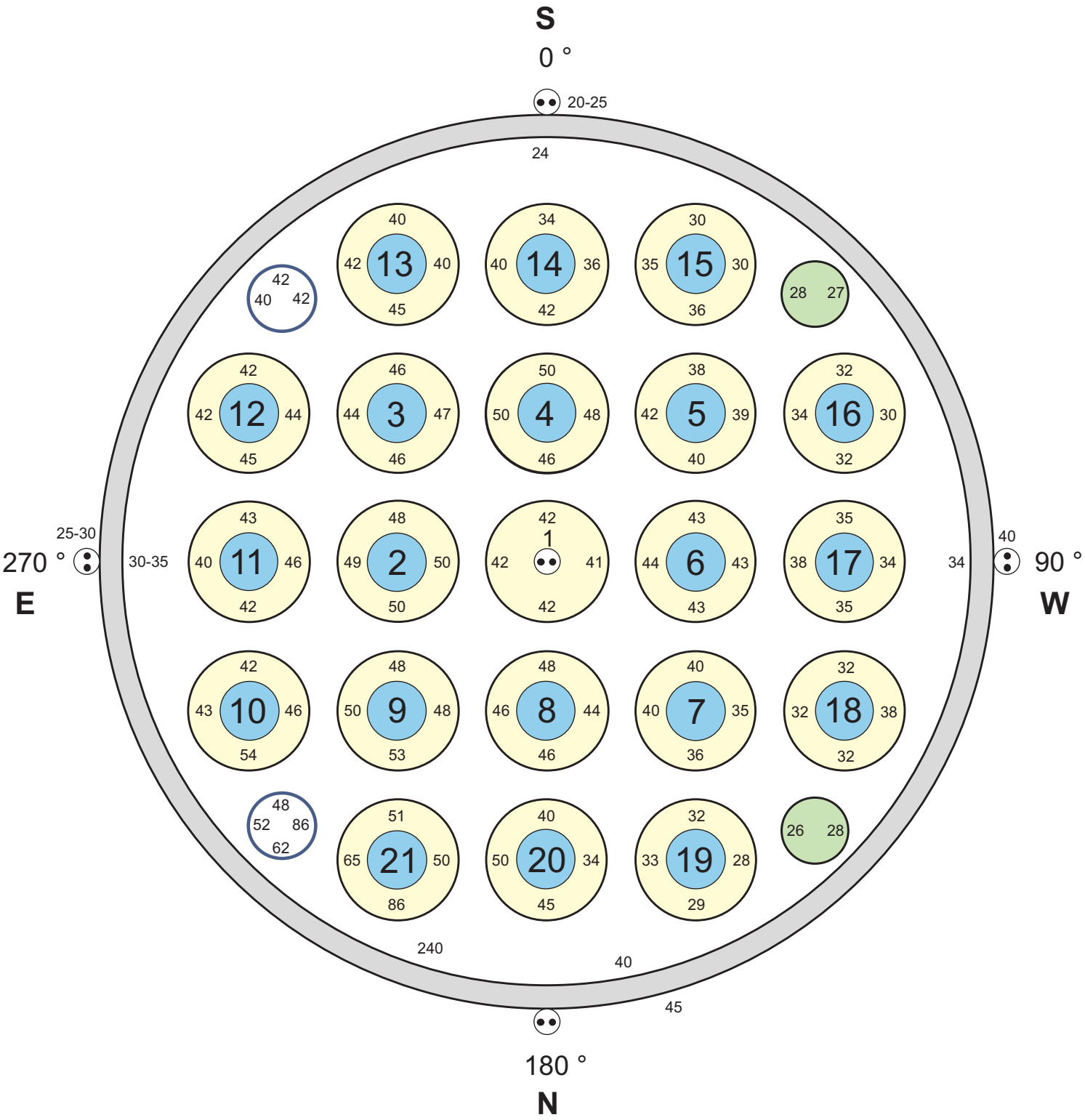

Test QUENCH-03; Cross section QUE-03-4 **Fig 129**

Oxide layer thicknesses at bundle elevation 750 mm

Δ Contact-zone between rods or shroud with locally diminished ZrO_2 shell thickness

–x partially dissolved ZrO_2 shell due to relocated melts

x remaining cladding completely oxidized

0 Cladding and ZrO_2 shell gone

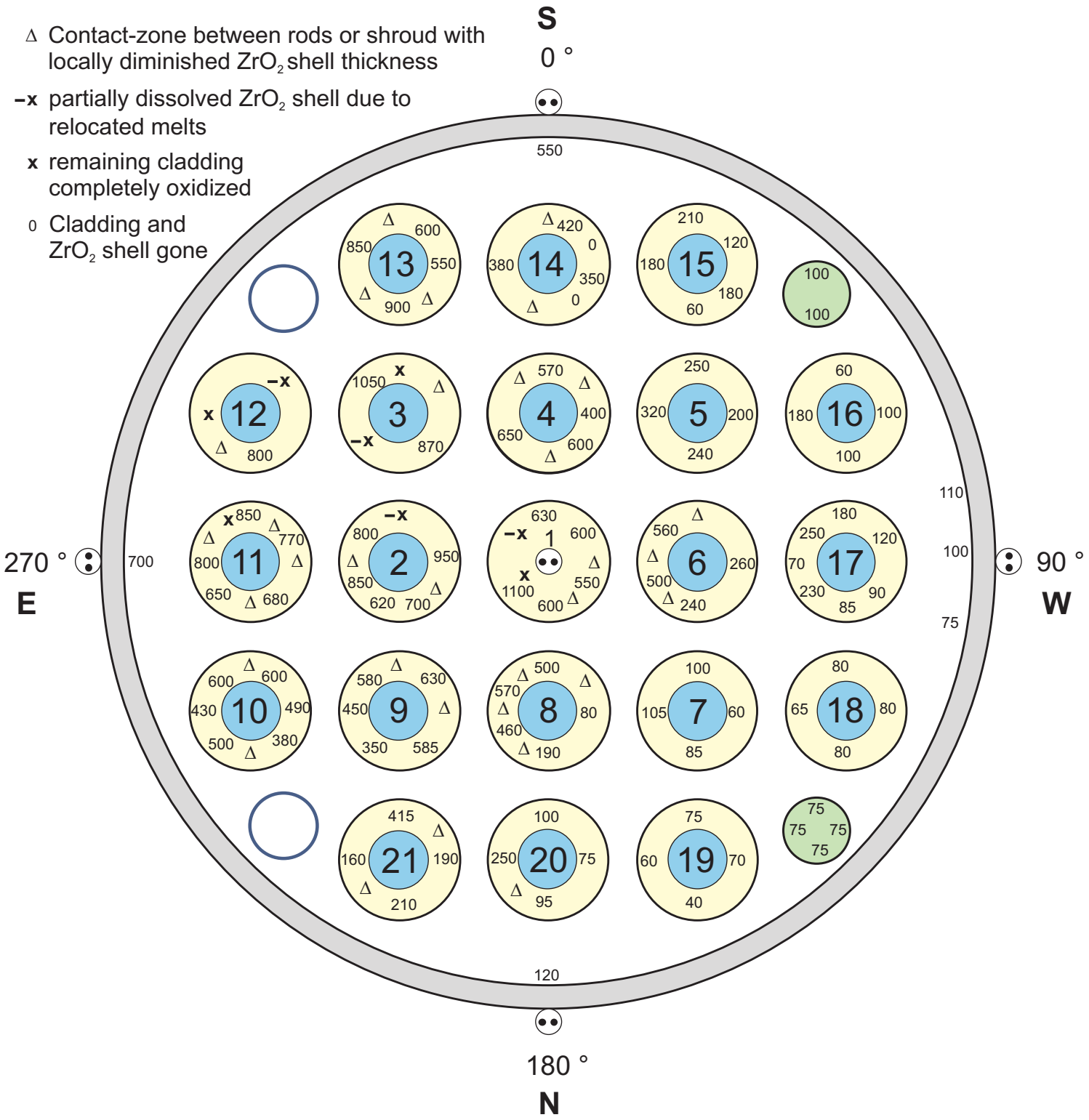

Test QUENCH-03; Cross section QUE-03-5 **Fig 130**

Oxide layer thicknesses at bundle elevation 800 mm

Δ Contact-zone between rods or shroud with locally diminished ZrO_2 shell thickness

x remaining cladding completely oxidized

0 Cladding and ZrO_2 shell gone

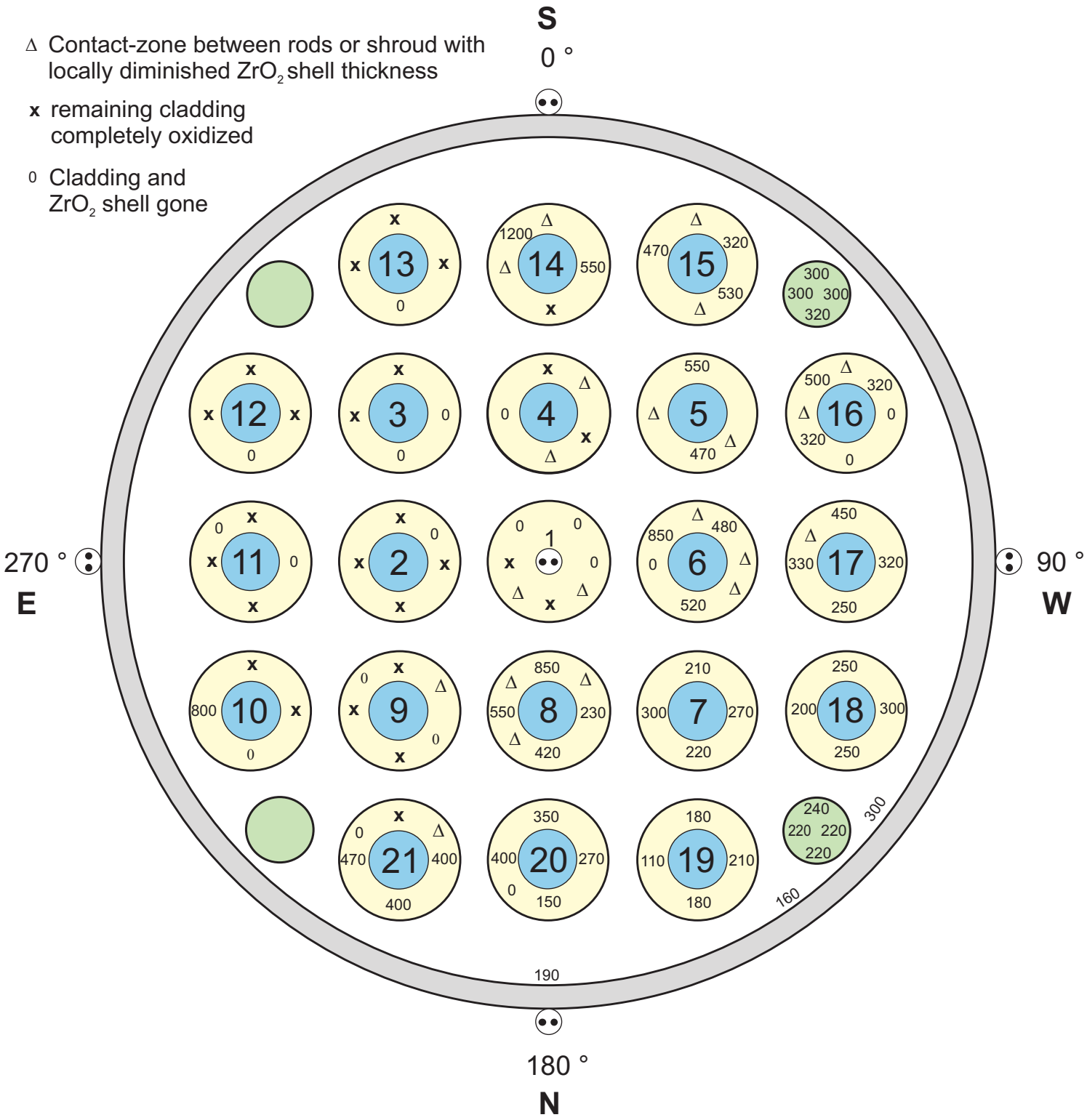

Test QUENCH-03; Cross section QUE-03-6 **Fig 131**

Oxide layer thicknesses at bundle elevation 950 mm

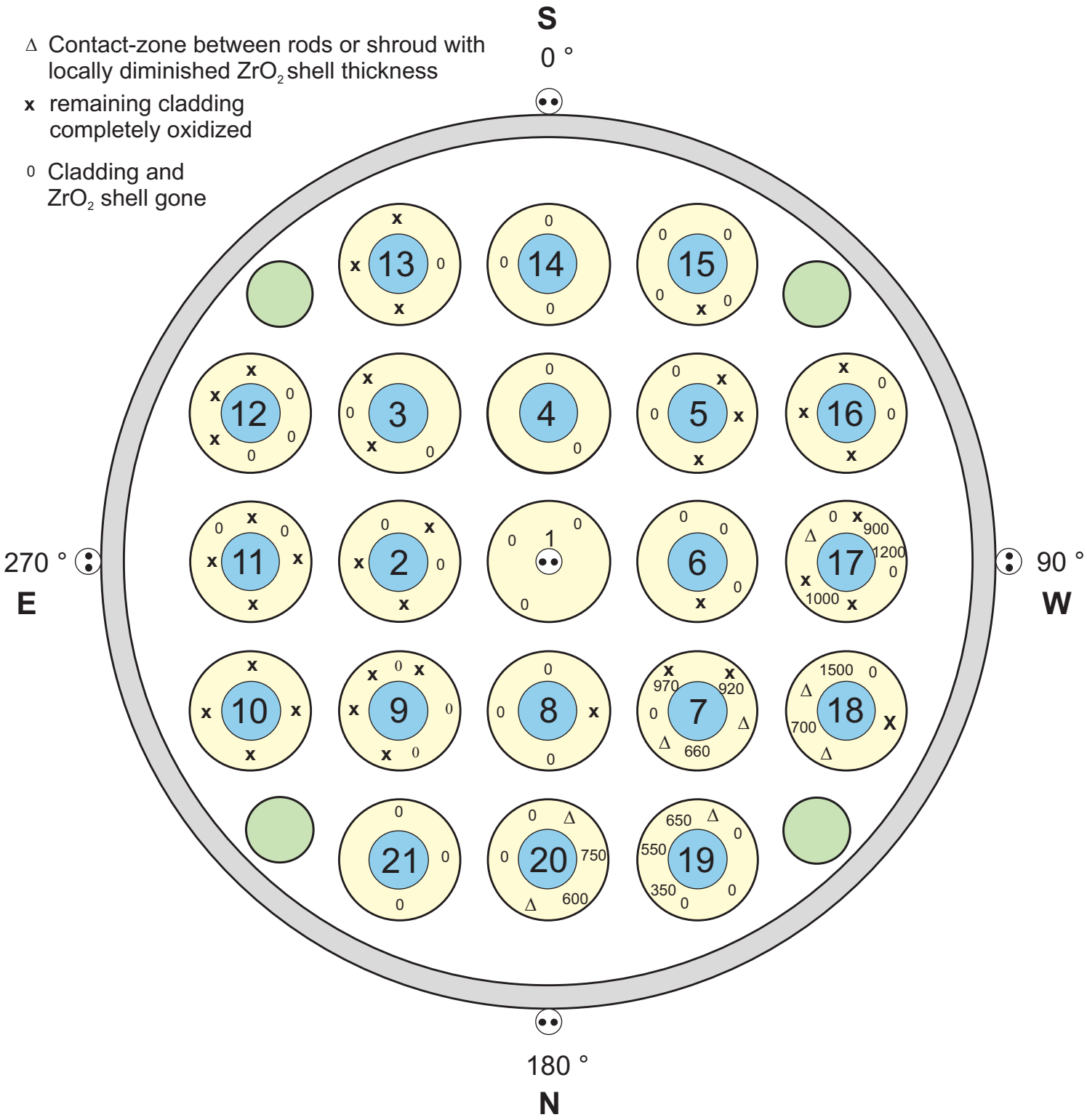

Test QUENCH-03; Cross section QUE-03-7 **Fig 132**

QUENCH-03:

Axial oxide layer thickness distribution

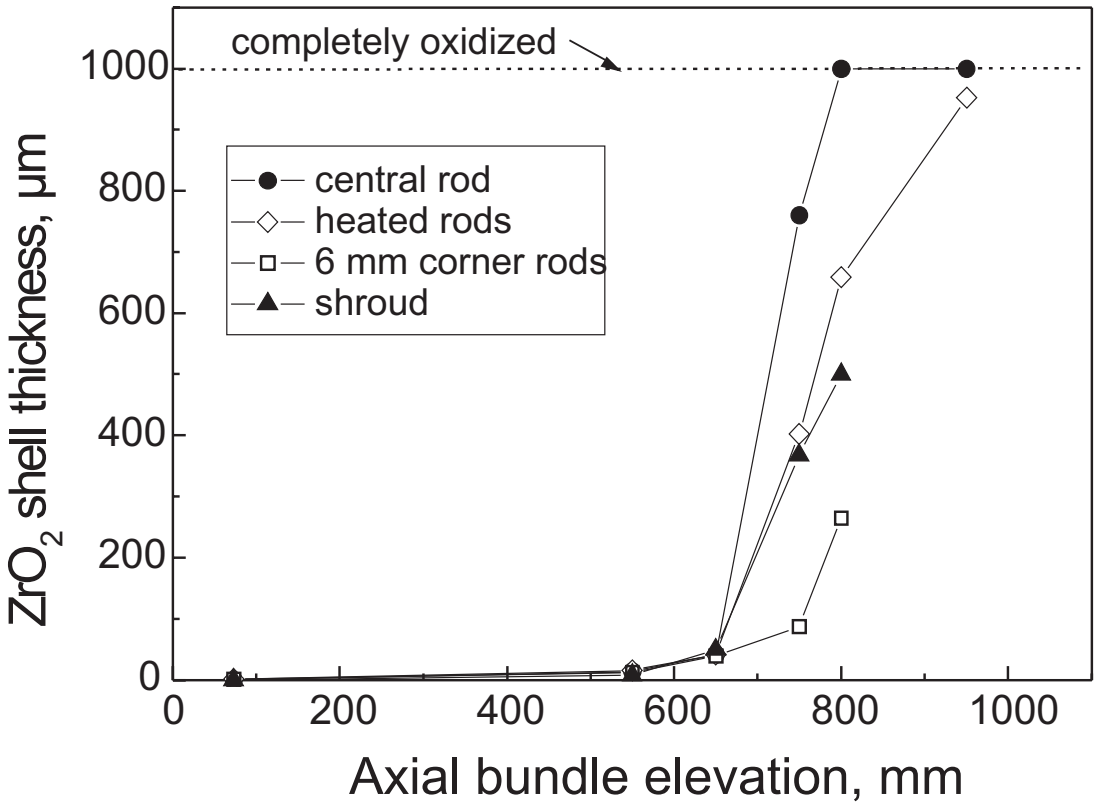

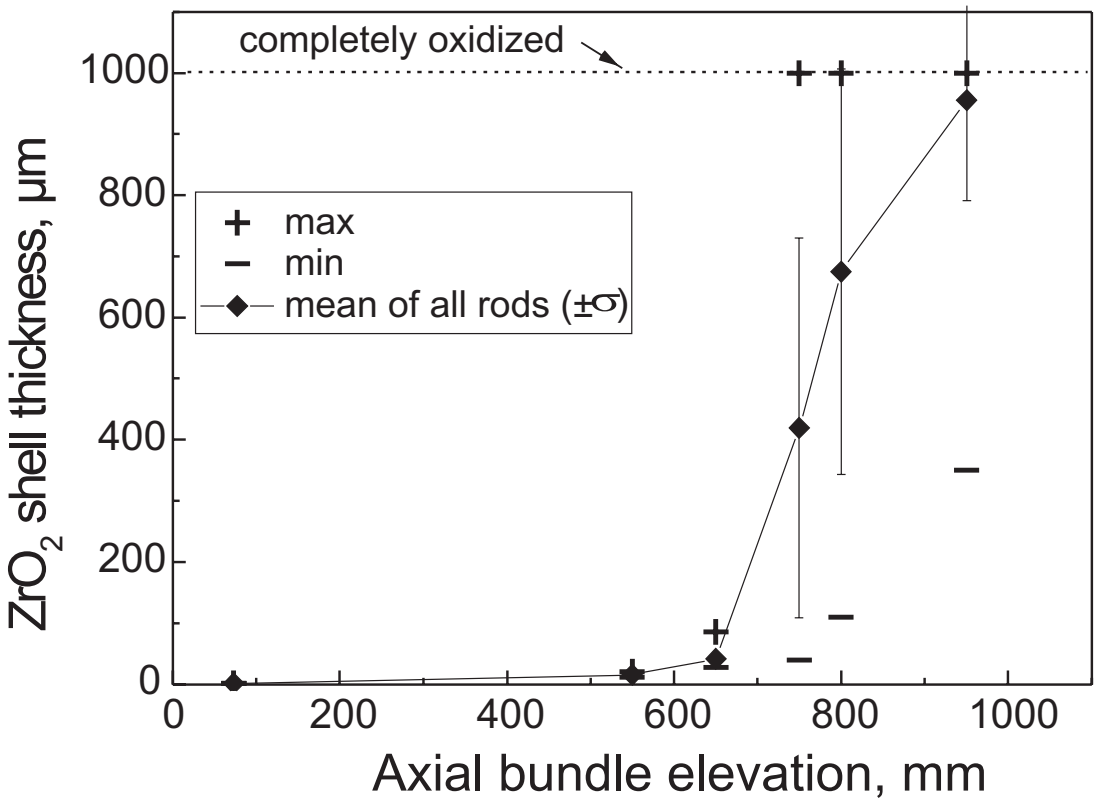

Fig 133

Figures to Calculational Results of QUENCH-02 and QUENCH-03

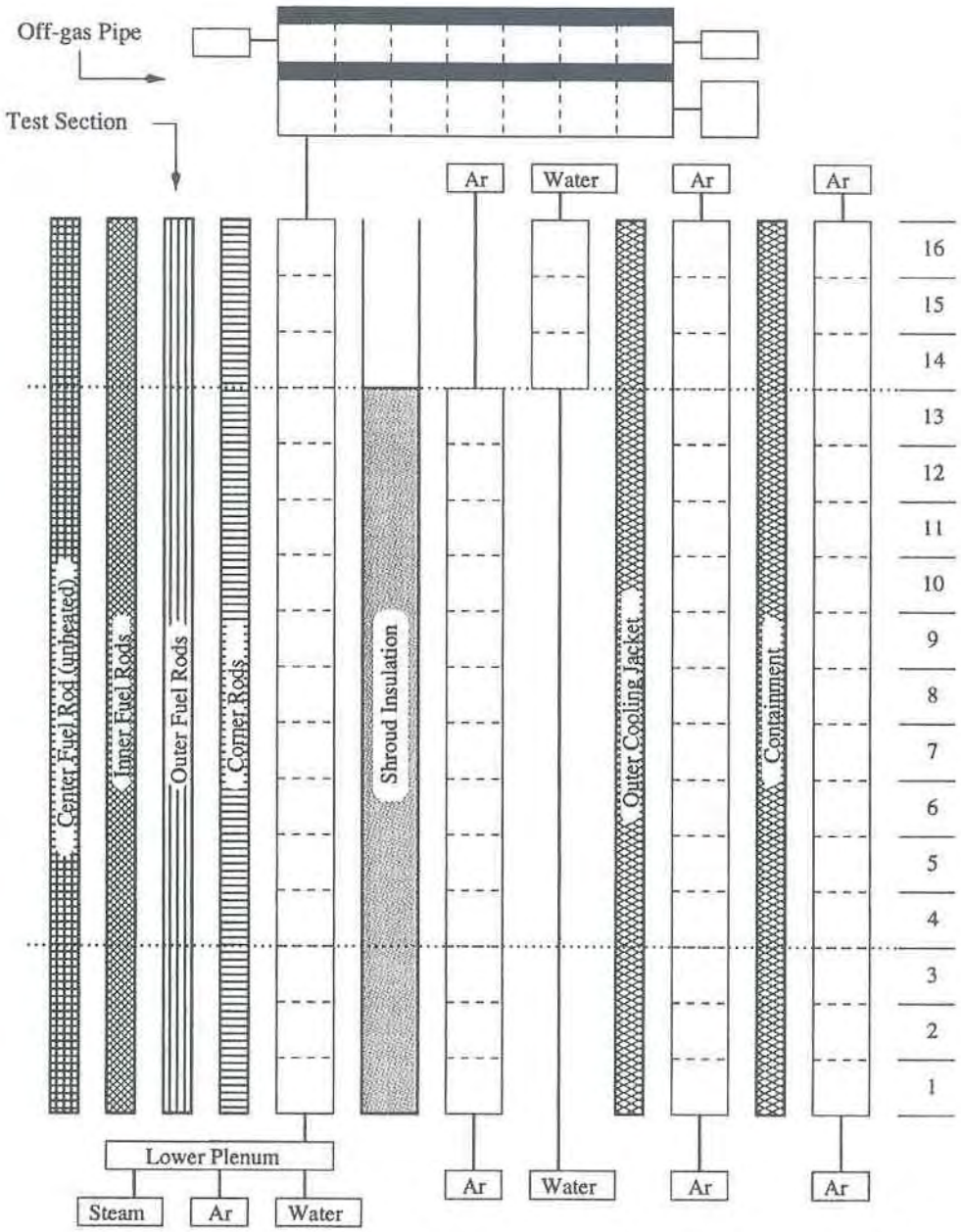
Off-gas Pipe
Test Section
Ar
Water
Ar
Ar
16
15
14
13
12
11
10
9
8
7
6
5
4
3
2
1
Center Fuel Rod (unheated)
Inner Fuel Rods
Outer Fuel Rods
Corner Rods
Shroud Insulation
Outer Cooling Jacket
Containment
Lower Plenum
Steam
Ar
Water
Ar
Water
Ar
Ar

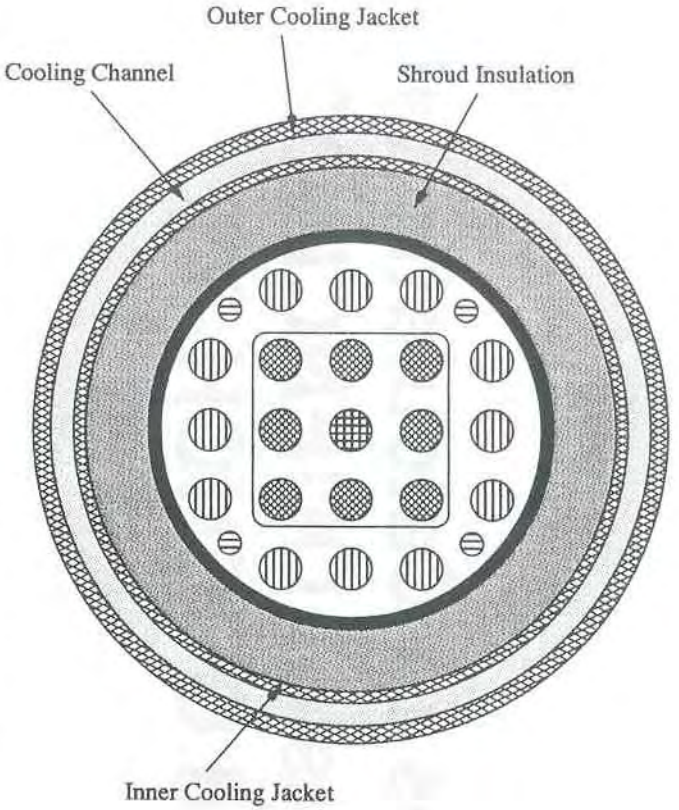
Outer Cooling Jacket
Cooling Channel
Shroud Insulation
Inner Cooling Jacket

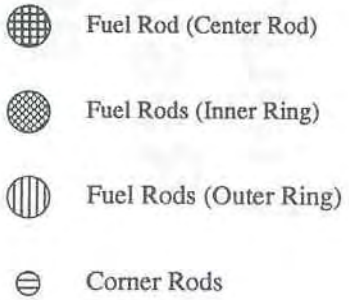
Fuel Rod (Center Rod)
Fuel Rods (Inner Ring)
Fuel Rods (Outer Ring)
Corner Rods

Fig. 134

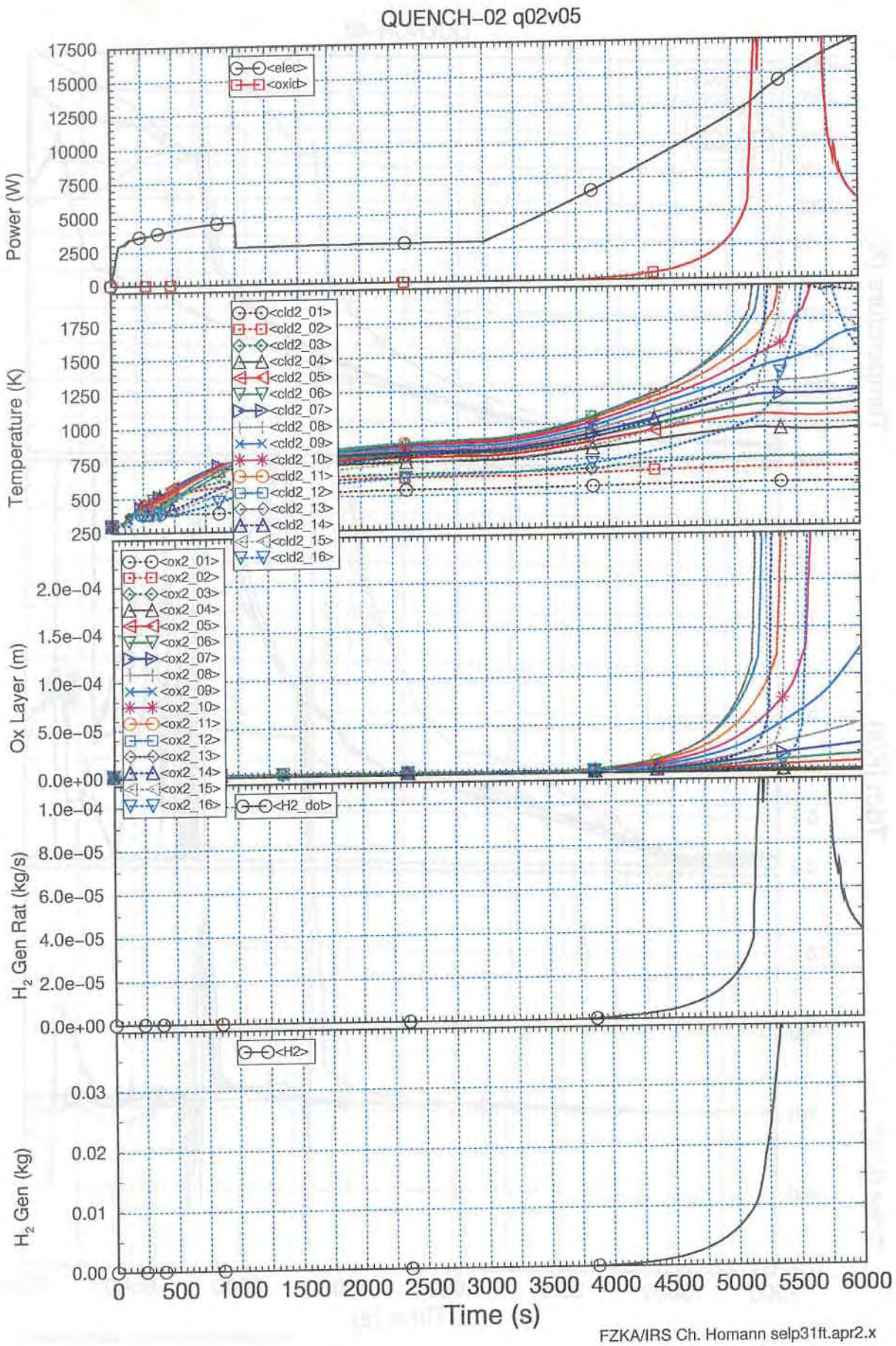
QUENCH–02 q02v05
Power (W)
<elec>
<oxid>
Temperature (K)
<cld2_01>
<cld2_02>
<cld2_03>
<cld2_04>
<cld2_05>
<cld2_06>
<cld2_07>
<cld2_08>
<cld2_09>
<cld2_10>
<cld2_11>
<cld2_12>
<cld2_13>
<cld2_14>
<cld2_15>
<cld2_16>
Ox Layer (m)
<ox2_01>
<ox2_02>
<ox2_03>
<ox2_04>
<ox2_05>
<ox2_06>
<ox2_07>
<ox2_08>
<ox2_09>
<ox2_10>
<ox2_11>
<ox2_12>
<ox2_13>
<ox2_14>
<ox2_15>
<ox2_16>
H2_dot
H2 Gen Rat (kg/s)
H2
H2 Gen (kg)
Time (s)
FZKA/IRS Ch. Homann selp31ft.apr2.x

Fig. 135

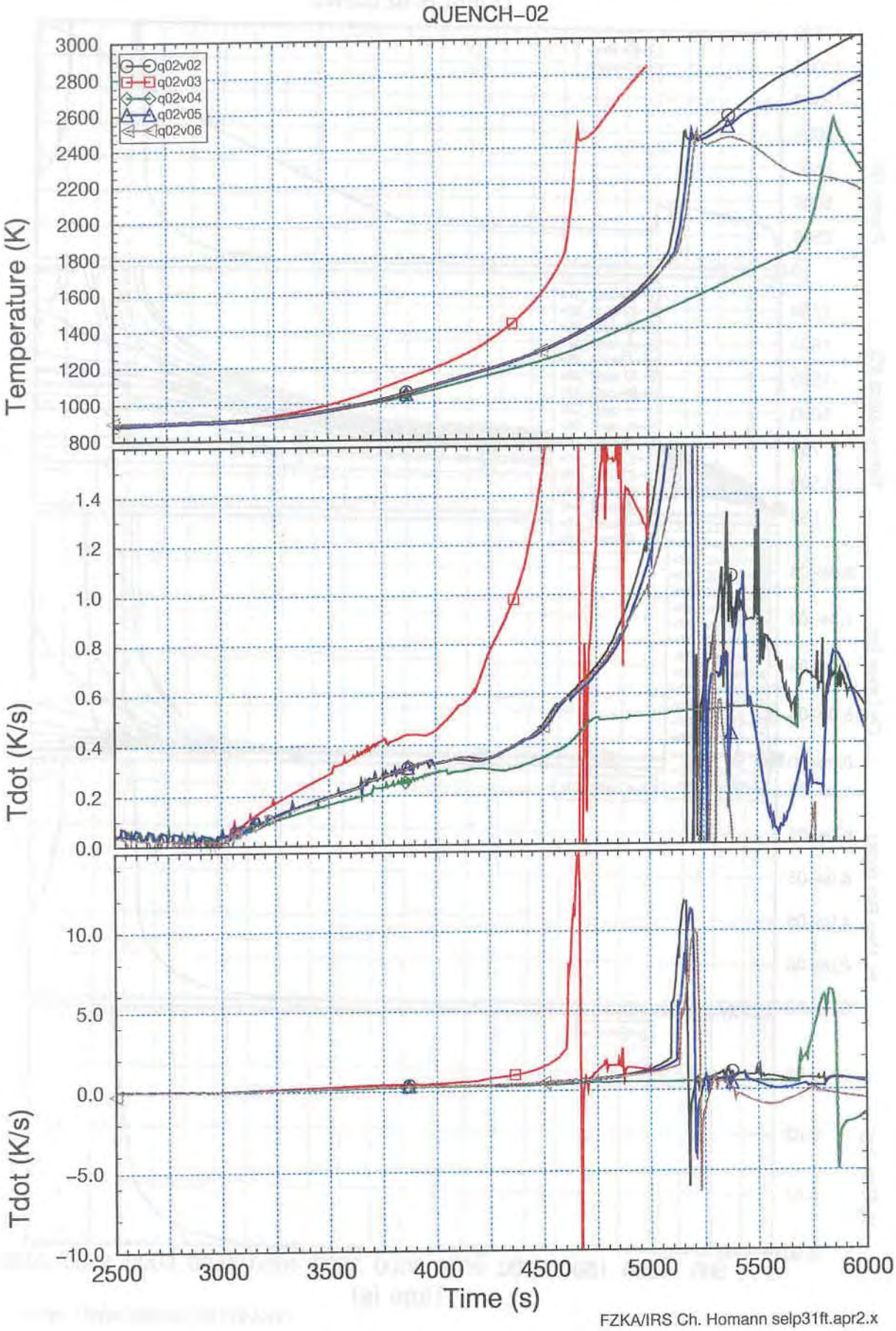
QUENCH-02
q02v02
q02v03
q02v04
q02v05
q02v06
Temperature (K)
Tdot (K/s)
Tdot (K/s)
Time (s)
FZKA/IRS Ch. Homann selp31ft.apr2.x

Fig. 136

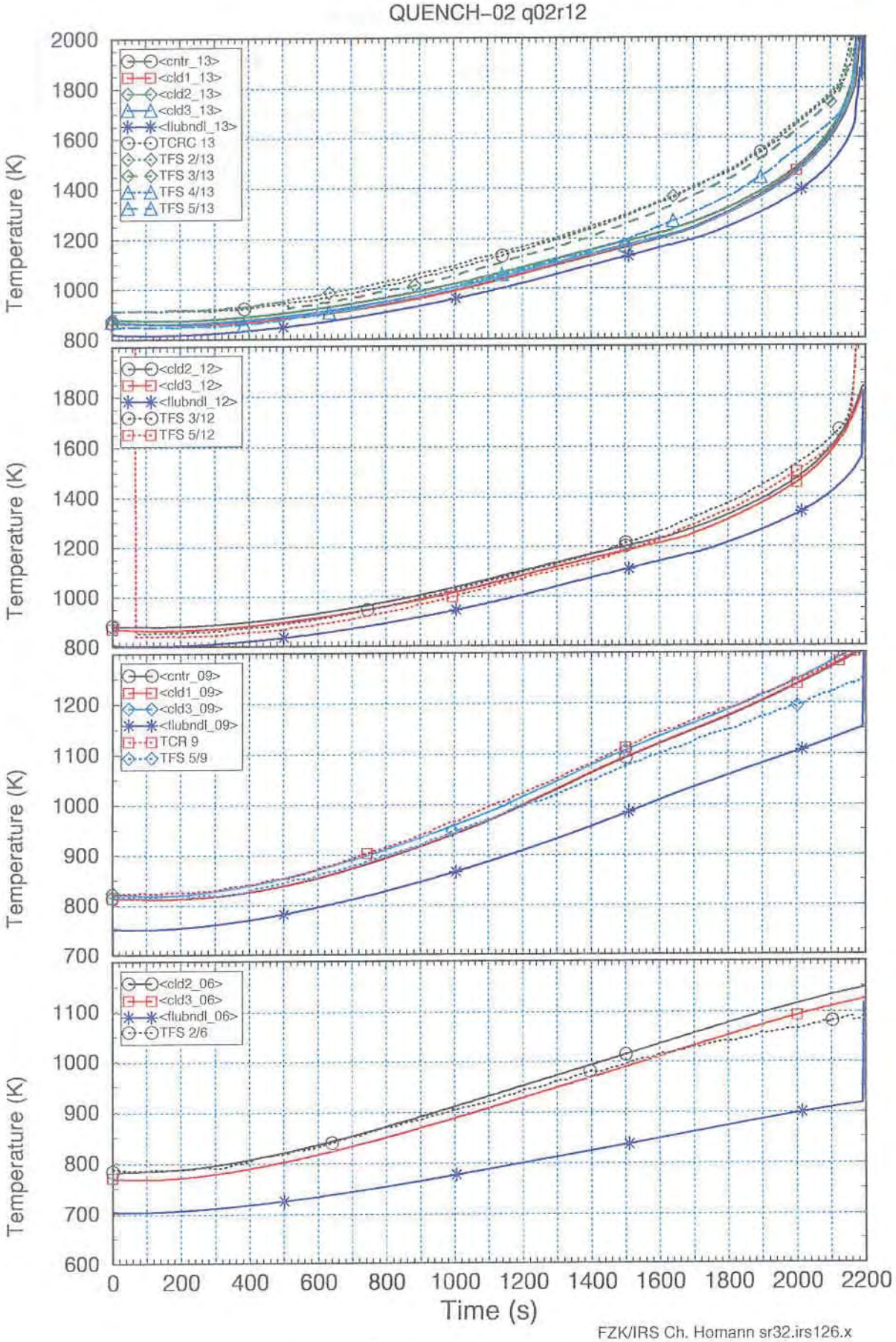
QUENCH–02 q02r12
Temperature (K)
<cntr_13>
<cld1_13>
<cld2_13>
<cld3_13>
<flubndl_13>
TCRC 13
TFS 2/13
TFS 3/13
TFS 4/13
TFS 5/13
<cld2_12>
<cld3_12>
<flubndl_12>
TFS 3/12
TFS 5/12
<cntr_09>
<cld1_09>
<cld3_09>
<flubndl_09>
TCR 9
TFS 5/9
<cld2_06>
<cld3_06>
<flubndl_06>
TFS 2/6
Time (s)
FZK/IRS Ch. Homann sr32.irs126.x

Fig. 137

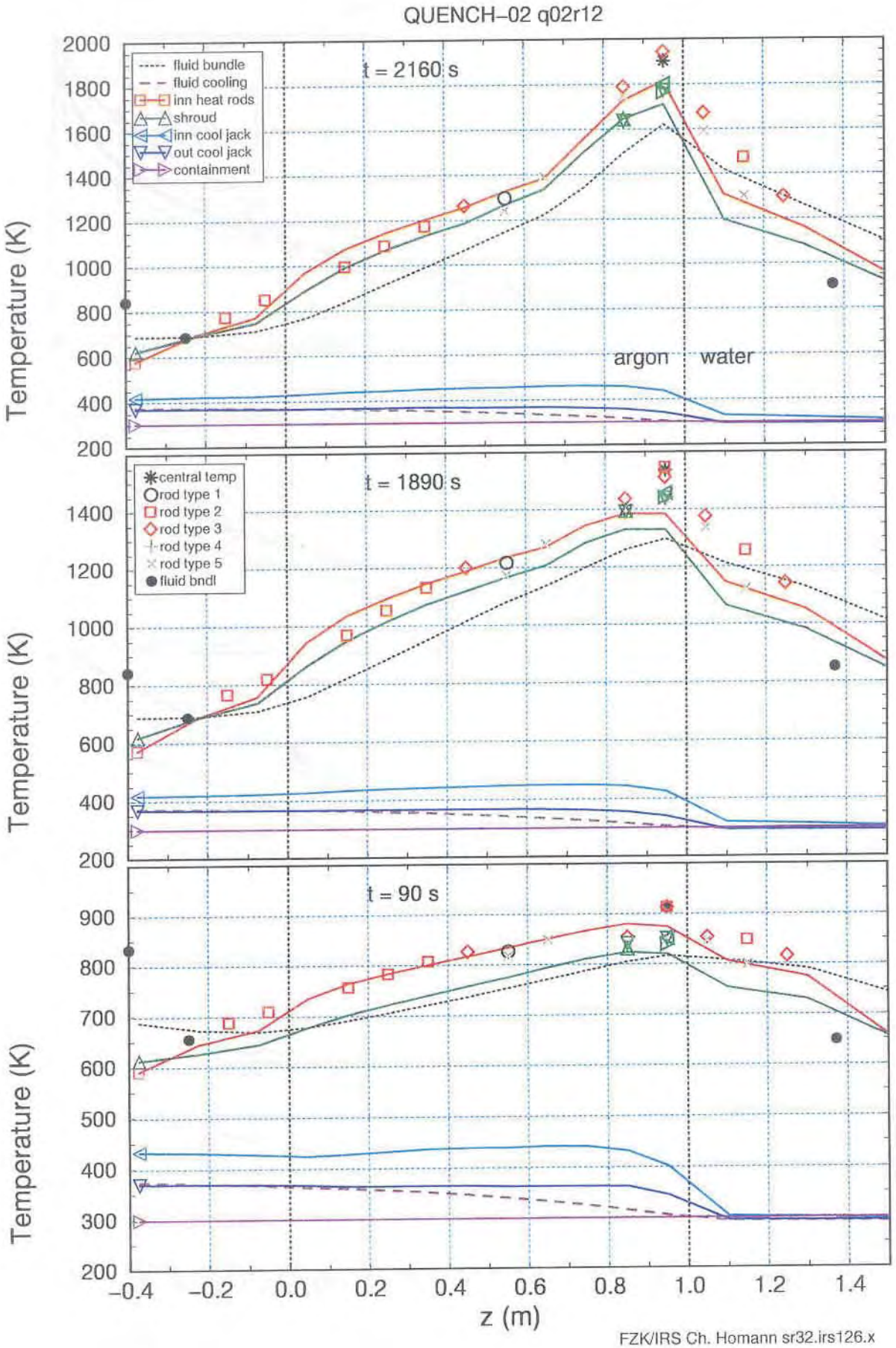
QUENCH–02 q02r12
fluid bundle
fluid cooling
inn heat rods
shroud
inn cool jack
out cool jack
containment
t = 2160 s
argon
water
central temp
rod type 1
rod type 2
rod type 3
rod type 4
rod type 5
fluid bndl
t = 1890 s
t = 90 s
Temperature (K)
z (m)
FZK/IRS Ch. Homann sr32.irs126.x

Fig. 138

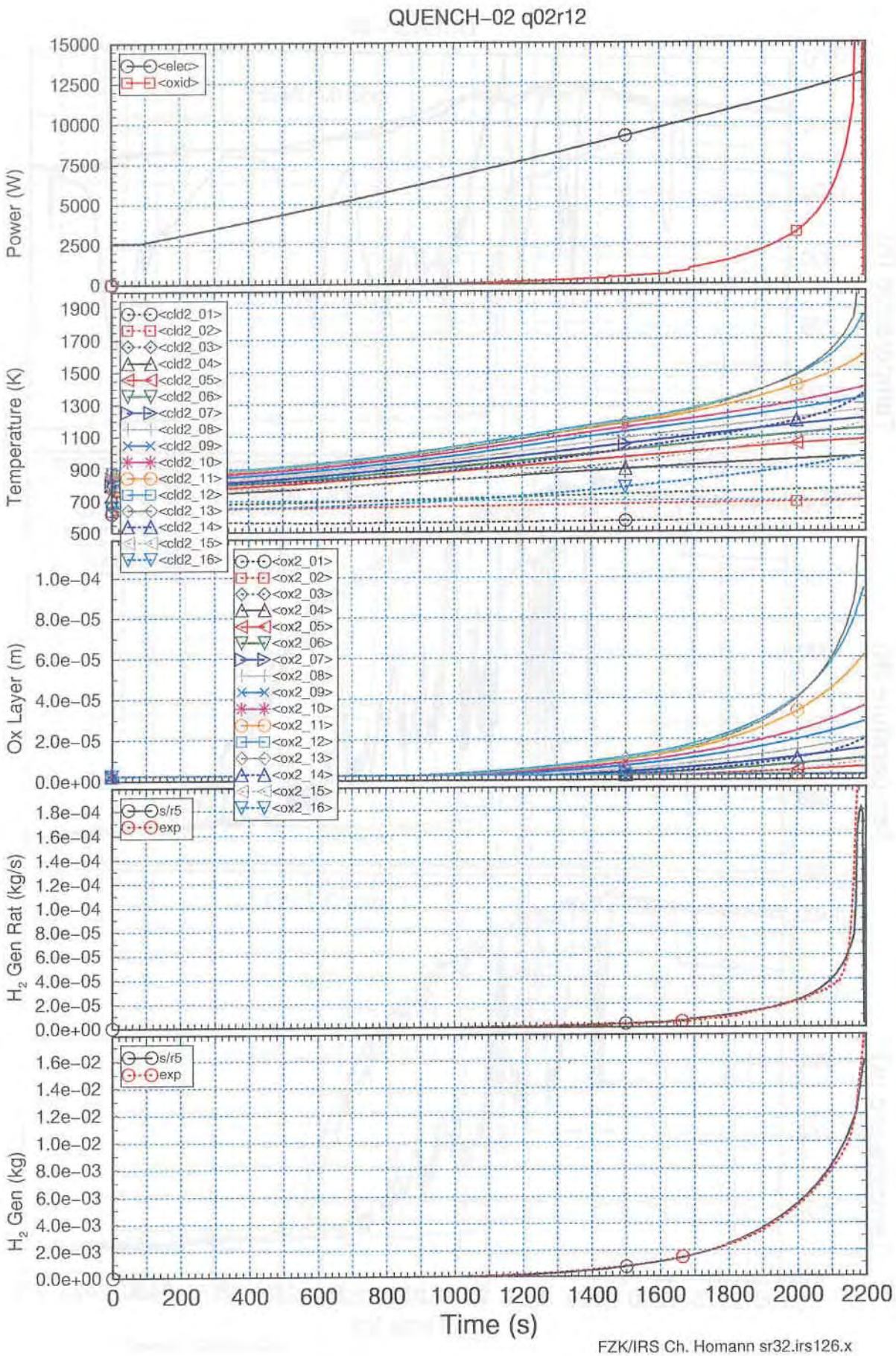
QUENCH–02 q02r12
Power (W)
<elec>
<oxid>
Temperature (K)
<cld2_01>
<cld2_02>
<cld2_03>
<cld2_04>
<cld2_05>
<cld2_06>
<cld2_07>
<cld2_08>
<cld2_09>
<cld2_10>
<cld2_11>
<cld2_12>
<cld2_13>
<cld2_14>
<cld2_15>
<cld2_16>
Ox Layer (m)
<ox2_01>
<ox2_02>
<ox2_03>
<ox2_04>
<ox2_05>
<ox2_06>
<ox2_07>
<ox2_08>
<ox2_09>
<ox2_10>
<ox2_11>
<ox2_12>
<ox2_13>
<ox2_14>
<ox2_15>
<ox2_16>
H2 Gen Rat (kg/s)
s/r5
exp
H2 Gen (kg)
s/r5
exp
Time (s)
FZK/IRS Ch. Homann sr32.irs126.x

Fig. 139

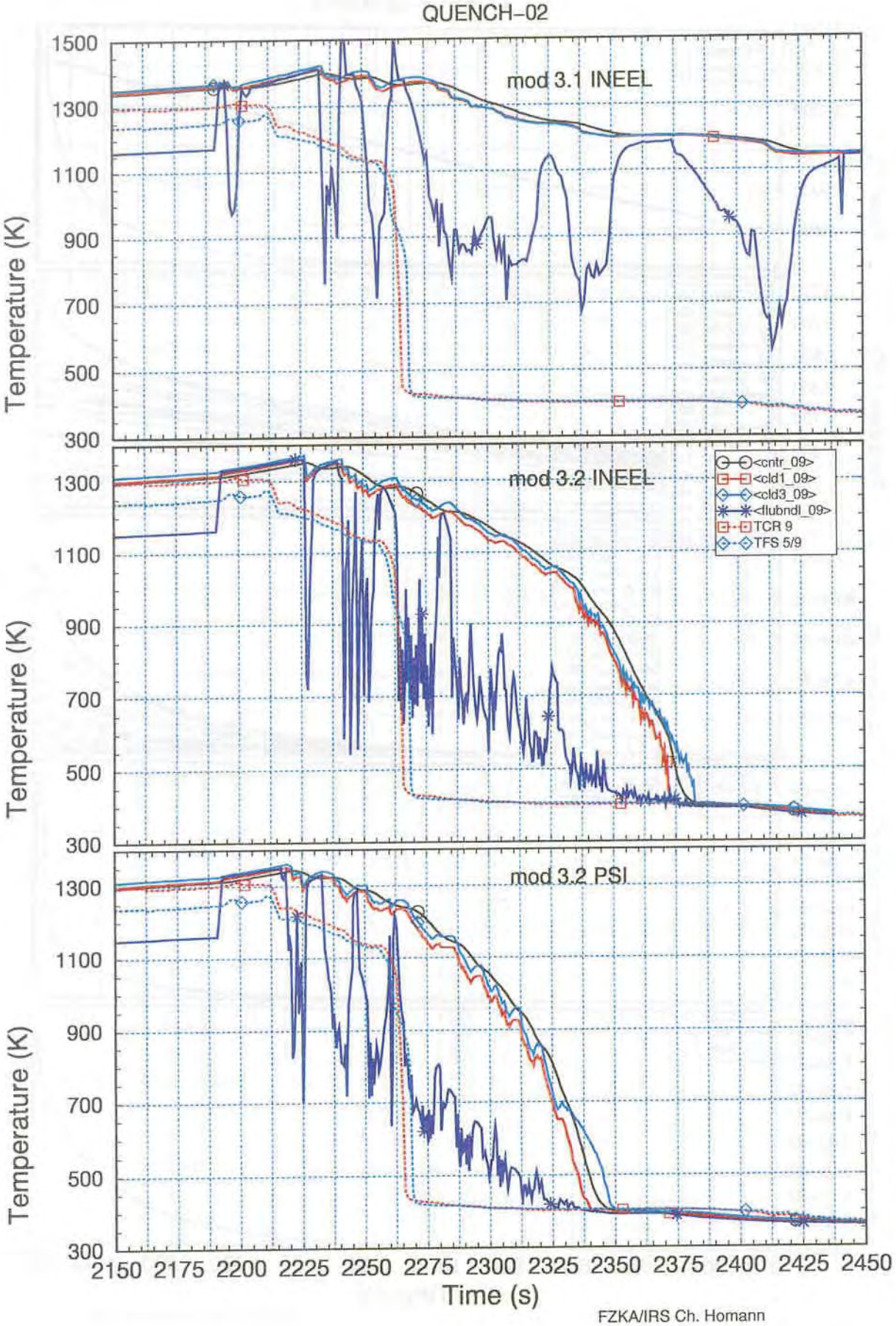
QUENCH-02
mod 3.1 INEEL
mod 3.2 INEEL
mod 3.2 PSI
<cntr_09>
<cld1_09>
<cld3_09>
<flubndl_09>
TCR 9
TFS 5/9
Temperature (K)
Time (s)
1500
1300
1100
900
700
500
300
2150 2175 2200 2225 2250 2275 2300 2325 2350 2375 2400 2425 2450
FZKA/IRS Ch. Homann

Fig. 140

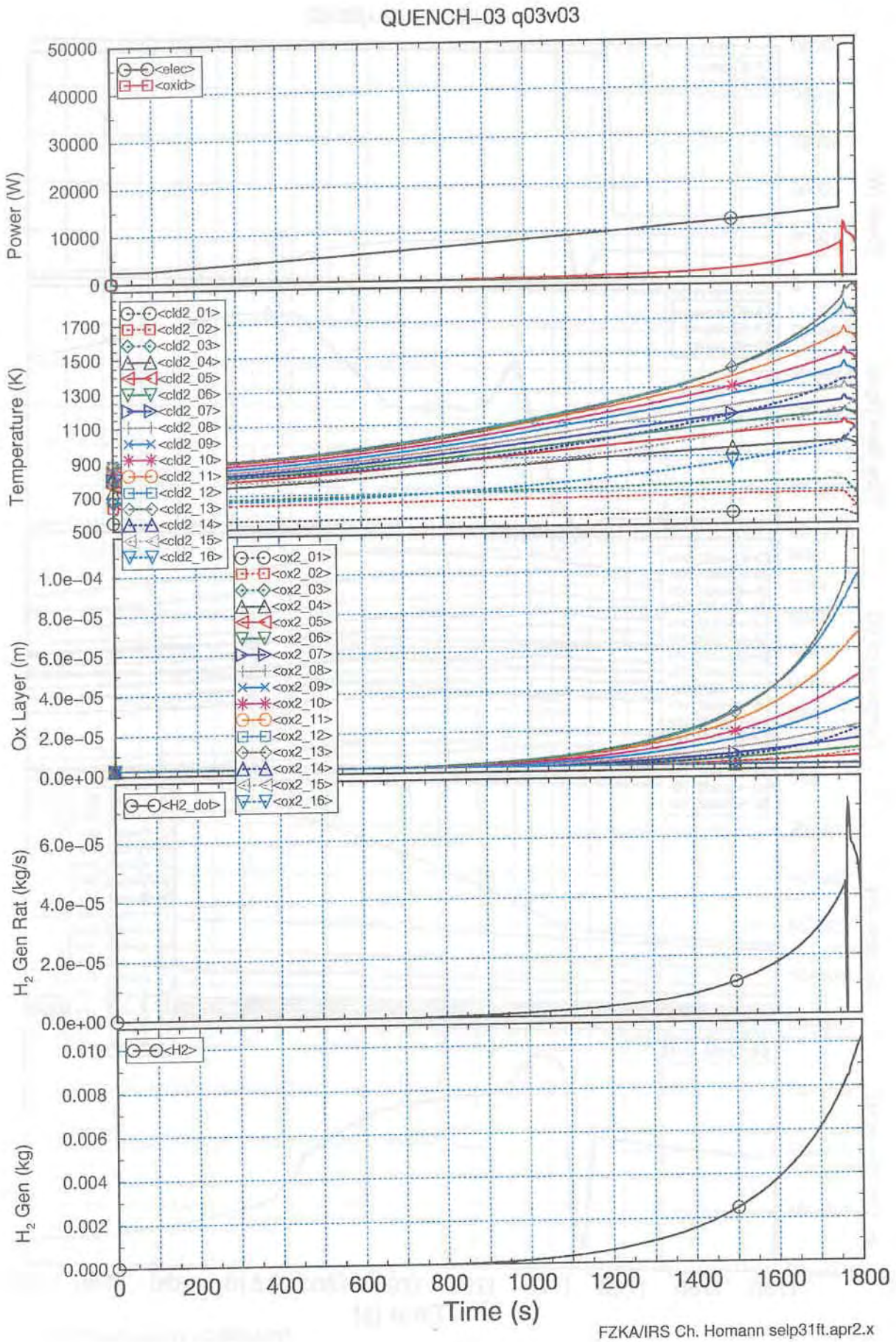
QUENCH–03 q03v03
Power (W)
50000
40000
30000
20000
10000
0
<elec>
<oxid>
Temperature (K)
1700
1500
1300
1100
900
700
500
<cld2_01>
<cld2_02>
<cld2_03>
<cld2_04>
<cld2_05>
<cld2_06>
<cld2_07>
<cld2_08>
<cld2_09>
<cld2_10>
<cld2_11>
<cld2_12>
<cld2_13>
<cld2_14>
<cld2_15>
<cld2_16>
Ox Layer (m)
1.0e–04
8.0e–05
6.0e–05
4.0e–05
2.0e–05
0.0e+00
<ox2_01>
<ox2_02>
<ox2_03>
<ox2_04>
<ox2_05>
<ox2_06>
<ox2_07>
<ox2_08>
<ox2_09>
<ox2_10>
<ox2_11>
<ox2_12>
<ox2_13>
<ox2_14>
<ox2_15>
<ox2_16>
H2 Gen Rat (kg/s)
6.0e–05
4.0e–05
2.0e–05
0.0e+00
<H2_dot>
H2 Gen (kg)
0.010
0.008
0.006
0.004
0.002
0.000
<H2>
0
200
400
600
800
1000
1200
1400
1600
1800
Time (s)
FZKA/IRS Ch. Homann selp31ft.apr2.x

Fig. 141

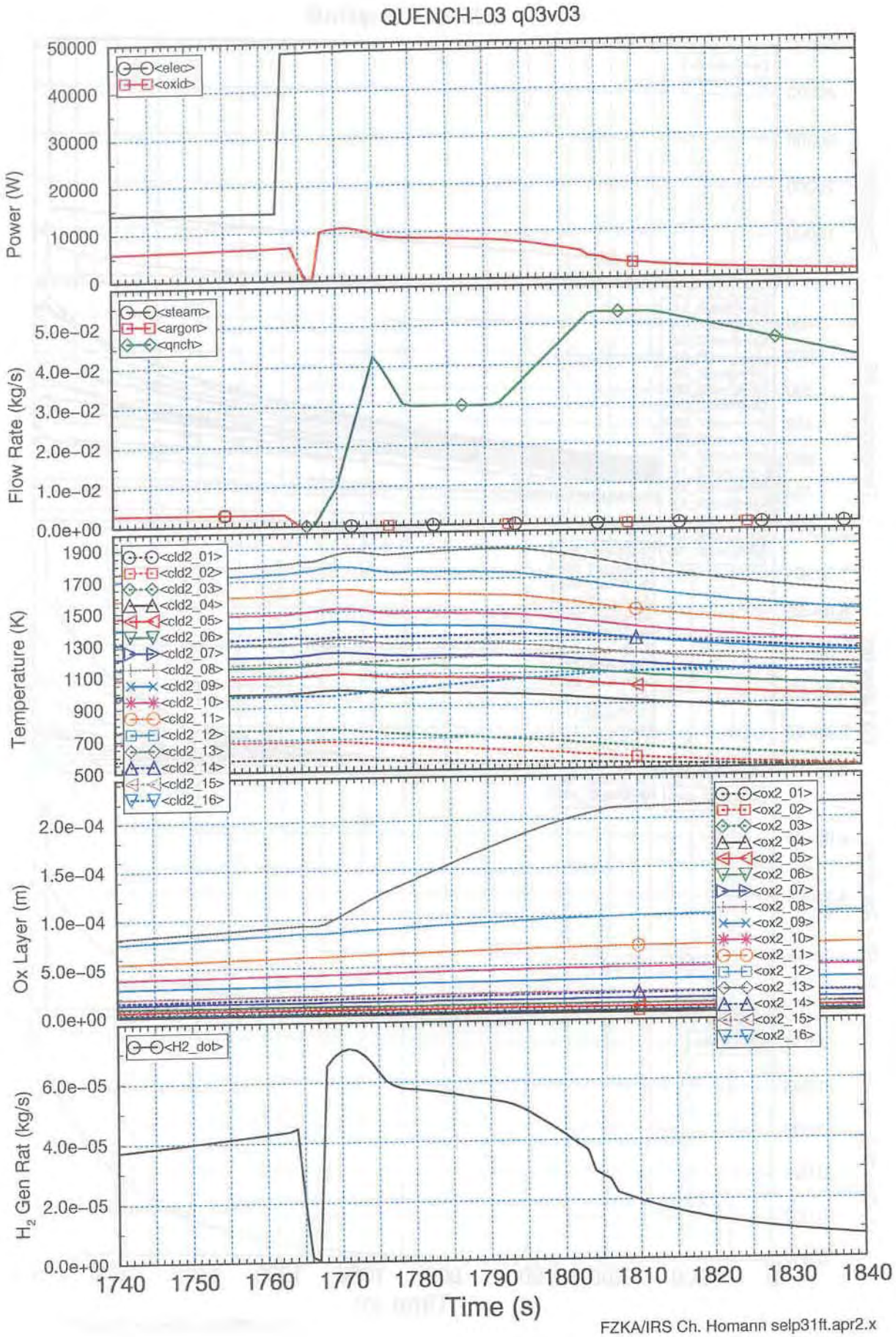
QUENCH–03 q03v03
Power (W)
<elec>
<oxid>
Flow Rate (kg/s)
<steam>
<argon>
<qnch>
Temperature (K)
<cld2_01>
<cld2_02>
<cld2_03>
<cld2_04>
<cld2_05>
<cld2_06>
<cld2_07>
<cld2_08>
<cld2_09>
<cld2_10>
<cld2_11>
<cld2_12>
<cld2_13>
<cld2_14>
<cld2_15>
<cld2_16>
Ox Layer (m)
<ox2_01>
<ox2_02>
<ox2_03>
<ox2_04>
<ox2_05>
<ox2_06>
<ox2_07>
<ox2_08>
<ox2_09>
<ox2_10>
<ox2_11>
<ox2_12>
<ox2_13>
<ox2_14>
<ox2_15>
<ox2_16>
H2 Gen Rat (kg/s)
<H2_dot>
Time (s)
FZKA/IRS Ch. Homann selp31ft.apr2.x

Fig. 142

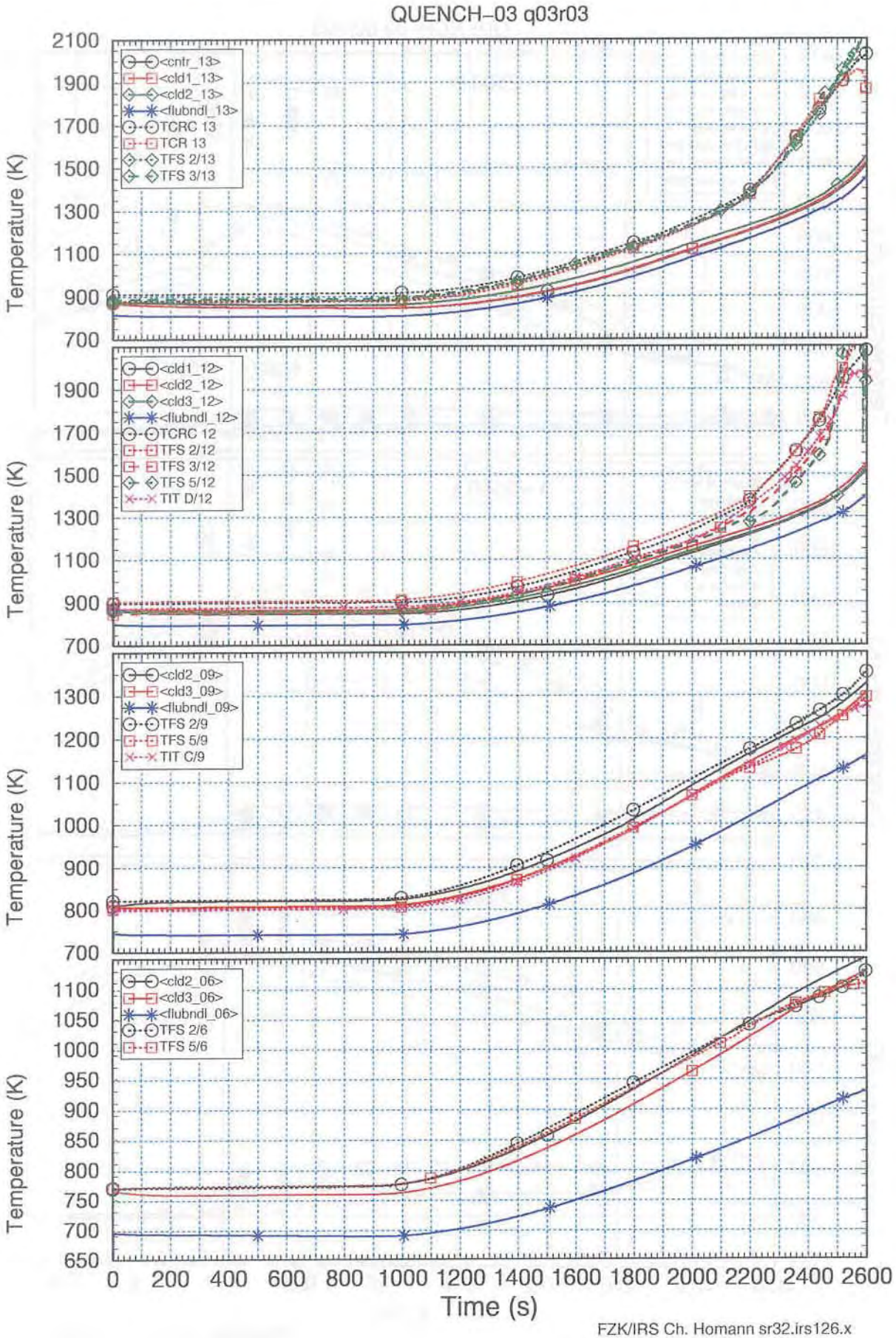
QUENCH–03 q03r03
Temperature (K)
<cntr_13>
<cld1_13>
<cld2_13>
<flubndl_13>
TCRC 13
TCR 13
TFS 2/13
TFS 3/13
<cld1_12>
<cld2_12>
<cld3_12>
<flubndl_12>
TCRC 12
TFS 2/12
TFS 3/12
TFS 5/12
TIT D/12
<cld2_09>
<cld3_09>
<flubndl_09>
TFS 2/9
TFS 5/9
TIT C/9
<cld2_06>
<cld3_06>
<flubndl_06>
TFS 2/6
TFS 5/6
Time (s)
FZK/IRS Ch. Homann sr32.irs126.x

Fig. 143

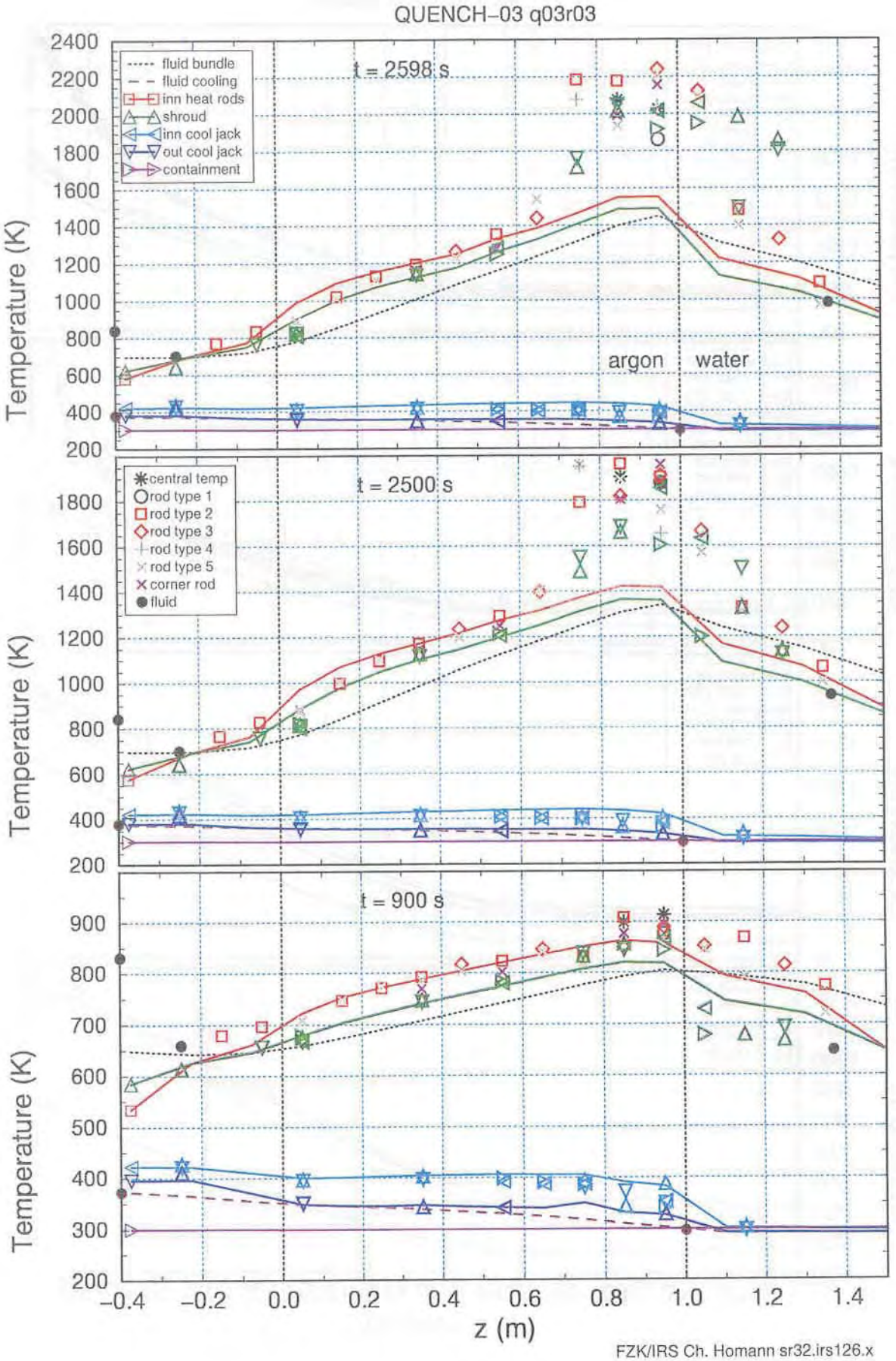
QUENCH–03 q03r03
fluid bundle
fluid cooling
inn heat rods
shroud
inn cool jack
out cool jack
containment
t = 2598 s
argon
water
central temp
rod type 1
rod type 2
rod type 3
rod type 4
rod type 5
corner rod
fluid
t = 2500 s
t = 900 s
Temperature (K)
z (m)
FZK/IRS Ch. Homann sr32.irs126.x

Fig. 144

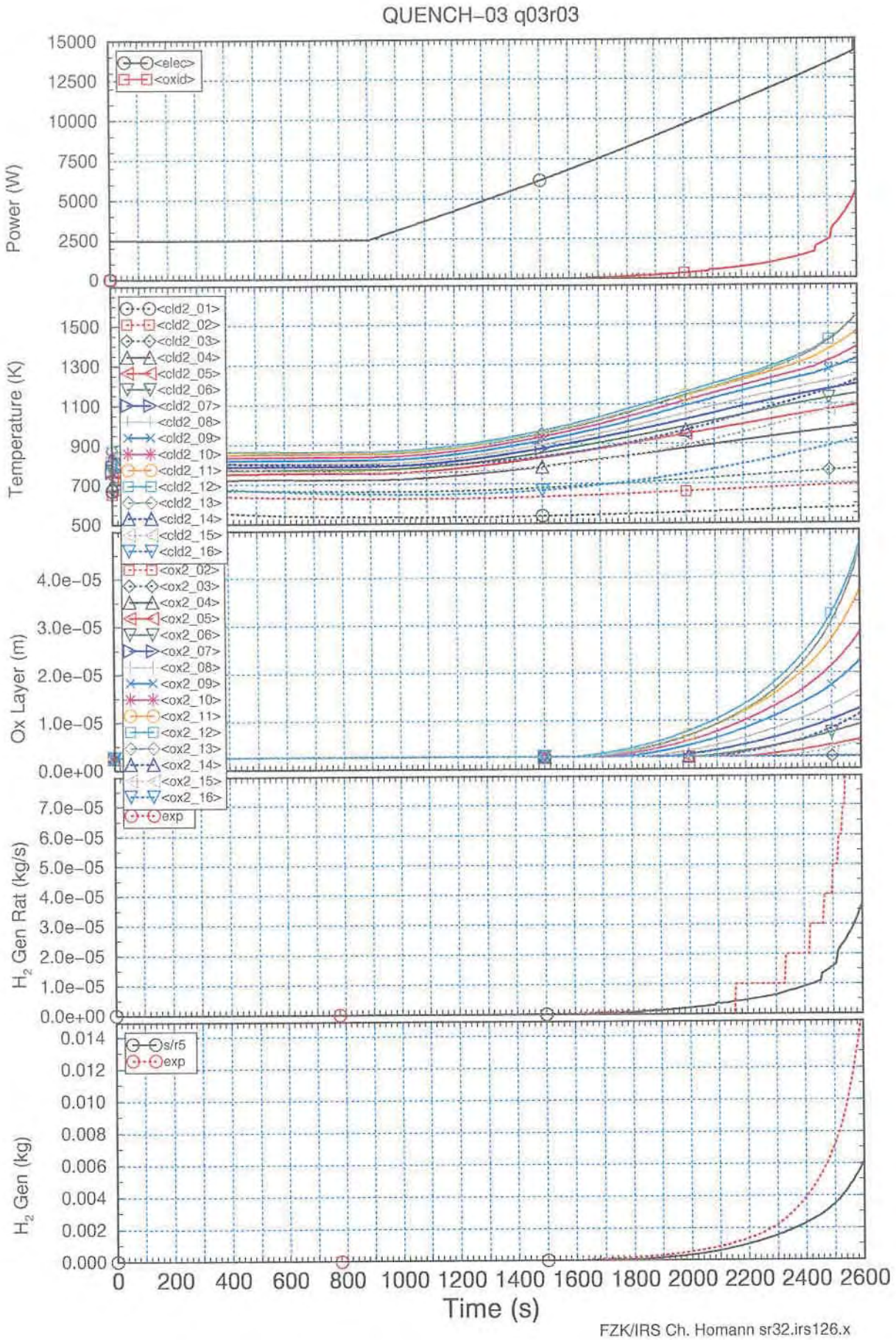
QUENCH–03 q03r03
Power (W)
<elec>
<oxid>
Temperature (K)
<cld2_01>
<cld2_02>
<cld2_03>
<cld2_04>
<cld2_05>
<cld2_06>
<cld2_07>
<cld2_08>
<cld2_09>
<cld2_10>
<cld2_11>
<cld2_12>
<cld2_13>
<cld2_14>
<cld2_15>
<cld2_16>
Ox Layer (m)
<ox2_02>
<ox2_03>
<ox2_04>
<ox2_05>
<ox2_06>
<ox2_07>
<ox2_08>
<ox2_09>
<ox2_10>
<ox2_11>
<ox2_12>
<ox2_13>
<ox2_14>
<ox2_15>
<ox2_16>
exp
H2 Gen Rat (kg/s)
s/r5
exp
H2 Gen (kg)
Time (s)
FZK/IRS Ch. Homann sr32.irs126.x

Fig. 145